THE CONCURRENT ATOMISTIC-CONTINUUM METHOD: ADVANCEMENTS AND APPLICATIONS IN PLASTICITY OF FACE-CENTERED CUBIC METALS

A Dissertation
Presented to
The Academic Faculty

by

Shuozhi Xu

In Partial Fulfillment
of the Requirements for the Degree
Doctor of Philosophy in the
G.W.W. School of Mechanical Engineering

Georgia Institute of Technology
December 2016

THE CONCURRENT ATOMISTIC-CONTINUUM METHOD: ADVANCEMENTS AND APPLICATIONS IN PLASTICITY OF FACE-CENTERED CUBIC METALS

Approved by:

Dr. David L. McDowell, Advisor
G.W.W. School of Mechanical Engineering
Georgia Institute of Technology

Dr. Laurent Capolungo
Materials Science and Technology Division
Los Alamos National Laboratory

Dr. Ting Zhu
G.W.W. School of Mechanical Engineering
Georgia Institute of Technology

Dr. Surya Kalidindi
G.W.W. School of Mechanical Engineering
Georgia Institute of Technology

Dr. Chaitanya S. Deo
G.W.W. School of Mechanical Engineering
Georgia Institute of Technology

Dr. Josh Kacher
School of Materials Science and Engineering
Georgia Institute of Technology

Date Approved: Nov 3rd, 2016

To my family

ACKNOWLEDGEMENTS

This dissertation would not have been possible without the support of my advisor Dr. David L. McDowell, whose excellent guidance, constant support, and encouragement over the past five years have contributed immensely to my professional development and shaped my research interests. I thank my reading committee for their valuable inputs that are instrumental in this research effort: Dr. Ting Zhu, Dr. Chaitanya S. Deo, Dr. Laurent Capolungo, Dr. Surya Kalidindi, and Dr. Josh Kacher. I also thank Dr. Min Zhou for his guidance during my teaching practicum.

This dissertation is based upon work primarily supported by the National Science Foundation as a collaborative effort between Georgia Tech (CMMI-1232878, D.L. McDowell, PI) and University of Florida (CMMI-1233113, Y. Chen, PI). The Carter N. Paden, Jr. Distinguished Chair in Metals Processing is also greatly acknowledged. This work used Blacklight, Comet, and Bridges on the Extreme Science and Engineering Discovery Environment (XSEDE), which is supported by National Science Foundation grant number ACI-1053575.

I thank my colleagues at Georgia Tech: Dr. Gustavo Castelluccio, Dr. Brett Ellis, Dr. William Musinski, Dr. Jagan Padbidri, Dr. Jeff Lloyd, Dr. Anirban Patra, Dr. Xin Dong, Dr. Shreevant Tiwari, Dr. Zachary Kraus, Dr. Matthew Priddy, Dr. Dengke Chen, Ben Smith, Jin Song, Conor Hennessey, Paul Kern, Joel Blumer, Evan Shimek, Brian Ferri, Noah Paulson, Aaron Tallman, Adrienne Muth, Luke Costello, Thomas Payne, Krzysztof Stopka, and Gary Whelan. I also thank Dr. Alexander Stukowski at Darmstadt University of Technology for providing the dislocation extraction algorithm code. I am grateful to the fruitful collaborations with the groups of Dr. Youping Chen at University of Florida and Dr. Liming Xiong at Iowa State University over the last four years. Discussions with Dr. Jinghong Fan at Alfred University have been invaluable in advancing my research.

I thank my parents, whose support and encouragement have helped me realize my potential. Most of all, I thank my wife Yanqing Su, for her patience and unwavering love

through all the highs and lows of our lives during these years.

TABLE OF CONTENTS

LIST OF TABLES

LIST OF FIGURES

LIST OF SYMBOLS OR ABBREVIATIONS

1D	One-Dimensional.
1NN	First Nearest Neighbor.
2D	Two-Dimensional.
2NN	Second Nearest Neighbor.
3D	Three-Dimensional.
a-CNA	Adaptive Common Neighbor Analysis.
AD	Atom Decomposition.
AFT	Atomistic Field Theory.
BCC	Body-Centered Cubic.
BDM	Bridging Domain Method.
BTD	Brittle-To-Ductile.
CAC	Concurrent Atomistic-Continuum.
CADD	Coupled Atomistic/Discrete Dislocation.
CMK	Crone-Munday-Knap.
CPFEM	Crystal Plasticity Finite Element Method.
CTB	Coherent Twin Boundary.
CZM	Cohesize Zone Method.
DD	Dislocation Dynamics.
DOF	Degree of Freedom.
DOFs	Degrees of Freedom.
DSC	Displacement Shift Complete.
DXA	Dislocation Extraction Algorithm.
EAM	Embedded-Atom Method.
FCC	Face-Centered Cubic.
FD	Force Decomposition.
FE	Friedel-Escaig.
FEM	Finite Element Method.

FL	Fleischer.
FR	Frank-Read.
GB	Grain Boundary.
GBs	Grain Boundaries.
GSFE	Generalized Stacking Fault Energy.
HCP	Hexagonal Close-Packed.
LAMMPS	Large-scale Atomic/Molecular Massively Parallel Simulator.
LJ	Lennard-Jones.
LRB	Lee-Robertson-Birnbaum.
MD	Molecular Dynamics.
MMM	Multiresolution Molecular Mechanics.
MPI	Message Passing Interface.
MS	Molecular Statics.
NEB	Nudged Elastic Band.
OVITO	Open Visualization Tool.
PAD	Periodic Array of Dislocations.
PBCs	Periodic Boundary Conditions.
PFM	Phase Field Method.
PK	Peach-Koehler.
PN	Peierls-Nabarro.
PR	Parrinello-Rahman.
QC	Quasicontinuum.
SB	Scattergood-Bacon.
SD	Spatial Decomposition.
SFE	Stacking Fault Energy.
STGB	Symmetric Tilt Grain Boundary.
STGBs	Symmetric Tilt Grain Boundaries.
SU	Structural Unit.
SUs	Structural Units.

TB	Twin Boundary.
TEM	Transmission Electron Microscopy.
XFEM	Extended Finite Element Method.

SUMMARY

Metal plasticity is a multiscale phenomenon that is manifested by irreversible microstructure rearrangement associated with nucleation, multiplication, interaction, and migration of dislocations. Long range elastic interactions between dislocations and other crystal defects are important to describe, along with the nonlocal, nonlinear dislocation core field. These requirements necessitate multiscale modeling techniques which (i) describe certain lattice defects and their interactions using fully resolved atomistics, (ii) preserve the net Burgers vector and associated long range stress fields of curved mixed character dislocations in a sufficiently large continuum domain in a fully three-dimensional model, and (iii) employ the same governing equations and interatomic potentials in both atomistic and continuum domains to avoid the usage of phenomenological parameters/criteria and *ad hoc* procedures for passing dislocation segments between the two domains. One such approach is the concurrent atomistic-continuum (CAC) method. Unlike many other concurrent multiscale approaches, the continuum domain in CAC admits motion of dislocations and intrinsic stacking faults through a lattice without necessity of adaptive mesh refinement while employing an underlying interatomic potential as the only constitutive relation and is thus a suitable tool for dislocation-mediated metal plasticity phenomena.

In this dissertation, the CAC method is advanced in multiple aspects and applied in a series of problems in plasticity of face-centered cubic (FCC) metals. First, four significant advancements in the CAC method have been made: (i) new types of finite elements are developed which yields a more accurate stacking fault energies and core structure in coarse-grained atomistic descriptions of dislocations, (ii) zero temperature, quasistatic CAC approaches are formulated to enable the constrained multiscale optimization for a sequence of non-equilibrium dislocation configurations in metals, (iii) mesh refinement schemes for both dynamic fracture and curved dislocation migration are implemented, and (iv) the code efficiency is improved using parallelized object-oriented programming. Subsequently, this

enhanced CAC method is employed to study multiple plasticity problems in a variety of FCC metals, including screw dislocation cross-slip in Ni, edge dislocation bowing out from a row of collinear obstacles in Al, dislocation multiplication from Frank-Read sources in Cu, Ni, and Al, as well as sequential slip transfer of curved dislocations across a $\Sigma 3\{111\}$ coherent twin boundary and a $\Sigma 11\{113\}$ symmetric tilt grain boundary in Cu, Al, and Ni. This work makes significant contributions to the fields of mechanics of materials and multiscale modeling. It is anticipated that the finding in this dissertation will improve physical understanding of dislocation-mediated plastic deformation processes in FCC metals and may assist in formulating constitutive laws and rules used in computational techniques at higher length scales.

CHAPTER I

INTRODUCTION

1.1 Motivation

1.1.1 The concurrent atomistic-contnuum method

Multiscale materials modelling methods can be categorized in terms of sequential and concurrent methods [254]. Sequential multiscale methods are approaches whereby simulations are first conducted at fine scale, the results of which are then processed to provide inputs to coarse-scale simulations; it follows that the fine-scale model is no longer required. Atomistic simulation methods can be viewed as sequential multiscale approaches, for example, since the interatomic potentials are informed by lower scale *ab initio* simulations.

Concurrent multiscale methods, as the name suggests, employ models at two or more length scales simultaneously [168]. Depending on whether the physical problem is decomposed into different regions, concurrent methods are further classified into two subcategories: hierarchical and partitioned-domain (also called domain decomposition) methods. Hierarchical methods make use of all length scales everywhere, i.e., with the coarse-scale model making regular appeals to the fine-scale model to determine a constitutive law and, conversely, the fine-scale model looking to the coarse-scale model for its boundary conditions [254]. Partitioned-domain methods, on the other hand, divide the problem into different contiguous, non-overlapping regions, all of which are updated concurrently in time [216]. In most partitioned-domain methods, atomistic resolution is retained where a large deformation gradient exists and/or explicit descriptions of nanoscale structure and phenomena are essential; otherwise, the continuum treatment is employed [306]. Chen et al. [53] reviewed the theoretical foundations of coarse graining methods and analyzed several representative coarse graining models. A review of 14 concurrent multiscale modelling methods is presented by Miller and Tadmor [172], and is further summarized by Tadmor and Miller [254]. In this dissertation, only partitioned-domain methods are addressed.

An example of a partitioned-domain method is the coupled atomistic/discrete dislocation (CADD) method [232]. The CADD model permits the transfer of dislocations across the interface between the atomistic and continuum domains. It has been employed to incorporate long range fields of dislocation pileups to study the impingement of dislocations on symmetric tilt grain boundaries (STGBs) in Al by Dewald and Curtin [70–72]. However, CADD is restricted in that a heuristic, *ad hoc* "detection band" is introduced to pass dislocations through the continuum/atomistic domain interface in that dislocations are detected on one side of the interface and inserted into the other. To the author's best knowledge, a full three-dimensional (3D) coupling of atomistic and discrete dislocation methods allowing curved dislocations of mixed character has not yet been achieved or is in early stages of consideration [56, 187].

Another partitioned-domain approach is the quasicontinuum (QC) method [255]. The QC method uses the change of deformation gradient to distinguish domains where full atomistic resolution is required from those where the deformation field varies more smoothly. Representative atoms (repatoms) are employed to reduce the degrees of freedom (DOFs) to a small fraction of those required in fully resolved atomistic simulations. The system energy, based on the repatoms, is minimized so that the lattice statics at 0 K is reproduced [171]. The QC method has been extended to include a dynamic, finite temperature formulation [75, 135, 253]. In such approaches, it is difficult to avoid introduction of a ghost force at the atomistic/continuum domain interface. Moreover, the continuum domain in QC simulations associated with local nodes does not admit displacement discontinuities such as dislocations, so the finite elements must be adaptively remeshed to full atomistic resolution along the slip propagation path, even well away from the domain interfaces; glide dislocations nucleated from either nanoindentation [227] or from a crack tip [234] must pass through a fully resolved atomistic domain which is usually relatively small due to its high computational cost and so the corresponding dislocation density is usually much higher than that in experiments [234].

Most partitioned-domain methods, including CADD and QC, treat the continuum domain such that lattice dislocations are either implemented via elastic constitutive relations, or they are not permitted at all. This motivated development of a new partitioned-domain

method which (i) describes certain lattice defects and their interactions using fully resolved atomistics, (ii) preserves the net Burgers vector and associated long range stress fields of curved, mixed character dislocations in a sufficiently large continuum domain in a fully 3D model, and preferably, (iii) employs the same governing equations and interatomic potentials in both domains to avoid the usage of phenomenological parameters, essential remeshing operations and *ad hoc* procedures for passing dislocation segments between atomistic and coarse-grained atomistic domains.

One such approach is the concurrent atomistic-continuum (CAC) method [297]. A CAC simulation model, in general, partitions the simulation cell into two domains: atomistic and coarse-grained domains, as will be further discussed in Chap. 2. Employing a unified atomistic-continuum integral formulation with elements that have discontinuities between them and the underlying interatomic potential as the only constitutive relation, CAC admits propagation of displacement discontinuities (dislocations and associated stacking faults) through a lattice in both domains [50]. Within each element in the coarse-grained domain, a finite element method (FEM) with Gaussian quadrature is used to calculate the force/energy of the integration points and update the nodal positions, from which the positions of atoms inside the element are interpolated [296, 297]. Between elements, neither displacement continuity nor interelement compatibility are required [300]. In this way, nucleation of dislocations and their transport between fully resolved atomistic and coarse-grained domains are permitted, without requiring heuristic rules or overlapping pad regions, especially for face-centered cubic (FCC) metals with planar dislocation core [42]. The non-singular dislocation core structure/energy/stress fields and Burgers vector are naturally accommodated in CAC to yield an accurate generalized stacking fault energy (GSFE) surface [300] and Peierls stress [301], as will be presented in Chap. 4.

The major advantage of the CAC method, compared to other partitioned-domain methods, is in the use of interelement discontinuity for dislocation nucleation and migration, facilitating seamless passage of dislocations between atomistic and coarse-grained domains. Other advantages of the CAC method include:

1. Unified governing equations and the same interatomic potential are employed in both

atomistic and coarse-grained domains, inherently providing the convergence of CAC simulations to fully resolved atomistics. Also, since all force/energy calculations are non-local, no ghost forces exist at the atomistic/coarse-grained domain interface in both undeformed and homogeneously deformed configurations.

2. Adaptive remeshing, which is costly and usually employed in multiscale methods to capture lattice defects in the case of continuous elements, is not essential in certain CAC applications, because interelement discontinuity admits the propagation of edge, screw, and mixed character dislocations albeit with a smeared treatment of the dislocation core/Burgers vector. This results in a consistent coarse-graining accuracy and efficiency compared to fully resolved atomistics.

3. Because the net Burgers vector and associated long range fields of dislocation arrays are preserved in the coarse-grained domain, CAC coarse graining can be employed in regions remote from lattice defects (e.g., interstitial/vacancy, voids, and interfaces), while full atomistic resolution should be employed in the vicinity of defects to reproduce dislocation/defect reactions.

The previous CAC approach, however, is limited by certain disadvantages. For example, in applying CAC to plastic deformation of FCC crystalline metals, dislocations in the coarse-grained domain are accomondated between elements with all surfaces corresponding to $\{111\}$ slip planes; however, the widely used rhombohedral element only permits dislocations in 9 out of 12 sets of equivalent $\{111\}\langle 110\rangle$ slip systems. Thus, other potential slip systems are omitted. In 2013, a hybrid element was developed to capture all 12 slip systems in FCC system [67]. However, the hybrid element is not employed in this dissertation due to its higher computational cost compared with a rhombohedral element of the same size: the former contains 122 integration points while the latter contains 64 integration points in the same first nearest neighbor (1NN) element, solved by 2^{nd} order Gaussian quadrature. Therefore, only certain line/planar defects that are important for FCC metal plasticity can be represented in the coarse-grained domain in the previous CAC implementation, e.g., $(a_0/2)\langle 110\rangle\{111\}$ full dislocations, $(a_0/6)\langle 112\rangle\{111\}$ Shockley partial dislocations,

intrinsic stacking faults, and dislocation intersection-induced jogs and kinks, where a_0 is the lattice parameter. Moreover, for migration of these defects, it is required that their paths should be aligned with interelement boundaries. Defects that are not allowed directly in the coarse-grained domain include, but are not limited to, extended dislocation core structures, stacking fault tetrahedra, extrinsic stacking faults, superjogs, general grain boundaries (GBs), arbitrary cracks, and extended sessile dislocation locks such as Lomer, Hirth, and Lomer-Cottrell locks. Point defects and climb of a Frank partial dislocation, which is usually assisted by formation and migration of point defects, may be admitted in the coarse-grained domain but are not expected to be accurately described. Note that the degree of accuracy is controlled by the mesh size.

It is therefore desirable to extend the CAC method by using mesh refinement schemes. For example, previous CAC simulations of brittle fracture show that the coarse-grained domain with hybrid elements satisfactorily predict local fracture behavior and an average stress-strain relation comparable with those resulting from fully resolved atomistic simulations with only 1.4% DOFs of the latter [67]. The coarse-grained domain works reasonably well in brittle fracture, which mainly involves the rupture of atomic bonds [28], because two neighboring elements are related by interatomic potentials. However, in ductile fracture involving a 3D, time-varying, complex dislocation network, which is relevant to plastic response near a crack tip, it is unlikely that the rhombohedral elements with a limited number of slip systems [297] or the hybrid elements of finite size [67] can render necessary resolution. Also, note that in brittle fracture [67], the element shape and lattice orientation are carefully designed such that the element surfaces are also the cleavage planes; for arbitrary lattice orientations, brittle fracture may not be as well described using CAC without mesh refinement.

Another disadvantage of the previous CAC method is that it only has a dynamic formulation [297]. Like most concurrent multiscale methods, an fs-scale time step, which is the smallest of all time scales involved to gain the needed accuracy, is employed in CAC. As a result, dynamic CAC simulations, like molecular dynamics (MD), are often performed in the "overdriven" regime, characterized by higher deformation rates ($> 10^7$ s^{-1}) and higher

stresses (on the order of several GPa) as compared to experiments [259]. In this regime, defect nucleation/migration is primarily stress-driven. Results based on dynamic CAC are thus directly useful only in predicting a material's response under shock loading conditions. In dislocation nucleation from a surface, a dynamic CAC simulation is more likely to predict multiple nucleation events, e.g., arrays of dislocation sources activated simultaneously, because it does not provide the time duration necessary for the thermally-assisted single dislocation nucleation event to occur. Another limitation of the dynamic CAC is that it is likely to miss subtle structural transitions that occur infrequently and under low applied stresses.

Therefore, there is a clear need to advance multiple aspects of the CAC approach to provide an improved tool for modeling dislocation-mediated metal plasticity. Specific advancements are summarized in Sec. 1.2 and detailed in Chap. 3.

1.1.2 Plasticity of face-centered cubic metals

Metal plasticity is a multiscale phenomenon that is manifested by irreversible microstructure rearrangement associated with nucleation, multiplication, interaction, and migration of dislocations [168]. Long range field interactions between dislocations are extremely important to describe, along with the dissociated character of partial dislocations [300]. The former necessitates large solution scales, while the latter demands treatment of core effects using accurate underlying interatomic potentials. Metal plasticity therefore requires concurrent coupling across various scales. While methods such as MD and dislocation dynamics (DD) have been widely employed for problems at spatial scales involving core effects and long range fields, respectively, efforts have been made to concurrently bridge the discrete and continuous descriptions, two fundamentally different approaches [216].

In the context of dislocation-mediated plastic deformation, CAC has been used to model dislocation nucleation from notched specimens [291, 292, 297] in Cu, Ni, and Al, nucleation and growth of dislocation loops in Cu, Al, and Si [294], dislocation-void interactions in Ni [298], and fast moving dislocations in Cu [296]. The success of these calculations suggests the viability of using CAC simulations to study other plasticity phenomena in a

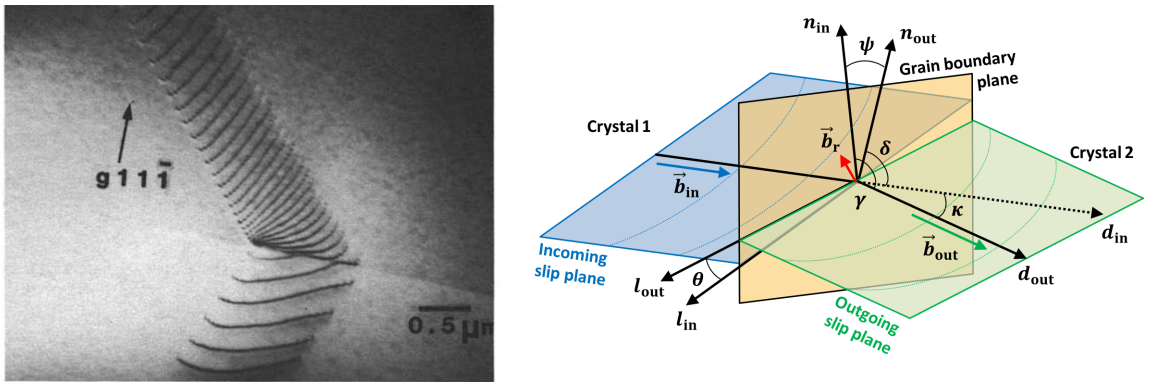

(a) (b)

Figure 1.1: (a) TEM observation of a $(a_0/2)\langle 110\rangle$ full dislocation pile-up penetrating a $\Sigma 3$ twin boundary and generating another array of dislocations in the second grain in 304 stainless steel [225]. (b) A 3D illustration of a series of curved dislocations on an incoming slip plane crossing a GB and gliding on an outgoing slip plane [169].

sufficiently large 3D model, which would normally be inaccessible to atomistics. Screw dislocation cross-slip, which is important in plastic deformation of metals due to its role in dynamic recovery via activation of a secondary slip system, is one such phenomenon. Another is dislocation multiplication from Frank-Read (FR) sources, a benchmark problem for multiscale simulations and one of the building blocks for more complicated 3D dislocation substructure evolution [44]. Lastly, the slip transfer of lattice dislocations across GBs (Fig. 1.1), which plays an important role in size-dependent plastic deformation in polycrystalline metals, merits further investigation with large scale concurrent simulations using multiscale approaches like CAC.

The mechanism for slip transfer of lattice dislocations that migrate to and interact with GBs is one of the most pressing yet unresolved issues facing grain boundary (GB) engineering from materials science or materials design perspectives, and polycrystal plasticity from a constitutive modeling perspective [168]. It is known that the strength of polycrystalline FCC metals varies characteristically with the average grain size [307]. For mean grain size above 10 nm, the Hall-Petch effect that a smaller average grain size results in a higher yield stress, is confirmed by experiments [209], constitutive modeling [59], and atomistic simulations [170]. For an FCC polycrystal with sufficiently large grains and few short-range dislocation interactions (e.g., during Stage I work hardening), the Hall-Petch effect can be

rationalized in terms of the dislocation pile-up model [200]. Since the stress on the leading dislocation is proportional to the applied stress and to the number of dislocations in the pile-up, the tip of the pile-up in a smaller grain that accommodates fewer dislocations experiences a lower stress [110]. Thus, a higher applied stress is required to reach the critical stress level on the incoming side of the GB to transfer slip through the interface. Regarding these slip transfer processes [140], three possible lattice dislocation/GB reactions have been identified: direct transmission of the incoming dislocation, absorption of the incoming dislocation into an extrinsic GB dislocation, and desorption of the GB dislocation into a neighboring grain or back into the original grain, as shown in Fig. 1.2. At low levels of plastic strain, plastic deformation within individual grains is mainly carried by multiplication/generation of lattice dislocations, the resistance to which is manifested as the strength of polycrystal [60]. For polycrystalline metals with an average grain size above 100 nm or so, yield strength is mainly controlled by the generation of lattice dislocations. Thus, dislocation pile-ups and associated slip transfer at GBs play an important role in size dependent initiation and progress of plastic deformation in polycrystalline metals [58].

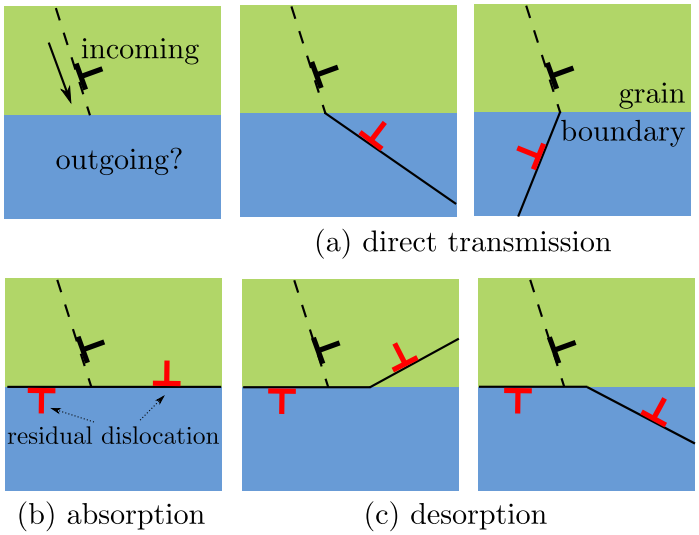

Figure 1.2: Illustrations of three possible single dislocation/GB reactions.

Although *in situ* transmission electron microscopy (TEM) experiments capture the real-time dynamic process of slip transfer [140], they are unable to discern 3D atomic-scale events

at the dislocation/GB interaction sites to yield quantitative information [121]. The multi-scale nature of the sequential transfer of slip across GBs, in which both the atomic scale structure of the interface and the long range fields of dislocation pile-ups are important, also poses challenges from the perspective of computational simulation [168]. For example, dislocation-based continuum approaches such as the crystal plasticity finite element method (CPFEM) [168] and DD [154] are not readily applicable to simulate the interactions between dislocations and GBs because they usually do not naturally incorporate the necessary microscopic DOFs associated with the GBs and other evolving internal state variables that relate to detailed slip transfer criteria. On the other hand, atomistic simulations, which are preferred to understand local GB structure-specific slip transfer responses, are limited by the size of the computational cell in terms of computing long range dislocation pile-up processes [241].

Therefore, there is a need to investigate a series of important FCC metal plasticity phenomena using the advanced CAC approach. This kind of coarse-grained modeling of slip transfer may assist in formulating constitutive laws and rules in describing plasticity of polycrystals that may be useful upstream in CPFEM and DD simulations. Specific applications of CAC simulations are summarized in Sec. 1.2 and detailed in Chaps. 4–9.

1.2 Dissertation objectives and significance of research

The main objectives of this dissertation are two-fold: (i) advancing the previously established CAC method [297] in four major aspects and (ii) applying the newly advanced CAC approach to study a series of important dislocation-mediated plasticity problems in FCC metals. Specific objectives of this dissertation, along with the significance of research, are to:

1. Develop new types of finite elements for a more accurate description of dislocations in the coarse-grained domain in CAC. To the author's best knowledge, this would be the first coarse-grained atomistic approach that can approximate dislocation core level effects without requiring adaptive mesh refinement to atomic scale resolution;

2. Formulate zero temperature CAC approaches to facilitate exploration of structure evolution nearer to minimum energy pathways. This is especially important for cases like slip transfer across GBs in which (i) common overdriven conditions associated with very high strain rates in dynamics and/or thermal fluctuation due to finite temperature need to be avoided and (ii) equilibrium GB structure evolution at the reaction sites requires an accurate description by sequential energy minimization;

3. Implement the mesh refinement schemes for the CAC method to expand its capability to handle the evolution of more complex extended defect structures than those previously studied;

4. Improve the code efficiency and readability using parallel object-oriented programming in FORTRAN 2003, in preparation for a public version of the CAC code. These improvements, with respect to the previous CAC implementation, are important from the computational perspective;

5. Apply the advanced CAC method to study certain benchmark problems, including GSFE, dislocation core structure/energy/stress fields, Peierls stress, surface indentation, dislocation migration between atomistic and coarse-grained domain interface, brittle-to-ductile (BTD) transition in dynamic fracture, and curved, mixed-character dislocation migration, in three FCC metals: Cu, Ni, and Al. For these benchmark simulations, the advanced CAC method is shown to provide largely satisfactory predictive results at much lower computational cost than the fully atomistic version of the same models. To quantify the coarse-graining error, a preliminary convergence and error analysis based on these results is presented;

6. Employ both dynamic CAC and MD simulations to explore the shear stress- and line length-dependent screw dislocation cross-slip in Ni. It is demonstrated that the CAC approach can accurately describe 3D cross-slip processes via two commonly observed mechanisms, as a complement to other numerical methods;

7. Use quasistatic CAC simulations of submicron-sized realizations to study the bowing

of edge dislocations from a row of collinear obstacles in Al. This work highlights the significance of the effects of adjacent bowed-out segments on cooperative dislocation bow-out;

8. Employ quasistatic CAC simulations to model an edge dislocation bowing out from an FR source in Cu, Ni, and Al. Three key characteristics of the FR source, including the dislocation nucleation/loop formation time, the critical shear stress, and critical dislocation configuration, are investigated. Results highlight the significance of directly simulating the FR source activities using fully 3D models and shed light on developing more accurate continuum models;

9. Perform CAC simulations to study sequential slip transfer of a series of curved dislocations from a given pile-up across a $\Sigma 3$ $\{111\}$ coherent twin boundary (CTB) in Cu and Al, with dominant leading screw character at the site of interaction. Results elucidate the discrepancies between atomistic simulations and experimental observations of dislocation/GB reactions and highlight the importance of directly modeling sequential dislocation slip transfer reactions using fully 3D models, with consideration of applied shear stress, dislocation line length, and dislocation line curvature;

10. Perform CAC simulations to address the slip transfer of dislocation pile-ups across two GBs in Ni, including a $\Sigma 3\{111\}$ CTB and a $\Sigma 11\{113\}$ symmetric tilt grain boundary (STGB). Results emphasize the role of specific GB structure in interface absorption-desorption reactions including evolution of the interface structure and identify the history effect of a sequence of dislocation reactions with the interface in light of irreversible evolution of the GB with each encounter.

1.3 Dissertation structure

This dissertation is organized as follows:

- In Chap. 2, a review of the theoretical foundation, mathematical formulation, and numerical implementation of the CAC method is provided in detail. This chapter

provides a background of the CAC approach that will be used throughout the dissertation.

- In Chap. 3, four major advances of the CAC method are presented, and are employed in the remainder of the dissertation. This chapter represents the work published in Refs. [300, 303, 306].

- In Chap. 4, certain benchmark problems are studied using the updated CAC method; a preliminary convergence and error analysis is conducted in the last section, Sec. 4.11. This chapter, establishing that the method adequately replicates essential aspects of dislocation fields, represents the work published in Refs. [300, 301, 306].

- In Chaps. 5–9, both quasistatic and dynamic CAC simulations are performed to study a series of plasticity problems including screw dislocation cross-slip, edge dislocations bowing-out from obstacles, dislocation multiplication from FR sources, and slip transfer of mixed-type curved dislocations across a $\Sigma 3$ CTB and a $\Sigma 11$ STGB in three FCC metals: Cu, Ni and Al. Each chapter is organized with introduction, methodology, results and discussion, and summary sections so that it is self-contained. These chapters represent the work published or submitted in Refs. [301–305].

- Chapter 10 summarizes the significant findings and overall contribution of this dissertation. Additional work and future research directions that build upon this dissertation are discussed.

CHAPTER II

BACKGROUND AND METHODOLOGY

2.1 Microcontinuum and atomic field theory

In classical local continuum mechanics, a material consists of mass points with infinitesimal size, which are continuously distributed and fill the entire region of space they occupy [20]. The micro-scale kinetics or dynamics are implicitly averaged. The physical properties of each point is determined only by the deformation and history of that point, i.e., each point behaves independently following the same constitutive law. Interactions between these points take place only through the balance equations. Therefore, continuum mechanics fails to describe the materials deformation at the atomic/micro level.

Limitations of classical continuum mechanics have motivated the development of various enhanced methods, a vast number of which aim at tackling the locality issue. Among these methods, a weakly nonlocal theory, microcontinuum field theory (also called generalized continuum theory) extends the classical field theory to microscopic space and time scales [82]. In the microcontinuum field theory, materials are envisioned as a continuum collection of deformable point particles. Each point particle, with a finite size, has a continuous internal deformation which is represented by some vectors attached to it. Accordingly, a particle is identified by its position vector $\mathbf{R}$ and some director vectors attached to this point $\boldsymbol{\Xi}_\alpha$ in the undeformed state. In a solid crystal, $\mathbf{R}$ describes the continuous lattice deformation, in which the material is viewed as a collection of infinitesimal point particles, while $\boldsymbol{\Xi}_\alpha$ consider each point particle with finite size and describe its continuous internal deformation. Both $\mathbf{R}$ and $\boldsymbol{\Xi}_\alpha$ have their own motions to the deformed states $\mathbf{r}$ and ξ_α at time t, respectively, i.e.,

$$\mathbf{R} \xrightarrow{t} \mathbf{r}, \qquad \boldsymbol{\Xi}_\alpha \xrightarrow{\mathbf{R},t} \xi_\alpha, \qquad \alpha = 1, 2, \ldots, N \tag{2.1}$$

Such a medium is called microcontinuum of grade N. By introducing $\boldsymbol{\Xi}_\alpha$, the microcontinuum naturally brings length and time scales into the field theories; by considering the

ratio of the external characteristic length to the internal characteristic length, the microcontinuum theories are nonlocal in character. For the first grade microcontinuum ($N = 1$), $\boldsymbol{\Xi}_1$ are three deformable directors, conferring each point particle nine extra DOFs compared to the local theory. This is the micromorphic continuum. The other two microcontinuum are microstretch and micropolar continuum, which can be achieved by constraining the director vectors in certain ways.

In micromorphic field theory, the motion of point particles are governed by conservation equations of mass, microinertia, generalized spin, linear momentum, and energy. Based on the micromorphic field theory, Chen and Lee [48] proposed a multiscale field theory, called the atomistic field theory (AFT), which views a crystalline material as a continuous collection of lattice points; embedded within each point is a unit cell with a group of discrete atoms. In this way, the micromorphic theory is connected with MD and is expanded to the atomic scale. Here, the local density function is continuous at the level of the unit cell, but discrete in terms of the discrete atoms inside the unit cell.

The theoretical foundation of the CAC method is the AFT. The same balance equations for both fully resolved atomistic and coarse-grained continuum domains are employed to compute the properties of general crystals [300]. In the continuum domain, the interatomic potential serves as the only constitutive relation. The AFT was originally designed with multi-component crystalline materials in mind [51, 52], and CAC has been applied on strontium titanate [312–314] and one-dimensional (1D) polyatomic crystals [290].

For monoatomic crystalline materials, for example pure metals, each primitive unit cell contains only one atom. Xiong et al. [297] performed CAC simulations to reproduce complex dislocation phenomena in FCC metals such as dislocation nucleation/migration and formation of multiple stacking fault ribbons. Deng et al. [68] and Deng and Chen [67] studied both wave and crack propagation, as well as the impact fracture in an ideal brittle material. More recently, the more accurate embedded-atom method (EAM) potential was incorporated into CAC simulations to study more general dislocation behavior such as migration of curved dislocations, formation of leading and trailing partial dislocations, dislocation loop coalescence, dislocation/phonon interactions, and dislocation/void interactions in FCC pure

crystals [292–296, 298].

2.2 Governing equations of the CAC method

Within the framework of atomic N-body dynamics, Chen [50] formulated the microscopic balance equations of the instantaneous mass, linear momentum, and internal energy. Fundamentally different from the form of coarse-grained particle models [32, 255, 308], the governing equations in AFT are expressed in terms of local densities [53]. While they can be expressed in terms of either Eulerian or Lagrangian coordinates, the governing equations are presented in Eulerian coordinates in this dissertation, i.e.,

$$\frac{\partial \rho}{\partial t} + \nabla_{\mathbf{r}} \cdot (\rho \mathbf{v}) = 0 \tag{2.2}$$

$$\frac{\partial (\rho \mathbf{v})}{\partial t} - \nabla_{\mathbf{r}} \cdot (\mathbf{t} - \rho \mathbf{v} \otimes \mathbf{v}) - \mathbf{f}_{\text{ext}} = 0 \tag{2.3}$$

$$\frac{\partial (\rho e)}{\partial t} - \nabla_{\mathbf{r}} \cdot (\mathbf{q} + \mathbf{t} \cdot \mathbf{v} - \rho e \mathbf{v}) - \mathbf{f}_{\text{ext}} \cdot \mathbf{v} = 0 \tag{2.4}$$

where ρ is the microscopic local mass density, t is the time, $\mathbf{r}$ is the physical space coordinates, $\mathbf{v}$ is the local velocity field, $\mathbf{f}_{\text{ext}}$ is the external body force field, $\mathbf{t}$ is the 2^{nd} rank momentum flux tensor, e is the energy, and $\mathbf{q}$ is the heat flux. Note that all local densities, including the stress and heat flux field, are defined as the time-interval averages of instantaneous quantities, as in the MD method, rather than the ensemble phase space averages employed in statistical mechanics. The local density is continuous in the physical space up to the point of structural instability (e.g., dislocation nucleation or fracture). For a monoatomic crystal, assuming that the temperature gradient is negligible and there is no external force density, Eq. 2.4 becomes trivial and Eq. 2.3 becomes

$$\begin{aligned}
&\frac{\partial (\rho \mathbf{v})}{\partial t} - \nabla_{\mathbf{r}} \cdot (\mathbf{t} - \rho \mathbf{v} \otimes \mathbf{v}) - \mathbf{f}_{\text{ext}} \\
=&\frac{\partial \rho}{\partial t}\mathbf{v} + \rho \frac{\partial \mathbf{v}}{\partial t} - \nabla_{\mathbf{r}} \cdot \mathbf{t} + \nabla_{\mathbf{r}} \cdot (\rho \mathbf{v} \otimes \mathbf{v}) \\
=&\frac{\partial \rho}{\partial t}\mathbf{v} + \rho \frac{\partial \mathbf{v}}{\partial t} - \nabla_{\mathbf{r}} \cdot \mathbf{t} + [\nabla_{\mathbf{r}} \cdot (\rho \mathbf{v})]\mathbf{v} + \rho \mathbf{v} \cdot \nabla_{\mathbf{r}} \mathbf{v} \\
=&\left[\frac{\partial \rho}{\partial t} + \nabla_{\mathbf{r}} \cdot (\rho \mathbf{v})\right] \mathbf{v} + \rho \left[\frac{\partial \mathbf{v}}{\partial t} + \mathbf{v} \cdot \nabla_{\mathbf{r}} \mathbf{v}\right] - \nabla_{\mathbf{r}} \cdot \mathbf{t} = 0.
\end{aligned} \tag{2.5}$$

In Eq. 2.5, the first term is zero because of Eq. 2.2; also given that

$$\frac{\partial \mathbf{v}}{\partial t} + \mathbf{v} \cdot \nabla_{\mathbf{r}} \mathbf{v} = \frac{\mathrm{d}\mathbf{v}}{\mathrm{d}t} = \ddot{\mathbf{r}} \tag{2.6}$$

and

$$\nabla_{\mathbf{r}} \cdot \mathbf{t} = \mathbf{f}_{\text{int}}, \tag{2.7}$$

the governing equation in CAC is [48]

$$\rho \ddot{\mathbf{r}} - \mathbf{f}_{\text{int}} = \mathbf{0} \tag{2.8}$$

where $\mathbf{f}_{\text{int}}$ is the internal force density and the superposed dots denote the material time second derivative.

2.3 Continuum quantities from atomistics

In a continuum, the instantaneous mechanical variables ρ, $\ddot{\mathbf{r}}$, and $\mathbf{f}_{\text{int}}$ are defined at each material point $\mathbf{r}$ in physical space. In an atomistic description, however, their values must be obtained in terms of the discrete values defined for each atom in the system (e.g., position, momentum, and energy) at atomic site $\mathbf{R}$ in phase space. In AFT, Chen and Lee [48] proposed that the phase space and physical space descriptions can be linked by a localization relation, i.e.,

$$\rho(\mathbf{r})\ddot{\mathbf{r}} = \Sigma_{k=1}^{N_{\text{atom}}} \delta(\mathbf{r} - \mathbf{R}^k) m^k \ddot{\mathbf{R}}^k \tag{2.9}$$

$$\mathbf{f}_{\text{int}}(\mathbf{r}) = \Sigma_{k=1}^{N_{\text{atom}}} \delta(\mathbf{r} - \mathbf{R}^k) \mathbf{F}^k \tag{2.10}$$

where N_{atom} is the number of atoms, the δ-function has units of inverse volume, and $\mathbf{F}^k$ is the total atomic force acting on atom k, having mass m^k and position $\mathbf{R}^k$. While the δ-function can be either a Dirac δ-function or some kind of distribution function, it must satisfy the following normalization over the simulation domain Ω:

$$\int_{\Omega(\mathbf{r})} \delta(\mathbf{r} - \mathbf{R}^k) \, \mathrm{d}\Omega(\mathbf{r}) = 1. \tag{2.11}$$

In this dissertation, a Dirac δ-function is employed, i.e.,

$$\delta(\mathbf{r} - \mathbf{R}^k) = \begin{cases} +\infty & \mathbf{r} = \mathbf{R}^k \\ 0 & \text{otherwise} \end{cases}. \tag{2.12}$$

If one denotes the continuum points $\mathbf{r}$ in physical space that correspond to discrete atoms $\mathbf{R}^k$ in phase space as $\mathbf{r}_k$, use of the Dirac δ-function indicates that in mapping phase

space into physical space, only the pointwise continuum quantities at $\mathbf{r}_k$ are sampled. The mechanical variables at $\mathbf{r}_k$ are related to the atomic values at $\mathbf{R}^k$ by

$$\rho(\mathbf{r}_k)\ddot{\mathbf{r}}_k = \frac{m^k}{\Omega^k}\ddot{\mathbf{R}}^k \tag{2.13}$$

$$\mathbf{f}_{\text{int}}(\mathbf{r}_k) = \mathbf{f}_k = \frac{\mathbf{F}^k}{\Omega^k} \tag{2.14}$$

where Ω^k is the volume of k^{th} atom. At this point, there are numerous ways to form the continuum field at *any* continuum point. For example, given a set of points $\mathbf{r}_k$, Delaunay tessellation can be constructed, where the 3D physical space is divided into tetrahedra whose vertices are at $\mathbf{r}_k$ [179,244]. Then, within each 4-atom tetrahedron, for a perfect lattice, the continuum quantities at *any* point can be linearly interpolated from their values at vertices. Line defects (dislocations) and plane defects (e.g., stacking faults and free surfaces) are considered as weak discontinuities, where the interpolation function differs. At a free surface, for example, the mechanical quantities should be truncated smoothly. This is because beyond the outer boundaries or within the inner boundaries, most mechanical quantities are meaningless. In addition, volume defects such as voids and cracks are considered as strong discontinuities and are excluded from the tessellation. It is beyond the scope of this dissertation to discuss the details in constructing the tessellation and the discussion below only concerns the continuum quantities at $\mathbf{r}_k$ for brevity.

2.4 Force calculation

In the CAC approach, there are atomistic domains and coarse-grained domains with different degrees of coarse-graining, as shown in Fig. 2.1. In the atomistic domain, atoms are updated in the same way as in MD (for dynamic CAC) or molecular statics (MS) (for quasistatic CAC); the atomic force $\mathbf{F}^k$ is calculated by the force theorem, i.e.,

$$\mathbf{F}^k = -\nabla_{\mathbf{R}^k} e_{\text{int}} \tag{2.15}$$

where e_{int} is the internal energy. In the coarse-grained domain, the force calculation is more complicated and is the main topic of this section. In both domains, the force on each atom/node depends on not only the deformation of that atom/node, but also its environment, making the CAC fully nonlocal.

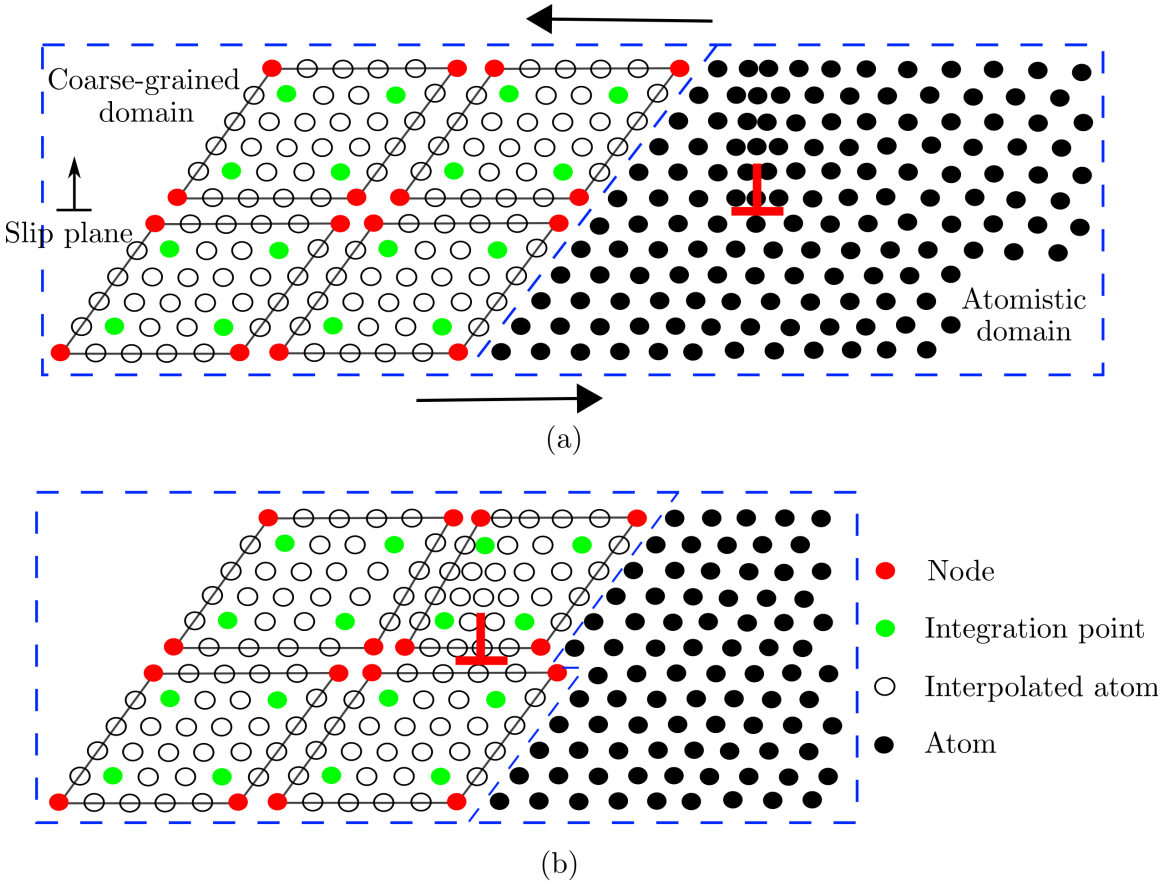

Figure 2.1: A 2D CAC simulation domain consisting of an atomistic domain (right) and a coarse-grained domain (left). The atomistic domain is composed of atoms (black circles), which follow the same governing equations in the atomistic simulation. The coarse-grained domain consists of elements of varying size that have discontinuities between them, each of which contains a large number of underlying atoms with the nodes (red circles) as the only DOFs. Only the force on integration points (green circles) and nodes are calculated. The positions of atoms within each element (open circles) are interpolated from the nodal positions. In 3D, elements have faces on {111} planes, the slip planes of FCC lattice, as shown in Fig. 2.2. Note that the 2D elements shown are for illustration purposes only. In (a), an edge dislocation (red $\perp$) is located in the atomistic domain. Upon applying a shear stress on the simulation cell, the dislocation migrates into the coarse-grained domain in (b), where its Burgers vector spreads out between elements that have discontinuities between them [300].

2.4.1 Discretization

To solve Eq. 2.8 in the coarse-grained domain, it can be daunting to compute the forces on each atom, so a finite element approach is employed. Note that the physical space $\mathbf{r}$ is continuous in a defect free perfect lattice, and so is the displacement field $\mathbf{u}$. Rhombohedral elements with all faces lying on {111} planes (Fig. 2.2) are selected for several reasons: (i) slip in FCC metals occurs along close-packed {111} planes, (ii) the elements conform to the FCC lattice, (iii) the smallest rhombohedral element is a primitive unit cell in the atomistic domain, and (iv) a balance between two-dimensional (2D) triangular elements (would be tetrahedral elements if in 3D) with high efficiency [68] and 3D hybrid elements with high accuracy [67].

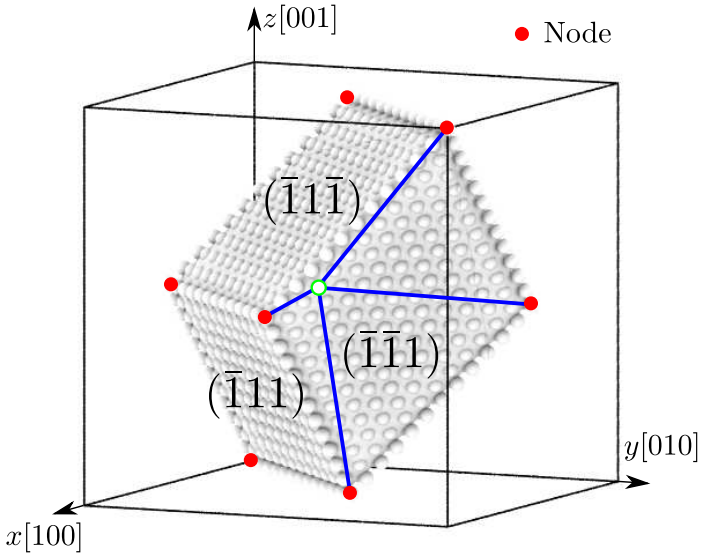

Figure 2.2: A 3D rhombohedral element with faces on {111} planes, the slip planes of FCC lattice. The position of each atoms within each element, e.g., the green open circle, is interpolated from the nodal positions (red solid circles) [305].

Within each element, lattice defects are not allowed and the displacement field has C^1 continuity. Between elements, however, neither displacement continuity nor strain compatibility is required. The lack of such requirements does not preclude description of a perfect lattice over large domains involving many elements, nor does it imply that all types of defects can be captured, particularly at high resolution. Lattice defects are accommodated by discontinuous displacements between elements, potentially including both sliding and

separation to accommodate brittle fracture [68] or dislocation glide [297]. Domains with full atomic resolution differ from coarse-grained domains by virtue of their ability to resolve lattice defects, for example dislocation cores, although the net Burgers vector of such defects can be captured in the coarse-grained description. Adaptive refinement of coarse-grained elements can be pursued to promote smooth transition of defect migration from atomistic to coarse-grained domains, as will be shown in Sec. 3.4.

The displacement field $\mathbf{u}$ is the difference between the reference and current configurations, i.e.,

$$\mathbf{u}(\mathbf{X}, t) = \mathbf{r}(\mathbf{X}, t) - \mathbf{X} \tag{2.16}$$

where $\mathbf{X}$ denotes the position of a material point in the reference configuration. Thus,

$$\ddot{\mathbf{r}} = \ddot{\mathbf{u}}, \tag{2.17}$$

and Eq. 2.8 becomes

$$\rho\ddot{\mathbf{u}} - \mathbf{f}_{\text{int}} = \mathbf{0}. \tag{2.18}$$

First, $\mathbf{u}$ within each element is discretized via the relation

$$\mathbf{u} = \mathbf{\Phi}_\xi(\mathbf{r})\mathbf{u}_\xi \tag{2.19}$$

where $\mathbf{u}$ is a 1×3 vector, ξ are the nodes, the shape function $\mathbf{\Phi}_\xi$ is a $1 \times N_{\text{npe}}$ vector, and $\mathbf{u}_\xi$ is a $N_{\text{npe}} \times 3$ matrix where N_{npe} is the number of nodes per element. For each node ξ, Φ_ξ is trilinear, i.e.,

$$\Phi_\xi = \frac{1}{8}(1 \pm \chi)(1 \pm \eta)(1 \pm \zeta) \tag{2.20}$$

where χ, η, and ζ are natural coordinates. Thus, it can be said that the displacement field is discretized by employing a piecewise continuous shape function.

Then, the weighted residual method is applied by multiplying Eq. 2.18 by a weight function Φ_ν and performing the integration over the simulation domain Ω, i.e.,

$$\int_{\Omega(\mathbf{r})} [\rho\Phi_\nu(\mathbf{r})\mathbf{\Phi}_\xi(\mathbf{r})\ddot{\mathbf{u}}_\xi - \Phi_\nu(\mathbf{r})\mathbf{f}_{\text{int}}(\mathbf{r})]\, \mathrm{d}\Omega(\mathbf{r}) = \mathbf{0} \quad \nu = 1, 2, \ldots, N_{\text{npe}}. \tag{2.21}$$

The Galerkin method is employed, by taking the shape function as the weight function. Equation 2.21 can be viewed as a system of equations for the time varying nodal displacements for the dynamic problem derived by the principle of virtual work. The second term

is the internal force that causes the nodal displacement. Since here one does not integrate by parts to decrease the continuity requirement on $\mathbf{u}$, Eq. 2.21 is *not* a weak form.

Writing Eq. 2.21 in matrix form, the first term becomes

$$\int_{\Omega(\mathbf{r})} \rho \mathbf{\Phi}_\nu(\mathbf{r}) \mathbf{\Phi}_\xi(\mathbf{r}) \ddot{\mathbf{u}}_\xi \, \mathrm{d}\Omega(\mathbf{r}) = \mathbf{M}\ddot{\mathbf{u}}_\xi = \mathbf{M}\ddot{\mathbf{R}}^\xi \tag{2.22}$$

where $\mathbf{\Phi}_\nu$ is an $N_{\mathrm{npe}} \times 1$ vector, $\ddot{\mathbf{R}}^\xi$ is a $N_{\mathrm{npe}} \times 3$ matrix, and

$$\mathbf{M} = \int_{\Omega(\mathbf{r})} \rho \mathbf{\Phi}_\nu(\mathbf{r}) \mathbf{\Phi}_\xi(\mathbf{r}) \, \mathrm{d}\Omega(\mathbf{r}) \tag{2.23}$$

is a $N_{\mathrm{npe}} \times N_{\mathrm{npe}}$ local mass matrix.

The second term of Eq. 2.21 can be replaced by a quadrature, i.e.,

$$\int_{\Omega(\mathbf{r})} \mathbf{\Phi}_\nu(\mathbf{r}) \mathbf{f}_{\mathrm{int}}(\mathbf{r}) \, \mathrm{d}\Omega(\mathbf{r}) = \sum_{\mu}^{N_{\mathrm{ipe}}} \omega'_\mu \mathbf{\Phi}_{\mu\nu} \mathbf{f}_\mu \tag{2.24}$$

where ω'_μ are the quadrature weight in terms of force density, $\mathbf{\Phi}_{\mu\nu}$ is a $N_{\mathrm{npe}} \times 1$ vector, and $\mathbf{f}_\mu$ is a 1×3 vector. While integration points μ can correspond to any material point in the continuum, μ corresponds to actual atoms in this dissertation. In this way, the calculation of force is straightforward, as indicated in Sec. 2.3. It follows that

$$\mathbf{f}_\mu = \frac{\mathbf{F}^\mu}{\Omega^\mu} \tag{2.25}$$

where 1×3 vector $\mathbf{F}^\mu$ is the atomic force at μ and Ω^μ is the volume of μ^{th} integration point.

Substituting Eqs. 2.22, 2.24, and 2.25 into Eq. 2.21 leads to

$$\mathbf{M}\ddot{\mathbf{R}}^\xi - \sum_\mu \omega_\mu \mathbf{\Phi}_{\mu\nu} \mathbf{F}^\mu = \mathbf{0} \tag{2.26}$$

where ω_μ, the quadrature weight in terms of atomic force, is related to ω'_μ by

$$\omega_\mu = \frac{\omega'_\mu}{\Omega^\mu}. \tag{2.27}$$

Changing the dummy index ν to ξ, Eq. 2.26 becomes

$$m^\xi \ddot{\mathbf{R}}^\xi - \boldsymbol{\mathcal{F}}^\xi = \mathbf{0} \tag{2.28}$$

where

$$\boldsymbol{\mathcal{F}}^\xi = m^\xi \mathbf{M}^{-1} \sum_\mu \omega_\mu \mathbf{\Phi}_{\mu\xi} \mathbf{F}^\mu. \tag{2.29}$$

Here, $\boldsymbol{\mathcal{F}}^{\xi}$, a $N_{\text{npe}} \times 3$ matrix, is the equivalent nodal force on nodes ξ. To ensure that $\boldsymbol{\mathcal{F}}^{\xi}$ is on the order of atomic force, it is required that

$$\mathcal{F}^{\xi} = \frac{\sum_{\mu} \omega_{\mu} \Phi_{\mu\xi} F^{\mu}}{\sum_{\mu} \omega_{\mu} \Phi_{\mu\xi}} \tag{2.30}$$

Comparing Eq. 2.29 with Eq. 2.30, must be satisfied is

$$m^{\xi} \mathbf{M}^{-1} \sum_{\mu} \omega_{\mu} \boldsymbol{\Phi}_{\mu\xi} = \boldsymbol{\Gamma} \tag{2.31}$$

where $\boldsymbol{\Gamma}$ is a $N_{\text{npe}} \times 1$ matrix with all elements unity. Equivalently,

$$\sum_{\mu} \omega_{\mu} \boldsymbol{\Phi}_{\mu\xi} = \frac{\mathbf{M}\boldsymbol{\Gamma}}{m^{\xi}} \tag{2.32}$$

where $\mathbf{M}\boldsymbol{\Gamma}$ is a $N_{\text{npe}} \times 1$ matrix, whose elements are the sum of rows in $\mathbf{M}$. A lumped mass matrix is used, whose diagonal elements of its inverse matrix $\mathbf{M}^{-1}$ are $N_{\text{npe}}/(m^{\xi} N_{\text{ape}})$. Then, for each node ξ,

$$\sum_{\mu} \omega_{\mu} \Phi_{\mu\xi} = \frac{N_{\text{ape}}}{N_{\text{npe}}}. \tag{2.33}$$

2.4.2 Integration points

While multiple choices of integration points μ and weight ω_{μ} satisfy Eq. 2.33, it is further restricted that

$$\sum_{\mu} \omega_{\mu} = N_{\text{ape}} \tag{2.34}$$

such that the total weight of the integration points within one element is the number of atoms it contains. The integration points play a similar role to the sampling atoms used in other concurrent multiscale methods such as virtual atom cluster [195], atom collocation method [310], and multiresolution molecular mechanics (MMM) [30–32, 308, 309, 311]. In these methods, the computational demand is reduced by only calculating the force of the sampling points, and Eq. 2.34 is usually satisfied.

In Eq. 2.24, the integral is approximated by a weighted sum of the evaluations of the integrand at a set of integration points μ. In numerical integration, the positions and weights of μ are usually determined by the order of the integrand. It is, however, difficult to employ a unified set of integration points within an element for two reasons:

1. The integrand $\mathbf{\Phi}_\nu(\mathbf{r})\mathbf{f}_{\text{int}}(\mathbf{r})$ can be a complicated and highly non-linear function of $\mathbf{r}$, whose order is usually difficult to anticipate *a priori*.

2. The variation of the integrand is not uniform within an element. Among all atoms, those close to the element surface can better "feel" what happens outside, i.e., their force are more sensitive to external influences. In contrast, the remaining "interior atoms" are arranged in a similar local lattice structure decided only by the element's overall deformation (i.e., trilinear interpolation function). For example, assume that an element initially represents a perfect lattice, where all atoms have the same force; then when a dislocation propagates between elements, the force of each "surface atom" vary substantially while those of the "interior atoms" remain nearly the same.

To circumvent this problem, each element is divided into a number of non-overlapping subregions, as shown in Fig. 2.3. In this way, one only needs to determine the order of the integrand within each subregion, which is usually lower than that within the entire element and is more easily approximated. The integration in Eq. 2.24 becomes

$$\int_{\Omega(\mathbf{r})} \mathbf{\Phi}_\nu(\mathbf{r})\mathbf{f}_{\text{int}}(\mathbf{r})\,\mathrm{d}\Omega(\mathbf{r}) = \sum_{\alpha}^{N_{\text{spe}}} \int_{\Omega_\alpha(\mathbf{r})} \mathbf{\Phi}_\nu(\mathbf{r})\mathbf{f}_{\text{int}}(\mathbf{r})\,\mathrm{d}\Omega_\alpha(\mathbf{r}) = \sum_{\alpha}^{N_{\text{spe}}} \sum_{\mu}^{N_{\text{ips}}} \omega'_\mu \mathbf{\Phi}_{\mu\nu}\mathbf{f}_\mu \tag{2.35}$$

where Ω_α is the volume of subregion α, N_{spe} the number of subregions per element, and N_{ips} the number of integration points per subregion. The accuracy of the quadrature in Eq. 2.24 depends on (i) how the element is divided and (ii) whether the evaluations at the integration points can *represent* the behavior of all atoms in the same subregion. Below, the integration within one subregion will be first discussed as this determines the division of the element.

The integrand $\mathbf{\Phi}_\nu(\mathbf{r})\mathbf{f}_{\text{int}}(\mathbf{r})$ in Eq. 2.24 is a $N_{\text{npe}} \times 3$ matrix, i.e.,

$$\begin{bmatrix} \Phi_1 \\ \vdots \\ \Phi_{N_{\text{npe}}} \end{bmatrix} \cdot \begin{bmatrix} f_{\text{int}}^\chi & f_{\text{int}}^\eta & f_{\text{int}}^\zeta \end{bmatrix} = \begin{bmatrix} \Phi_1 f_{\text{int}}^\chi & \Phi_1 f_{\text{int}}^\eta & \Phi_1 f_{\text{int}}^\zeta \\ \vdots & \vdots & \vdots \\ \Phi_{N_{\text{npe}}} f_{\text{int}}^\chi & \Phi_{N_{\text{npe}}} f_{\text{int}}^\eta & \Phi_{N_{\text{npe}}} f_{\text{int}}^\zeta \end{bmatrix}. \tag{2.36}$$

Taking the first element $\Phi_1 f_{\text{int}}^\chi$ of the matrix as an example, it is assumed that within

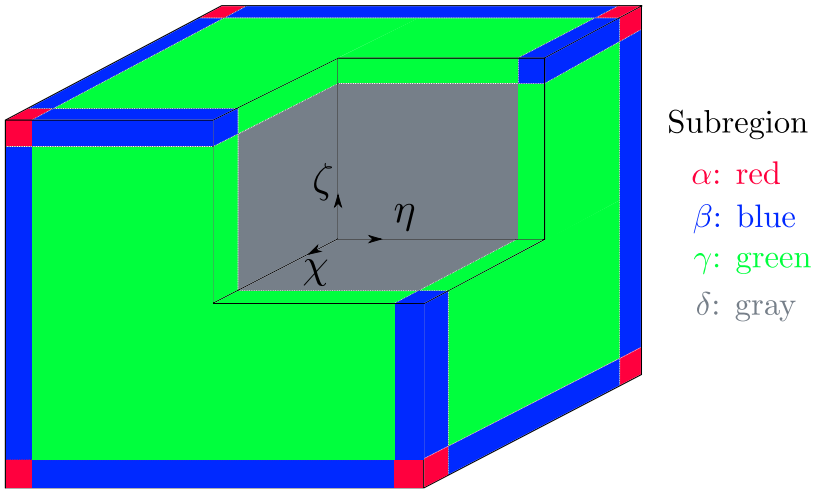

Figure 2.3: A 3D illustration of the subregions within an rhombohedral element in natural coordinates in CAC simulations. The atoms are not shown. Four types of subregions, α, β, γ, and δ, are marked in red, blue, green, and gray, respectively. In this dissertation, within each subregion there is one integration point. The same type of subregion may contain different numbers of atoms in different types of elements, so the relevant integration points have different weights, according to Eq. 2.41. The "surface atoms" are located in subregions α, β, and γ, while the "interior atoms" are contained by subregion δ [300].

each subregion, the force density is piecewise constant, i.e.,

$$f_{\text{int}}^{\chi}(\mathbf{r}) = f_{\mu}^{\chi}, \tag{2.37}$$

except at the boundary, because different subregions have a different f_{μ}^{χ}, which is continuous at the boundary. Moreover, since the force density is related to the deformation gradient, the assumption only applies when the deformation gradient remains nearly the same within an element, regardless of the order of the shape function. In practice, however, the force density gradient across the subregion boundary is small because it is essentially calculated between two neighboring atomic sites. So the boundary effect is negligible. Within subregion α, the integral on the first element in the matrix in Eq. 2.36 becomes

$$\int_{\Omega_\alpha(\mathbf{r})} \Phi_1(\mathbf{r}) f_{\text{int}}^{\chi}(\mathbf{r})\, \mathrm{d}\Omega_\alpha(\mathbf{r}) = f_{\mu}^{\chi} \int_{\Omega_\alpha(\mathbf{r})} \Phi_1(\mathbf{r})\, \mathrm{d}\Omega_\alpha(\mathbf{r}) \tag{2.38}$$

where the shape function for node 1, $\Phi_1(\mathbf{r})$, is trilinear with respect to $\mathbf{r}$, regardless of the subregion. The Gaussian quadrature rule suggests that in 1D integration on interval $[a, b]$, one integration point located at $(b + a)/2$ with weight $(b - a)$ can yield an exact result for a linear polynomial integrand [46]. Thus, in this dissertation, the 1$^{\text{st}}$ order Gaussian

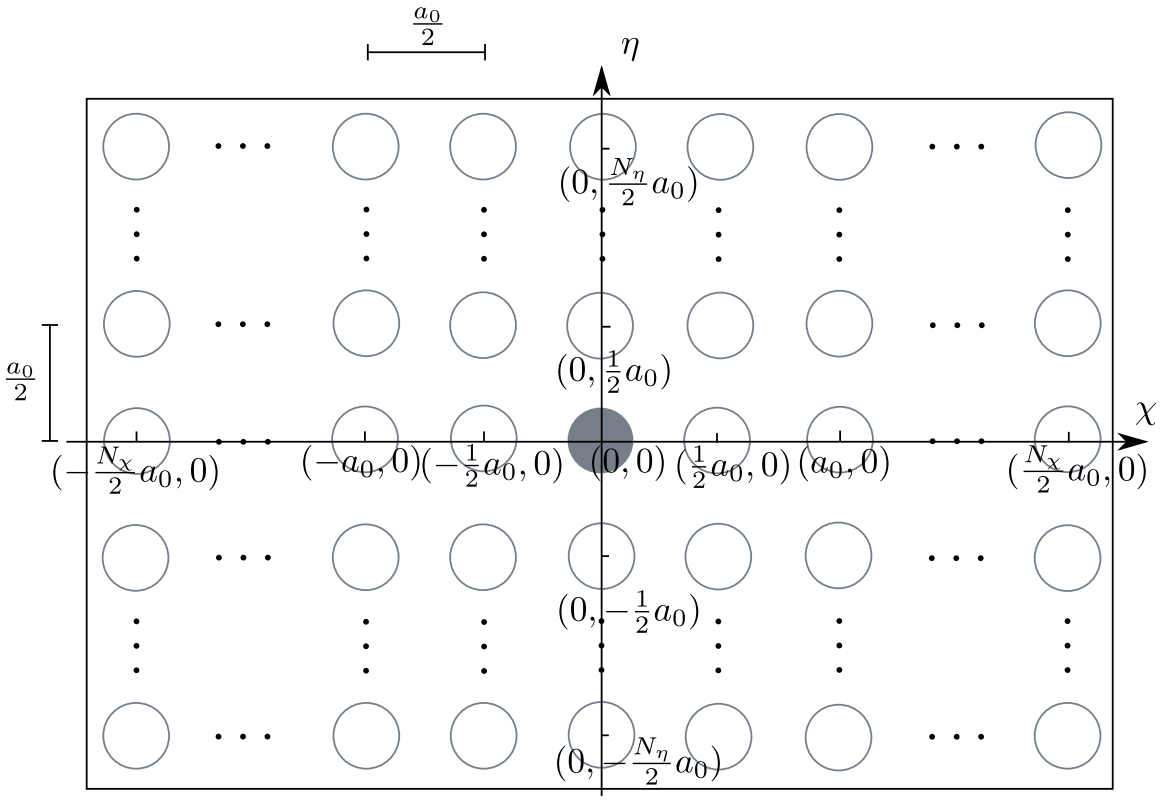

Figure 2.4: An illustration of a 2D subregion containing $(2N_\chi + 1) \times (2N_\eta + 1)$ atoms in natural coordinates. The filled circle in the origin is the integration point. The open circles are non-integration-point atoms. The boundaries of the subregion along χ and η directions are $[-(N_\chi + \frac{1}{2})\frac{a_0}{2}, (N_\chi + \frac{1}{2})\frac{a_0}{2}]$ and $[-(N_\eta + \frac{1}{2})\frac{a_0}{2}, (N_\eta + \frac{1}{2})\frac{a_0}{2}]$, respectively. Note that in the field description of an element, an integration point can be any continuum point. In this dissertation, the actual atoms are chosen because the force calculation is straightforward [300].

quadrature is employed for the numerical integration. A higher order Gaussian quadrature is desired if the force density varies within each subregion and/or a higher order shape function is employed; the exact force density function within a subregion depends on both the size/position of the subregion and the interatomic potentials. For 2D integration within a subregion illustrated in Fig. 2.4, the interval along the χ and η directions are $[-(N_\chi + \frac{1}{2})\frac{a_0}{2}, (N_\chi + \frac{1}{2})\frac{a_0}{2}]$ and $[-(N_\eta + \frac{1}{2})\frac{a_0}{2}, (N_\eta + \frac{1}{2})\frac{a_0}{2}]$, respectively. Thus, the integration point should be located at $(0, 0)$ with weight

$$\omega'_\mu = \omega'_\chi \omega'_\eta = \left(N_\chi + \frac{1}{2}\right)\left(N_\eta + \frac{1}{2}\right) a_0^2. \tag{2.39}$$

In a 2D subregion, Ω^μ is the area of a unit cell in natural coordinates, i.e.,

$$\Omega^\mu = \frac{a_0^2}{4}. \tag{2.40}$$

Substituting Eqs. 2.39 and 2.40 into Eq. 2.27, one has

$$\omega^\mu = (2N_\chi + 1)(2N_\eta + 1), \tag{2.41}$$

which suggests that the weight of an integration point is the number of atoms within the same subregion. The same conclusion holds for a 3D subregion. Equation 2.34 is therefore satisfied.

2.4.3 Embedded-atom method potential

In both atomistic and coarse-grained domains, the force $\mathbf{F}$ on atoms or integration points is calculated using Eq. 2.15. The EAM formulations for potential energy and force are given by [64],

$$e_{\text{int}} = \frac{1}{2}\sum_i \sum_{\substack{j \\ j\neq i}} V(R^{ij}) + \sum_i F(\bar{\rho}^i) \tag{2.42}$$

$$\mathbf{F}^k = \sum_{\substack{j \\ j\neq k}} \left\{ \frac{\partial V(R^{kj})}{\partial R^{kj}} + \left[\frac{\partial F(\bar{\rho}^k)}{\partial \bar{\rho}^k} + \frac{\partial F(\bar{\rho}^j)}{\partial \bar{\rho}^j} \right] \frac{\partial \rho(R^{kj})}{\partial R^{kj}} \right\} \frac{\mathbf{R}^{kj}}{R^{kj}}. \tag{2.43}$$

Here, V is the pair potential, F is the embedding potential, $\bar{\rho}$ is the host electron density, $\mathbf{R}^{kj}$ is the vector from atom k to atom j with norm R^{kj}

$$\mathbf{R}^{kj} = \mathbf{R}^j - \mathbf{R}^k \tag{2.44}$$

$$\bar{\rho}^k = \sum_{j\neq k} \rho^{kj}(R^{kj}) \tag{2.45}$$

where ρ is the local electron density between an atomic pair. Equation 2.15 suggests that the force applied on an atom is the negative variation of the internal energy with respect to its displacement. In the atomistic domain, each atom has an independent degree of freedom (DOF), so one can fix all atoms but k in calculating $\mathbf{F}^k$.

In the coarse-grained domain, however, when integration points μ and their neighbors j are in the same element, they are bound by the interpolation function, so one cannot move μ while fixing j. In this regard, the force required to move an atom by the same

displacement is slightly larger than that in an atomistic domain because of the collective displacements of other atoms, given the nonlocal force field.

2.5 Piecewise continuous interpolation function

In a 3D element, the "surface atoms" are located in subregions α, β, and γ, while the "interior atoms" are in subregion δ, as shown in Fig. 2.3. One way to distinguish the displacements of the two types of atoms is to apply different shape functions and interpolation functions in different subregions. In this dissertation, however, the same shape function is employed for all atoms within an element, with the subregions having different integration points and weights. Moreover, it is assumed that the deformation of the k^{th} atom within an element, including the integration points, conforms to that of the element, i.e.,

$$\mathbf{R}^k = \boldsymbol{\phi}_{k\xi}\mathbf{R}^\xi \tag{2.46}$$

where the first order interpolation function $\boldsymbol{\phi}$ is the same as the trilinear shape function Φ. In this way, each element domain with interpolation according to Eq. 2.46 contains a hyperelastic defect-free lattice that can only have homogeneous deformation, and the element is isoparametric. Since interelement discontinuity is allowed, this essentially represents a piecewise continuous interpolation function in each element.

For more general multicomponent crystalline materials, the interpolation function fails to properly describe the internal atomic positions within the unit cells. In the case of higher order shape functions, employing the trilinear interpolation function results in subparametric elements. However, in this dissertation, only monoatomic FCC pure metals are considered with a trilinear shape function, so the trilinear interpolation function applies.

2.6 Dynamic CAC

It is straightforward to apply Eq. 2.8 to solve the dynamic problem for any prescribed homogeneous temperature [297]. In the atomistic domain, by substituting Eqs. 2.13 and 2.14 into Eq. 2.8, it is shown that for the k^{th} atom,

$$m^k\ddot{\mathbf{R}}^k - \mathbf{F}^k = \mathbf{0}, \tag{2.47}$$

which is simply Newton's second law. Similarly, in the coarse-grained domain, for the ξ^{th} node,

$$m^{\xi}\ddot{\mathbf{R}}^{\xi} - \mathbf{F}^{\xi} = \mathbf{0}. \tag{2.48}$$

The Velocity Verlet form [273] of the Brünger-Brooks-Karplus integrator [36] is then employed in both domains to update atoms and nodes. With all information at time t, the velocity is first advanced by half time step $\Delta t/2$, i.e.,

$$\dot{\mathbf{R}}(t + \frac{\Delta t}{2}) = \left(1 - \gamma\frac{\Delta t}{2}\right)\dot{\mathbf{R}}(t) + \frac{\Delta t}{2m}\mathbf{F}(t) \tag{2.49}$$

where γ is the damping coefficient. It has been recently shown that γ is not an artificial parameter *per se*, but rather serves as a surrogate for the phonon drag on dislocation motion [295]. In the atomistic domain, m is the atomic mass and $\mathbf{F}$ is the atomic force; in the coarse-grained domain, m is the normalized lumped mass and $\mathbf{F}$ is the equivalent nodal force calculated by Eq. 2.29. The position is then updated via [306]

$$\mathbf{R}(t + \Delta t) = \mathbf{R}(\Delta t) + \dot{\mathbf{R}}(t + \frac{\Delta t}{2})\Delta t. \tag{2.50}$$

At the end of the step, the velocity at time $(t + \Delta t)$ is obtained by

$$\dot{\mathbf{R}}(t + \Delta t) = \frac{1}{1 + \gamma\frac{\Delta t}{2}}\left[\dot{\mathbf{R}}(t + \frac{\Delta t}{2}) + \frac{\Delta t}{2m}\mathbf{F}(t + \Delta t)\right]. \tag{2.51}$$

2.7 Discussion

2.7.1 Nonlocal nodes

In the QC method, the repatoms are categorized into local and nonlocal types, according to a *nonlocality* criterion [255]. Local repatoms are used when the energy of an element is determined only by its deformation gradient. A large deformation gradient is manifested where the deformation is plastic due to emergent lattice defects, and so the eigenvalue of the deformation gradient can capture the *nonlocality*, which is used to decide if the repatoms are local or nonlocal and if certain continuous elements need to be refined.

In CAC simulations, each element is a hyperelastic body that can only have elastic deformation, and the relative displacement (slip) between elements accommodates plastic

deformation such as dislocation migration. In QC, in contrast, the deformation is continuous. Thus, the deformation gradient within a single element in CAC is generally smaller than that in QC in the presence of plasticity; in other words, the deformation gradient alone cannot be used to assess the *nonlocality* in CAC. On the other hand, for general formulations all nodes must be nonlocal, prepared for any possible case. Therefore, all force calculations in CAC simulations are nonlocal, i.e., across the atomistic/coarse-grained domain interface, the motion of nodes causes forces on atoms and vice versa. When the interface lies within an infinitely large perfect lattice subject to a homogeneous deformation, the forces on all k^{th} atoms in the atomistic domain and those on all μ^{th} integration points in the coarse-grained domain are the same, because the trilinear interpolation function precisely represents the atomic positions under homogeneous deformation of the overall domain, i.e.,

$$\mathbf{F}^k = \mathbf{F}^\mu = \mathbf{F}_{\text{homo}}. \tag{2.52}$$

Substituting Eq. 2.52 into Eq. 2.30, it follows that the equivalent nodal force on all ξ^{th} nodes are $\mathbf{F}_{\text{homo}}$, i.e., no extra force is introduced compared with an equivalent full atomistic model. Therefore, there is no ghost force at the domain interface in both undeformed and homogeneously deformed lattice configurations.

2.7.2 Equivalent nodal force

In the coarse-grained domain, the equivalent nodal force $\boldsymbol{\mathcal{F}}^\xi$ is defined in Eq. 2.29. While the choice of the integration points have been discussed in Sec. 2.4.2, one may wonder why the atomic force of the node is not directly adopted instead, i.e.,

$$\boldsymbol{\mathcal{F}}^\xi = \mathbf{F}^\xi. \tag{2.53}$$

The equation implies that the nodes are the only integration points. Employing Eq. 2.34, it is identified that

$$\omega_\xi = \frac{N_{\text{ape}}}{N_{\text{npe}}}, \tag{2.54}$$

which suggests that one node represents a group of ω_ξ number of atoms. This choice of integration points overestimates the force if the nodes do not reside in a perfect lattice.

For example, when a node is at a corner of a cubic simulation cell in the vicinity of three free surfaces, its force is larger than the atomic force of an atom inside an perfect lattice. Equation 2.54 means that the group of ω_ξ number of atoms represented by the node identically has the same environment (i.e., at the corner), which will unavoidably lead to the overestimation of the force. In practice, adopting Eq. 2.53 results in large displacement of the nodes on traction free boundaries within a few simulation steps, for example.

A similar instability of the nodal integration scheme occurs in the meshfree particle method. Beissel and Belytschko [16] found that although the nodal integration of a Galerkin approximation is faster and easier to implement than the quadrature method, it results in a spatial instability. One approach to stabilize the integration is to use additional quadrature points [76]. Later, Xiao and Belytschko [287] and Rabczuk et al. [198] concluded that while the interpolation in Eulerian coordinate affects material instability, an interpolation in Lagrangian coordinates promotes numerical stability. In CAC simulations, such interpolation is realized by the application of a piecewise continuous interpolation function within elements, which is essentially of Lagrangian type although the balance laws are expressed in Eulerian coordinates.

2.7.3 Stress calculation

In CAC, the 2$^{\text{nd}}$ rank Cauchy stress tensor $\boldsymbol{\sigma}$ is calculated *a posteriori*. In the atomistic domain, the average stress of a region with volume Ω_{at} is given by [49]

$$\boldsymbol{\sigma}_{\text{at}} = \frac{1}{\Omega_{\text{at}}} \sum_k \Omega^k \boldsymbol{\sigma}^k = \frac{1}{\Omega_{\text{at}}} \sum_k \left[\frac{1}{2} \sum_{\substack{j \\ j \neq k}} \mathbf{R}^{kj} \otimes \mathbf{F}^{kj} - m^k \dot{\mathbf{R}}^k \otimes \dot{\mathbf{R}}^k \right] \tag{2.55}$$

where $\boldsymbol{\sigma}^k$ is the atomic stress at atom k with volume Ω^k.

In the coarse-grained domain, the average stress of a region with volume Ω_{cg} is given by [300]

$$\boldsymbol{\sigma}_{\text{cg}} = \frac{1}{\Omega_{\text{cg}}} \sum_I^{N_{\text{ele}}} \sum_\mu \omega_\mu \boldsymbol{\Phi}_{\mu\xi} \Omega^\mu \boldsymbol{\sigma}^\mu = \frac{1}{\Omega_{\text{cg}}} \sum_I^{N_{\text{ele}}} \sum_\mu \omega_\mu \boldsymbol{\Phi}_{\mu\xi} \left[\frac{1}{2} \sum_{\substack{j \\ j \neq \mu}} \mathbf{R}^{\mu j} \otimes \mathbf{F}^{\mu j} - m^\mu \dot{\mathbf{R}}^\mu \otimes \dot{\mathbf{R}}^\mu \right] \tag{2.56}$$

where $\boldsymbol{\sigma}^\mu$ is the atomic stress at integration point μ with volume Ω^μ and velocity $\dot{\mathbf{R}}^\mu$ which is interpolated from that of the node, i.e.,

$$\dot{\mathbf{R}}^\mu = \boldsymbol{\phi}_{\mu\xi}\dot{\mathbf{R}}^\xi. \tag{2.57}$$

The equivalent nodal stress at node ξ, $\mathcal{S}^\xi$, which is on the same order of the atomic stress, is

$$\mathcal{S}^\xi = \frac{\sum_\mu \omega_\mu \boldsymbol{\Phi}_{\mu\xi}\boldsymbol{\sigma}^\mu}{\sum_\mu \omega_\mu \boldsymbol{\Phi}_{\mu\xi}}. \tag{2.58}$$

Note that since the atomic stress at atom k or integration point μ is symmetric [254], so is the equivalent nodal stress. In a CAC simulation cell, the average stress is

$$\boldsymbol{\sigma}_{\text{sys}} = \frac{\boldsymbol{\sigma}_{\text{at}}\Omega_{\text{at}} + \boldsymbol{\sigma}_{\text{cg}}\Omega_{\text{cg}}}{\Omega_{\text{at}} + \Omega_{\text{cg}}}. \tag{2.59}$$

2.7.4 Coarse-graining efficiency in one iteration

In estimating the ideal coarse-graining efficiency in one iteration, ψ_{cg}, it is first assumed that each atom or integration point has N_{nei} number of neighbors within the cutoff distance; then, in one element in the coarse-grained domain, there are $N_{\text{ipe}}N_{\text{nei}}$ unique atomic pairs. In the equivalent atomistic domain, there are $N_{\text{ape}}N_{\text{nei}}/2$ unique atomic pairs. This suggests that $\psi_{\text{cg}} = N_{\text{ape}}/(2N_{\text{ipe}})$. If $N_{\text{ape}} = 2197$, $\psi_{\text{cg}} = 40.69$ for a 1NN element and $\psi_{\text{cg}} = 8.79$ for a second nearest neighbor (2NN) element. Moreover, ψ_{cg} increases with the element size, as shown in Fig. 2.5.

ψ_{cg} is calculated based on the assumption that only the pairs between the integration points and their neighbors are taken into account. Thus, it agrees well with the actual efficiency using a pair potential. In calculating the force on one integration point μ using the EAM potential, however, one needs to know the host electron density of its neighbors j (i.e., $\bar{\rho}^j$ in Eq. 2.43), which requires considering pairs between j and j's neighbors. The direct calculation of all these pairs includes a significant number of repeated computations because the atoms involved are located in close proximity. An alternative method to calculate $\bar{\rho}$ will be presented in Sec. 3.2. Note that the coarse-graining efficiency shown in Fig. 2.5 is calculated by comparing the number of arithmetic operations required in both domains in one iteration. Hence, ψ_{cg} is also the efficiency of dynamic CAC.

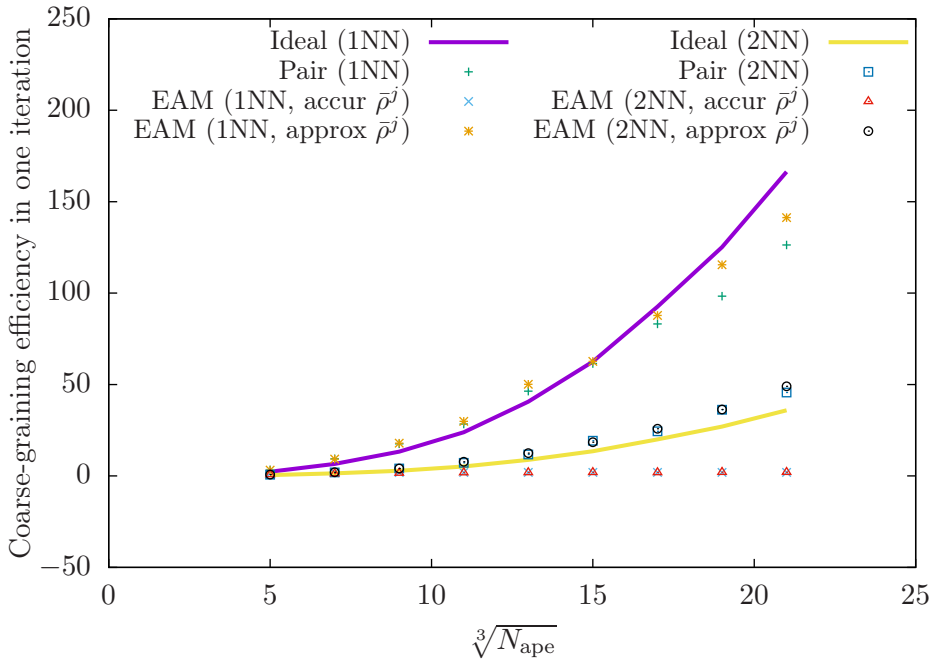

Figure 2.5: Coarse-graining efficiency of CAC simulations as a function of element size. Time for both force/energy calculation and neighbor list updating is included. Both employing EAM potentials, EAM (accur $\bar{\rho}^j$) calculates the host electron density $\bar{\rho}$ of all atoms, while EAM (approx $\bar{\rho}^j$) only calculates $\bar{\rho}$ of the integration points and it is assumed that all atoms in the same subregion within one element have the same $\bar{\rho}$ as that of the integration point, as will be discussed in Sec. 3.2. It is found that both pair and EAM potentials (with proper approximation) give coarse-graining efficiency of about 150 for 1NN element and about 50 for 2NN element when $N_{\text{ape}} = 9261$ [300].

CHAPTER III

ADVANCEMENT OF THE CAC APPROACH

In this chapter, four significant advancements in the CAC method on the basis of Chap. 2 are presented:

1. The code efficiency is improved using parallelized object-oriented programming (Sec. 3.1);

2. New types of finite elements are developed that yield a more accurate stacking fault energy (SFE) and core structure/energy/stress fields in coarse-grained atomistic descriptions of dislocations (Sec. 3.2);

3. Zero temperature CAC approaches are formulated to enable the constrained multiscale optimization for a sequence of non-equilibrium dislocation configurations in metals to more accurately model complex reaction pathways for extended defects than can be obtained using MD (Sec. 3.3);

4. Mesh refinement schemes for both dynamic fracture and curved dislocation migration are implemented (Sec. 3.4).

3.1 CAC Algorithm

Due to the similarity between CAC and atomistic simulations regarding lattice structure and force/energy calculations, the CAC algorithm adopts common atomistic techniques. Newton's third law is employed in the atomistic domain to promote efficiency in calculating the force, pair potential, local electron density, and stress. The short-range neighbor search adopts a combined Verlet list [273] and link-cell [6] methods. Simulation results are visualized using ParaView [222], an open source software, such that CAC results are accessible to a larger community.

There are two major issues regarding the imposition of periodic boundary conditions (PBCs) in CAC simulations with coarse-graining that do not exist in standard atomistic

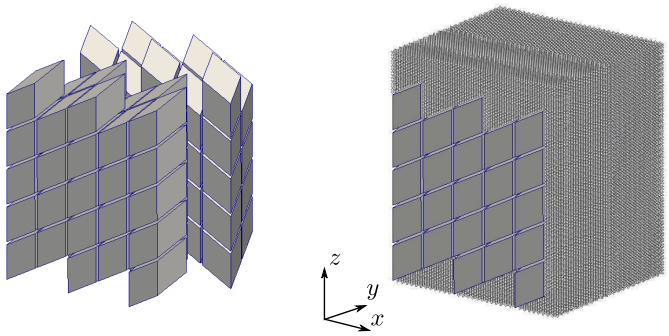

(a) (b)

Figure 3.1: (a) A simulation cell consists of only elements, with jagged boundaries. (b) Atomistic domains are introduced to "fill in" the interstices between planar boundaries of a cubic simulation cell and element boundaries [300].

simulations:

1. In the coarse-grained domain, the surfaces of the rhombohedral elements correspond to {111} planes. While facilitating the description of dislocation nucleation and migration, this prevents one from constructing a parallelepipedonal coarse-grained domain with arbitrary lattice orientations relative to surfaces of the overall simulation cell. If one only uses rhombohedral elements in the model, the simulation box will most likely have jagged boundaries, as shown in Fig. 3.1(a). To facilitate application of PBCs, one can fill in the jagged interstices at simulation cell boundaries with atoms, as shown in Fig. 3.1(b).

2. The other issue in implementation of PBCs is that an object crossing through one face of the simulation box should enter the box through the opposite face. In atomistic simulations, this is realized via displacing certain atoms to bring them back inside the simulation box [254], i.e.,

$$R^{\chi} = \begin{cases} R^{\chi} + L^{\chi}, & \text{if } R^{\chi} < R^{\chi}_{\text{lb}} \\ R^{\chi} - L^{\chi}, & \text{if } R^{\chi} > R^{\chi}_{\text{hb}} \end{cases} \tag{3.1}$$

where R^{χ} is the position of an atom along the χ direction, L^{χ}, R^{χ}_{lb}, and R^{χ}_{hb} are the length, lower bound, and higher bound of the simulation box along the χ direction. In the coarse-grained domain, however, care must be taken when not all nodes of one

element are displaced, i.e., an element is cut through by a periodic boundary. In this case, the nodal positions should be reinstated to interpolate the positions of atoms within the element. Subsequently, the reinstated nodes and some of the interpolated atoms are displaced following Eq. 3.1. The procedure is shown in Fig. 3.2.

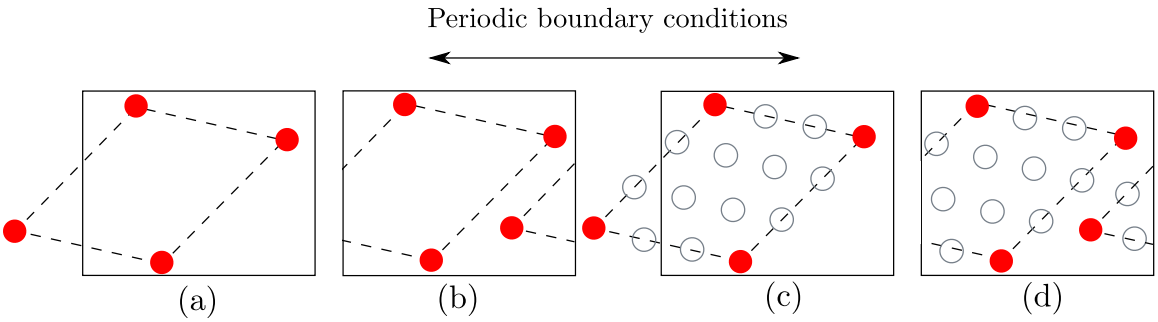

Figure 3.2: A 2D illustration of a simulation cell with PBCs along the direction marked by a double ended arrow. Red filled circles are nodes and grey open circles are interpolated atoms within an element whose boundary is illustrated by black dash lines. (a) An element is cut through by the periodic boundary with one node crossing the left boundary. (b) It follows that the node enters the simulation box through the right boundary. (c) In interpolating the positions of atoms within the element, the nodal position is reinstated. (d) Subsequently, the node and some interpolated atoms are displaced following Eq. 3.1 [300].

3.1.1 Parallelism

The CAC simulations run in parallel using the Message Passing Interface (MPI) [102]. It is thus important to assign processor approximately the same workload. Among the three parallel algorithms commonly employed in atomistic simulations — atom decomposition (AD), force decomposition (FD), and spatial decomposition (SD), SD yields the best scalability and the smallest communication overhead between processors [190]. Unlike AD and FD, the workload of each processor in SD, which is proportional to the number of interactions, is unfortunately not guaranteed to be the same. In CAC, the simulation cell has nonuniformly distributed integration points (in the coarse-grained domain) and atoms (in the atomistic domain), such that the workload is poorly balanced if one assigns each processor an equally-sized cubic domain as in full atomistics [188], as shown in Fig. 3.3(a). This workload balance issue is not unique to CAC, but also encountered by other concurrent multiscale modeling methods [187]. In CAC, two methods have been proposed to achieve a

perfect or near perfect workload balance:

1. In SD-based parallel CAC simulations with both atomistic and coarse-grained domains, only the force/energy/host electron density of the integration points and atoms (referred to as evaluation points) are computed. Since the local density of interactions does not significantly vary within the simulation cell, the number of evaluation points is used as an approximation of the workload and each processor domain is assigned approximately the same number of evaluation points, which is re-evaluated at regular time intervals [39]. It follows that at periodic boundaries filled in with atoms or in the vicinity of lattice defects where full atomistics is employed, the processors are assigned smaller domains that contain more atoms than other processors whose domains contain more nodes [300].

2. An alternative approach is the FD, where the interactions between atomic pairs — either between the integration points and their neighbors in the coarse-grained domain or between the atoms and their neighbors in the atomistic domain — are evenly but spatially randomly assigned to each processor [306], as shown in Fig. 3.3(b).

In this dissertation, the SD algorithm is employed unless indicated otherwise; the AD approach, used in MMM [31], is not considered due to its high communication overhead. A flowchart of the CAC simulation algorithm based on SD is given in Fig. 3.4, while the dynamic CAC scheme is shown in Fig. 3.5.

Another issue that requires special attention is the overlapping domain between neighboring processors, which is common in parallel finite element implementations. In Fig. 3.6, e.g., element 1 is shared between processors P_1, P_2, P_4, and P_5. The algorithm described below is used to automatically address the shared element implementation:

1. For element 1, P_1, P_2, and P_5 contain some non-overlapping integration points while processor P_4 does not have any integration point. One processor, e.g., P_1, is chosen as the host processor for this element.

2. P_1, P_2, and P_5 calculate the force/energy of its own integration points, which are then sent to P_1.

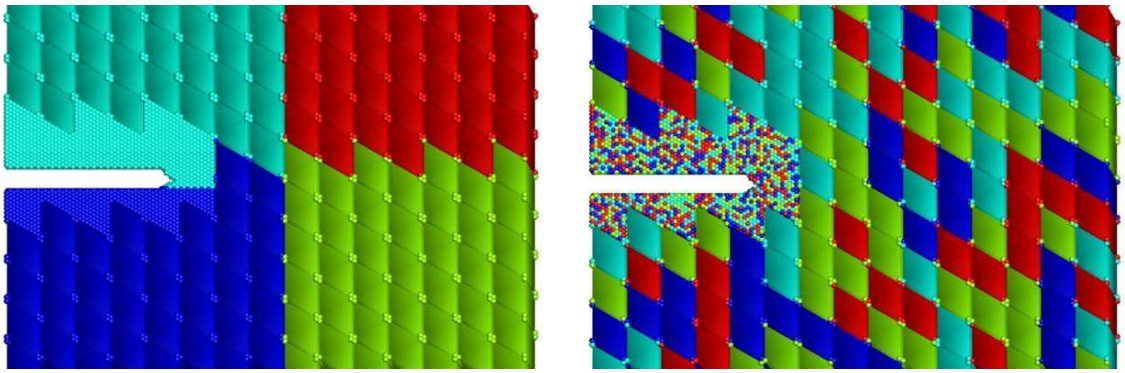

(a) spatial decomposition with equally-sized domains

(b) force decomposition

Figure 3.3: Illustrations of two decomposition approaches in parallel CAC, where different processors are assigned domains with different colors: light blue, red, dark blue, and green. (a) SD with equally-sized domains for each processor; the processors assigned with light and dark blue domains have a heavier workload because they need to calculate the quantities of all atoms in the atomistic domain that are more densely positioned. (b) FD with a perfectly balanced workload between processors [306].

3. P_1 calculates the equivalent nodal force/energy of this element based on the data it receives from the other processors using Eqs. 2.29 and 3.12.

4. P_1 varies the nodes along a certain direction (which is a function of the equivalent nodal force) before sending the updated nodal positions to all other processors.

Note that in Fig. 3.6, although processors P_4 does not contain any integration points but only an non-integration-point atom k, it still needs to access the updated nodal positions from P_1. This is because the position of k is needed by other atoms P_4 contains in doing the nonlocal force/energy calculations.

Although the employment of elements that have discontinuities between them in CAC simulation results in a larger number of nodes for an identical number of elements relative to a continuous formulation, it shares advantages with the discontinuous Galerkin FEM [57]. First, the local formulation promotes the parallelism of the algorithm; second, the assembly of a global mass matrix is not required, and so the memory is less demanding; third, in the case that one element is shared by more than one processor, the overlapping element boundary does not need to be communicated between processors; finally, higher order elements can be implemented locally without concerning the compatibility with its

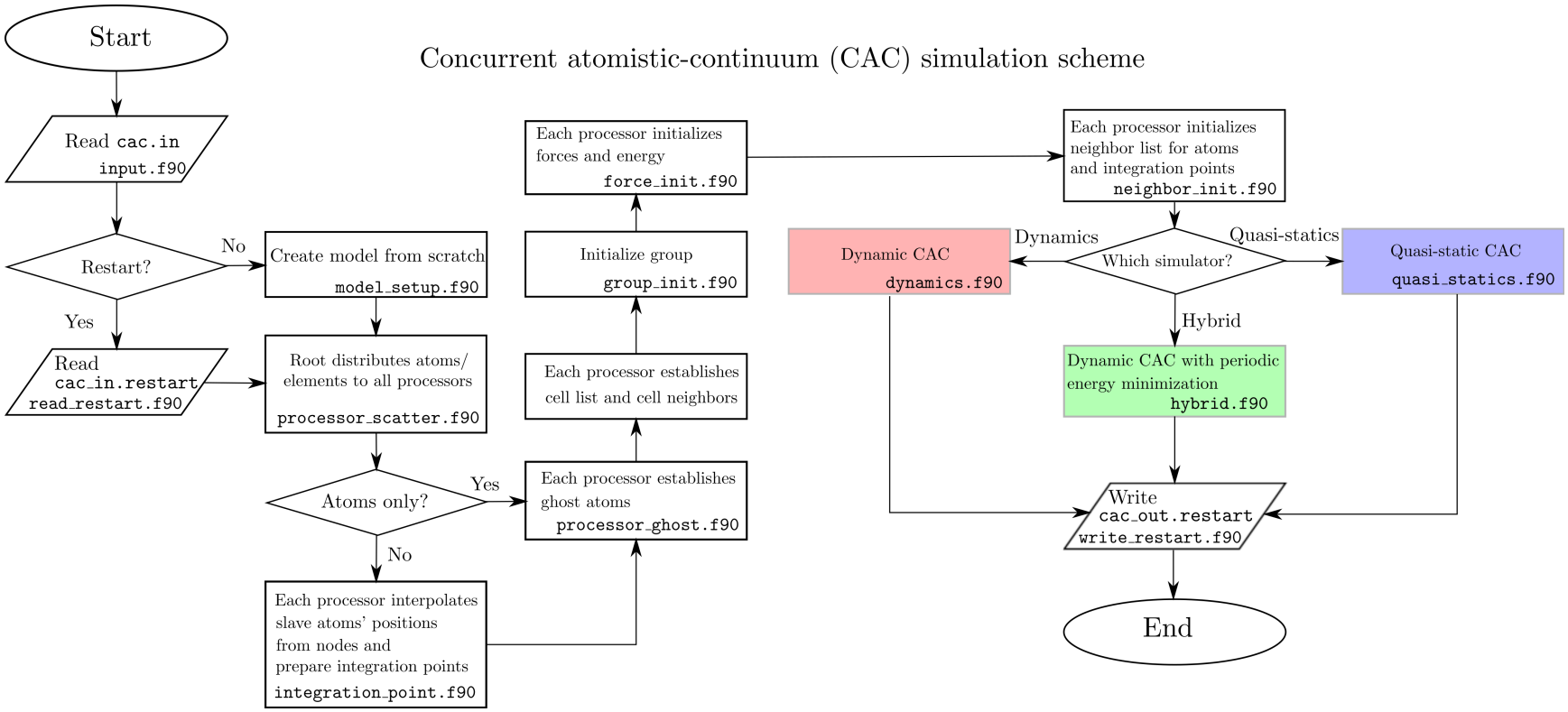

Figure 3.4: CAC simulation scheme, parallelized using the SD algorithm.

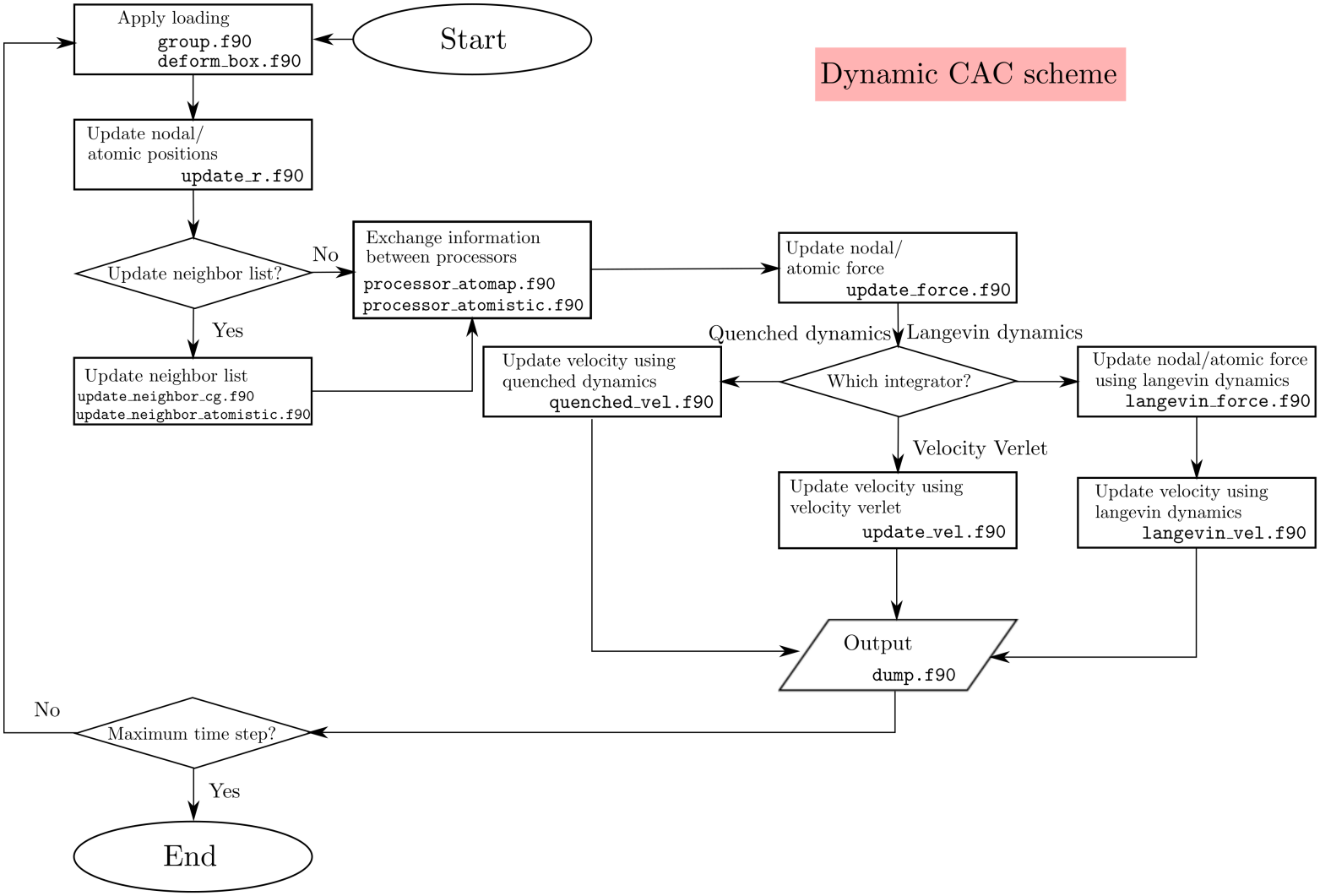

Figure 3.5: Dynamic CAC simulation scheme.

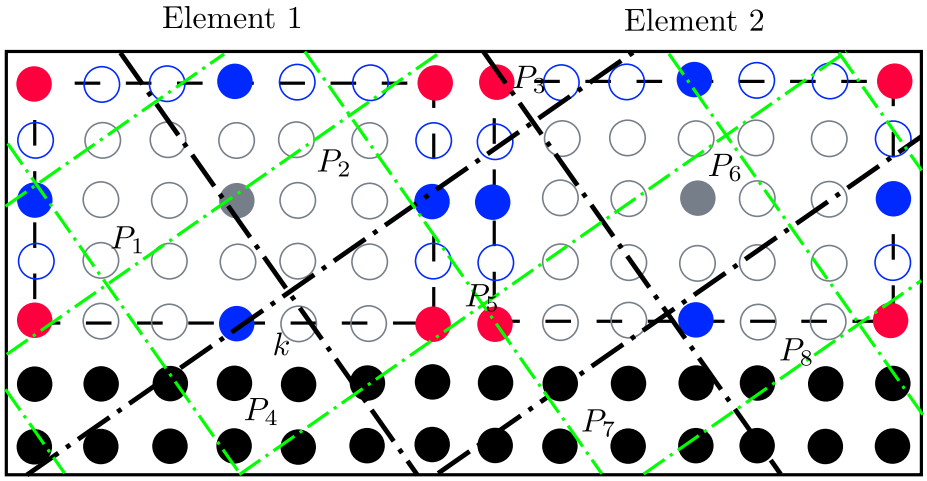

Figure 3.6: A 2D illustration of dividing a simulation cell containing 2 elements and 28 atoms in natural coordinates into a number of link-cells (green and black dot-dash lines) and processor domains (black dot-dash lines). Elements are illustrated by black dash lines, where red (nodes), blue, and grey filled circles are integration points, open circles are non-integration-point atoms. The black filled circles are atoms in the atomistic domain [300].

neighbors, both p- and h-adaptive mesh refinement methods become more convenient to implement.

Although the overlapping elements in the coarse-grained domain lead to a lower parallel efficiency than the fully resolved atomistics, it is worth noting that the parallel efficiency of coarse-graining is not the primary attractive feature of CAC, but rather its ability to extend the spatial scale under consideration to large dimensions, incorporating many body defect field interactions. This is quite difficult to achieve using classical atomistic methods [300].

3.2 New types of finite elements

Equation 2.37 suggests that the force density field within one element is approximated by a piecewise constant function. To ensure that the approximation is accurate, one first needs to determine the spatial variation of atomic force $\mathbf{F}^k$, which is related to the force density via Eq. 2.14, within one element. Then one identifies a coarse subregion with large number of atoms where the atomic force does not vary much, and a fine subregion where the atomic force has a substantial gradient. Note that although the force/energy caused by one atom is effective at an infinitely large distance, the interaction between a pair of atoms is negligible when separated farther than a cutoff distance r_c. In particular, for the EAM potentials

employed in this dissertation, the force/energy changes very little beyond the 2NN and third nearest neighbor distances, respectively, as shown in Fig. 3.7. This suggests that to provide a reasonable approximation for energy minimization, the atoms beyond 2NN distance from the element surface can be taken as "interior atoms". This assumption will be validated quantitatively in Sec. 4.1.

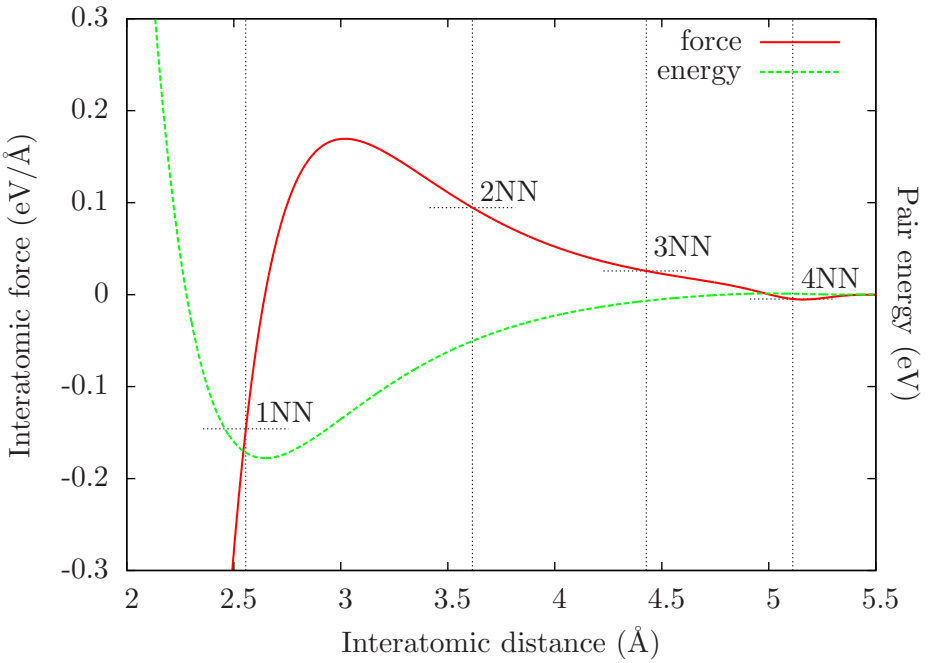

Figure 3.7: The interatomic force and pair energy are calculated using the Cu EAM potential [174] with respect to the interatomic distance. Change in the pair energy is negligible when the interatomic distance is beyond the 2NN distance, whereas change in the force is negligible beyond the third nearest neighbor distance. This suggests that sampling atoms within 2NN distance from the element surface may provide a reasonable approximation for force/energy calculations. The same can be said for Ni and Al [173]. Note that the host electron density is assumed constant, so only the force contribution from the pair potential is shown here [300].

Following these ideas, two types of elements are developed in CAC simulations: 1NN and 2NN elements. Figure 3.8 illustrates the division of subregions in a 2D element, with gray representing the "interior atoms", both red (nodes) and blue the "surface atoms". A coarse subregion is employed to contain all "interior atoms" because they are beyond a certain distance from the element surface along both the χ and η directions and are assumed to have the same force/energy. For the "surface atoms", more highly resolved subregions are adopted. Note that some atoms, e.g., atom β, lie on the surface along the η direction

but are far from the surface in terms of the χ direction. One can then assume that atom β and atoms in similar positions (e.g., β_1 and β_2) have the same force/energy and so they are in the same subregion.

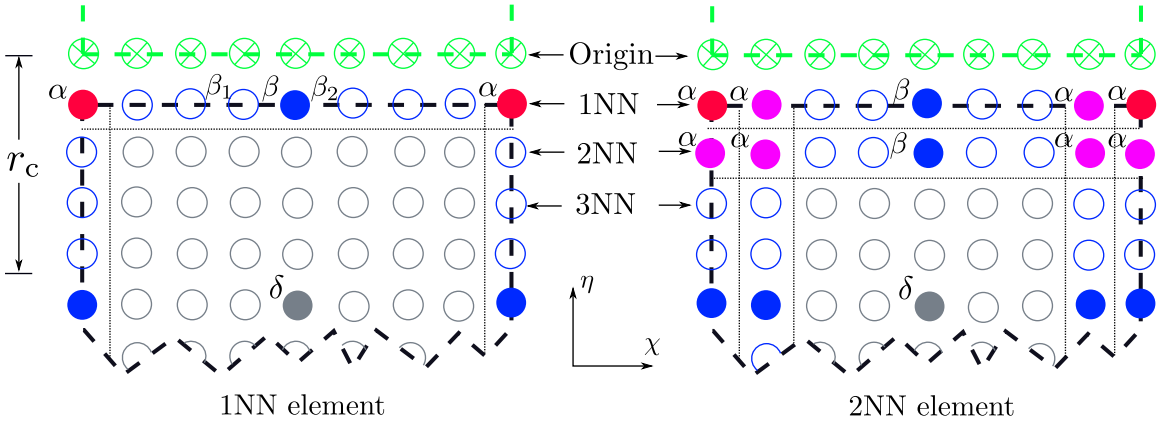

Figure 3.8: A 2D illustration of part of a 1NN (left) and a 2NN (right) element in natural coordinates in CAC simulations. Here, r_c is the cutoff distance of the interatomic potential. The element is divided into a number of subregions by dotted lines, each of which contains one integration point (filled circle) that is located in the center of the subregion. The gray circles are the "interior atoms" and both red and blue are the "surface atoms". The red circles are also the nodes from which all atoms within an element are interpolated. Within a 3D element, there are 27 and 125 integration points in a 1NN and a 2NN element, respectively, regardless of the element size [300].

As discussed in Sec. 2.4.2, in general, the subregions are located symmetrically with respect to the axes in natural coordinates and the integration points are in the center of the subregion; it is therefore required that the subregions and elements have an odd number of atoms along each axis. The number of each type of subregion and weight of relevant integration points in a 3D element are shown in Tab. 3.1. Within each element, there are 27 and 125 integration points for 1NN and 2NN types, respectively, regardless of the element size N_{ape}. Equation 2.34 holds for both element types, i.e., for a 1NN element,

$$8 + 12 \times \left(\sqrt[3]{N_{\text{ape}}} - 2\right) + 6 \times \left(\sqrt[3]{N_{\text{ape}}} - 2\right)^2 + \left(\sqrt[3]{N_{\text{ape}}} - 2\right)^3 = N_{\text{ape}}, \tag{3.2}$$

and for a 2NN element,

$$64 + 48 \times \left(\sqrt[3]{N_{\text{ape}}} - 4\right) + 12 \times \left(\sqrt[3]{N_{\text{ape}}} - 4\right)^2 + \left(\sqrt[3]{N_{\text{ape}}} - 4\right)^3 = N_{\text{ape}}. \tag{3.3}$$

Two layers of atoms are in the "surface" of the 2NN element, compared to only one layer of atoms in the 1NN element. Consequently, the 2NN element better captures the variation

Table 3.1: Number of each type of subregion and weight of relevant integration points in 3D 1NN and 2NN elements [300]. The subregions are illustrated in Fig. 2.3.

Element type		Subregion type			
		α	β	γ	δ
1NN	Number	8	12	6	1
	Weight	1	$\sqrt[3]{N_{\text{ape}}}-2$	$\left(\sqrt[3]{N_{\text{ape}}}-2\right)^2$	$\left(\sqrt[3]{N_{\text{ape}}}-2\right)^3$
2NN	Number	64	48	12	1
	Weight	1	$\sqrt[3]{N_{\text{ape}}}-4$	$\left(\sqrt[3]{N_{\text{ape}}}-4\right)^2$	$\left(\sqrt[3]{N_{\text{ape}}}-4\right)^3$

of force/energy due to the interelement displacement discontinuity (e.g., dislocations), and so better describes the associated surface rearrangement/reconstruction. In practice, elements in the vicinity of a free surface and dislocations should be of 2NN type, while those in perfect lattice can be of 1NN type to reduce the computational intensity. Moreover, since the justification of the 2NN element is based on the interatomic force/energy-distance relation, the proper "thickness" of the "surface" region depends on the interatomic potential. For example, for a longer range interatomic potential, one needs elements with a thicker "surface" region.

Note that although the integration points in CAC are analogous to the sampling points, e.g., in MMM [30–32, 308, 309, 311], they do not serve the same purpose. MMM is a coarse-grained atomistic method with no continuum concept such as stress or strain employed in its framework [309], while CAC is based on a continuous field theory [50]. It is also noteworthy to mention that in earlier CAC work, both nodal integration [68] and 2^{nd} order Gaussian quadrature [67, 290, 292–298, 312–314] are employed. The 2^{nd} order Gaussian quadrature in CAC also divides a 3D element into subregions as in Fig. 2.3 and the positions of each type of subregion are similar to those in the 1NN element shown in Fig. 3.8. However, the positions and weights of the integration points are different from those presented in Tab. 3.1. In this dissertation, the subregions are divided such that the 1^{st} order Gaussian quadrature yields exact solutions based on the assumption in Eq. 2.37, with 1 integration point in each subregion compared with 2 in the 2^{nd} order Gaussian quadrature.

For the EAM potential, as mentioned in Sec. 2.7.4, direct calculation of the host electron density $\bar{\rho}$ of all interpolated atoms is computationally expensive; while providing accurate

$\bar{\rho}$ of the integration points μ and their neighbors j, this method also calculates $\bar{\rho}$ of a large number of unused interpolated atoms, especially so in a large element with sparse integration points. It is shown that this method gives a low coarse-graining efficiency ψ_{cg} around 2.5 for $N_{\text{ape}} = 2197$. Therefore, a similar approximation as in the force/energy calculation is introduced such that within one element, $\bar{\rho}$ of the interpolated atoms in one subregion is assumed equal to that of the integration points in the same subregion. In this way, one needs only to calculate $\bar{\rho}$ of the integration points, and the coarse-graining efficiency is increased substantially, which is shown as EAM (approx $\bar{\rho}^j$) in Fig. 2.5. It is found that if $N_{\text{ape}} = 9261$, $\psi_{\text{cg}} \approx 150$ for 1NN element and $\psi_{\text{cg}} \approx 50$ for 2NN element. Note that in parallel computing, a similar method as in Sec. 3.1 is needed to estimate $\bar{\rho}$ in the elements shared by multiple processors. In this dissertation, the approximation that within one element all atoms in one subregion have the same host electron density is applied, unless indicated otherwise.

3.3 Zero temperature CAC approaches

3.3.1 Introduction

Many concurrent multiscale methods can be employed to conduct both equilibrium and non-equilibrium finite temperature dynamic simulations. In most of these methods, the atoms in the atomistic domain are usually updated following the same way as in MD, in which the temperature is a function of atomic velocity/kinetic energy. As a result, the temperature can be tuned about the desired value using a thermostat, e.g., a Nosé-Hoover thermostat [111].

In the continuum domain, it remains a challenge to handle the dynamics in a manner consistent with that of the atomistic domain [296]. The very idea of "temperature" is not particularly well defined. As such, it is difficult to construct a uniform temperature formulation for both atomistic and continuum domains.

One of the most direct and convenient ways of running concurrent dynamic simulations is to view the nodes in the coarse-grained domain as atoms and to treat the nodal velocity as atomic velocity [32,311]. It follows that one simply substitutes the nodal velocity for the

atomic velocity in the temperature formulation, with the weight of nodes coming into play; for example, in equilibrium dynamic CAC [295, 297], the kinetic energy is defined as

$$E_{\text{kin}} = \sum^{N_{\text{ele}}} E_{\text{kin}}^{\text{ele}} = \sum^{N_{\text{ele}}} \frac{1}{2} m \sum_{\xi} \omega_{\xi} v_{\xi}^2 \tag{3.4}$$

where ξ is the index of node, ω_{ξ} is the weight of node ξ, m is the mass of an atom, and N_{ele} is the number of elements. The temperature T is then

$$T = \frac{2E_{\text{kin}}}{(3N_{\text{node}} - 3)k_{\text{B}}} \tag{3.5}$$

where N_{node} is the number of nodes and k_{B} is the Boltzmann constant.

In the literature, this straightforward yet semi-quantitative extension of quasistatics to dynamics has been employed in several multiscale methods, including multiresolution molecular dynamics [32] and early QC implementation [228]. A key limitation of this approach is the aphysical impedance to phonon propagation due to the non-uniform mesh combined with a transition to a different formulation, e.g., at the atomistic/continuum domain interface [171]. In particular, the shortest wavelength phonon that can propagate through the continuum domain equals the characteristic length of the element. Thus, short wavelength phonons in the atomistic domain cannot be transmitted into the continuum domain with lower nodal density and are reflected back into the atomistic domain, resulting in localized, aphysical heating in the latter. In this regard, Cai et al. [43] and E and Huang [77] proposed *ad hoc* methods to reduce the spurious wave reflection at the domain interface.

Another issue of this approach is the stability of the continuum domain in dynamic simulations. For example, Junge et al. [119] found that the displacement-based atomistic/continuum coupling in a fully-dynamic setting with no damping is inherently unstable. To stabilize the dynamics of nodes, "zero temperature dynamics" including damped dynamics (e.g., Langevin dynamics) or quenched dynamics [229] can be employed, which usually results in a "dynamics" at very low temperature [171]. Direct application of thermostat (e.g., NPT or NVT ensemble) to the coarse-grained continuum domain, as in MD, is questionable for that the temperature T in the continuum domain is ill-defined.

Another way to address the dynamics in the continuum domain is to configure certain material properties as temperature-dependent. In CADD [232], e.g., one uses thermostat to maintain the temperature in the atomistic domain, while in the continuum domain, properties related to DD (e.g., elastic constant, lattice parameter, dislocation mobility, SFE) vary as a function of temperature, as long as such a function is validated [56]. The continuum is considered as a large, constant temperature heat bath which does not accept the heat dissipated by the atomistic domain thermostat [231]. Close to the atomistic/continuum domain interface, the "graded stadium damping" is employed in the atomistic domain, i.e., the velocity of atoms are reduced gradually from atomistic domain interior to the domain interface where all atoms have a zero velocity [187, 196]. The CADD approach employing a quasistatic finite element solution in the continuum domain can thus simulate the equilibrium finite temperature dynamics, yet is unable to deal with the non-equilibrium finite temperature dynamics in which the temperature gradient and heat transfer are essential.

The thermodynamic coupling between the two domains is further complicated in some multiscale methods that employ a "hand-shake" or "pad" region, in which the nodes and atoms overlap. In the literature, *ad hoc* approaches are usually employed; more often, it is claimed that the regions of interest in simulations are far from the hand-shake region or domain interface and so the interference is negligible [172].

Therefore, there is a need to extend the previous dynamics-only CAC method to the regime of zero temperature simulations. In the following, two zero temperature CAC approaches — quenched dynamic CAC and quasistatic CAC — are proposed. In atomistic simulations, both methods are shown to adequately avoid typical issues related to overdriven kinetics in MD [256].

3.3.2 Quenched dynamic CAC

In quenched dynamic CAC [303], the atomic/nodal velocities are adjusted by atomic/equivalent nodal forces [300] following the "quick-min" MD approach [254] which, like dynamic CAC (Sec. 2.6), performs damped dynamics but without the damping term. Specifically, at each

step in quenched dynamics, the velocity of each atom/node, calculated by Eq. 2.51, is projected in the direction of the atomic/nodal force, with its component that is normal to the force discarded; then if the new velocity is antiparallel to the force, it is zeroed, i.e.,

$$\dot{\mathbf{R}} = \begin{cases} \mathbf{0}, & \text{if } \dot{\mathbf{R}} \cdot \mathbf{F} < 0 \\ \frac{(\dot{\mathbf{R}} \cdot \mathbf{F})\mathbf{F}}{|\mathbf{F}|^2}, & \text{otherwise} \end{cases} . \tag{3.6}$$

The idea of quenched dynamics is to gradually drain energy by occasionally zeroing certain velocity components such that the system energy is forced towards a minimum at 0 K [254]. In particular, the "quick-min" method is often employed in atomistic simulations to find the minimum energy path in nudged elastic band (NEB) calculations [327].

3.3.3 Quasistatic CAC

In this section, a quasistatic analog of the CAC method is proposed, similar in character to MS. At 0 K, coarse-grained MS simulations are useful for probing the energy landscape of the material system, and help to distinguish structural contributions to mechanical properties from common overdriven conditions associated with very high strain rates in MD and/or thermal fluctuation due to finite temperature, as discussed in Sec. 1.1.1. Note that in the quasistatic implementation of CAC, there is no dynamic or inertial effects, so the accelerations of the atoms/nodes are zero, and inertial effects, which involve both the atomic mass in the atomistic domain and the mass matrix in the coarse-grained domain, does not influence the simulation result.

The goal of the quasistatic implementation of the CAC approach is to minimize the energy of the system for each increment of system loading, which has contributions from both atomistc (e_{at}) and coarse-grained (e_{cg}) domains, i.e.,

$$e_{\text{int}}(\mathbf{R}) = e_{\text{at}}(\mathbf{R}_{\text{atom}}) + e_{\text{cg}}(\mathbf{R}_{\text{node}}) \tag{3.7}$$

where e_{int} is the internal energy and $\mathbf{R}$ is the positions of all atoms and nodes, distinguished by associated subscript. The goal is to find $\mathbf{R}$ such that e_{int} is at the minimum when the system is subject to certain boundary conditions. When only fully resolved atomistic domains are considered in the simulation, e_{int} is the summation of well defined atomic energy

of all atoms $e_{\text{at}}(\mathbf{R}_{\text{atom}})$ computed using the interatomic potential, and so the quasistatic CAC method reduces to standard MS.

The quasistatic CAC simulation scheme is summarized by the recipe in Tab. 3.2 and Fig. 3.9. In practice, to have a reasonably fast convergence of the energy minimization process, a loading step size $\Delta\lambda$ varying from $0.001a_0$ to $0.01a_0$ is employed, where a_0 is the lattice parameter. The minimization is considered to converge when the absolute energy variation between successive iterations divided by the energy magnitude of the latest iteration is smaller than 10^{-5} or 10^{-6}.

Table 3.2: Quasistatic CAC algorithm. λ is the controlled loading and $\Delta\lambda$ is the loading step size [300].

Step	Atomistic domain	Coarse-grained domain	Methods
1	Initialize $\mathbf{R}^k(\lambda)$	Initialize $\mathbf{R}^\xi(\lambda)$	
2		Calculate $\mathbf{R}^k(\lambda)$ from $\mathbf{R}^\xi(\lambda)$	Eq. 2.46
3	Calculate $\mathbf{F}^k(\lambda)$	Calculate $\mathbf{F}^\mu(\lambda)$	Eq. 2.43
4		Calculate $\boldsymbol{\mathcal{F}}^\xi(\lambda)$	Eq. 2.30
5	Calculate $\mathbf{d}^k(\lambda)$	Calculate $\mathbf{d}^\xi(\lambda)$	
6	Calculate $\alpha(\lambda)$		line search
7	$\mathbf{R}^k(\lambda) = \mathbf{R}^k(\lambda) + \alpha(\lambda)\mathbf{d}^k(\lambda)$	$\mathbf{R}^\xi(\lambda) = \mathbf{R}^\xi(\lambda) + \alpha(\lambda)\mathbf{d}^\xi(\lambda)$	
8	Calculate $e_{\text{int}}(\mathbf{R})$ if necessary		Eq. 3.7
9	Repeat from step 2 until the tolerance is reached		
10	Advance loading step, get $\mathbf{R}(\lambda + \Delta\lambda)$		
11	Repeat from step 2		

3.3.4 Combined quenched dynamic and quasistatic CAC

A combined approach of quenched dynamic CAC accompanied by periodic quasistatic energy minimization in the simulations is also developed, as shown in Fig. 3.10. This combined approach is important for the simulations of slip transfer in Chaps. 8 and 9 since multiple dislocations are driven towards the GB interface. As a result, the dislocated ensemble evolves away from equilibrium and periodic energy minimization must therefore be regarded as a means of constrained optimization for a sequence of nonequilibrium configurations of these extended defects.

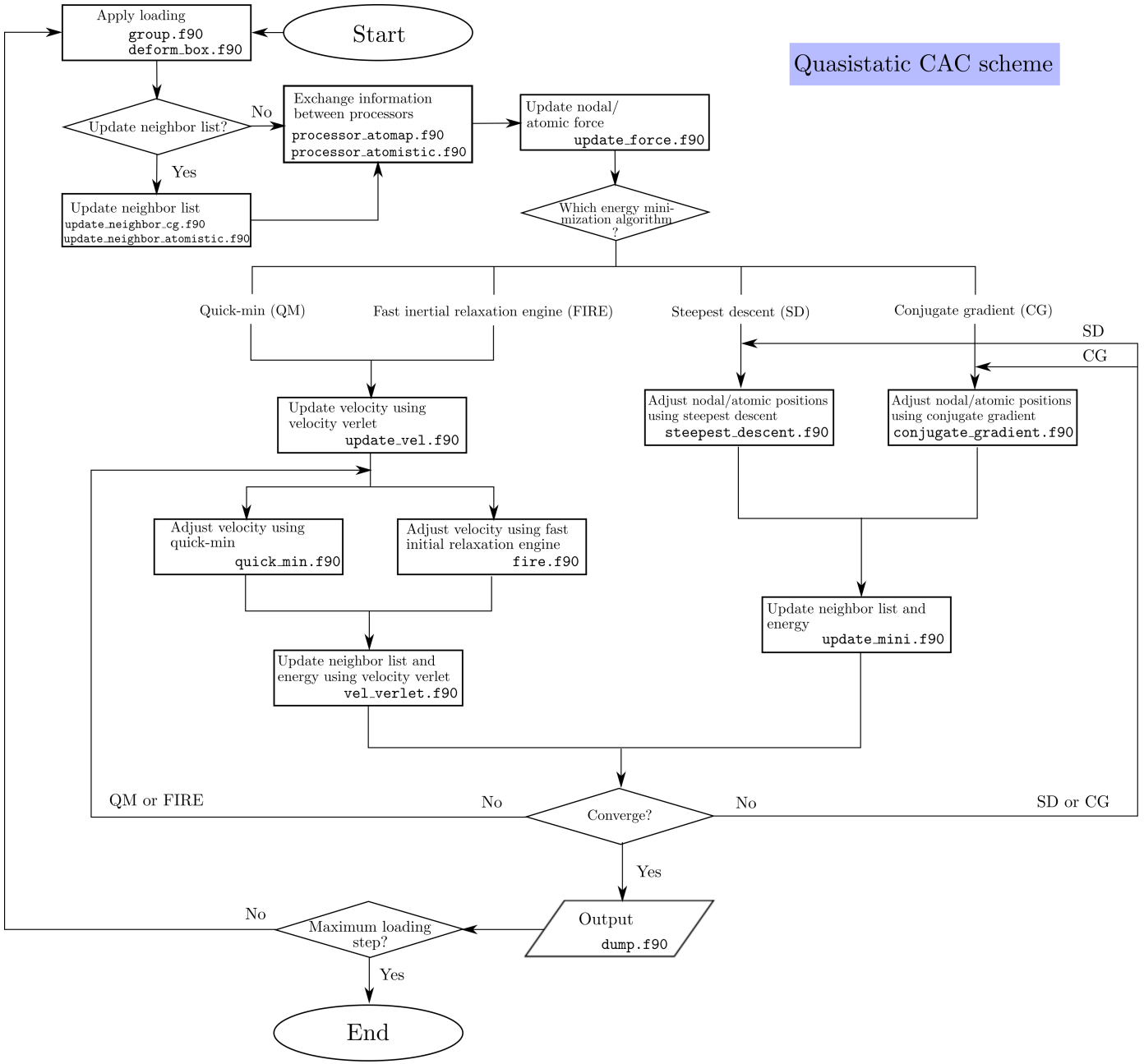

Figure 3.9: Quasistatic CAC simulation scheme.

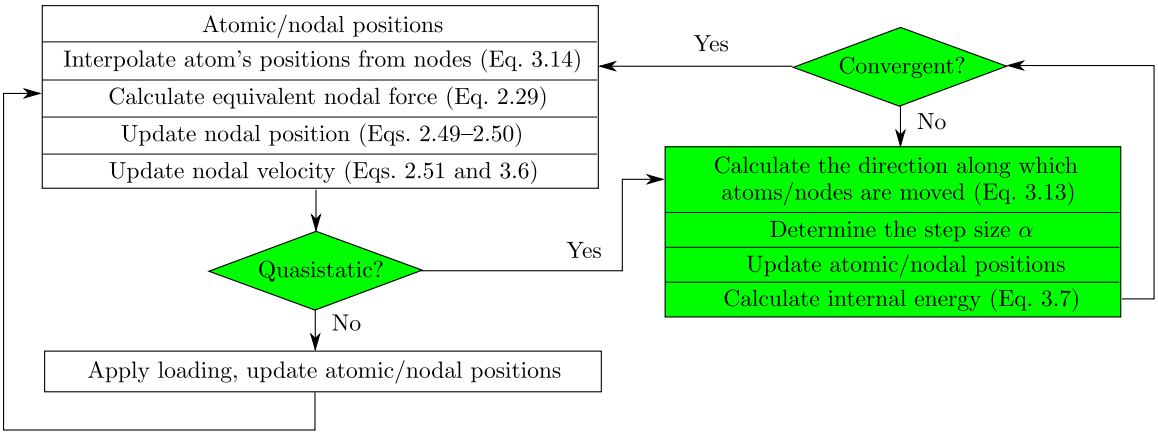

Figure 3.10: Combined quenched dynamic and quasistatic CAC algorithm. The quasistatic part is highlighted in green, while the remaining procedures belong to the quenched dynamic CAC.

3.3.5 Energy calculation

In the atomistic domain, the internal energy e_{int} is the sum of the potential energy of all atoms. Since the force vector field is the negative gradient of the internal energy scalar, it becomes zero when the energy scalar is at the minimum, and vice versa.

In the coarse-grained domain, however, explicitly calculating the energy of all atoms is quite cumbersome. A formulation of e_{int} must be constructed to fulfill two requirements. The first is that for element I, its energy e_I equals that given by Eq. 2.42, i.e.,

$$e_I = \sum_{k}^{N_{\text{ape}}} e^k \tag{3.8}$$

where N_{ape} is the number of atoms per element. The second requirement is that the global equivalent nodal force vector is zero when e_{int} is at its minimum.

Equation 2.30 suggests that the equivalent nodal force is a linear combination of the atomic force on the integration points. This motivates constructing e_{int} as a linear combination of the atomic energy of the integration points, i.e.,

$$e_{\text{cg}} = \sum_{I}^{N_{\text{ele}}} e_I = \sum_{I}^{N_{\text{ele}}} \sum_{\xi}^{N_{\text{npe}}} \sum_{\mu}^{N_{\text{ipe}}} \omega_\mu \Phi_{\mu\xi} e^\mu \tag{3.9}$$

where N_{ele} is the number of elements in the system, N_{ipe} is the number of integration points per element, and e^μ is the atomic energy of integration point μ.

Similar to Eq. 2.37, within a subregion, $e^k = e^\mu$ for all atoms k, i.e.,

$$\sum_{k}^{\omega_\mu} e^k = \omega_\mu e^\mu. \tag{3.10}$$

Therefore, the element energy in Eq. 3.9 becomes

$$\begin{aligned} e_I &= \sum_{\xi}^{N_{\text{npe}}} \sum_{\mu}^{N_{\text{ipe}}} \omega_\mu \Phi_{\mu\xi} e^\mu = \sum_{\xi}^{N_{\text{npe}}} \sum_{\mu}^{N_{\text{ipe}}} \Phi_{\mu\xi} \sum_{k}^{\omega_\mu} e^k \\ &= \sum_{\mu}^{N_{\text{ipe}}} \sum_{k}^{\omega_\mu} e^k \sum_{\xi}^{N_{\text{npe}}} \Phi_{\mu\xi} = \sum_{\mu}^{N_{\text{ipe}}} \sum_{k}^{\omega_\mu} e^k = \sum_{k}^{N_{\text{ape}}} e^k, \end{aligned} \tag{3.11}$$

and the first requirement is satisfied.

Regarding the second requirement, when e_{cg} is at its minimum, so is the energy of each integration point e^μ, which leads to zero $\mathbf{F}^\mu$ and $\boldsymbol{\mathcal{F}}^\xi$. The second requirement is thus fulfilled. Its converse, however, is *not* necessarily true, because zero $\boldsymbol{\mathcal{F}}^\xi$ could be achieved by a combination of non-zero $\mathbf{F}^\mu$, where e_{cg} is *not* at its minimum. Nevertheless, experience shows that such exception rarely if ever occurs.

Following the equivalent nodal force and applying the earlier assumptions in dividing one element into subregions, the equivalent nodal energy of node ξ is defined as

$$\mathcal{E}^\xi = \frac{\sum_\mu \omega_\mu \Phi_{\mu\xi} e^\mu}{\sum_\mu \omega_\mu \Phi_{\mu\xi}} \tag{3.12}$$

which is of the same order as the atomic energy.

3.3.6 Energy minimization

A system at equilibrium corresponds to a local minimum on the potential energy surface. The energy minimization of a many-body system requires that the DOFs are systematically varied until the global minimum is reached. A generic non-linear energy minimization algorithm consists of three steps [254]:

1. For each DOF in global position vector $\mathbf{R}$, find the global direction vector $\mathbf{d}$ and the global step size α;

2. Update $\mathbf{R}$ to $\mathbf{R} + \alpha\mathbf{d}$ to get the minimum of potential energy along $\mathbf{d}$ (in CAC, the golden section search method is employed to determine α [46]);

3. Calculate the new potential energy, update $\mathbf{d}$.

Non-linear energy minimization methods differ from each other in that the direction vector $\mathbf{d}$ is computed in different ways. Steepest descent and conjugate gradient methods are employed in CAC simulations. Both methods use the negative gradient of potential energy as the initial direction; from the second step, however, the steepest descent method uses the current negative gradient while the conjugate gradient method uses the negative gradient conjugated to the current potential surface — the latter gradient is calculated using the Polak-Ribière formula in CAC [254]. Iteration ceases when some tolerance criterion is satisfied.

In a CAC simulation, whenever the negative gradient vector of potential energy is needed, one adopts the current global force vector $\mathbf{F}_{\text{global}}$, in which the atomic force vector is concatenated with the equivalent nodal force vector, i.e.,

$$\mathbf{F}_{\text{global}} = \begin{bmatrix} F_{\text{atom}}^{1x} \\ F_{\text{atom}}^{1y} \\ \vdots \\ F_{\text{atom}}^{N_{\text{atom}}y} \\ F_{\text{atom}}^{N_{\text{atom}}z} \\ 0 \\ 0 \\ \vdots \\ 0 \\ 0 \end{bmatrix} + \begin{bmatrix} 0 \\ 0 \\ \vdots \\ 0 \\ 0 \\ \mathcal{F}_{\text{node}}^{1x} \\ \mathcal{F}_{\text{node}}^{1y} \\ \vdots \\ \mathcal{F}_{\text{node}}^{N_{\text{node}}y} \\ \mathcal{F}_{\text{node}}^{N_{\text{node}}z} \end{bmatrix} \tag{3.13}$$

where N_{atom} and N_{node} are the number of atoms and nodes, respectively.

In practice, however, the same scalar step size α is applied for all DOFs. While this has numerical benefits, a constraint is accordingly applied on the minimization process, such that the energy of each atom cannot reach its individual minimum simultaneously. This means that the computed minimum system energy is slightly higher than the exact result. The length of the global force vector is also only *close to* zero when the minimized e_{int} is found, and vice versa. It follows that there are two equivalent tolerance criteria: (i) the

energy variation between successive iterations is close to zero and (ii) the length of the global force vector is sufficiently small. The second criterion suggests that one could minimize the system energy by directly zeroing the global force vector. Two methods to do this — the quenched dynamics method [229] and the fast inertial relaxation engine [29] — are also included in CAC, as shown in Fig. 3.9. Note that these two methods, like in the large-scale atomic/molecular massively parallel simulator (LAMMPS), can be used in both zero temperature dynamic and quasistatic CAC. During the energy minimization, the size/shape of the simulation box can be adjusted to converge to the desired stress tensor [254].

3.3.7 Coarse-graining efficiency of energy minimization

The coarse-graining efficiency in quasistatic CAC is more complicated than ψ_{cg} in Sec. 2.7.4, which is only the efficiency within one iteration of the dynamic CAC method. This is because the quasistatic approach involves an outer iteration loop which sets the search direction and an inner iteration loop in which a line search algorithm is performed.

In particular, in the coarse-grained domain, (i) the efficiency in one iteration is higher because only force/energy on integration points are calculated; (ii) in theory, the outer iteration converges in at most n steps where n is the number of DOFs in system, and so the outer iteration loop (i.e., determining the search direction) converges faster than the atomistic domain because of a reduced n; and (iii) the inner loop (i.e., line search algorithm to find the global step size) takes the same number of iterations as for the atomistic domain because the magnitude of direction vector for one node (i.e., equivalent nodal force) is on the same order as that for one atom. It is therefore expected that while the coarse-graining efficiency of energy minimization should be higher than that of the dynamic CAC method, it is limited by the line search algorithm, whose convergence rate varies from case to case.

In this section, a single 60° mixed-type dislocation in Cu is energy minimized in the coarse-grained domain with different boundary conditions, after the dislocation is created by a Volterra knife [300]. The coarse-graining efficiency of the energy minimization is calculated at each simulation step by $\psi = t_{\text{at}}/t_{\text{cg}}$, where t is the runtime for each case, as shown in Fig. 3.11. With periodic boundaries applied along the dislocation line direction, it

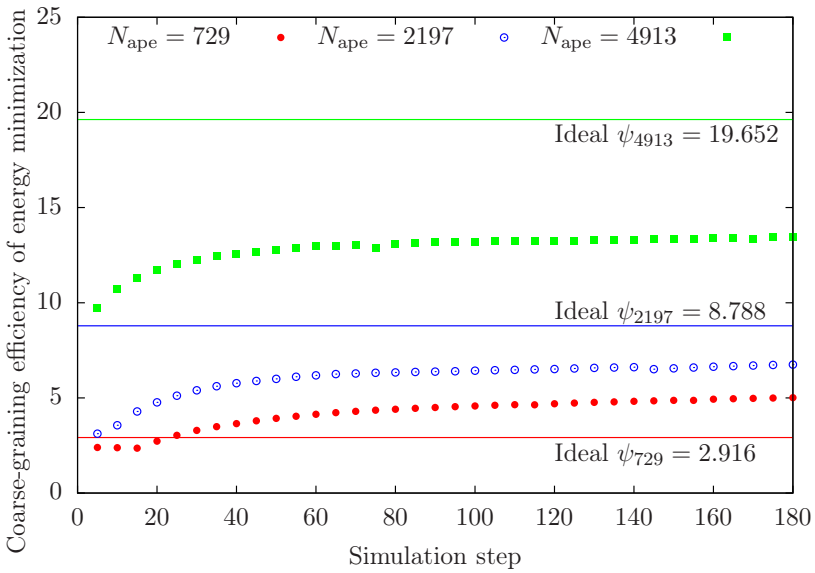

(a) Periodic boundaries

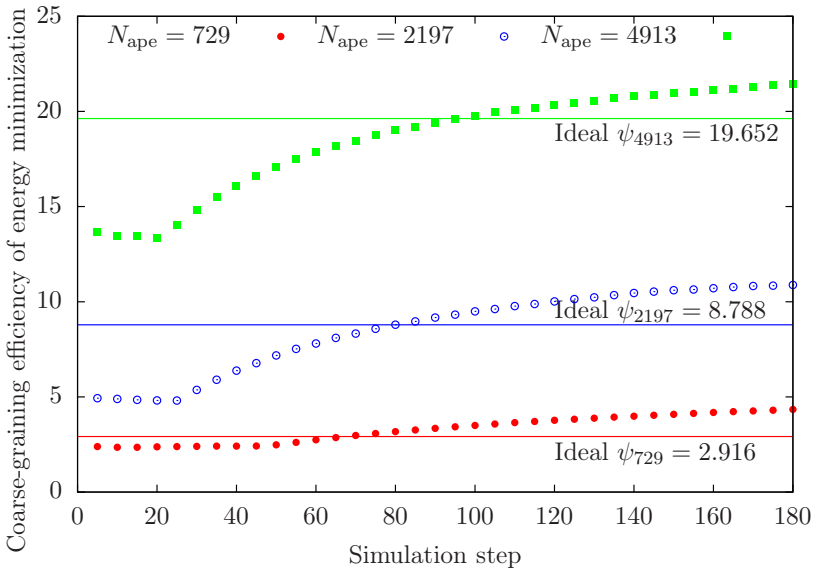

(b) Non-periodic boundaries

Figure 3.11: Coarse-graining efficiency of energy minimizing a single 60° mixed type dislocation in a model (a) with PBCs and (b) without PBCs along the dislocation line direction. It is found that while filling in the periodic boundaries with atoms reduces the efficiency, the quasistatic approach achieves a higher coarse-graining efficiency relative to the dynamic method because the outer iteration loop converges faster [300].

is found that: (i) compared with the last 150 simulation steps, ψ of the first 30 steps is lower due to the low efficiency in energy minimizing traction free surfaces (which occurs in the first 30 steps), and (ii) larger elements give higher ψ. However, except for the smallest element ($N_{\text{ape}} = 729$), ψ is lower than the ideal full coarse-graining efficiency in one iteration. This is

attributed to the atoms that fill in the periodic boundaries — a model with larger elements requires a larger number of atoms to fill in at the boundaries.

Therefore, ψ of energy minimizing the same dislocation in fully coarse-grained models is investigated with non-PBCs along the dislocation line direction, as shown in Fig. 3.11(b). The lower efficiency at the initial stage lasts about 80 simulation steps because more traction free surfaces need to be relaxed. After that, ψ becomes higher than the ideal efficiency in one iteration because the outer iteration loop converges faster.

3.4 Mesh refinement schemes

3.4.1 Introduction

Most modeling and simulation in mechanics of materials involves numerical discretization, either temporal, spatial, or both [20]. For example, the derivative of a single variable function can be approximated by a difference quotient; an integral can be thought as an infinite sum of rectangles of infinitesimal width [46]. In continuum mechanics, the most commonly employed approach for spatial discretization is the FEM, which converts partial differential equations into variational integral equations to find approximate solutions to boundary value problems [329]. In so doing, the continuum domain is partitioned into a number of smaller subdomains, over each of which the governing equations can be solved more easily. The discretization error of FEM is thus determined by whether the domain is well partitioned and whether each subdomain, i.e., an element, is correctly solved. This is analogous to approximating a curve by connecting many tiny straight segments: shorter segments should be employed where the target curve has a high curvature.

The employment of continuous subdomains with varying sizes in spatial discretization becomes problematic in the presence of nanoscale defects; in such cases, the continuum approximation begins to break down. Atomistic simulations such as MD and MS are more suitable for modeling defects such as nanoscale cracks or dislocation cores. In these nonlocal particle methods, spatial discretization is not necessary and defects are naturally admitted. However, the high computational cost of atomistic simulations makes their application to larger domains impractical. Thus, numerous concurrent multiscale methods have been

developed to connect the continuum domain with the atomistic one when both are updated concurrently in time [216].

Most concurrent multiscale methods divide the system into atomistic and continuum domains, as discussed in Sec. 1.1.1. While the atomistic domain is considered to render the "exact" solution within the uncertainty of the interatomic potential, it should be applied only in the neighborhood of area of interest, e.g., defects, to reduce the number of DOFs in the system [254]. Such a pre-partitioned domain works well when the spatial distribution of defects is invariant or when defects migrate along prescribed paths. In a more realistic case, however, the locations and migration paths of defects are difficult to predict *a priori*. Unlike in FEM where all subdomains are of continuum character, a concurrent multiscale simulation concerns subdomains of both continuum nature and discrete atoms. This suggests that a larger numerical error could occur as the system evolves if the continuum domain, which cannot explicitly model nanoscale defects, is not converted to discrete atoms, as necessary. Therefore, it is crucial and natural for most concurrent multiscale methods, especially in time dependent dynamic problems, to re-partition the domain down to the atomic scale on-the-fly, a process known as adaptive remeshing in FEM. Concurrent multiscale methods augmented with mesh refinement, either adaptive or non-adaptive, are referred to as mesh-refining multiscale methods in this section.

In FEM, there are three remeshing techniques: (i) reducing or increasing the mesh size (h-refinement), (ii) varying the polynomial degree of the interpolation basis (p-refinement), and (iii) relocating or moving a mesh (r-refinement), where the refinement criterion is often expressed in form of the relative error in total strain energy [329]. A combination of these procedures, e.g., hp-refinement, is also widely employed. In mesh-refining multiscale methods, similar procedures can be adopted to decide whether a larger atomistic domain and/or a higher order continuum domain become necessary. To the author's best knowledge, most mesh-refining multiscale methods employ h-refinement. The key is to maintain the atomic-scale resolution around certain defects, e.g., dislocations, in a subdomain such that it encompasses the highly nonlinear and nonlocal behavior through mesh refinement.

3.4.2 A review of adaptive multiscale modeling methods

In the QC method [255], a dislocation nucleated in the atomistic domain cannot migrate into the continuum domain unless the mesh is locally refined to atomic scale to render the dislocation. Several adaptive QC methods have been proposed, where elements are refined to distributions of atoms according to eigenvalues of the right stretch tensor [228], Green's strain [185], or a goal-oriented *a posteriori* error estimator [8]. The same error estimator can also be used to remove unnecessary representative atoms (repatoms) from the mesh [171], similar to the h-refinement through which a collection of atoms is coarsened into a continuum. Moreover, the QC mesh can also be adaptively refined with p-refinement, e.g., using variable-node elements [137]. However, the adaptive QC method has several issues [306]:

1. Linear triangular/tetrahedral finite elements are usually employed in QC because the refinement can be easily achieved through a constrained Delaunay triangulation [138]. Nevertheless, a linear triangular/tetrahedral element has constant strain, suggesting that it gives reasonably accurate results only in areas with small strain gradient. Moreover, the accuracy of tetrahedral elements in 3D is more sensitive to the degree of refinement of the mesh compared with more flexible hexahedral type elements [202]. In other words, a larger region in the vicinity of defects needs to be refined within tetrahedral elements compared with that for hexahedral elements to achieve the same accuracy.

2. In QC, continuous elements are employed where each node is shared by multiple neighboring elements. Thus the mesh refinement must be carefully conducted such that the interelement compatibility is always satisfied. In addition, the shape of elements does not correspond to the underlying lattice, while new atoms converted from elements during refinement must fall on actual atomic sites in the reference lattice [171]. A Cauchy-Born type method is required to locate the current atomic sites from the deformed elements. All these add to the complexity of adaptive QC methods. While

variable-node elements have been developed to handle the interelement compatibility [130, 149], their implementation in adaptive QC remains challenging, e.g., it is not straightforward to construct the shape functions for a 3D variable-node element with arbitrary nodes on its edges and/or surfaces.

3. For a dislocation to pass through the continuum domain, all elements along its trajectory need to be adaptively converted to nonlocal repatoms. The consequence of this continuous refinement is that the final model could become increasingly computationally expensive if the dislocation travels substantial distance. Although the atomistic domain behind the dislocation (where local lattice is perfectly restored) could be "coarsened" back to continuum domain, it is desirable that such refining and coarsening processes are minimized.

In the CADD method [232], dislocations can move from an atomistic to a continuum domain where dislocations interact with each other through a long range elastic stress field dictated by continuum theory. In CADD, deformation near the atom/continuum interface can reach a value at which a larger size atomistic domain is needed, necessitating mesh refinement [187]. Motivated by the key idea in CADD that the discontinuities due to dislocation-mediated slip in the continuum domain do not have to be retained at full atomistic resolution, Gracie and Belytschko [98, 99] developed an adaptive method combining the extended finite element method (XFEM) and the bridging domain method (BDM) to model moving dislocations. A crucial component of the adaptive XFEM-BDM framework is that the displacement discontinuities are specified through a step function across the active slip planes in a continuum region by means of XFEM enrichments [17, 18, 175]. In adaptive XFEM-BDM, the mesh is refined and coarsened based on either of these two criteria: (i) the broken inter-atomic bonds and (ii) the errors in atomic displacements associated with introducing a continuum field [177]. However, the Burgers vectors associated with the enrichment function for the discontinuity are assumed constants. Therefore, applying this method to other types of discontinuities such as stacking faults, partial dislocations, and

twinning is not straightforward. For example, it is not clear how the SFE can be incorporated into XFEM in a manner consistent with atomistic descriptions. In 2D XFEM-BDM, the mesh is refined and coarsened according to the distance traveled by dislocations from the bridging domain [177]. In 3D, however, neither the bridging domain nor the travel distance are defined unambiguously, rendering the application of this method to complex dislocation network formation difficult, if not impossible [306].

In summary, most mesh-refining multiscale methods for passing dislocations between atomistic and continuum domains can be classified into two types based on whether the dislocations are permitted in the continuum. The first type includes the QC-like methods, in which all elements in the continuum domain need to be refined locally to atomic scale fidelity to address dislocations. Consequently, the number of DOFs scales with the defect volume, even with the aid of mesh coarsening. The second type includes the CADD-like methods, where the continuum domain describes lattice defects by either constitutive relations or lattice elasticity with dislocation field interactions, in the same way as in DD, cohesize zone method (CZM), or XFEM. Compared with methods of the first type, mesh refinement in the second type of method is less demanding. For example, dislocations exist in both DD and XFEM while cracks can be handled in both CZM and XFEM. Other types of discontinuities, such as point defects and complex dislocation junctions, may only be described accurately in the atomistic domain, and so mesh refinement is still necessary. For both types of mesh-refining multiscale methods, one common issue is the geometric complexity during the mesh adaptation, due to either the interelement compatibility requirement in the first type of method or the heuristic dislocation passing/enrichment strategies between two domains in the second type of method.

3.4.3 Development of mesh refinement schemes for CAC

In this section, the CAC method is extended by implementing two mesh refinement schemes. The similarity of the CAC method to FEM ensures its convergence and stability, and facilitates the mesh refinement procedure; for example, an *a posteriori* error estimator as in FEM can be introduced to assess the accuracy of the CAC method with mesh refinement

schemes. In the coarse-grained domain, elements that have discontinuities between them permit dislocation migration. As a result, unlike the first type of mesh-refining multiscale method discussed above, the elements in the coarse-grained domain in the vicinity of a dislocation do not have to be refined to the atomic scale. Additionally, there is no ghost force at the atomistic/coarse-grained domain interface, through which dislocations can pass smoothly. This feature distinguishes CAC from the second type of method.

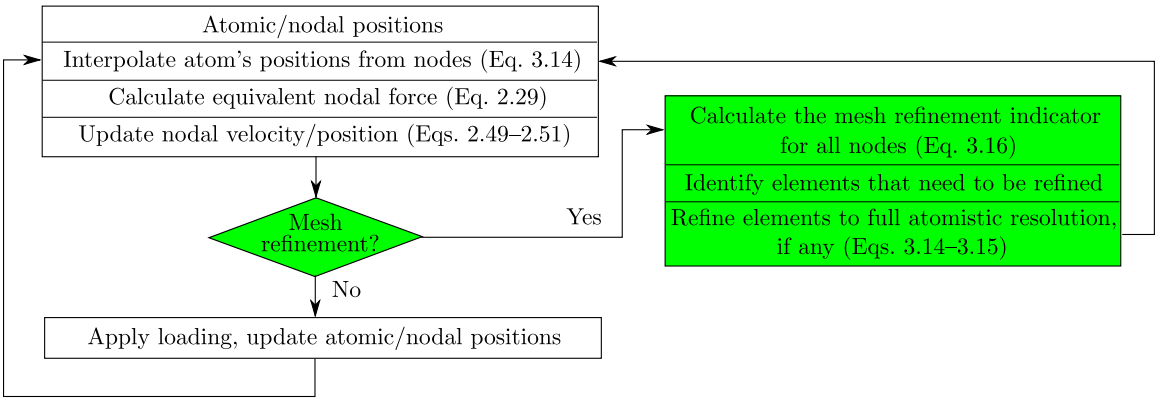

Figure 3.12: Dynamic CAC simulation algorithm with mesh refinement schemes. The mesh refinement procedures are highlighted in green, while the remaining procedures belong to the original dynamic CAC simulation scheme [306].

Unlike in FEM and most multiscale methods where a continuous mesh is employed, CAC accommodates dislocations between elements. The advantages of CAC in mesh refinement include (i) no interelement compatibility is enforced after refinement, which simplifies the procedure, (ii) a minimum number of elements are refined to pass dislocations, and (iii) it is straightforward to determine the positions of new atoms because the elements in CAC are assumed to correspond to actual atomic sites in a lattice, i.e.,

$$\mathbf{R}^k = \boldsymbol{\phi}_{k\xi}\mathbf{R}^\xi \tag{3.14}$$

$$\dot{\mathbf{R}}^k = \boldsymbol{\phi}_{k\xi}\dot{\mathbf{R}}^\xi \tag{3.15}$$

where $\boldsymbol{\phi}_{k\xi}$ is the trilinear interpolation function, $\mathbf{R}^\xi$ ($\dot{\mathbf{R}}^\xi$) and $\mathbf{R}^k$ ($\dot{\mathbf{R}}^k$) are the positions (velocities) of node ξ and atom k, respectively. Note that Eq. 3.14 is the same as Eq. 2.46. These features distinguish CAC from most mesh-refining multiscale methods and facilitate an efficient and straightforward implementation of mesh refinement schemes. A flowchart

of the dynamic CAC simulation algorithm with mesh refinement schemes is illustrated in Fig. 3.12.

From the perspective of numerical solution parallelization, mesh refinement results in an immediate unbalance of workload between processors because the processors assigned with new atoms now have more tasks than that for the original elements. Thus, parallel algorithms should be designed such that mesh refinement is accompanied by that the workload is dynamically re-distributed between processors.

3.4.4 Adaptive mesh refinement scheme for dynamic fracture

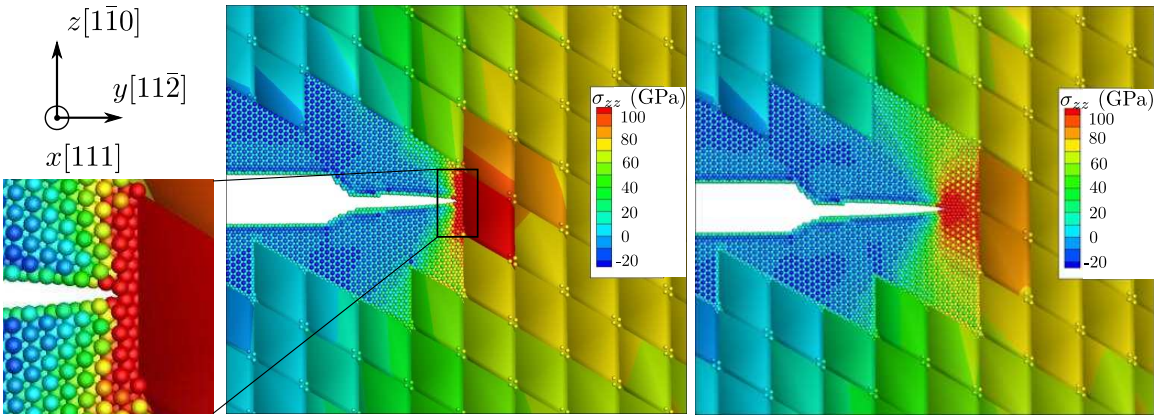

(a) unrefined (b) refined

Figure 3.13: (a) Without mesh refinement, the crack tip intersects the atomistic/coarse-grained domain interface at a location away from the interelement boundary, where a stress concentration occurs; the crack can neither propagate any further nor nucleate any dislocations. (b) With mesh refinement, the crack tip is again within the atomistic domain, and the stress concentration due to incompatibility of crack path is alleviated by restoring full atomistic DOFs. Nodes and atoms are colorred by tensile stress along the z direction, σ_{zz}. The lattice orientations are specified as $x[111]$, $y[11\bar{2}]$, and $z[1\bar{1}0]$ [306].

In dynamic fracture, a crack can either propagate in a brittle manner or respond plastically by nucleating dislocations on multiple slip planes. A notched specimen of FCC Cu is employed for CAC simulations with atomistic resolution in the vicinity of an edge crack and coarse elements employed elsewhere. As an increasing remote tensile stress is applied to the system along the direction normal to the crack plane, atomic bonds at the crack tip are broken and the crack extends. With lattice orientations of $x[111]$, $y[11\bar{2}]$, and $z[1\bar{1}0]$, it is found that without mesh refinement, as the crack tip intersects the atomistic/coarse-grained

domain interface away from an interelement boundary, a stress concentration occurs; the crack cannot propagate any further owing to the kinematic incompatibility with the original crack path, as shown in Fig. 3.13(a). If the elements in front of the crack tip are refined, the stress concentration is alleviated immediately as the crack tip is again within the atomistic domain, as shown in Fig. 3.13(b). These observations motivated development of an adaptive mesh refinement scheme to address dynamic fracture.

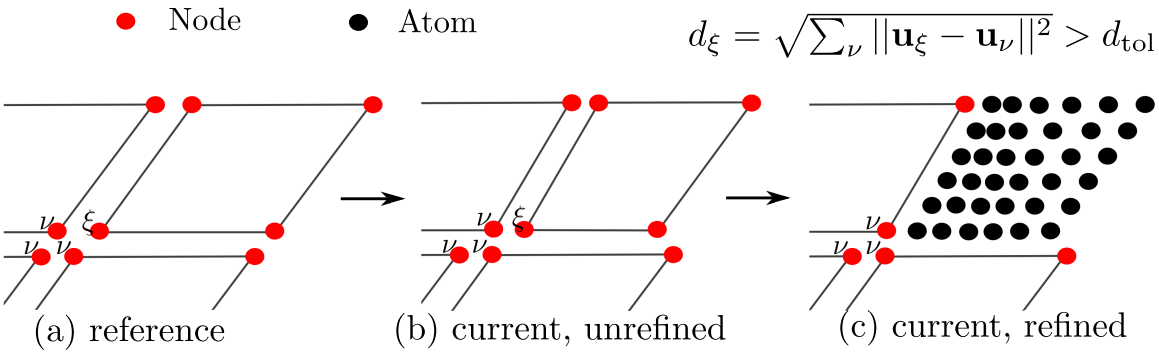

Figure 3.14: 2D illustrations of adaptive mesh refinement procedure. (a) In the reference configuration, node ξ has 3 neighboring nodes ν; (b) periodically, the displacement of all four nodes are calculated by Eq. 3.16; (c) when $d^\xi > d_{\text{tol}}$, the element containing ξ is refined. The atoms in (c) are linearly interpolated from the nodes using their shape functions in undeformed configuration [306].

Unlike in FEM and most multiscale methods with a continuous mesh, e.g., QC, neither displacement continuity nor strain compatibility between the elements is required here. In CAC, the magnitude of the discontinuity between elements is considered by assigning each node ξ a value d^ξ defined by

$$d^\xi = \sqrt{\sum_\nu ||\mathbf{u}^\xi - \mathbf{u}^\nu||^2} \tag{3.16}$$

where $\mathbf{u}$ is the nodal displacement vector and node ν is the neighbor of node ξ defined in the initial undeformed configuration. This discontinuity measurement is used to identify the need for mesh refinement. In 2D and 3D, each node has 3 and 7 neighboring nodes located in different elements, respectively; a 2D illustration is shown in Fig. 3.14. In undeformed configurations, $d^\xi = 0$; in the presence of defects between elements, d^ξ becomes non zero. When any node ξ has a d^ξ exceeding a specified tolerance, d_{tol}, which is a function of a_0, an element is refined to full atomistic resolution by Eqs. 3.14 and 3.15.

Indeed, this is analogous to the use of deformation gradient in the QC approach to signal the need for adaptive remeshing. Compared with continuous FEM, the employment of elements that have discontinuities between them in CAC makes it more convenient to perform local mesh refinement without updating the global matrix thereafter or concerning the compatibility with its neighbors. The nature of the local formulation also promotes the parallelism of the algorithm as well as the workload rebalancing between processors during mesh refinement. Unlike in QC where the elements are constructed independently of the underlying lattice, the element boundaries in CAC are assumed to correspond to actual atomic sites, simplifying the procedure of locating the new atoms from refined elements. Note that the criterion defined in Eq. 3.16 can only be used to trigger refinement of elements into full atomic resolution, but not vice versa, nor can it be used to decide when to split a large element into multiple smaller ones.

It is emphasized that for various mesh refinement criteria there always exists a tradeoff between accuracy, ease of implementation, and efficiency in selection. Regardless of which criterion is adopted, the goal of an adaptive mesh refinement scheme is to detect and update subdomains which otherwise do not give accurate descriptions, so as to achieve a solution having a specified accuracy in an optimal fashion. By re-evaluating d^{ξ} periodically, an adaptive mesh refinement scheme will be employed to model dynamic fracture in Sec. 4.9.

3.4.5 Mesh refinement scheme for dislocation migration

One major advantage of CAC is the admittance of dislocation nucleation and migration between elements in the coarse-grained domain. However, CAC employs more nodes than other concurrent multiscale methods for the same number of elements. Therefore, a mesh refinement scheme for dislocation migration must take full advantage of the elements that have discontinuities between them by ensuring that a minimum number of elements are refined corresponding to dislocations that are not aligned with interelement boundaries. Possible scenarios in which mesh refinement is necessary for dislocation migration include, but are not limited to, (i) a dislocation migrating from an atomistic to a coarse-grained domain, as shown in Fig. 3.15(a), (ii) from the coarse-grained domain with smaller elements

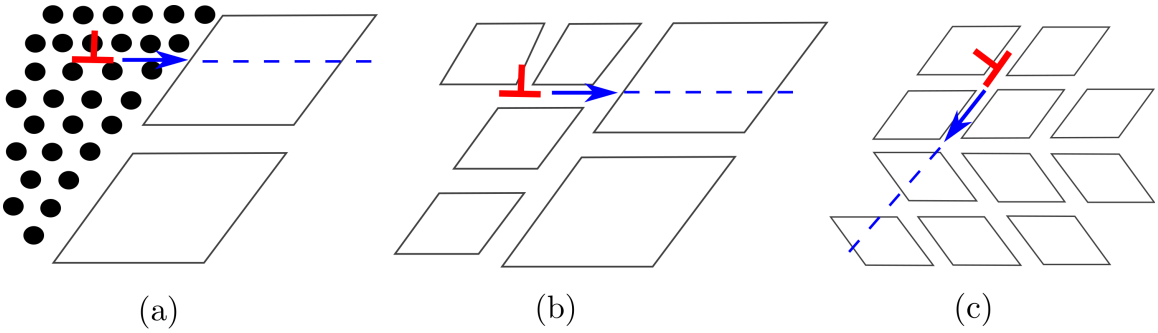

Figure 3.15: Possible scenarios in which mesh refinement is necessary: (a) dislocation migration along an arbitrary path from an atomistic to a coarse-grained domain; (b) dislocation migration from the coarse-grained domain with smaller elements to that with larger elements; (c) dislocation migration within the same coarse-grained domain with a uniform element size but in a case when the elements are not aligned perfectly. Note that the situations encountered in a 3D model can be much more complicated than those shown in these 2D cases [306].

to that with larger elements, as shown in Fig. 3.15(b), and (iii) within the same coarse-grained domain with a uniform element size but for which elements are not aligned perfectly, as shown in Fig. 3.15(c).

An adaptive mesh refinement criterion based on Eq. 3.16 is useful for cases involving a complex dislocation network, e.g., 3D dislocation nucleation under an indenter or from a void/precipitate/crack surface. However, this method refines all elements along the dislocation pathway, similar to the first type of mesh-refining multiscale methods discussed in Sec. 3.4.2. As such, a non-adaptive mesh refinement scheme is implemented in CAC based on manual remeshing to pass dislocations. The position of a dislocation is tracked by analysing the output data every 100 time steps. If some elements are to be refined, the simulation is terminated manually, before the configurations (positions and velocities of all nodes and atoms), as well as the indices of elements to be refined, are saved to restart files. Then a new simulation begins by reading the restart files and refining the marked elements following Eqs. 3.14 and 3.15.

3.5 Summary

In this chapter, four distinct advancements of the CAC approach are introduced. This work contributes to advancing the CAC method in the following ways:

1. The code is upgraded from the original FORTRAN 77 to object-oriented FORTRAN 2003. A number of new features have been added to make the program more general, user-friendly, extensible, and 20 times more efficient. New features of the code include: (i) common atomistic techniques (Newton's third law, Verlet list and link cell methods for short range neighbor search) have been employed, (ii) PBCs become available by filling in extra atoms at the jagged interstices, (iii) integration points in individual elements are shared among multiple processors to minimize the amount of data communication and improve the parallel efficiency, (iv) the spatially unbalanced work load between processors, which is a common issue in multiscale modeling, is alleviated by adaptively assigning approximately the same number of "evaluation points" to different processors, (v) besides the force and stress, energy on each node is calculated, (vi) a novel approach is implemented to calculate the equivalent nodal force in the coarse-grained domain for the EAM potential, and (vii) the neighbor list for the force/energy calculation is now updated on-the-fly, which allows a smaller cutoff distance;

2. Two zero temperature CAC approaches are formulated to enable modeling of the behavior for the precise energy landscape, avoiding issues related to overdriven kinetics of dislocations in dynamic simulations. It is shown that the energy minimized structure is more rapidly achieved in the coarse-grained domain than in the atomistic domain;

3. Numerical implementation is detailed in a mathematically rigorous matter, where the choice of integration point and Gaussian quadrature are explained. A 2NN element with first order Gaussian quadrature in each subregion is proposed in CAC for the first time;

4. Two mesh refinement schemes are proposed for the CAC method. They will be employed in dynamic fracture of a notched specimen (Sec. 4.9) and curved dislocation migration (Sec. 4.10), respectively.

CHAPTER IV

APPLICATIONS OF CAC TO CERTAIN BENCHMARK PROBLEMS AND A PRELIMINARY CONVERGENCE/ERROR ANALYSIS

In this chapter, both quasistatic and dynamic CAC simulations are performed to study certain benchmark problems, including (i) GSFE (Sec. 4.1), (ii) stress field of a single dislocation (Sec. 4.2), (iii) core structure of a single dislocation (Sec. 4.3), (iv) core radius and energy of a single dislocation (Sec. 4.4), (v) Peierls stress of a single dislocation (Sec. 4.5), (vi) surface indentation (Sec. 4.6), (vii) dislocation migration between atomistic and coarse-grained domains (Sec. 4.7), (viii) overall Burgers vector of dislocations (Sec. 4.8), (ix) BTD transition in dynamic fracture (Sec. 4.9), and (x) curved dislocation migration (Sec. 4.10), in FCC Cu, Ni, and Al. In the last two problems, the dynamic CAC framework furnished with two mesh refinement schemes presented in Sec. 3.4 is adopted. In all other cases, the quasistatic CAC introduced in Sec. 3.3.3 is employed, in which the energy minimization is achieved using the conjugate gradient method after each deformation increment step. In each case, multiple loading step sizes are evaluated such that the results are step size independent. The minimization is considered to converge when the absolute energy variation between successive iterations divided by the current energy magnitude is smaller than 10^{-6}.

When more than one material is studied in the same case, models are of the same size except for a different lattice parameter a_0. In the coarse-grained domain, 2NN elements with $N_{\text{ape}} = 2197$ are employed unless indicated otherwise. In the remainder of the dissertation, unless indicated otherwise, the calculations involving the atomic structures, including disregistry, von Mises local shear/strain invariant, and Burgers vector, are performed after the atomic positions are interpolated from the nodal positions following Eq. 2.46; simulation results are visualized using Tecplot®, ParaView [222], and Open Visualization Tool (OVITO) [245]. In Sec. 4.11, a preliminary convergence and error analysis based on the results is presented. In the end, a summary is presented in Sec. 4.12.

Here and in the remainder of the dissertation, unless stated otherwise, EAM potentials for Cu [174] and Ni and Al [173] are employed because they well reproduce the GSFE curve as predicted by experiments [47].

4.1 Generalized stacking fault energy

Both the stable and unstable SFE on {111} planes along ⟨112⟩ directions are relevant in modeling dislocation nucleation and migration in FCC metals [270]. In the atomistic domain, the GSFE is calculated as

$$e_{\mathrm{SF}} = \frac{e_{\mathrm{at}} - e_{\mathrm{coh}} N_{\mathrm{atom}}}{A_0} \tag{4.1}$$

where e_{at} and N_{atom} are the total energy and number of atoms, respectively, e_{coh} is the cohesive energy per atom, and A_0 is the faulted area. The atoms considered are usually up to 8 to 10 layers on each side of the stacking fault [331]. Figure 4.1 shows that considering only 2 layers of atoms on each side is sufficient to calculate the GSFE on $(1\bar{1}1)$ plane along $[1\bar{1}\bar{2}]$ direction in Cu. This is also true for Al and Ni.

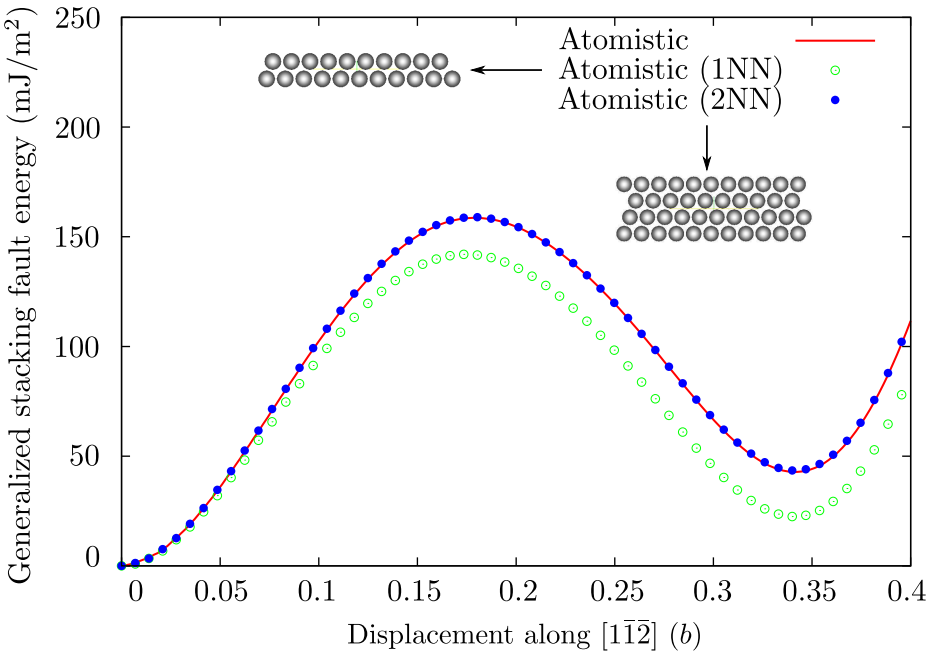

Figure 4.1: Relaxed GSFE on $(1\bar{1}1)$ plane along $[1\bar{1}\bar{2}]$ direction in Cu in a fully atomistic domain. b is the magnitude of Burgers vector $\mathbf{b} = (a_0/2)[1\bar{1}\bar{2}]$. Consideration of only 2 layers of atoms on each side of the stacking fault is sufficient to reproduce results of full atomistics [300].

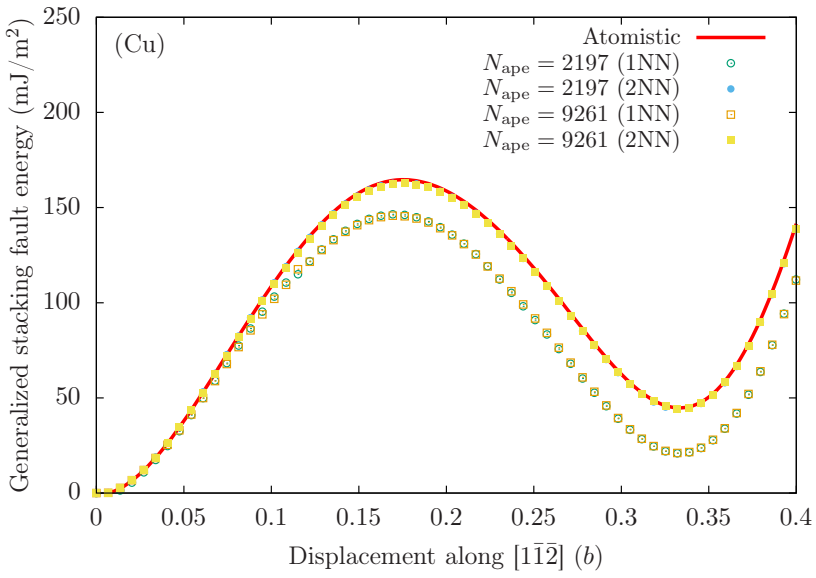

(a) Cu

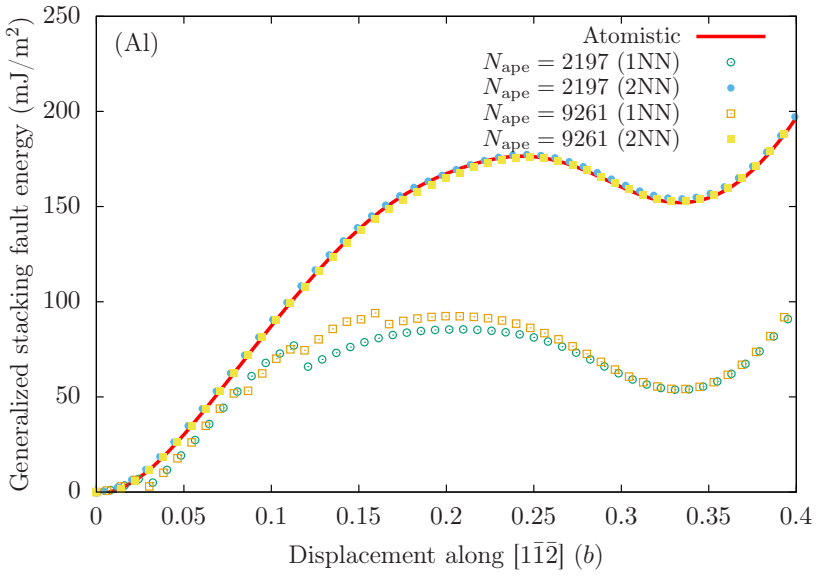

(b) Al

Figure 4.2: Relaxed GSFE on $(1\bar{1}1)$ plane along $[1\bar{1}\bar{2}]$ direction in both Cu and Al in the coarse-grained domain. b is the magnitude of Burgers vector $\mathbf{b} = (a_0/2)[1\bar{1}\bar{2}]$. The 2NN element provides more accurate predictions than the 1NN element [300].

In the coarse-grained domain, the 1NN and 2NN elements consider only the force/energy up to 1 and 2 layers of atoms on each side, respectively, of the interface. In calculating the SFE, e_{at} and N_{atom} in Eq. 4.1 are replaced by e_{cg} and $N_{node}N_{ape}/8$, respectively, where 8 comes from the fact that each element has 8 node. Figure 4.2 shows that the 2NN element gives more accurate results in both Cu and Al compared to fully resolved atomistics than

the 1NN element, regardless of the element size. Both stable and unstable SFE (γ_{sf} and γ_{usf}) as well as their ratio γ_{sf}/γ_{usf} provided by 1NN element are lower than those of the atomistic domain. As suggested by Van Swygenhoven et al. [270], a lower γ_{sf}/γ_{usf} ratio is accompanied by a higher energy barrier to nucleate the trailing partial dislocation. This finding explains the previous observation using 1NN elements that the amplitudes of strain bursts in the stress-strain curves after yielding are larger in the coarse-grained domain than the atomistic domain [292].

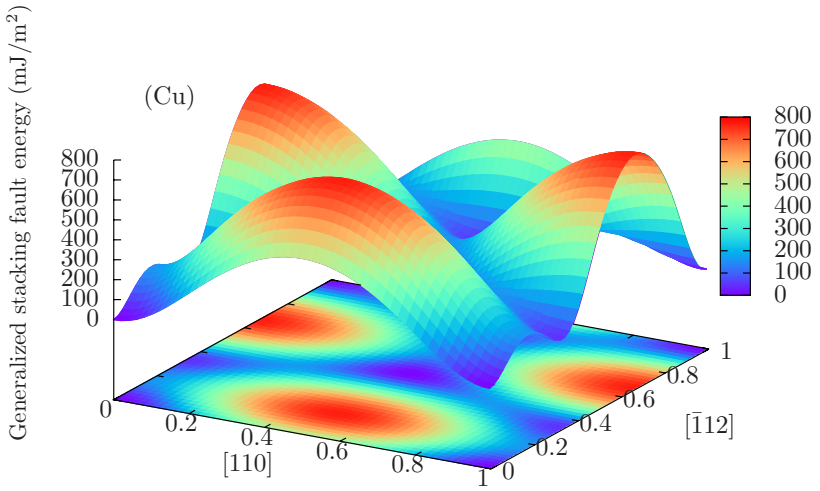

(a) Cu

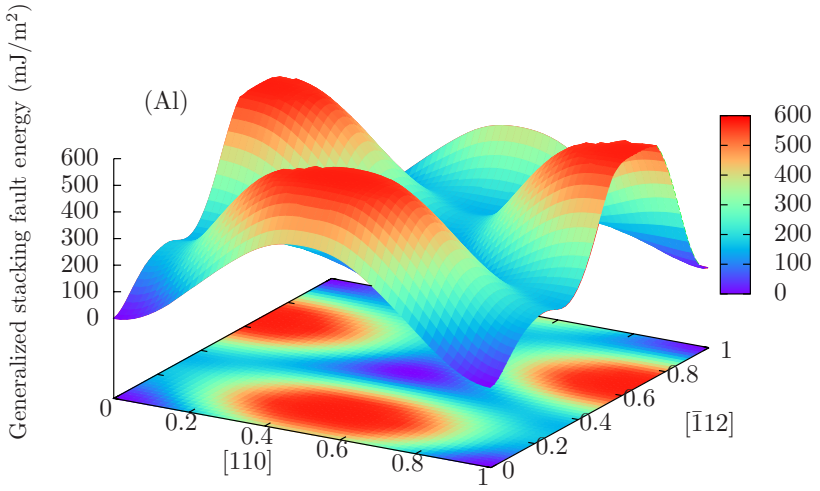

(b) Al

Figure 4.3: Relaxed GSFE surface on $(1\bar{1}1)$ plane along both $[1\bar{1}\bar{2}]$ and [110] directions in both Cu and Al in the coarse-grained domain. The energy surface is close to the results given in the full atomistics, with the relative error less than 5% [300].

The study is then extended to the GSFE surface that is on $(1\bar{1}1)$ plane along both $[1\bar{1}\bar{2}]$

and [110] directions. The energy surface obtained in the coarse-grained domain (Fig. 4.3) is close to that of the fully atomistics, with the relative error less than 5%.

As discussed in Sec. 2.4.2, the newly developed 2NN elements better capture dislocation-mediated surface rearrangement/reconstruction, leading to improved characterization of the GSFE. To the author's knowledge, no other coarse-grained atomistic approaches in the literature are able to accurately describe dislocation core level effects in the coarse-grained domain without full atomistic mesh refinement.

4.2 Stress fields of a single dislocation

In FCC metals, a perfect dislocation is dissociated into an extended one that consists of two Shockley partial dislocations separated by a stacking fault. In describing the reactions between dislocations and lattice defects, it is important to obtain reasonably accurate stress fields. In this section, the stress fields of a single pure edge, pure screw, or 60° mixed type dislocation with Burgers vector $\mathbf{b} = (a_0/2)\langle 110\rangle$ in both atomistic and coarse-grained domains are explored in Cu, Ni, and Al with element size N_{ape} varying from 125 to 4913. The dislocation is created by displacing a part of the model along a certain $\langle 110\rangle$ direction on a $\{111\}$ plane, i.e., a Volterra displacement. The total displacement, $a_0/\sqrt{2}$, is reached in 180 simulations steps with $0.004a_0$ each step [300]. Then dynamic simulations are conducted at several descending temperatures from 300 K to 10 K followed by quasistatic relaxation [106]. The model size is 102 nm by 101 nm by 10 nm in thickness, with PBCs applied on the last dimension (i.e., the dislocation line direction) while other boundaries are assumed traction free.

The stress profile in Cu around a single pure edge/screw dislocation is shown in Fig. 4.4 and that around a 60° mixed-type dislocation is given in Fig. 4.5, both in Cu. It is found that the maximum magnitude of the shear stress at dislocation core decreases with an increasing element size, while the far field stress away from the core is preserved. The preservation of the long range stress fields is expected because the elasticity theory considers that the stress field of one dislocation at a long distance is mainly determined by its Burgers vector and character angle, which are the same in the coarse-grained domain as in the atomistic

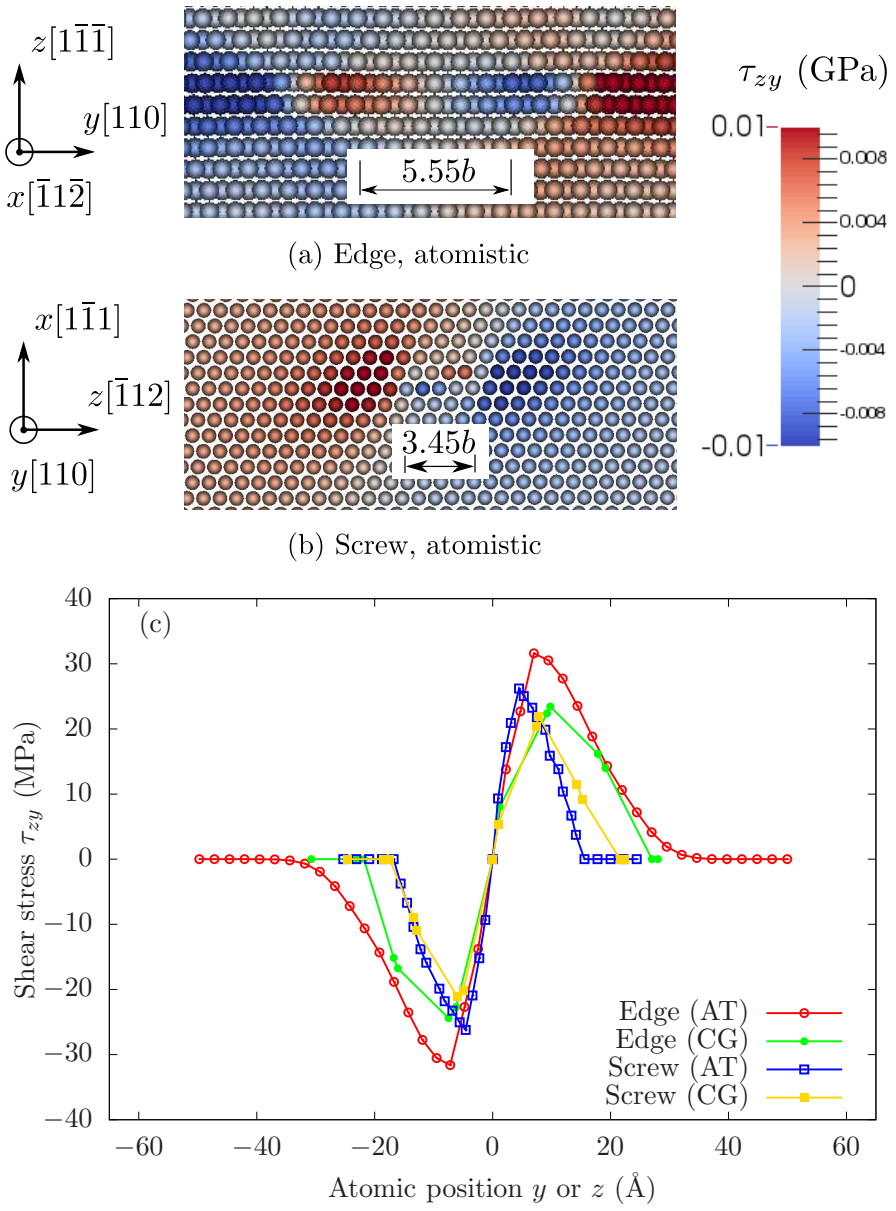

Figure 4.4: Snapshots of the shear stress fields around a single dislocation with (a) pure edge and (b) pure screw character in the atomistic domain for Cu. PBCs are applied along the dislocation line direction, i.e., the x axis in (a) and the y axis in (b). These models are employed to calculate the stacking fault width, full dislocation core radius, Peierls stress, and dislocation core energy. The shear stress τ_{zy} profiles of a single dislocation along the y (edge) or the z (screw) direction in both atomistic (AT) and coarse-grained (CG) domains with the element size $N_{\text{ape}} = 2197$ are given in (c). The stacking fault width, which is defined as the distance between two points with maximum shear stress magnitude, is larger in the coarse-grained domain than in the atomistic domain [301].

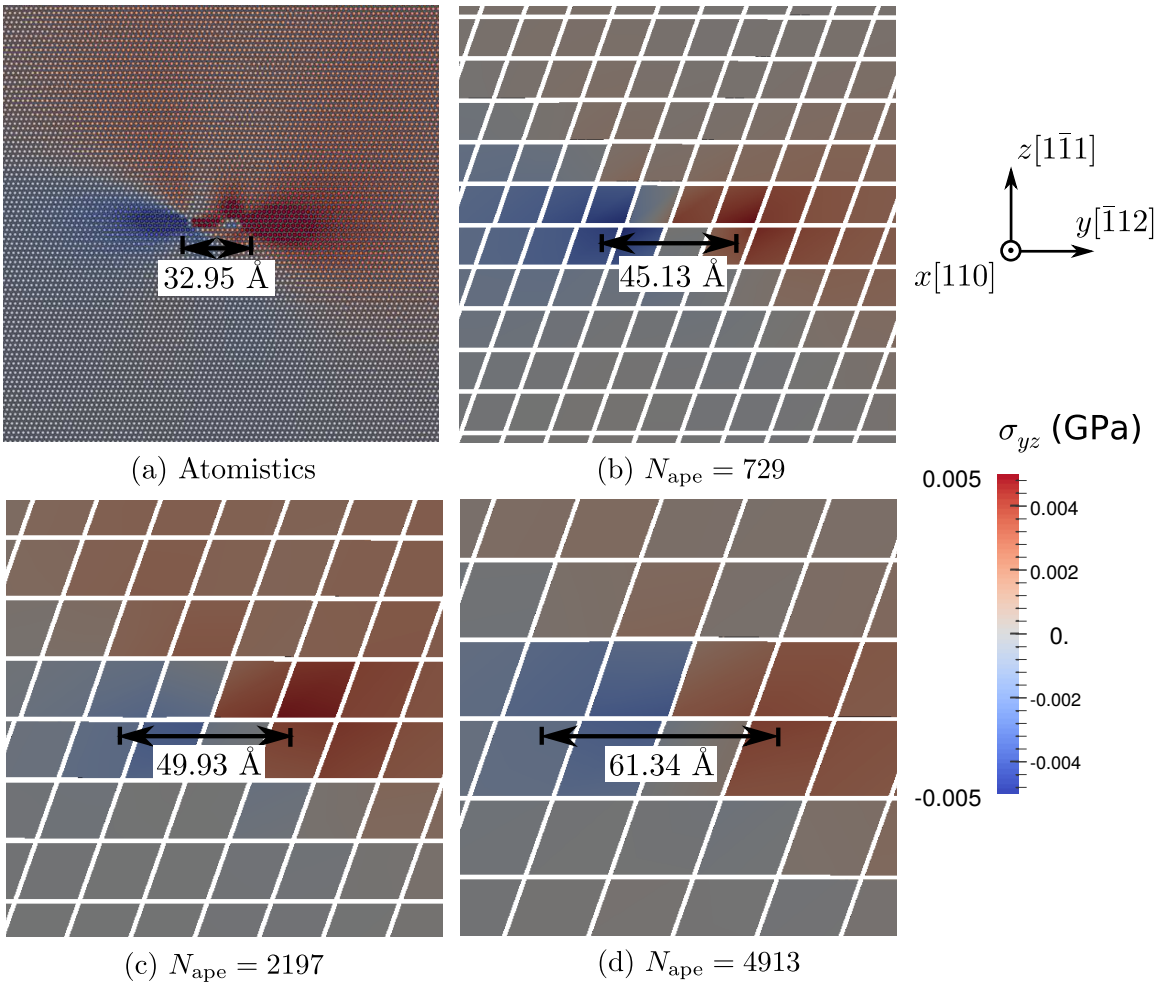

(a) Atomistics (b) $N_{\text{ape}} = 729$

(c) $N_{\text{ape}} = 2197$ (d) $N_{\text{ape}} = 4913$

Figure 4.5: Snapshots of the shear stress fields around a single 60° mixed type dislocation in both atomistic and coarse-grained domains in Cu. A higher degree of coarse-graining gives a wider stacking fault, as well as a reduced maximum magnitude of shear stress. Here, the stacking fault width is defined as the distance over which the disregistry parallel to the Burgers vector is greater than 1/4 of the magnitude of the Burgers vector. In the coarse-grained domain, the far field stress away from the dislocation core is preserved. Note that σ_{yz} is for the edge component only since it is zero for the screw component [300].

domain, as will be discussed in Sec. 4.8. Moreover, if one defines the stacking fault width as the distance between two points with maximum shear stress magnitude, it is shown that the stacking fault width increases with a higher degree of coarse-graining.

4.3 Core structure of a single dislocation

Besides the stress fields, it is also important for the coarse-grained domain to model a reasonably accurate dislocation core structure. In this section, a single 60° mixed type

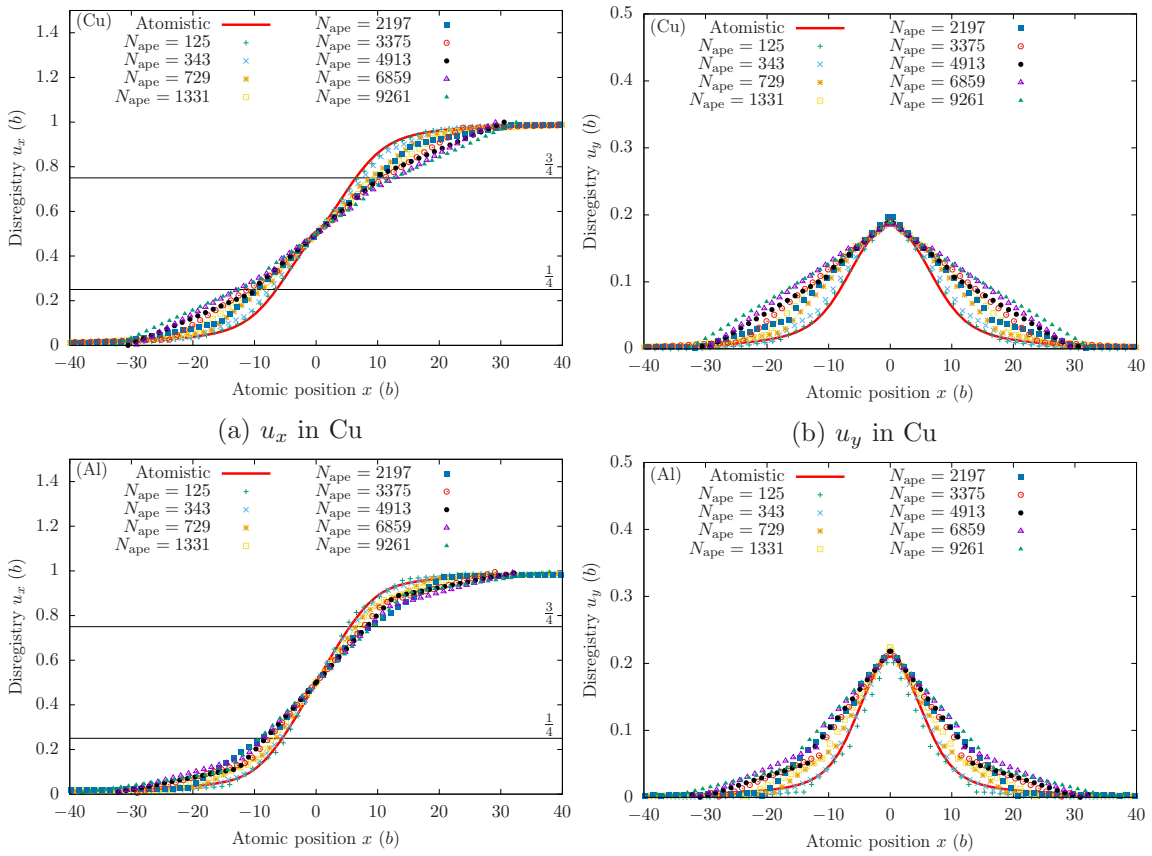

(a) u_x in Cu

(b) u_y in Cu

(c) u_x in Al

(d) u_y in Al

Figure 4.6: The disregistry u_x and u_y are the displacements of the dislocation core atoms from their perfect crystal positions parallel to and normal to Burgers vector $\mathbf{b} = (a_0/2)[\bar{1}01]$, respectively. The results in the coarse-grained domain with varying element size N_{ape} from 125 to 9261 are compared with those of the atomistic domain in both Cu and Al. The disregistry is $b/2$ at the center of the dislocation. In the coarse-grained domain, there is a linear correlation between disregistry and atomic position within an element, due to the trilinear interpolation function [300].

dislocation with Burgers vector $\mathbf{b} = (a_0/2)[\bar{1}01]$ in the coarse-grained domain is studied, in both Cu and Al with element size N_{ape} varying from 125 to 9261. Disregistry, which is the displacement of dislocation core atoms from their perfect crystal positions, is employed to represent the core structure, as shown in Fig. 4.6; u_x and u_y are the disregistry parallel to and normal to the Burgers vector, respectively. It is found that in the coarse-grained domain, there is a linear correlation between disregistry and atomic position within an element, due to the trilinear interpolation function. Thus, as the element size increases, the coarse-grained domain gives a "flatter" dislocation core structure, which agrees with

the larger distance between two partial dislocations. It is therefore advisable to employ a smaller element (e.g., $N_{\text{ape}} = 125$) to better capture the dislocation core structure in the coarse-grained domain.

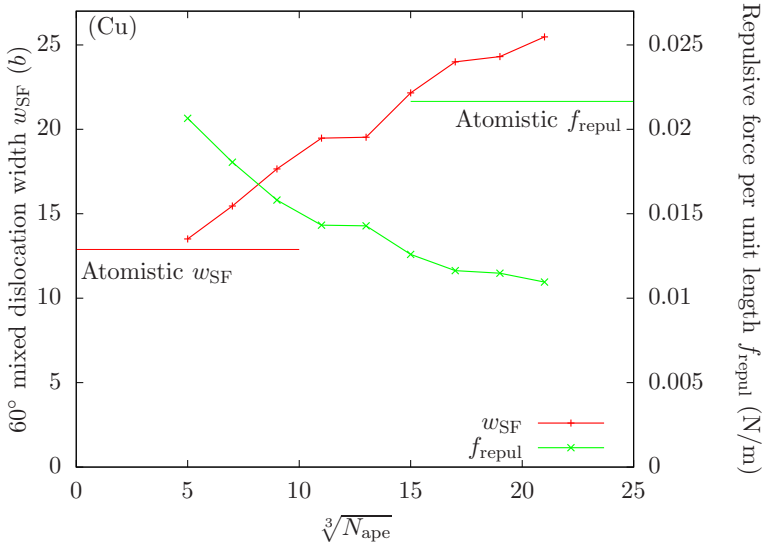

(a) Cu

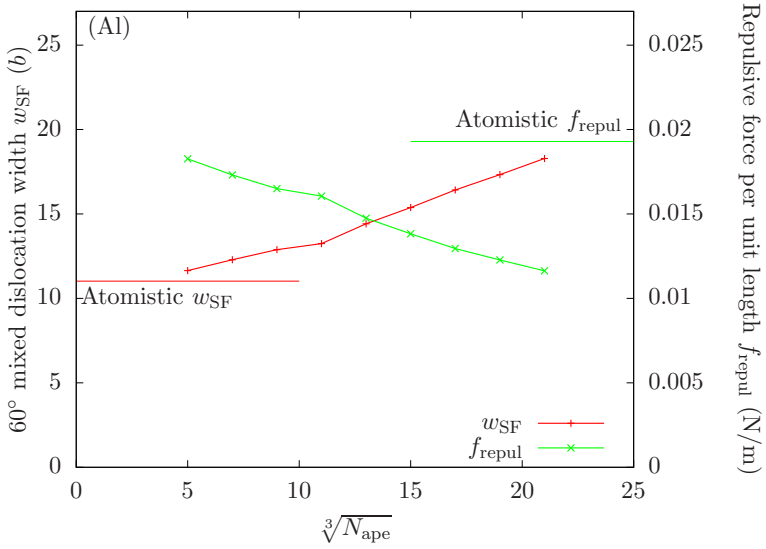

(b) Al

Figure 4.7: In both Cu and Al, the coarse-grained domain gives a larger stacking fault width w_{SF} than the atomistic domain, and w_{SF} increases with element size. As a result, the repulsive force per unit length between two partial dislocations, f_{repul}, decreases with element size. f_{repul} is calculated using Eq. 4.2. For Cu, $\mu = 23.65$ GPa and $b_{\text{p}} = 1.4758$ Å; for Al, $\mu = 26.2$ GPa and $b_{\text{p}} = 1.6534$ Å [300].

If one defines the stacking fault width w_{SF} of the 60° mixed type dislocation as the

distance over which the disregistry parallel to the Burgers vector is greater than 1/4 of the magnitude of the Burgers vector, it is shown that for both Cu and Al, the coarse-grained domain gives a larger w_{SF} than the atomistic domain. Also, w_{SF} increases with element size N_{ape}, as shown in Fig. 4.7. According to Frank's rule, a repulsive force per unit length f_{repul} exists between leading and trailing partial dislocations [114]. Assuming that the Poisson's ratio is zero, for any dislocation line orientation, one may write

$$f_{\mathrm{repul}} = \frac{\mu b_{\mathrm{p}}^2}{4\pi w_{\mathrm{SF}}} \tag{4.2}$$

where μ is the shear modulus and b_{p} is the magnitude of Burgers vector of the partial dislocations. Consequently, f_{repul} in the coarse-grained domain is smaller than that in the atomistic domain, and the larger the element, the smaller the f_{repul}. Besides the repulsive force, there is also an attractive force per unit length f_{attra} acting to bring the partials together: the coarse-grained domain gives accurate f_{attra} because the latter is provided by the stable SFE.

In the atomistic domain, f_{attra} balances f_{repul}. In the coarse-grained domain, however, the difference between f_{attra} and f_{repul} must be compensated by an extra force caused by the constraint of the atomic position imposed by the trilinear interpolation function, i.e.,

$$f_{\mathrm{attra}} = f_{\mathrm{repul}} + f_{\mathrm{constr}} \tag{4.3}$$

where f_{constr} increases with element size.

4.4 Core radius/energy of a single dislocation

To estimate the full dislocation core radius r_0, the strain energy per unit length E_{strain} of a straight dislocation with length L_{d} is calculated by subtracting cohesive energy from the total energy of a cylinder with a radius r with the dislocation along its centroid axis, i.e.,

$$E_{\mathrm{strain}}(r) = \frac{1}{L_{\mathrm{d}}}[E_{\mathrm{total}}(r) - N_{\mathrm{atom}} e_{\mathrm{coh}}] \tag{4.4}$$

where N_{atom} is the number of atoms within the cylinder. Following Ref. [184], r_0 is defined as the cylinder radius beyond which $E_{\mathrm{strain}}(r)$ increases linearly with $\ln r$, and so the core energy $E_{\mathrm{core}} = E_{\mathrm{strain}}(r_0)$. While r_0, which is used to partition the total energy of a

dislocation into core and elastic energies, can be any arbitrary value [42, 146], the goal in this section is to examine if the coarse-grained and atomistic domains give similar r_0 and E_{core} for the same geometry under the same boundary conditions; a comparison of r_0 and E_{core} between different materials is not important.

Table 4.1: Stacking fault width w_{SF} (in b), full dislocation core radius r_0 (in b), Peierls stress σ_{P} (in MPa), and dislocation core energy E_{core} (in eV/nm) for pure edge and pure screw dislocations in both atomistic (AT) and coarse-grained (CG) domains for Cu, Ni, and Al. w_{SF} is defined as the distance between two points with maximum shear stress magnitude. In each domain/material, $E_{\text{core}} = E_{\text{strain}}(r_0)$ following Eq. 4.4, with r_0 being its respective core radius [301].

	Cu		Ni		Al	
	Edge	Screw	Edge	Screw	Edge	Screw
w_{SF} (AT)	5.55	3.45	4.71	3.02	2.60	1.42
w_{SF} (CG)	6.96	4.47	5.85	4.08	3.04	1.97
r_0 (AT)	4.97	2.32	3.01	2.46	1.97	1.16
r_0 (CG)	5.52	2.64	3.83	2.73	2.35	1.47
σ_{P} (AT)	2.50	62.50	64.50	441.50	16.50	78.50
σ_{P} (CG)	1.50	45.50	59.50	374.50	14.50	58.50
E_{core} (AT)	1.7	1.2	1.9	0.9	2	1.6
E_{core} (CG)	2.4	1.9	3.1	1.3	2.5	2.2

Variations of the strain energy E_{strain} as a function of the cylinder radius r for Ni, calculated by Eq. 4.4, are given in Fig. 4.8(a). It is found that while the coarse-grained domain gives a higher strain energy E_{strain} near the dislocation core than the atomistic domain, E_{strain} increases linearly with $\ln r$ beyond r_0 with the same slope for the same type of dislocation in both domains. Figure 4.8(b) show that in Ni, the coarse-grained domain has a larger r_0 and E_{core} than the atomistic domain; both quantities converge to the atomistics as the elements become smaller and contain fewer atoms. Values of stacking fault width w_{SF}, full dislocation core radius r_0, and dislocation core energy per unit length E_{core} of pure edge and pure screw dislocations in both atomistic and coarse-grained domains for three FCC metals are given in Tab. 4.1. As expected, r_0 is larger than half of w_{SF} in all cases, because the energy function outside r_0 is elastic.

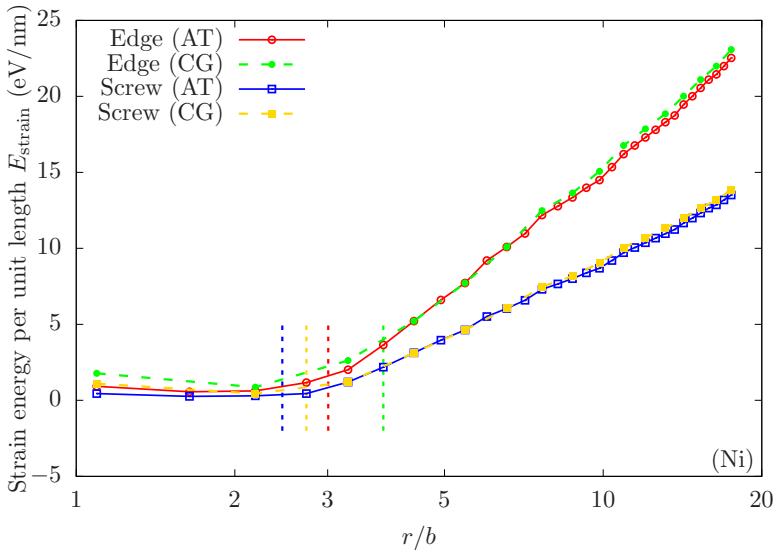

(a)

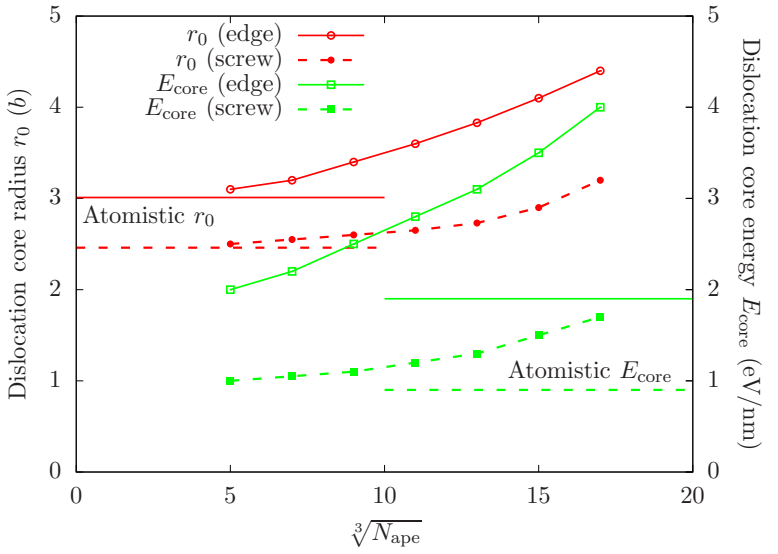

(b)

Figure 4.8: (a) Strain energy per unit length as a function of cylinder radius r for Ni in both atomistic (AT) and coarse-grained (CG) domains, calculated by Eq. 4.4. The vertical lines represent the radius $r = r_0$ beyond which the strain energy increases linearly with $\ln r$, where r_0 is taken as the core radius. (b) In Ni, the coarse-grained domain has a larger core radius r_0 and core energy $E_{\text{core}} = E_{\text{strain}}(r_0)$ than the atomistic domain; both quantities converge to the atomistics (horizontal lines) as each element has a smaller number of atoms N_{ape} [300].

4.5 Peierls stress

The Peierls stress σ_{P} is defined as the minimum stress required to translate a dislocation from one Peierls valley to the next at 0 K [158]. Following the method of Srinivasan et al. [243], quasistatic simulations are conducted with an increment of shear stress $\Delta\tau_{zy} = 1$ MPa for $\langle 110 \rangle \{111\}$ slip system, until both partial dislocations suddenly jump to next valley positions, corresponding to a stress τ'_{zy}. Then $\sigma_{\mathrm{P}} = \tau'_{zy} - \Delta\tau_{zy}/2$, the values of which in Cu, Ni, and Al are given in Tab. 4.1.

It is found that, within a reasonable range, the coarse-grained domain in CAC predicts a larger w_{SF}, a larger r_0, a lower σ_{P}, and a higher E_{core}, compared with fully resolved atomistics; these are expected because of the flattened, spread out dislocation core structure in the coarse-grained domain along element boundaries [42, 300]. In particular, as E_{core} is positively correlated with the dislocation mobility [139], the coarse-grained domain is expected to have a higher dislocation mobility, in agreement with Ref. [296].

4.6 Indentation at a surface

Materials with a high surface-area-to-volume ratio have mechanical properties that differ from bulk materials [328]. For example, the hardness of a nano-thin film is known to be a function of the film thickness, and the nano-indentation process has been widely studied using atomistic simulations. In coarse-graining, however, the lattice deformation at a free surface may not be accurately captured due to its localized nature [185]: the trilinear interpolation function poses a restriction on the atomic configuration, particularly when a large element is employed. Moreover, the assumption that all atoms in a subregion have the same force/energy is only valid when the deformation gradient within an element remains nearly the same, which is not the case for highly inhomogeneous deformation. Therefore, it is instructive to quantify the ability of the coarse-grained domain in describing nano-indentation, shedding light on the treatment of free surfaces in CAC.

Fully atomistic and fully coarse-grained simulations are first performed to analyse the nano-indentation on a thin film in both Cu and Al, as shown in Fig. 4.9. PBCs are applied along both the x and y directions, while the z direction is traction free. A plane indenter is

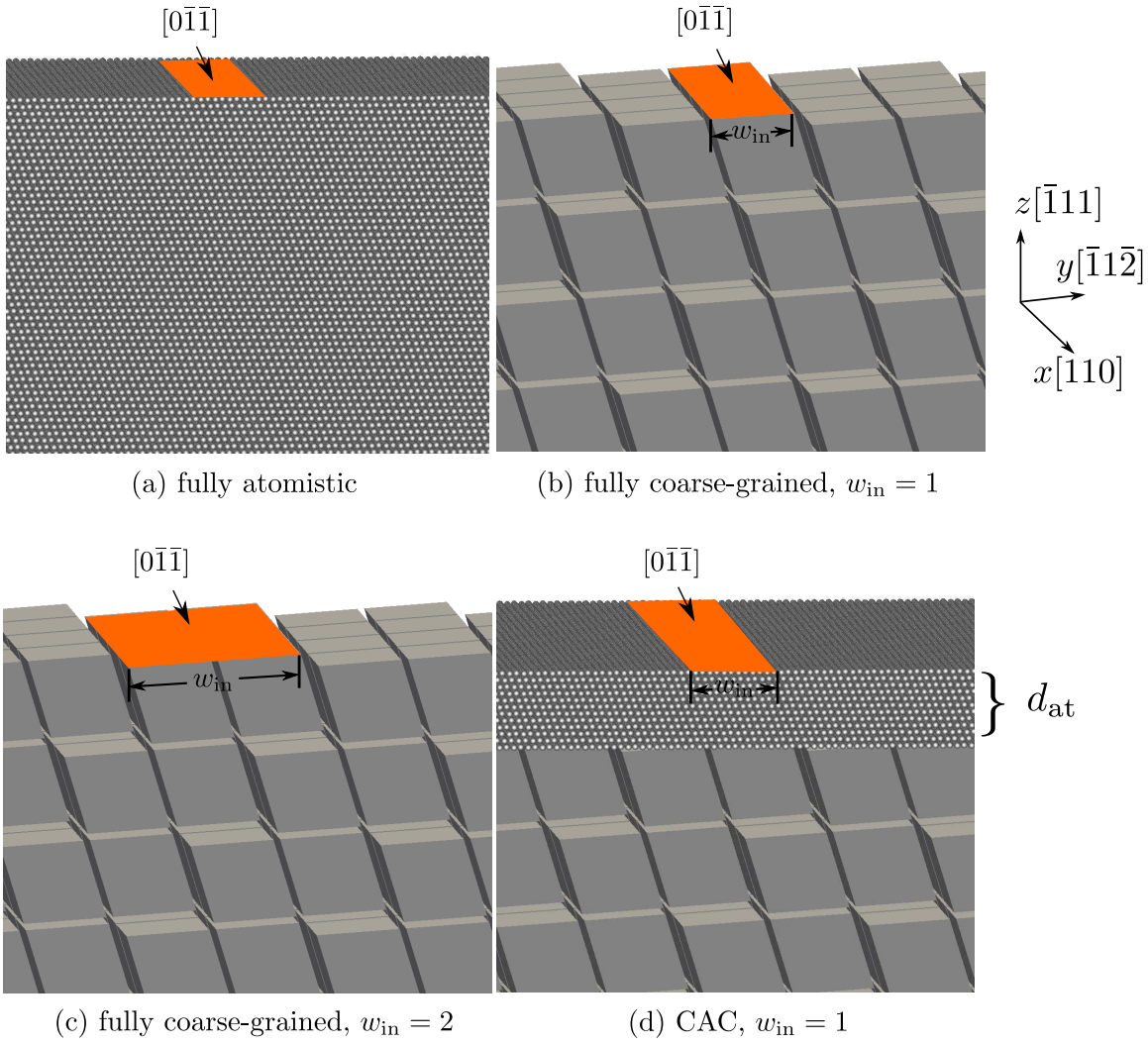

(a) fully atomistic (b) fully coarse-grained, $w_{\text{in}} = 1$

(c) fully coarse-grained, $w_{\text{in}} = 2$ (d) CAC, $w_{\text{in}} = 1$

Figure 4.9: Simulation cells of surface indentation by (a) fully atomistic, (b) and (c) fully coarse-grained with different indenter width w_{in}, and (d) CAC simulations with an atomistic domain at the free surface. PBCs are applied along both the x and y directions. To apply the periodic boundaries in the coarse-grained domain, the jagged interstices are filled in with atoms, which are not shown here. A plane indenter is applied along $[0\bar{1}\bar{1}]$ direction by $0.001a_0$ each step in Cu, while the bottom layers of atoms/nodes are fixed. In (d), different d_{at} are employed to quantify the free surface deformation [300].

applied along $[0\bar{1}\bar{1}]$ direction by $0.001a_0$ each step, while the bottom layers of atoms/nodes are fixed. To eliminate the effects of all cell boundaries but the free surface, sufficiently large models are employed. In Cu, all models have the same size of 18.41 nm by 23.02 nm by 18.16 nm. Simulations in Figs. 4.9(b–c) use the same model but different indenter width w_{in}: along the y direction the indenter spans over either 1 or 2 elements. Element sizes N_{ape} of 343 and 2197 are employed independently. During the indentation, the force on the

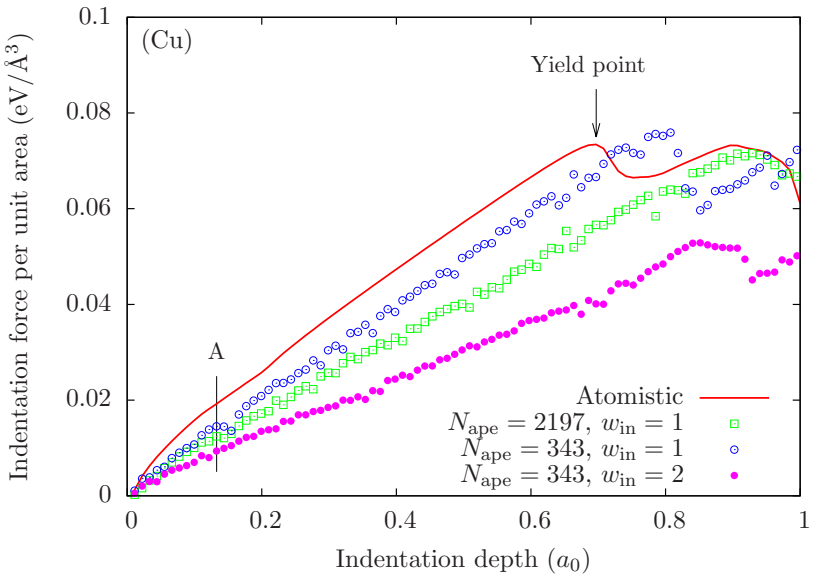

(a) Cu

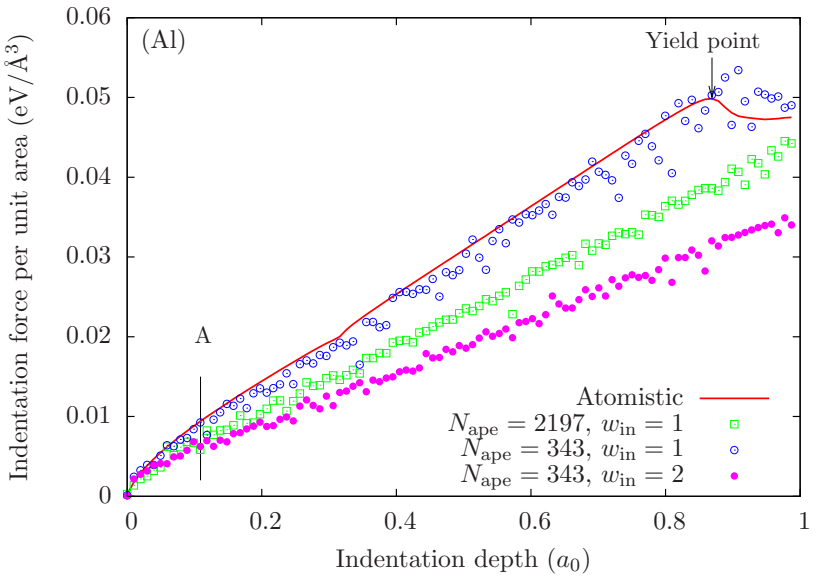

(b) Al

Figure 4.10: Indentation force-depth curves obtained from the fully atomistic and fully coarse-grained simulations in both Cu and Al, as shown in Fig. 4.9(a–c). In the fully coarse-grained simulations, element sizes N_{ape} of 343 or 2197 are employed, with the indenter spanning over 1 or 2 element along y direction. Compared with the full atomistics, the fully coarse-grained model gives a lower and non-monotonically increasing force in the elastic stage. In addition, the deviation is larger with larger element or wider indenter. Point A corresponds to the indentation depth of $0.144a_0$, at which the snapshots are shown in Fig. 4.11 [300].

indenter along the z direction is calculated then divided by the indentation area.

The indentation force-depth curves are plotted in Fig. 4.10. Compared with the fully

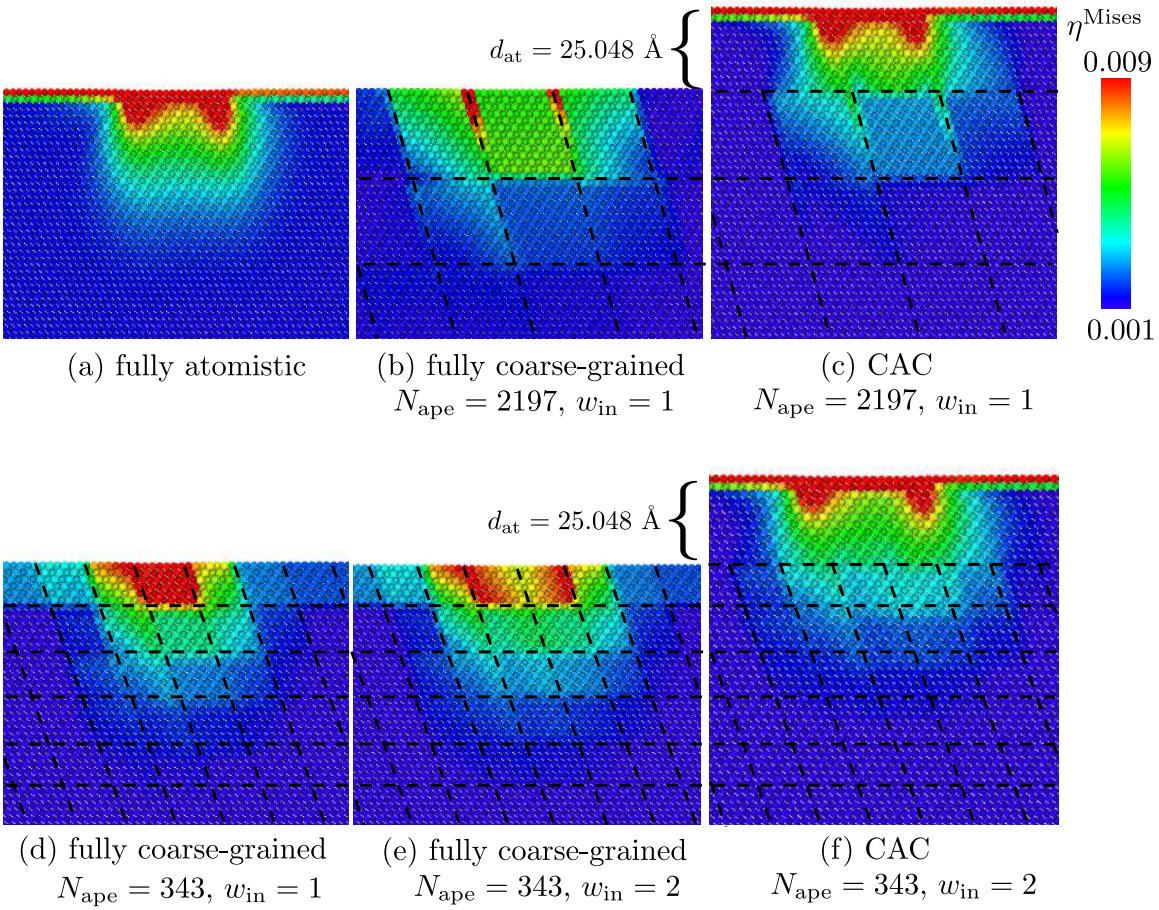

Figure 4.11: Snapshots of surface indentation in fully atomistic, fully coarse-grained, and CAC simulations in Cu. The indentation depth is $0.144a_0$, corresponding to point A in Fig. 4.10(a). Atoms are colored by von Mises local shear invariant η^{Mises} (Eq. 4.5). In the coarse-grained domain, element sizes N_{ape} of 343 or 2197 are employed and the indenter spans over either 1 or 2 elements. It is shown that the shear deformation is localized between the elements, a phenomenon more pronounced with a larger element size or a wider indenter [300].

atomistic model, the fully coarse-grained model gives a lower and non-monotonically increasing force in the elastic stage, a phenomenon more pronounced with a larger element size or a wider indenter spanning. This was not observed in the stress-strain curve of a Lennard-Jones (LJ) potential Cu sample subject to a uniaxial tension where the dislocations were also nucleated from the free surface of the coarse-grained domain [297]. This is perhaps due to the fact that the uniaxial stress is a quantity averaged over the system while the indentation force here is calculated locally. To further explore the phenomenon, the von Mises local shear invariant of each atom, η^{Mises}, is calculated using OVITO [245],

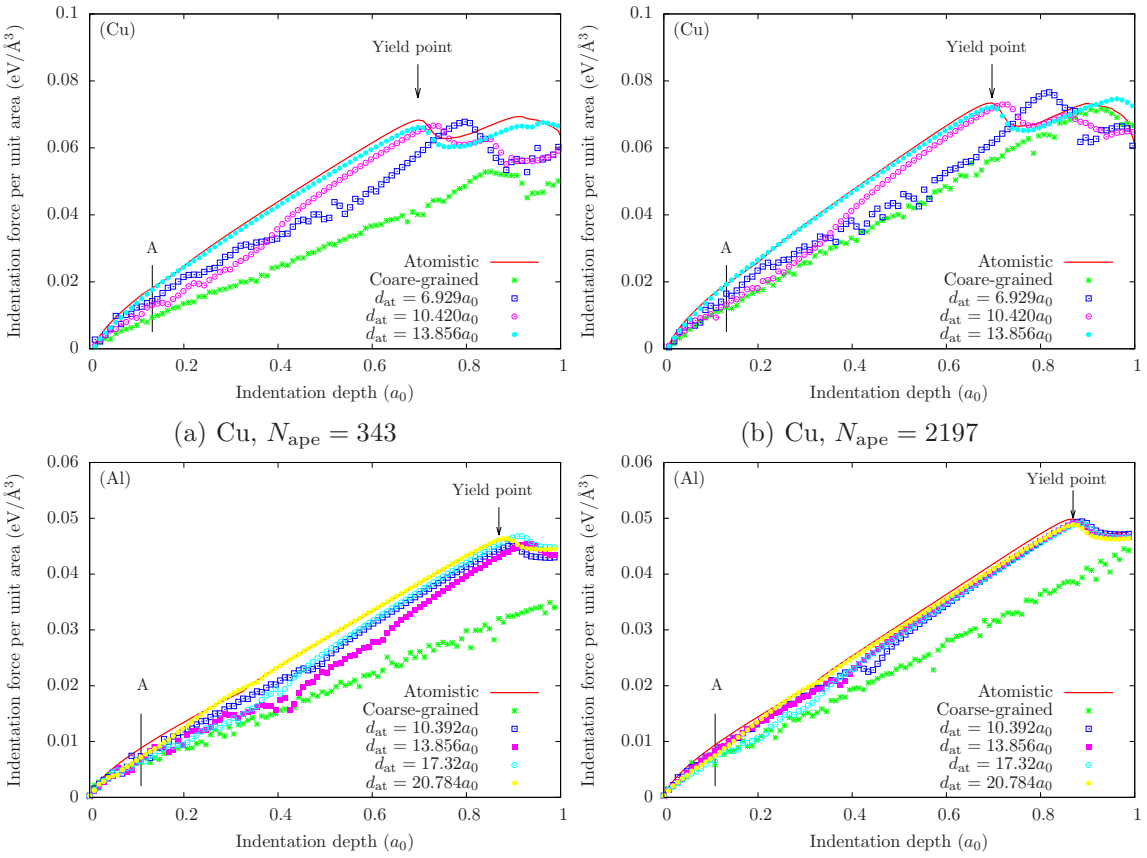

(a) Cu, $N_{\text{ape}} = 343$ (b) Cu, $N_{\text{ape}} = 2197$

(c) Al, $N_{\text{ape}} = 343$ (d) Al, $N_{\text{ape}} = 2197$

Figure 4.12: Indentation force-depth curve obtained from the simulations in both Cu and Al as shown in Fig. 4.9. The indenter spans along the y direction over 1 element when $N_{\text{ape}} = 2197$ or 2 elements when $N_{\text{ape}} = 343$. Free surface atomistic domains with different thickness d_{at} are introduced. The optimal thickness is the smallest d_{at} that results in a monotonically increasing force. It is shown that the optimal d_{at} depends on the material, but not on the underlying degree of coarse-graining. Point A corresponds to the indentation depth of $0.144a_0$, at which the snapshots are shown in Fig. 4.11 [300].

following the formulation by Shimizu et al. [233], i.e.,

$$\eta^{\text{Mises}} = \sqrt{E_{12}^2 + E_{13}^2 + E_{23}^2 + \frac{(E_{11} - E_{33})^2 + (E_{22} - E_{33})^2 + (E_{11} - E_{22})^2}{6}} \tag{4.5}$$

where E_{ij} are the components of the Green-Lagrange strain tensor $\mathbf{E}$, which is calculated by

$$\mathbf{E} = \frac{1}{2}(\mathbf{F}^\top \mathbf{F} - \mathbf{I}) \tag{4.6}$$

where $\mathbf{I}$ is the 2$^{\text{nd}}$ rank identity tensor and $\mathbf{F}$ is the deformation gradient considering only the nearest neighbor interactions in the initial undeformed configuration [330].

Snapshots of simulations in Cu with atoms colored by η^{Mises} are given in Fig. 4.11. The indentation depth is $0.144a_0$, corresponding to point A in Fig. 4.10(a). It is found that in the coarse-grained domain, the shear deformation is localized between elements, a phenomenon more pronounced with larger element sizes. This is due to the trilinear interpolation function employed within the element. In other words, the elastic shear deformation in the coarse-grained domain is confined to a smaller zone than that in the atomistic domain, so a smaller force is sufficient to cause the lattice deformation accommodating the same indentation depth. It is also found that the larger the indenter, the smaller the force per unit area, in agreement with the MS simulations [266]. Similar phenomena are also found in Al and Ni.

The results suggest that when a surface is subject to indentation, the local lattice deformation is not as well reproduced in the coarse-grained domain as in the atomistic domain. Therefore, it is advisable to not apply the indentation directly on a coarse-grained free surface. Instead, fully resolved atomistics should be employed in the vicinity of the indenter when the local elastic deformation gradients are significant. To quantify the required atomistic domain size, a series of CAC simulations are performed. Atomistic domains with different thickness d_{at} are employed at the surface where the indentation is applied.

The indentation force-depth curves in Fig. 4.12 show that the larger the d_{at}, the closer the CAC simulation results are to those of the full atomistics. While the shear invariant distribution in the atomistic domain is the same as that in the fully atomistic model, it is disturbed by the atomistic/coarse-grained domain interface and localized between the elements in the coarse-grained domain, as shown in Figs. 4.11(c) and 4.11(f). The effect of the coarse-graining decreases with an increasing d_{at}. The optimal atomistic domain thickness is defined as the smallest d_{at} that results in a monotonically increasing force prior to the yield point. The optimal d_{at} values are $13.856a_0$ in Cu and $20.784a_0$ in Al, regardless of the degree of coarse-graining in the model. Thus, it is concluded that the optimal d_{at} depends on the material, but not the underlying coarse-grained domain.

4.7 Dislocation migration through the interface between atomistic and coarse-grained domains

One major advantage of CAC compared to the other partitioned domain methods is that dislocations can pass between atomistic and coarse-grained domains without heuristic rules or special provisions. When the slip planes are aligned with the planes between elements, the dislocations pass the domain interface smoothly instead of being reflected or pinned. However, Sec. 4.3 reveals that a single dislocation has different core structure in atomistic and coarse-grained domains. This raises the question of how the stacking fault width varies as the dislocation migrates across the interface between the two domains and whether this interface significantly affects the dislocation migration. Thus, four cases are considered to clarify distinctions of dislocation migration in fully atomistic, fully coarse-grained, and CAC models in both Cu and Al. The 60° mixed type dislocation is chosen because it has both edge and screw components and is more general. All models have the same overall size of 11.46 nm by 17.36 nm by 22.45 nm in Cu. The indentation process and the force calculation are the same as in Sec. 4.6, except that the indenter moves $0.01a_0$ each step. To eliminate the free surface effect, the top layers (traction free surface) is fixed except those below the indenter, as well as the bottom layers. The fixed atoms/nodes are labeled by the red boxes in Fig. 4.13.

No significant change of the indentation force is observed when the dislocation migrates across the interface between atomistic and coarse-grained domains, as shown in Fig. 4.14. Using the same method in Sec. 4.3, the structure of a 60° mixed type dislocation core across the domain interface is analyzed and shown in Fig. 4.15. It is shown that the interface only slightly alters the atomic positions in its vicinity, and the dislocation has a correct core structure once it migrates into the atomistic domain. These results indicate that the domain interface only slightly affects the dislocation migration process in quasistatic CAC [300].

To further understand the dislocation dissociation across the interface, a dislocation extraction algorithm (DXA) [247] is employed to visualize the partial dislocations, as shown in Figs. 4.16 and 4.17. The DXA is based on a discrete Burgers circuit integral over the elastic displacement field and is able to distinguish dislocations with different Burgers vector. It

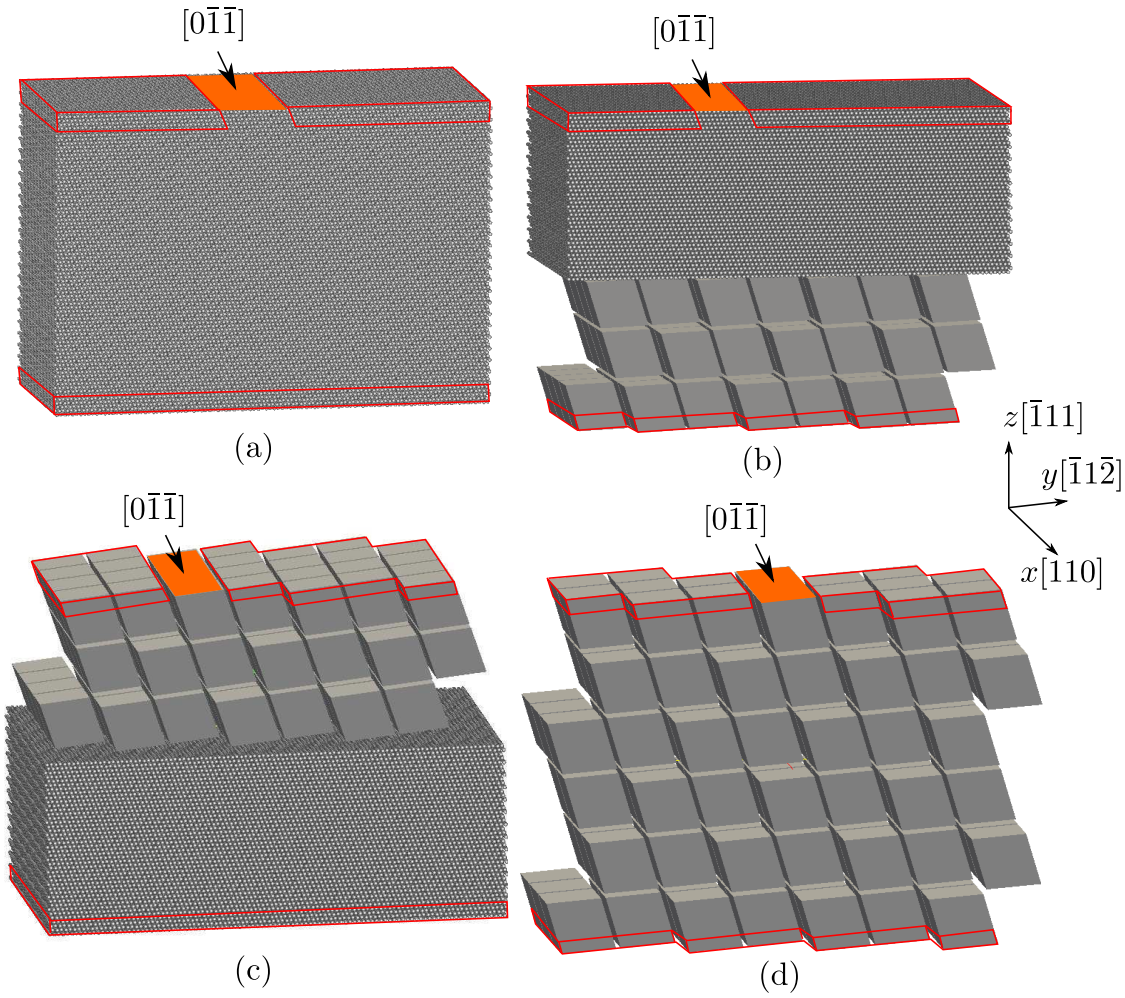

Figure 4.13: Four cases comparing the dislocation migration through the interface between atomistic and coarse-grained domains in Cu and Al: (a) fully atomistic case, (b) from atomistic to coarse-grained domain, (c) from coarse-grained to atomistic domain, and (d) fully coarse-grained case. PBCs are applied along both the x and y directions. To apply the periodic boundaries in the coarse-grained domain, the jagged interstices are filled in with atoms, which are not shown here. The indenter moves $0.01a_0$ each step in Cu along [0$\bar{1}\bar{1}$] direction. The atoms/nodes illustrated by the red boxes are fixed [300].

is found that subject to the indentation, a series of 60° mixed type dislocations are nucleated and dissociated into partials with intrinsic stacking fault in between. In Fig. 4.16(a), the stacking fault has a correct width in the atomistic domain. With further indentation, the leading partial is first impeded by the domain interface while the trailing partial is unaffected, resulting in a narrower dislocation, as shown in Fig. 4.16(b). Later, the trailing partial is also slowed down by the interface while the leading partial is now migrating steadily in the coarse-grained domain (Fig. 4.16(c)). The delay of the partial dislocations

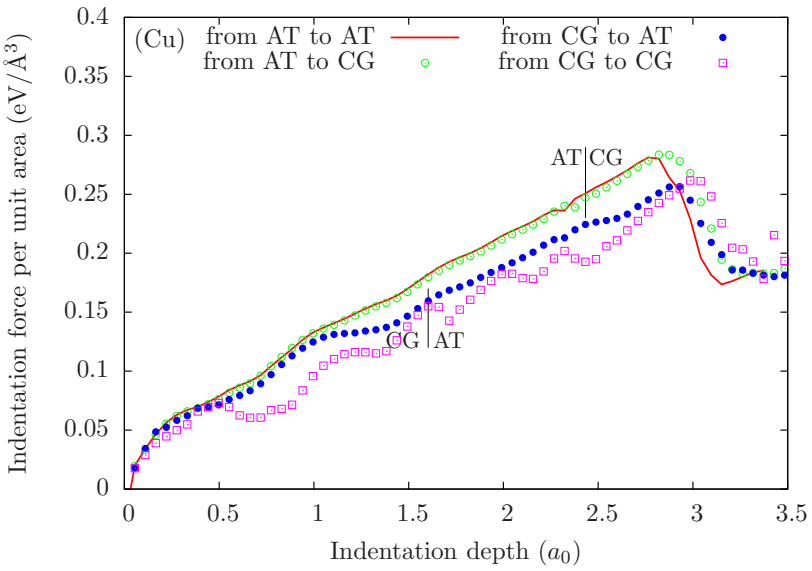

(a) Cu

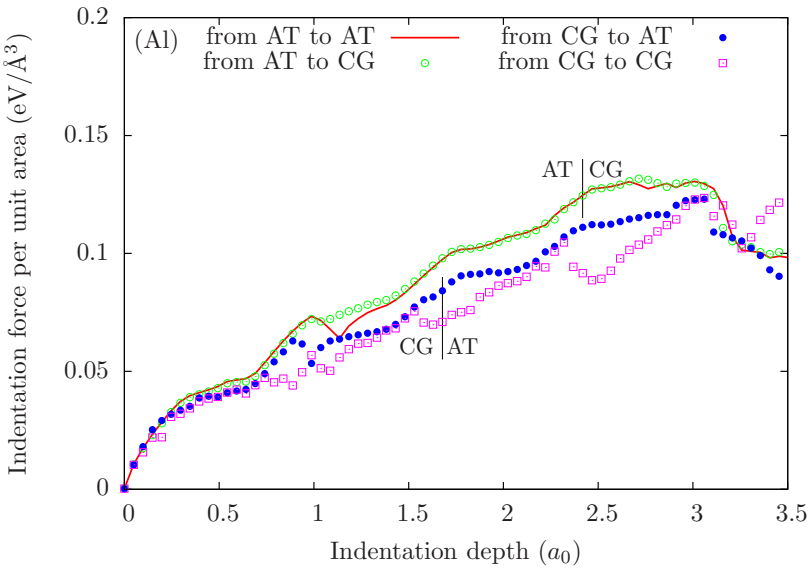

(b) Al

Figure 4.14: Indentation force-depth curve obtained from the simulations in both Cu and Al as shown in Fig. 4.13. No significant change of force is observed when the first dislocation migrates across the interface between atomistic and coarse-grained domains [300].

is due to the change of the packing sequence in the stacking fault, where the disregistry of atoms are rearranged to have a linear correlation with their positions. It follows that the stacking fault becomes wider in the coarse-grained domain, as shown in Fig. 4.16(d). Note that the variation of stacking fault width is not observed when the dislocation migrates in an individual domain. Dislocation mobility approximations are not relevant to quasistatic

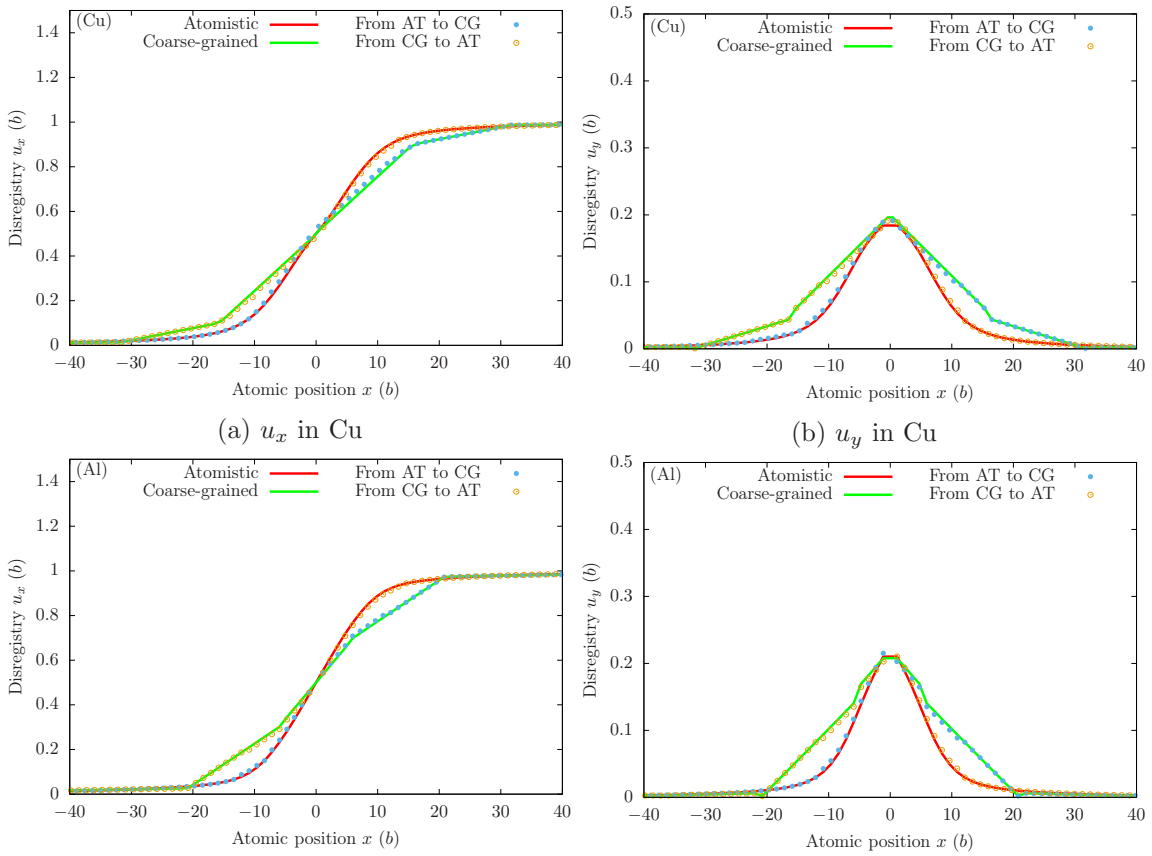

(a) u_x in Cu

(b) u_y in Cu

(c) u_x in Al

(d) u_y in Al

Figure 4.15: The 60° mixed type dislocation core is located across the interface ($x = 0$) such that half of it is in the atomistic domain while the other half the coarse-grained domain in both Cu and Al. The disregistry u_x and u_y of dislocation, calculated using the method in Sec. 4.3, are compared with those in fully atomistic and fully coarse-grained models. The Burgers vector $\mathbf{b} = (a_0/2)[110]$. It is shown that the interface only slightly alters the atomic positions in its vicinity, and the dislocation has a correct core structure once it migrates into the atomistic domain [300].

CAC.

When the dislocation migrates from the coarse-grained domain to the atomistic domain, the propagation of both leading and trailing partials is facilitated by the domain interface (Fig. 4.16(e–g)) due to a more relaxed environment in full atomistics. Consequently, the stacking fault has a correct width once it migrates into the atomistic domain, as shown in Fig. 4.16(h). The domain interface itself, as well as the coarse-grained domain, do not influence the dislocation behavior in the atomistic domain when the dislocation is not immediately adjacent to the interface. Similar phenomena are observed in Al, as shown in

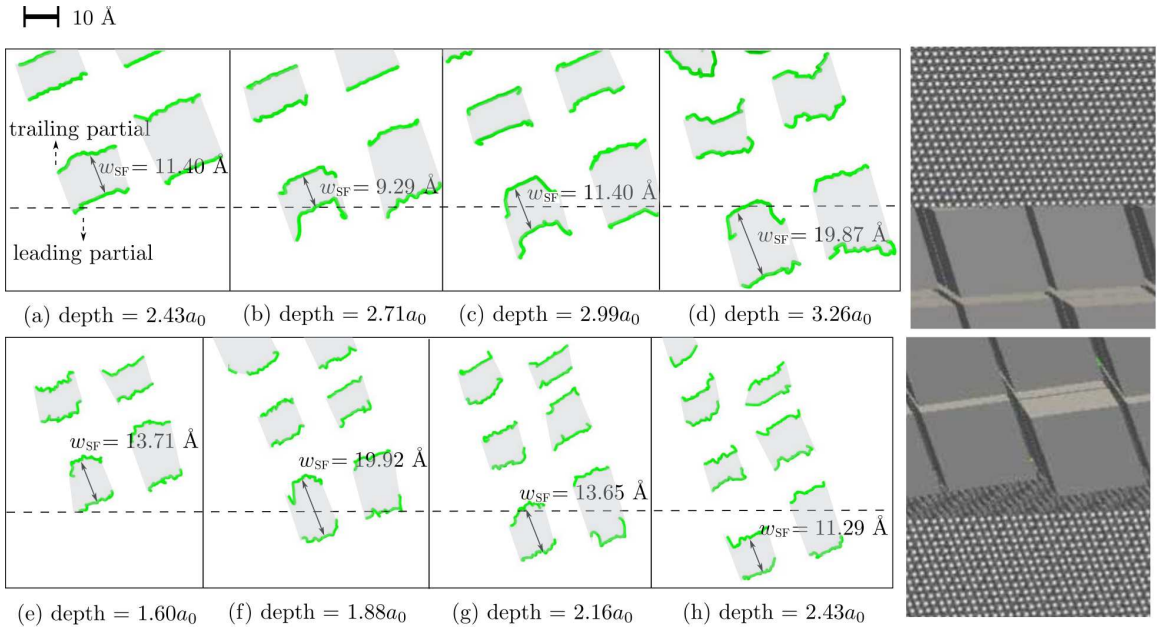

Figure 4.16: Snapshots of dislocation migration from the atomistic to the coarse-grained domain (a–d), as well as in the opposite direction (e–h) for Cu. The green curves refer to $(a_0/6)\langle 112\rangle$ Shockley partial dislocation lines. The gray ribbons are the intrinsic stacking fault. To apply the periodic boundaries in the coarse-grained domain, the jagged interstices are filled in with atoms, which are not shown here. The domain interface in the first case delays both partial dislocations while the one in the second case facilitates the dislocation migration [300].

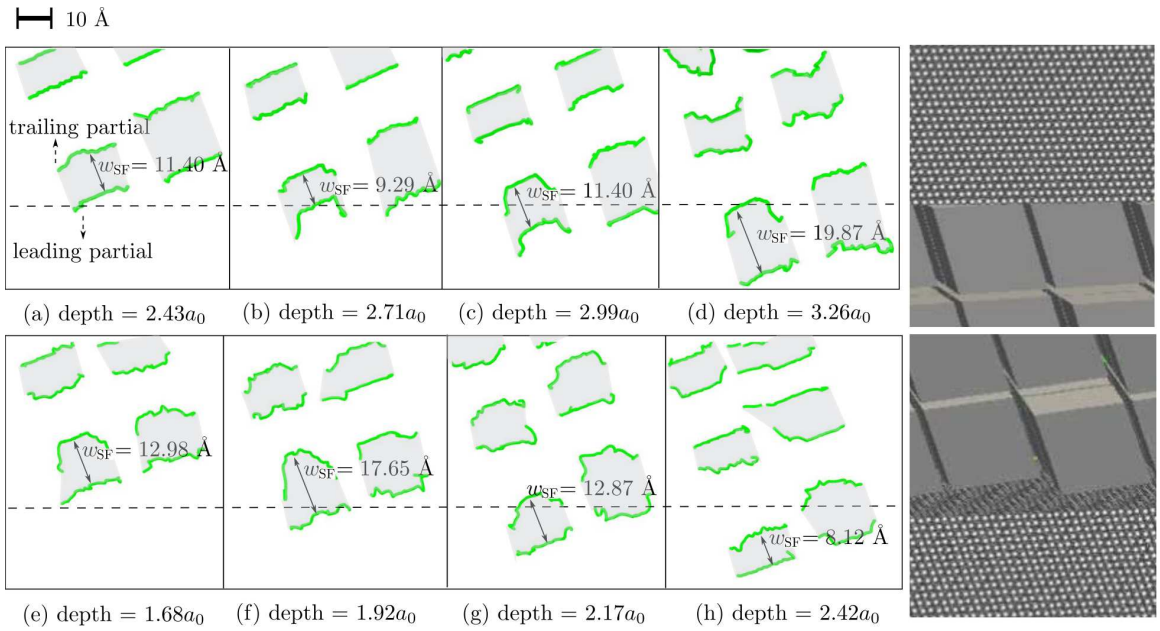

Figure 4.17: The same snapshots of dislocation migration as Fig. 4.16, but for Al. Similar phenomena are observed [300].

Fig. 4.17.

4.8 Overall Burgers vector of dislocations

Using the models in Figs. 4.13(a) and 4.13(d), the overall Burgers vector in both fully atomistic and fully coarse-grained domains is studied with varying element sizes in Al. It is found in Fig. 4.18 that some $(a_0/2)\langle 110\rangle$ perfect dislocations are nucleated under the indenter in the atomistic domain, while only $(a_0/6)\langle 112\rangle$ Shockley partials are formed in the coarse-grained domain. At the same indentation depth $2.62a_0$, the overall Burgers vector of dislocations on the same slip plane is the same in both atomistic and coarse-grained domains. The results using EAM potentials with approximated $\bar{\rho}^j$ proposed in Sec. 3.2 are only slightly different from those employing EAM potentials with accurate $\bar{\rho}^j$, as discussed in Sec. 2.7.4. Similar phenomena are observed in Cu and Ni.

The elasticity theory upon which the DD method is established considers that the stress fields of one dislocation at a long distance are mainly determined by its Burgers vector and character angle, because the dislocation core effect is usually small and local [38]. In CAC, although a wider dislocation core is given, the overall Burgers vector and the character angle of a dislocation are preserved, and so long range stress fields of these dislocations are preserved. Furthermore, within the same framework, dissociation of full dislocations and dislocation/dislocation interactions using CAC can be accurately described for short range interactions simply by refining the element size. In practice, coarse graining in CAC is only employed to capture the longer range structures/fields in regions remote from atomistically resolved reactions of interest, so its coarse-graining approximation of details of the dislocation core does not greatly impact the accuracy of computed interactions that are critical to the modeling of the many metal plasticity phenomena.

In the coarse-grained domain, the dissociation of a 60° mixed type dislocation into partials is affected by the degree of coarse graining in view of the altered packing sequence in the stacking fault. These imply that the core structures and dislocation interactions are better described in the atomistic domain, an intuitive result. In addition, elements with graded sizes should be applied in a way that smaller elements are used in the vicinity of the

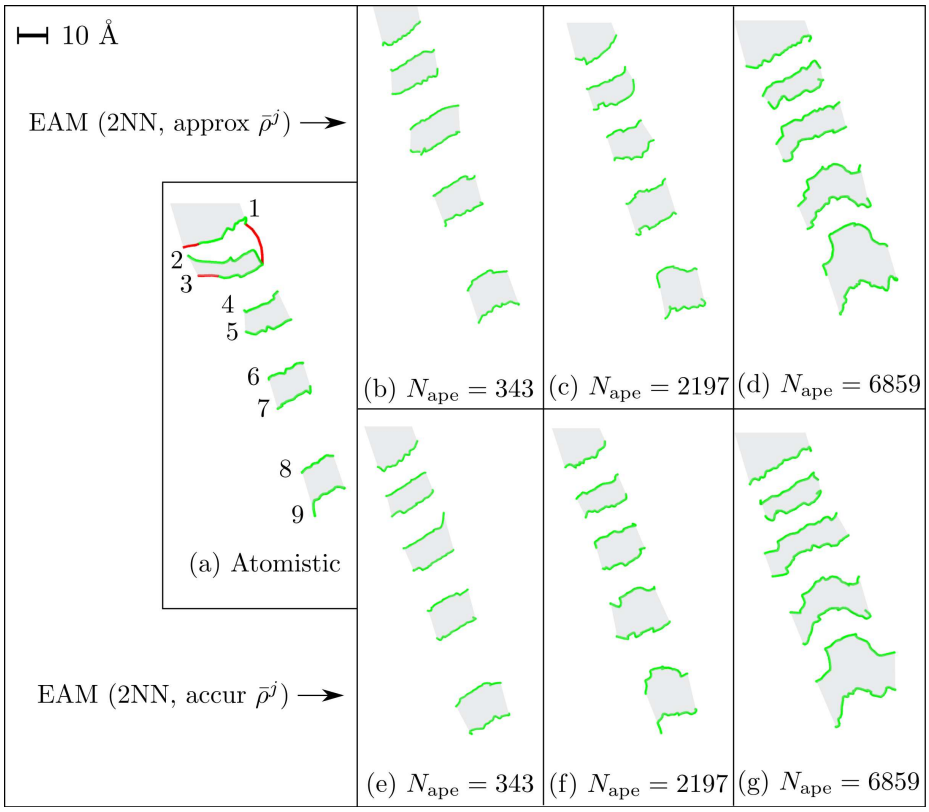

Figure 4.18: Snapshots of dislocation migration subject to indentation in both fully atomistic and fully coarse-grained domains with varying element size for Al. The green and red curves refer to $(a_0/6)\langle 112\rangle$ Shockley partial and $(a_0/2)\langle 110\rangle$ perfect dislocations, respectively. The gray ribbons are the intrinsic stacking fault. It is shown that while only Shockley partials are nucleated in the coarse-grained domain, several perfect dislocations are formed in fully atomistic model. At the same indentation depth $2.62a_0$, the overall Burgers vector of 9 partial dislocations on the same slip plane is the same, regardless of the element size or whether the EAM potential is employed with approximated $\bar{\rho}^j$ [300].

atomistic domain (where dislocation nucleation and primary interactions occur) while larger elements are adopted to address long range fields of arrays of dislocations. Although it was shown earlier using an LJ potential that dislocation/dislocation interactions are reasonably well replicated in the coarse-grained domain [292], the results with EAM potentials remain to be studied in detail.

4.9 Brittle-to-ductile dynamic fracture

The fundamental mechanism of brittle versus ductile response of stressed crack tips is the competition between cleavage fracture by atomic decohesion and plastic deformation by dislocation nucleation and migration [55, 299]. In particular, a BTD transition of crack

behavior is favored by conditions of high temperature, low strain rate [55], small specimen/grain size [223], a large number of dislocation sources, high dislocation mobility [103], and large stress/strain [3].

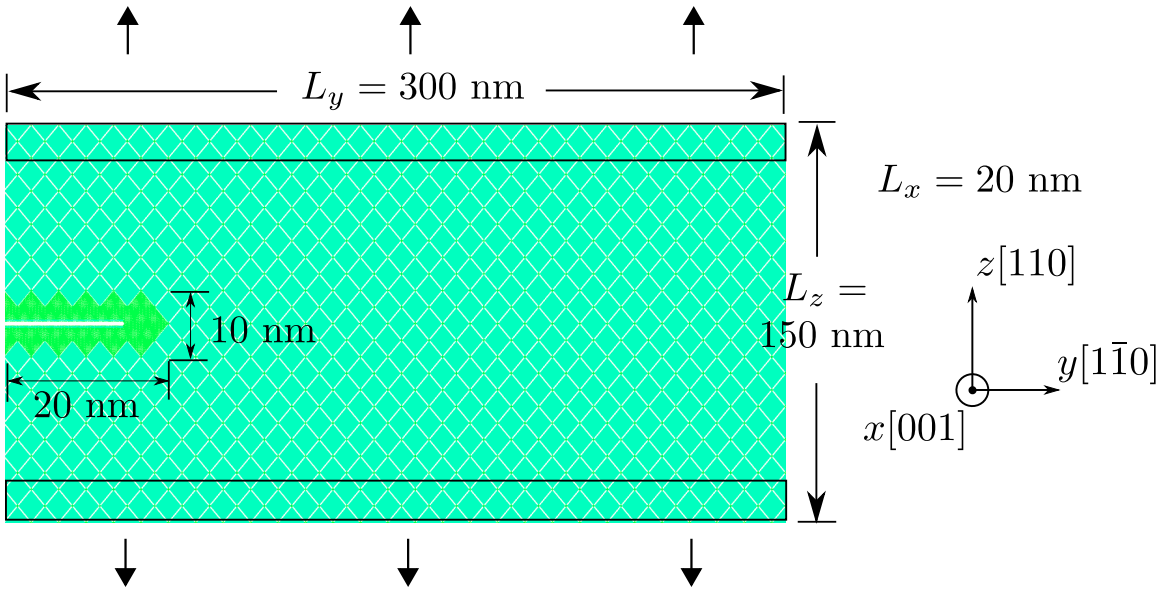

Figure 4.19: Simulation cell for dynamic fracture of an FCC Cu specimen. An atomistic domain with about 11,312 atoms is applied around the crack; elsewhere, 1414 elements with 8000 atoms per element are employed. Both top and bottom layers of elements are displaced uniformly to introduce a tensile displacement-controlled condition [306].

The simulation cell for dynamic fracture in CAC is shown in Fig. 4.19. The notched specimen, which consists of FCC Cu atoms, has a size of 20 nm $\times$ 150 nm $\times$ 100 nm along the x, y, and z axes, respectively. PBCs are imposed along the x direction, while cell boundaries normal to the y and z directions are traction free and fixed, respectively. An FCC crystal is chosen because it is inherently ductile and thus serves as a paradigm for plastic fracture [4]. The lattice orientations are $x[001]$, $y[1\bar{1}0]$, and $z[110]$. In total, there are 1414 elements with 8000 atoms per element. About 11,312 atoms are employed within a volume of 20 nm $\times$ 20 nm $\times$ 10 nm around the crack, which is created by deleting 5 layers of atoms normal to the z direction. This corresponds to about 11.3 million atoms in an equivalent full atomistic model. Bonding for this model crystal is described by a simple two-body LJ potential, i.e.,

$$V(r) = 4\epsilon \left[\left(\frac{\sigma}{r}\right)^{12} - \left(\frac{\sigma}{r}\right)^{6} \right] \tag{4.7}$$

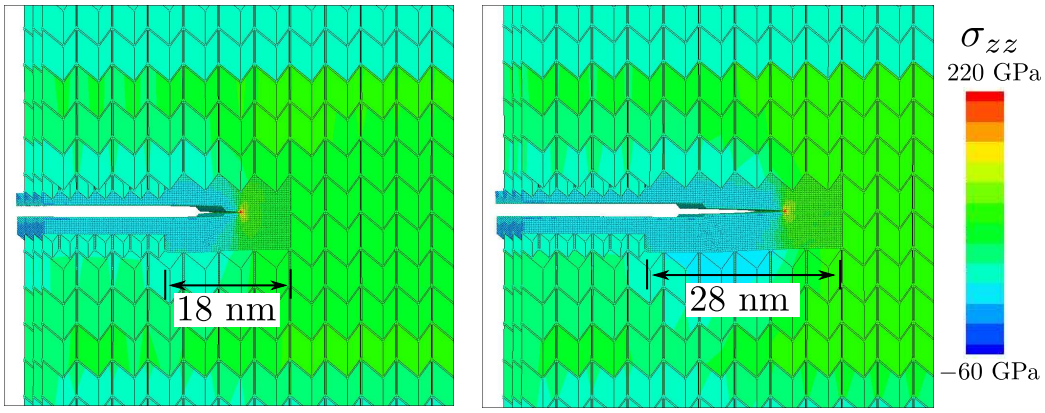

(a) $\delta = 0.225$ nm (b) $\delta = 0.375$ nm

Figure 4.20: The crack propagates in a brittle manner at a low strain in an adaptive CAC simulation. Nodes and atoms are colored by local tensile stress σ_{zz}. At (a) $\delta = 0.225$ nm and (b) $\delta = 0.375$ nm, the crack extends by 18 nm and 28 nm, respectively. Here, the view in Fig. 4.19 is rotated by about 10° around the z axis to better image the 3D crack [306].

where r is the distance between atoms, $\epsilon = 0.167$ eV, and $\sigma = 2.315$ Å [131]. The lattice parameter a_0 and cutoff distance are 3.616 Å and 5.38635 Å, respectively. Compared with a more realistic EAM potential, the LJ potential overestimates the vacancy formation and migration energies [64] and favors the BTD transition [2]; however, the intent in this section is to establish the viability of the adaptive mesh refinement procedure for CAC, instead of shedding light on improved understanding of dynamic fracture. The FD method is employed for parallelization. No thermostat is employed in the atomistic domain, i.e., an NVE ensemble with a zero damping coefficient γ defined in Sec. 2.6; in the coarse-grained domain, $\gamma = 0.005$.

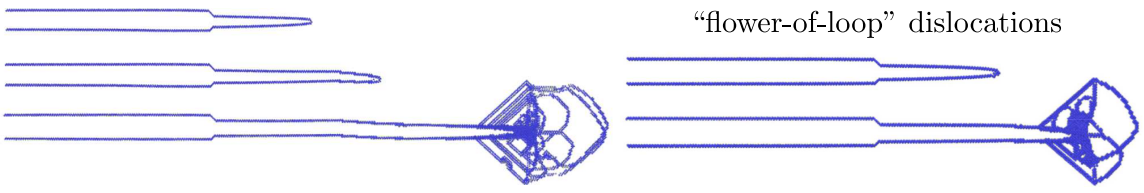

(a) CAC (b) MD

Figure 4.21: Snapshots of "flower-of-loop" dislocations emitted from the crack tip during ductile fracture in both (a) CAC and (b) MD simulations. Atoms with centrosymmetry parameter [126] smaller than 1.3 are deleted [306].

Assigning zero initial velocities to all atoms and nodes, the simulation cell is subject to tension by relative vertical displacement δ of the top and bottom layers of elements. Two

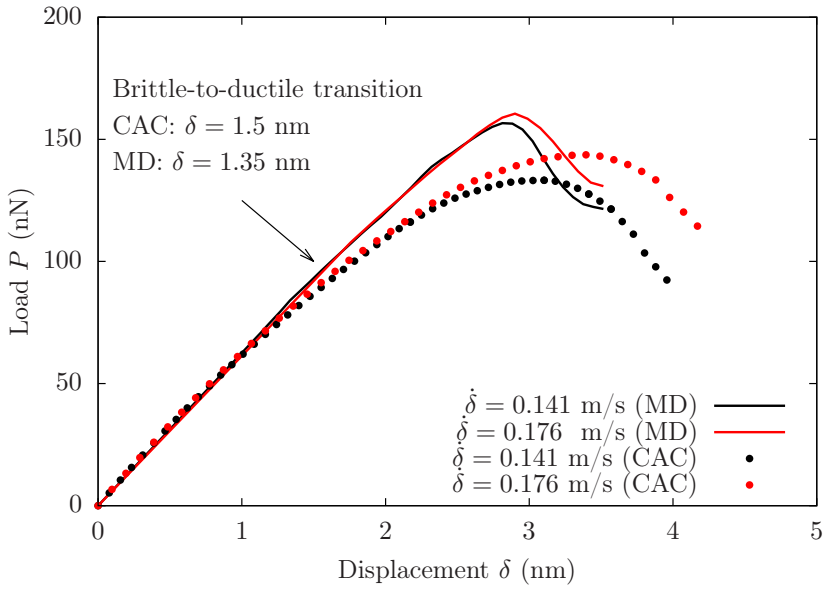

Figure 4.22: Load-displacement curves of dynamic fracture at two displacement rates in both CAC and MD simulations. It is found that for both rates, the BTD transition occurs at $\delta = 1.5$ nm and 1.35 nm in CAC and MD simulations, respectively [306].

displacement rates are employed: $\dot{\delta} = 0.141$ m/s and 0.176 m/s, with a time step $\Delta t = 5$ fs in both domains. As the simulation evolves, d^{ξ}, defined in Eq. 3.16, is evaluated on all nodes at every time step; then an element is refined if any of its node has a $d^{\xi} > (\sqrt{6}/12)a_0$. The top and bottom layers of elements on which the displacement is directly applied are excluded from the mesh refinement procedure to avoid unnecessary computational cost. Dislocation activity at the crack tip is monitored every 10 time steps using the centrosymmetry parameter [126]. Subject to a tensile displacement-controlled condition, the originally sharp crack tip in the fully resolved atomistic domain is slightly blunted before the crack begins to propagate in a brittle manner without emitting any dislocations from the tip, as shown in Fig. 4.20. This marks the beginning of dynamic instability. As the crack speed increases, the energy at the crack tip accumulates. As a result, when the crack passes the middle region of the model, it responds plastically, where a "flower-of-loop" shape of dislocations are nucleated on multiple slip planes, as shown in Fig. 4.21. At both displacement rates, the BTD transition, which is marked by dislocation nucleation from crack tip, occurs at $\delta = 1.5$ nm. By $\delta = 4.5$ nm, about 110 elements have been refined to full atomic resolution. Note that this type of uniform displacement-controlled loading has been employed in many

MD simulations [199, 215, 317] and is equivalent to applying rigid grips in a tensile testing machine. The chosen boundary conditions, while not precluding crack re-direction and branching [33, 67, 129], promote stable crack extension and add a constraint to the crack growth behavior such that the crack is inclined to propagate along the horizontal direction even in the presence of small perturbations like inhomogeneities or numerical errors. The double cantilever beam type of loading, which may introduce unstable crack propagation [282], is not employed here for that the focus of this study is on exploring whether the mesh refinement scheme is able to refine all elements in front of the crack tip. Because the mesh refinement criterion does not involve the crack propagation trajectory but only considers the relative displacement between neighboring nodes which indicates the crack tip position, this mesh refinement scheme should work for the case of unstable crack extension as well.

To assess the accuracy of the adaptive mesh refinement approach, MD simulations of the equivalent full atomistic models are performed at the same displacement rate using LAMMPS [190]. The same LJ potential is used. An NVE ensemble is employed with PBCs applied along the x axis, which is consistent with the atomistic domain in CAC. In both CAC and MD, the load P is calculated by averaging the total load applied on the top and bottom layers of elements/atoms. It is found that the adaptive CAC gives similar load-displacement responses as MD and both methods show that a higher displacement rate leads to a higher specimen peak load. In MD, the BTD transition occurs at $\delta = 1.35$ nm with a smaller crack length for both displacement rates than that of CAC, as shown in Fig. 4.22. In addition, MD gives a slightly higher peak load than adaptive CAC, which is attributed to the reflection of waves of short wavelength at the atomistic/coarse-grained domain interface [290]. Two separate simulations at a much lower displacement rate show that the BTD transition does not occur in either CAC or MD, i.e., the crack continues propagating throughout the whole specimen, leaving a very clean crack surface behind.

4.10 Curved dislocation migration

As discussed in Sec. 3.4.5, while the elements that have discontinuities between them in CAC accommodate dislocations, mesh refinement is still sometimes necessary to model dislocation migration. Consider scenarios in Fig. 3.15 as an example, Xiong et al. [292] suggested that when the slip direction of a dislocation moving from an atomistic domain is not aligned with the interelement boundaries, it can either migrate on the atomistic/coarse-grained domain interface before moving into the nearest interelement boundary or be pinned by the interface followed by nucleation of a new dislocation within the nearest interelement boundary. However, neither of the migration paths are physically correct since a dislocation should continue to migrate on the original slip plane, in the absence of climb, cross-slip, obstacles, etc.

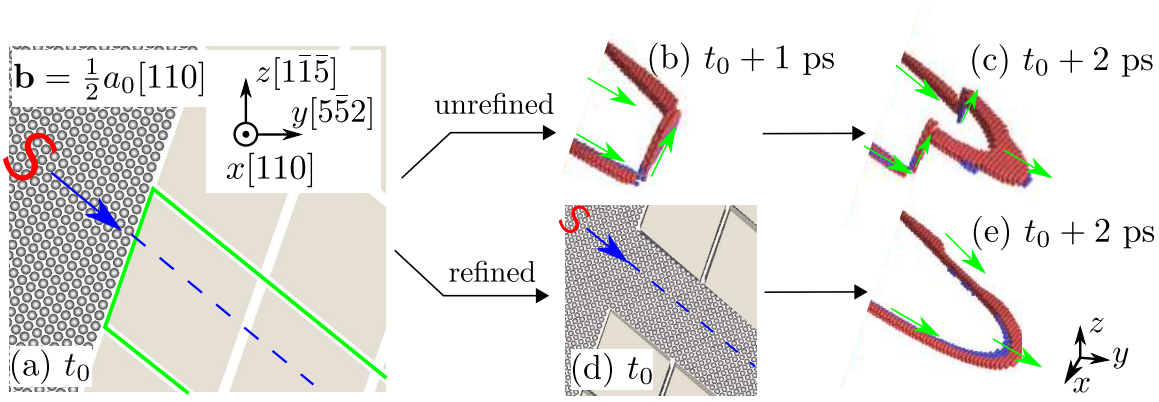

Figure 4.23: (a) An illustration of the scenario where the slip plane of a curved dislocation migrating from the atomistic domain is not aligned with the interelement boundaries in the coarse-grained domain. The curved dislocation (red S) has dominant leading screw character. If the elements marked by the solid green lines in (a) are not refined, the dislocation double cross-slips over the domain interface before continuing gliding on a parallel slip plane, as shown in (b) and (c). (d) If the elements within the solid green lines are refined to full atomistic resolution, the dislocation continues gliding on the same slip plane without cross-slip, as shown in (e). Atoms in (b), (c), and (e) are colored by a-CNA [246]: red are of HCP local structure, blue are BCC, while FCC and unrecognised atoms are deleted. A slightly different view, which is illustrated in the bottom right corner, is taken for (b), (c), and (e) to better image the dislocation double cross-slip and migration [306].

In this section, a dynamic CAC simulation is performed to explore the scenario where the slip plane of a mixed character curved dislocation with dominant leading screw character

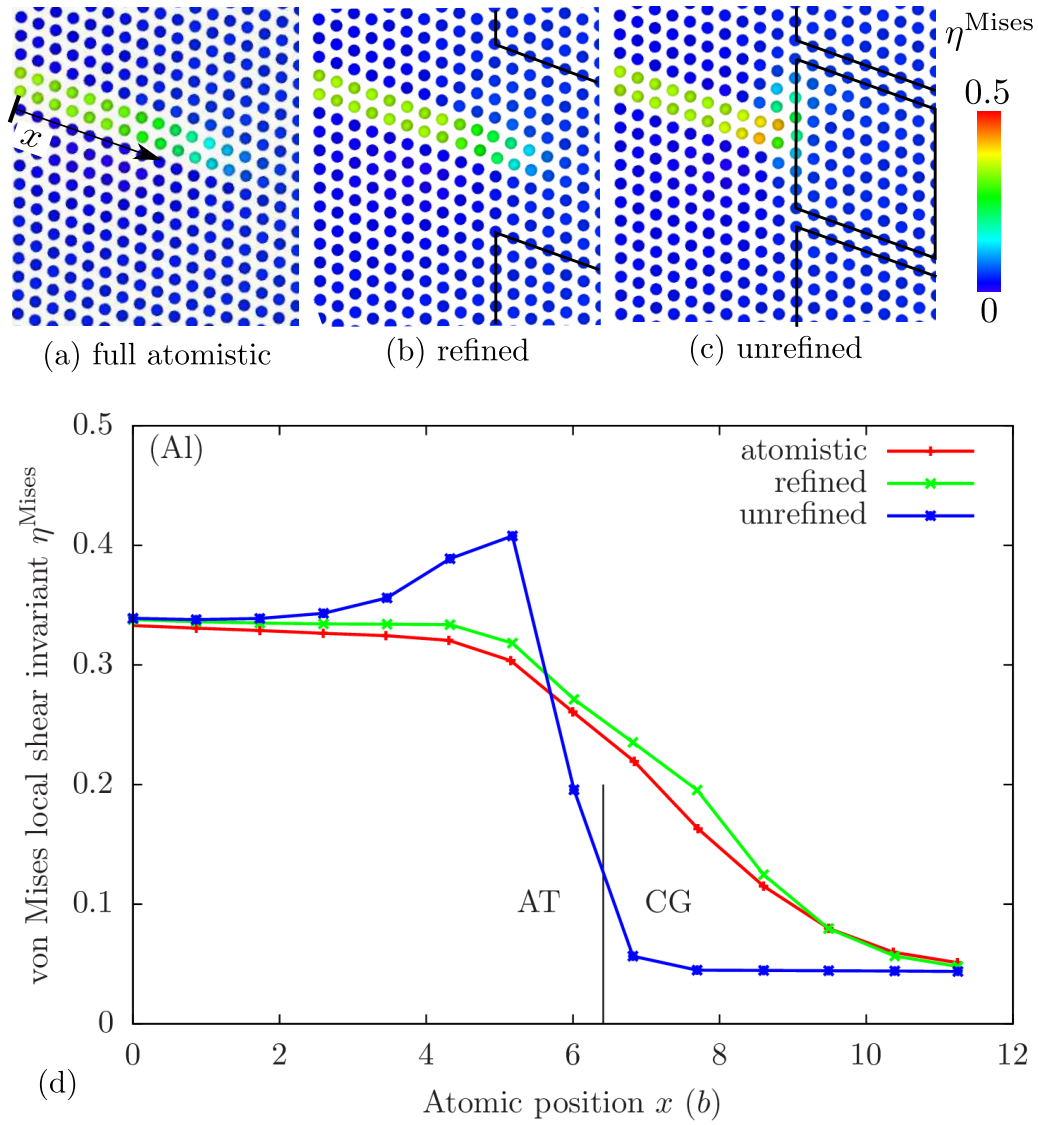

Figure 4.24: Atoms are colored by von Mises local strain invariant η^{Mises} (defined in Eq. 4.5) in (a) full atomistic simulations, (b) CAC simulations with mesh refinement, and (c) CAC simulations without mesh refinement. In (d), it is found that the CAC simulations with mesh refinement give a η^{Mises} profile along the dislocation close to that of full atomistic simulation, while a strain concentration at the atomistic/coarse-grained domain interface occurs in the CAC simulation without mesh refinement [306].

migrating from the atomistic domain is not aligned with the interelement boundaries in the coarse-grained domain, as shown in Fig. 4.23(a). The EAM potential [174] is employed for FCC Cu. The lattice parameter and cutoff distance are 3.615 Å and 5.60679 Å, respectively. A homogeneous out-of-plane shear stress of 1 GPa is applied to drive the curved dislocation migration, with a time step of 2 fs and a damping coefficient $\gamma = 1$ in both atomistic and

coarse-grained domains. It is found that if the elements marked by the solid green lines in Fig. 4.23(a) are not refined, the curved dislocation double cross-slips over the domain interface before continuing gliding on a parallel slip plane, as shown in Figs. 4.23(b–c); an aphysical back stress is introduced to overcome the minimum energy barrier of double cross-slip [194], which is about 4 eV [124]. In CAC, two mesh refinement approaches are implemented for dislocation migration: (i) a large element is manually divided into two smaller ones with their boundaries along the dislocation path [293] and (ii) the entire element is refined to atomic scale, within which the dislocation can pass smoothly; the second approach is shown in Figs. 4.23(d–e).

In Fig. 4.24, the strain profiles between two simulations with and without mesh refinement are compared. It is shown that the CAC simulation with mesh refinement gives a von Mises local strain invariant η^{Mises} (defined in Eq. 4.5) profile along the dislocation close to that of full atomistic simulation, while a strain concentration at the coarse-grained/atomistic domain interface occurs in the CAC simulation without mesh refinement.

4.11 A preliminary convergence and error analysis

As pointed out by Yang et al. [309], while many multiscale methods have been proposed, few corresponding convergence and error analyses exist. Some mathematical and/or numerical analyses include, but are not limited to, those of QC [132, 151, 152, 159, 269], heterogeneous multiscale method [78], bridging scale method [258], atomistic-to-continuum coupling [160], and MMM [309]. Previous work of Xiong et al. [293, 297] shows that in dynamic CAC, the coarse-grained domains give closer results to those of the full atomistics when finer elements or larger models are employed. In this section, a preliminary convergence and error analysis of quasistatic CAC is presented.

The fully atomistic MS result is taken as the "exact solution" that a quasistatic fully coarse-grained or quasistatic CAC simulation should be compared with. Thus, the atomistic domain, except the region in adjacent to the atomistic/coarse-grained domain interface, yields an exact result since it employs the same governing equation as MS without interference from the domain interface. The coarse-grained domain, however, introduces numerical

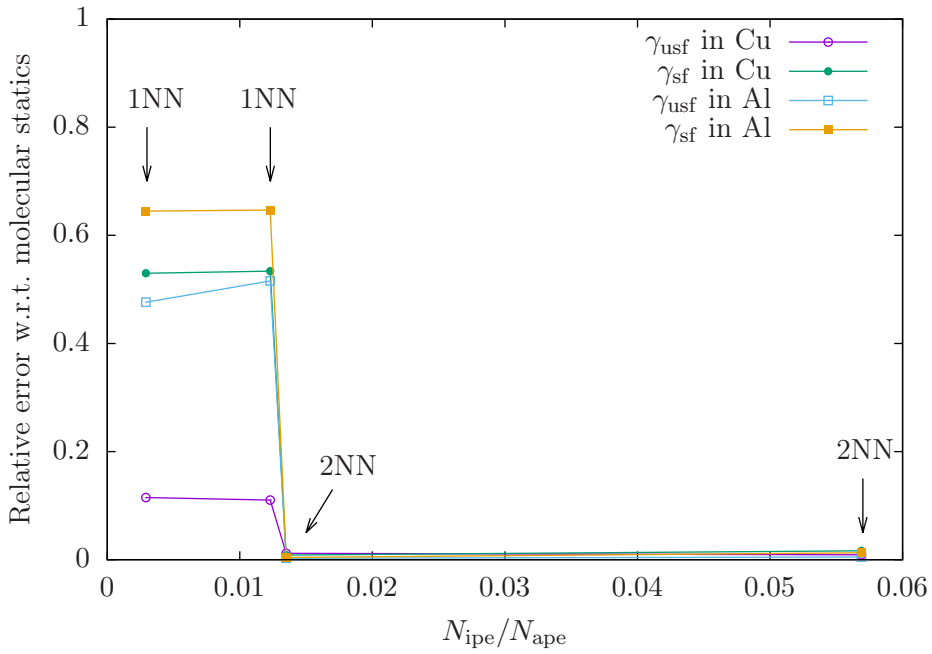

Figure 4.25: The relative errors of both γ_{usf} and γ_{sf} in both Cu and Al calculated in the coarse-grained domain using both 1NN and 2NN elements. Each element contains either 2197 or 9261 atoms. The values of SFE are from Fig. 4.2. It is shown that the relative errors reduce to nearly zero with an increasing $N_{\text{ipe}}/N_{\text{ape}}$ [300].

errors due to two main approximations: (i) discretization error by using the trilinear shape function and interpolation function and (ii) integration error by dividing an element into subregions and adopting the integration points. In the case of a non-homogeneous deformation, the approximations also introduce errors to regions in the atomistic domain that are in the vicinity of the domain interface because of the nonlocal force/energy. It is beyond the scope of this dissertation to distinguish different sources of error in each domain and perform a comprehensive convergence and error analysis; rather, some simulation results in this chapter are analyzed to show the convergence and error of quasistatic CAC with respect to MS as a function of (i) ratio of the number of integration points per element, N_{ipe}, to the number of atoms per element, N_{ape}, (ii) element size N_{ape}, and (iii) the atomistic domain thickness d_{at} (Fig. 4.9(d)) at a surface subject to indentation. The convergence is illustrated by the relative error e_{rel} between two scalars A, i.e.,

$$e_{\text{rel}} = \frac{|A_{\text{cal}} - A_{\text{MS}}|}{|A_{\text{MS}}|} \tag{4.8}$$

where A_{MS} is the result from MS and A_{cal} is obtained by either fully coarse-grained or CAC

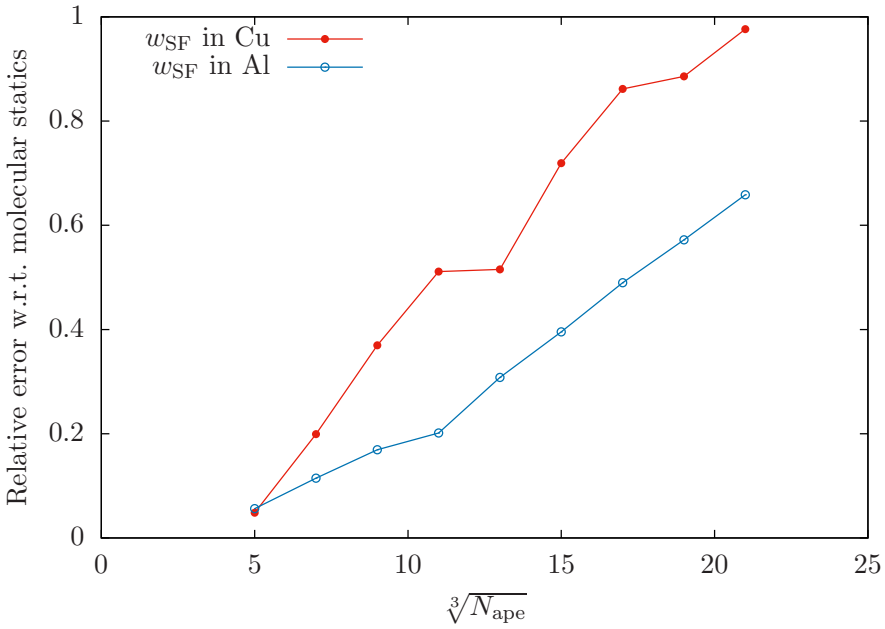

Figure 4.26: The relative errors of the stacking fault width w_{SF} of a 60° mixed type dislocation in both Cu and Al calculated in the coarse-grained domain using 2NN elements with varying element size N_{ape}. The values of w_{SF} are from Fig. 4.7. It is shown that the relative errors reduce to nearly zero with the smallest N_{ape} [300].

simulations.

1. In Sec. 4.1, the GSFE along $[1\bar{1}\bar{2}]$ direction in the coarse-grained domain is calculated using both 1NN and 2NN elements. Each element contains either 2197 or 9261 atoms. The relative errors of both γ_{usf} and γ_{sf} in both Cu and Al decrease to nearly zero when $N_{ipe}/N_{ape} > 0.013$, as shown in Fig. 4.25. From the perspective of numerical integration, a larger number of integration points yields an exact result for higher order integrand, which is desired for larger element. As N_{ipe}/N_{ape} approaches 1, the integration error tends to disappear while the discretization error still exists. It is shown that for the element sizes studied here, the 2NN type captures well the SFE in both materials, so extra integration points beyond 2NN are not necessary.

2. In Sec. 4.3, the stacking fault width w_{SF} of a single 60° mixed type dislocation in the coarse-grained domain is calculated using the 2NN elements as a function of the element size N_{ape}. Figure 4.26 shows that w_{SF} in both Cu and Al approach the MS results as N_{ape} decreases. The smallest element contains 125 atoms, suggesting that all

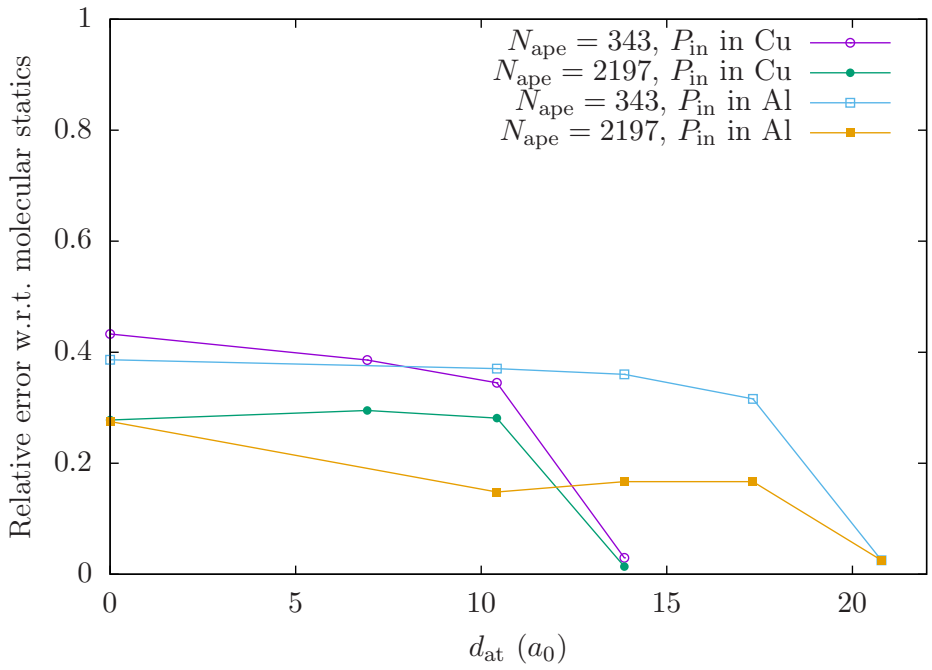

Figure 4.27: The largest relative errors of the indentation force per unit area P_{in} between $d_{\text{in}} = 0.1a_0$ and the yield point in both Cu and Al in the nano-indentation simulations. In the underlying coarse-grained domain, each element contains either 343 or 2197 atoms. The values of P_{in} are from Fig. 4.12. It is shown that the relative errors reduce to nearly zero with the largest d_{at} [300].

atoms are taken as integration points and the integration error is zero. However, the total error is not zero because of the discretization error. With a larger element, the integration errors increase due to a smaller $N_{\text{ipe}}/N_{\text{ape}}$. Although the largest element results in a relative error of nearly 1, this does not significantly affect the dislocation behaviors in the atomistic domain, as concluded in Sec. 4.7.

3. In Sec. 4.6, atomistic domains with different thickness d_{at} are employed at the indentation surface. In the underlying coarse-grained domain, each element contains either 343 or 2197 atoms. The indentation force per unit area P_{in} is studied with respect to the indentation depth d_{in} to quantify the free surface effect. The largest relative errors of P_{in} between $d_{\text{in}} = 0.1a_0$ and the yield point in each case is calculated, as shown in Fig. 4.27. The convergence of P_{in} to the MS result with an increasing d_{at} indicates that the effect of the atomistic/coarse-grained domain interface is negligible at a finite distance.

4.12 Summary

In this chapter, both dynamic and quasistatic CAC simulations are conducted to study certain benchmark problems in dislocation plasticity for FCC pure metals of Cu, Ni, and Al. The capabilities of the advanced CAC method, validated by comparing with equivalent fully atomistic simulations, are explored by investigating the behavior of dislocations in the coarse-grained domain, as a prelude to modeling large numbers of dislocations in Chaps. 5–9. Results are summarized as follows:

1. It is found that the ratio of relaxed stable to relaxed unstable SFE is lower in the 1NN element than that in atomistics, explaining the previous observation in the stress-strain curves that the amplitudes of strain bursts after yielding are larger in CAC using 1NN elements;

2. For a pure edge, pure screw, or 60° mixed type dislocation, direct evidence is provided to show that the long range stress fields are preserved in the coarse-grained domain; near the dislocation core center, it is found that a larger element results in a smaller maximum magnitude of shear stress;

3. Dislocation core structures in the coarse-grained domain are systematically studied for the first time. For a 60° mixed type dislocation, there is a linear correlation between the disregistry and the atomic position within an element, so the larger the element, the wider the stacking fault;

4. Both atomistic and coarse-grained domains give the same trend that a screw dislocation has a smaller stacking fault width, a smaller core radius, a higher Peierls stress, and a lower core energy, than an edge dislocation. With a decreasing element size, the coarse-grained values converge to those of fully resolved atomistic simulations;

5. Because of the coarse-graining error, the atomistic domain should be applied instead of a coarse-grained model where the local elastic deformation is significant;

6. Dislocation migration across the atomistic/coarse-grained domain interface, which is treated artificially in most coarse-grained methods, is explored. Attention is paid

in the variation of dislocation core structure across the interface, proving that the interface only slightly affects the dislocation migration;

7. The overall Burgers vector of dislocations on the same slip plane is the same in both atomistic and coarse-grained domains;

8. An adaptive mesh refinement CAC method is used to study the BTD transition in dynamic fracture of a notched specimen. Compared with MD, the adaptive CAC approach gives similar load-displacement responses and local stresses at crack tip, as well as an accurate prediction of the BTD transition, while eliminating most of the DOFs;

9. A mesh refinement scheme is applied to a scenario where the slip plane of a curved dislocation migrating from the atomistic domain is not aligned with the interelement boundaries in the coarse-grained domain. The CAC simulation performed with mesh refinement gives a local strain invariant profile along a dislocation close to that of a full atomistic simulation, while a strain concentration at the atomistic/coarse-grained domain interface occurs in the CAC simulation without mesh refinement;

10. A preliminary convergence and error analysis shows that the fully coarse-grained quasistatic implementation provides convergence to fully resolved MS energy minimization by virtue of the inherent consistency of the same underlying interatomic potential in both domains. Similar results are found in two FCC crystalline materials with distinct SFE.

This chapter does not intend to shed light on improved understanding of dislocation core level phenomena, but rather to establish that the method adequately replicates essential aspects of dislocation fields. It should be emphasized that despite a systematic increase of coarse-graining error in certain quantities relative to fully resolved atomistics with an increasing element size, the CAC method facilitates parametric studies of models at much larger scales with the same computational burden. While all computations in this chapter use 3D models, the study of larger domains and larger scale curved dislocations of mixed

character is left to the next chapters. For example, an issue of great relevance that challenges the length scale limits of classical atomistic simulations is the multiple, successive reactions of leading dislocations in long range pile-ups against atomistically resolved GBs or interfaces. Exploring this matter using CAC is the task of Chaps. 8 and 9.

CHAPTER V

SCREW DISLOCATION CROSS-SLIP IN NI

5.1 Introduction

Cross-slip of screw dislocations is important for dynamic recovery of metals because it assists dislocations to bypass obstacles and in annihilating each other at the end of Stage II work hardening [114]. Without cross-slip, the dislocation density and work hardening rate would not be reduced sufficiently, resulting in a less ductile material. Cross-slip is relevant to the process of dislocation bypass of preciptates [237] and voids [108], affecting the obstacle strengthening. Among many possible cross-slip mechanisms [201], including the Washburn model, the Schoeck-Seeger model, the Duesbery model, and the Püschl model, the Friedel-Escaig (FE) [83] and Fleischer (FL) mechanisms [88] are usually considered the most prominent [116]. According to the FE mechanism, the leading and trailing partial dislocations in a short segment of a screw dislocation are constricted and recombined before folding over and re-dissociating on the cross-slip plane; the resulting cross-slipped segment acts as a nucleus, facilitating other segments to switch to the cross-slip plane as well. According to the FL mechanism, with the aid of a stair-rod dislocation $1/6\langle 110\rangle$ [114], the leading and trailing partial dislocations can simultaneously exist on the cross-slip and primary planes, respectively; in other words, the stacking faults need not fully constrict at the plane intersection [37]. In FCC systems, atomistic simulations reveal that the detailed process of dislocation cross-slip is determined by a complex local stress state [124].

The dominating mechanism in a given cross-slip process depends on many factors. According to atomic scale simulations of cross-slip in FCC crystals, the FL mechanism is favored in the low temperature, high-stress limit, while the FE mechanism is favored in the high temperature, low-stress limit [42]. For example, a significant amount of dislocations cross slip via the FL mechanism as they propagate through the grain in an Al nanocrystal subject to a uniaxial tensile stress of 1.6 GPa [26]. Previous NEB calculations in Al

show that there exists a critical dislocation line length below which a dislocation segment cross-slips via the FL mechanism, whereas a segment with length above this follows the FE model [116]. In Cu and Ni, which have a higher energy barrier to cross-slip than Al, most atomistic simulations predict the FE mechanism [205,206]. Nevertheless, based on atomistic simulatoins at 0 K, Duesbery [74] found that cross-slip in Cu via the FL model is possible, provided that the driving force is large enough. The coupled influences of applied shear stress and dislocation line length on the cross-slip process, especially in the competition between the FL and FE mechanisms, have not been quantified, to the best of the author's knowledge.

In this chapter, both CAC and MD methods are employed to simulate the cross-slip process of a single screw dislocation using PBCs in FCC Ni. The cross-slip process by which a screw dislocation moves from one slip plane to another has been observed in CAC simulations in Sec. 4.10, yet not analyzed quantitatively. Emphasis in this chapter will be placed on (i) how the resolved applied shear stress affects the cross-slip mechanism and (ii) whether the same dislocation line length-dependence of cross-slip observed for Al [116] applies to Ni. The critical shear stress for cross-slip, which plays an important role in plasticity in crystalline metals, will also be calculated as a function of the dislocation line length. From the methodological viewpoint, this chapter will show the viability of using CAC simulations to accurately model 3D screw dislocation cross-slip, as a complement to fully resolved atomistic modeling [147], DD [115], CPFEM [5], *ab initio* simulations [284], the Peierls-Nabarro (PN) type of model [157, 180], and line tension theory [192, 248].

5.2 Methodology

Figure 5.1 presents the simulation cell for a single screw dislocation cross-slip in an FCC Ni single crystal. The lattice orientations are $x[1\bar{1}\bar{2}]$, $y[110]$, and $z[1\bar{1}1]$. With the lattice parameter $a_0 = 3.52$ Å, the simulation cell has a size of 67.18 nm by 77.66 nm by 68.51 nm. Note that the same cell is employed in all CAC and MD simulations, except that there are finite elements in the CAC model.

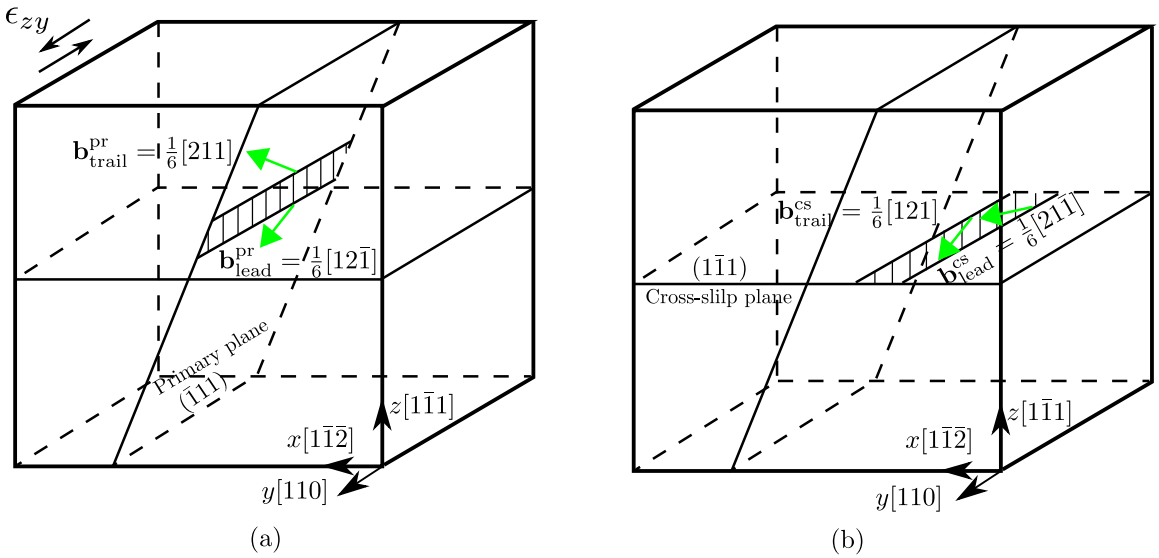

Figure 5.1: Simulation cell for dislocation cross-slip. (a) A single screw dislocation splits into two 30° Shockley partial dislocations on the primary slip plane $(\bar{1}11)$. (b) Subject to a shear strain ϵ_{zy}, the screw dislocation moves onto the cross-slip plane $(1\bar{1}1)$ and is dissociated into another set of two Shockley partials [305].

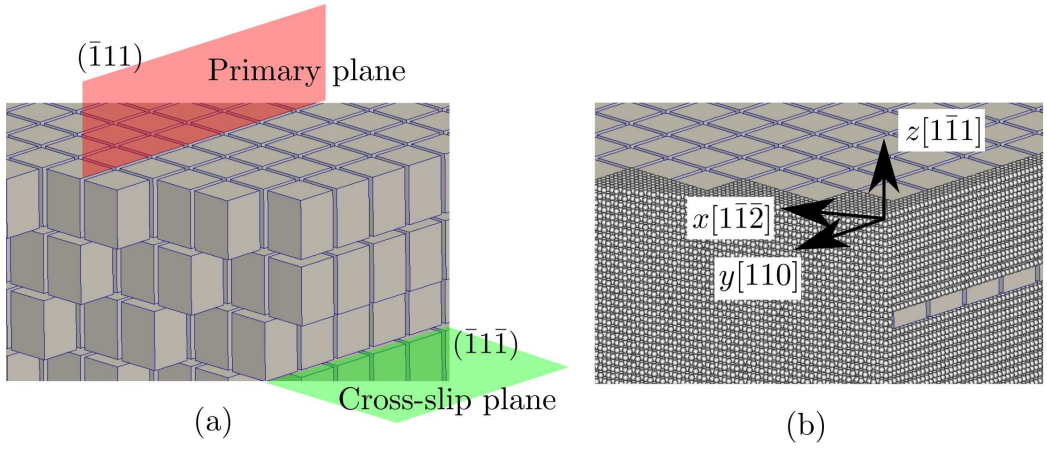

Figure 5.2: In a CAC model with $N_{\mathrm{ape}} = 729$, (a) only the coarse-grained domain with rhombohedral elements is shown and (b) atoms are filled in at the periodic boundaries along both the x and y directions [305].

3D rhombohedral elements are used in the coarse-grained domain in the CAC model [297], with surfaces corresponding to {111} slip planes and the jagged interstices of elements at the periodic boundaries filled in with atoms [300], as shown in Fig. 5.2. In the coarse-grained domain, all partial dislocations, on either the primary or the cross-slip plane, contain no pre-existing kink because the [110] dislocation line direction is aligned with the element edge. There is no jog along any dislocation either. Hence, this CAC model agrees with the

classicial cross-slip process without influences of kinks and jogs [205].

In the coarse-grained domain, a uniform element size with cases varying from 125 to 4913 atoms per element is adopted. On the one hand, a larger element size, N_{ape}, results in a smaller number of elements, N_{ele}. On the other hand, a model with a larger element size requires a larger number of atoms to fill in at the periodic boundaries. The net effect is that there exists an element size corresponding to which the number of DOFs $N_{\text{DOF}} = 8N_{\text{ele}} + N_{\text{atom}}$ is minimum for the overall simulation cell, where 8 comes from the fact that each element has 8 nodes. As shown in Tab. 5.1, the smallest $N_{\text{DOF}}/N_{\text{atom}}^{\text{full}} = 4.87\%$ with $N_{\text{ape}} = 1331$. In Fig. 5.1, the length of the dislocation line in one periodic cell $L_{\text{d}} = L_y = 77.66$ nm, where L_y is the length of the simulation cell along the y direction. As a result, there are $N_{\text{atom}}^{\text{full}} = 32,902,272$ atoms in the equivalent full atomistic model, which would be highly computationally intensive. To explore the effect of L_{d}, cases with L_y of 6.47 nm, 12.94 nm, 25.88 nm, 38.83 nm, 51.76 nm, and 64.71 nm, respectively, are also investigated, while the length of the simulation cell along both the x and z axes remain unchanged.

Table 5.1: The number of elements N_{ele}, number of atoms N_{atom}, number of DOFs N_{DOF}, and the ratio of N_{DOF} to the number of atoms in a fully resolved atomistic simulation $N_{\text{atom}}^{\text{full}} = 32,902,272$, with varying number of atoms per element N_{ape}. It is found that the value of $N_{\text{DOF}}/N_{\text{atom}}^{\text{full}}$ is not a monotonic function of N_{ape}.

N_{ape}	125	343	729	1331	2197	3375	4913
N_{ele}	258,483	93,280	43,369	23,658	14,218	9,183	6270
N_{atom}	591,897	907,232	1,286,271	1,413,474	1,665,326	1,909,647	2,097,762
N_{DOF}	2,659,761	1,653,472	1,633,223	1,602,738	1,779,070	1,983,111	2,147,922
$N_{\text{DOF}}/N_{\text{atom}}^{\text{full}}$	8.08%	5.03%	4.96%	4.87%	5.41%	6.03%	6.53%

The problem common to most fs-scale time step dynamic methods, such as MD or dynamic CAC, is the difficulty to capture rare events such as thermally activated cross-slip [275]. Thus, simulations must be carefully designed to capture cross-slip in reasonable wall time. Here, a straight screw dislocation with Burgers vector $\mathbf{b} = (a_0/2)[110]$ is introduced on the primary plane $(\bar{1}11)$; PBCs are applied along both the x and y directions to simulate an array of evenly spaced, infinitely long, initially straight dislocation lines [124]. The boundaries normal to the z axis are assumed traction free, which does not strongly affect

the line tension of a screw dislocation [187]. After energy minimization, a homogeneous simple shear strain ϵ_{zy} is applied, acting mainly on the cross-slip plane $(1\bar{1}1)$ and with much reduced extent on the primary plane, following the idea of Schoeck and Seeger [208]. Note the shear strain is applied within one time step, to avoid the sensitivity of the cross-slip mechanism to strain rate [26]. Then the shear stress is maintained constant under an NPT ensemble at 10 K using a PR barostat [186] with time step of 2 fs [306]. Independent simulations with an increment of shear stress $\Delta\tau_{zy} = 10$ MPa are conducted such that the critical shear stress τ_{c} is the minimum stress at which the cross-slip event is observed within 50 ps. In some cases with a certain combination of τ_{zy} and L_{d}, a full atomistic simulation, i.e., MD simulation, is performed with the same time step and temperature. It is found that the critical stresses determined by low temperature dynamic simulations, via either dynamic CAC or MD, are close to those calculated by quasistatic simulations, via either quasistatic CAC or MS, yet the dynamic simulations reveal the detailed cross-slip process and are thus employed in this chapter.

It should be emphasized that although the length scale of material volume explored in this chapter is accessible by classical MD, this is highly computationally expensive to pursue. It will be shown that CAC simulations can accurately describe the cross-slip process, at significantly reduced computational cost. To identify dislocations in the coarse-grained domain in the CAC model, the atomic positions are interpolated from the nodal positions before they are processed by adaptive common neighbor analysis (a-CNA) [246] using OVITO [245]. Moreover, a DXA [247] is employed to distinguish the FE mechanism, in which the dislocation is fully constricted to have Burgers vector $(a_0/2)\langle 110\rangle$ at the plane intersection, from the FL mechanism, in which a stair-rod dislocation with Burgers vector $(a_0/6)\langle 110\rangle$ is formed at the intersection.

5.3 Results and discussion

Throughout the remainder of this chapter, the superscripts 'pr' and 'cs' are used to distinguish the primary and cross-slip planes, whereas the subscripts 'lead', 'trail', and 'sr' refer to the leading partial, trailing partial, and stair-rod dislocations, respectively.

5.3.1 Dislocation dissociation

In both atomistic and coarse-grained domains, a full screw dislocation on the primary plane is dissociated into two 30° Shockley partial dislocations, i.e.,

$$\frac{1}{2}a_0[110]^{\text{pr}} \rightarrow \frac{1}{6}a_0[12\bar{1}]^{\text{pr}}_{\text{lead}} + \frac{1}{6}a_0[211]^{\text{pr}}_{\text{trail}} \tag{5.1}$$

which is energetically favorable according to Frank's rule [110]. The force per unit length on a partial dislocation can be obtained by the Peach-Koehler (PK) formula: $\mathbf{F} = (\mathbf{b} \cdot \boldsymbol{\sigma}) \times \mathbf{t}$, where $\boldsymbol{\sigma}$ is the applied shear stress tensor whose only non-zero components are τ_{yz} and τ_{zy}, $\mathbf{t}$ is the unit tangent vector of the dislocation line along the y axis, and $\mathbf{b}$ should be transformed to the spatial Burgers vector. It is found that as the two partials have Burgers vector with the same screw but opposite edge components, the applied stress acts on the screw components to translate the stacking fault ribbon rigidly, while on the edge components to compress the ribbon [201].

On the cross-slip plane, the same full dislocation splits into a different set of two 30° Shockley partials, i.e.,

$$\frac{1}{2}a_0[110]^{\text{cs}} \rightarrow \frac{1}{6}a_0[21\bar{1}]^{\text{cs}}_{\text{lead}} + \frac{1}{6}a_0[121]^{\text{cs}}_{\text{trail}} \tag{5.2}$$

where the stacking fault ribbon is expanded by the Escaig stress [83] acting on the edge components of the partials according to the PK formula.

5.3.2 Implications of coarse-graining

The atoms filled in at the jagged boundaries, however, may result in aphysical phenomena. This is because, as will be shown later, it is easier for the dislocation to cross-slip in the atomistic domain than in the coarse-grained domain. Consequently, at a certain stress level, a dislocation may bow out first at the periodic boundaries along the y axis, followed by bowing out of the remaining central segments that are in the coarse-grained domain, a process that may be mistaken for the FE mechanism, as shown in Fig. 5.3. This coarse-graining effect is more pronounced for a shorter dislocation line where the fraction of the atomistic domain at the PBCs becomes larger. Therefore, in any CAC simulation, if the dislocation

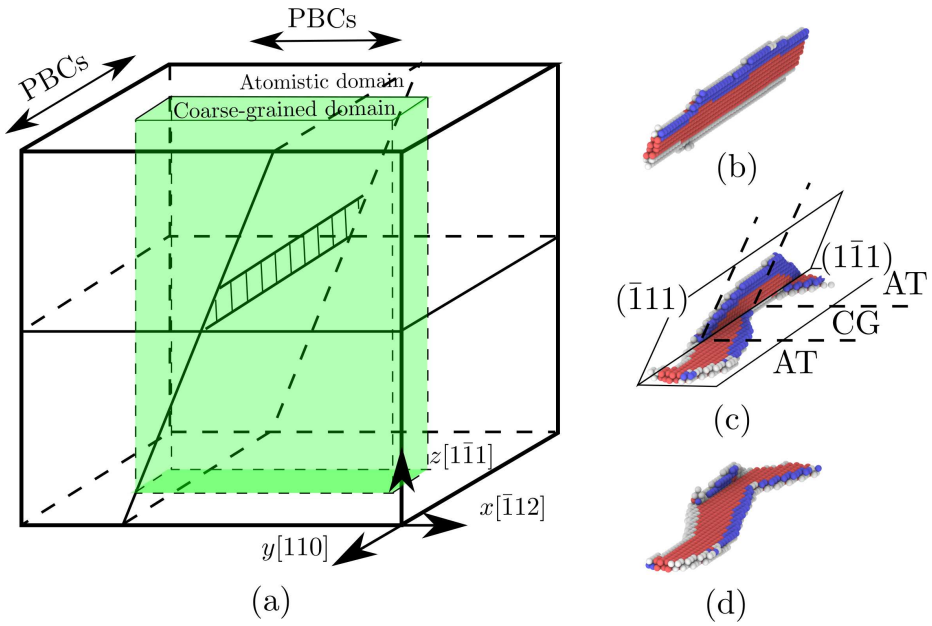

Figure 5.3: (a) An illustration of the simulation cell containing a screw dislocation with an atomistic (AT) domain at the PBCs; the green cube in the center of the model is the coarse-grained (CG) domain. The length of the simulation cell along the y direction, i.e., the dislocation line length L_{d}, is 12.94 nm. (b–d) The dislocation, which is originally on the primary plane $(\bar{1}11)$, bows out first at the periodic boundaries, followed by the remaining central segments also switch to the cross-slip plane $(1\bar{1}1)$. Atoms in (b–d) are colored by a-CNA [246], where red are of local HCP structure, blue are BCC atoms, white are unknown, while all FCC atoms are removed.

bow-out is initiated at the periodic boundaries, we consider its mechanism inconclusive and perform an equivalent MD simulation.

5.3.3 Cross-slip via the Fleischer mechanism

As stated before, the FE mechanism requires the two Shockley partials to be fully constricted at the plane intersection before the full dislocation is re-dissociated onto the cross-slip plane. Conceptually, such a process can be well accommodated in CAC because both partial and full dislocations are on {111} planes. Indeed, a screw dislocation segment changing its slip plane via the FE mechanism has been presented in Sec. 4.10. The FL mechanism, however, involves a stair-rod dislocation $(a_0/6)[\bar{1}10]$ on (001) plane, which does not belong to the set of {111} planes exhibited between elements. Thus, a question arises as to whether the FL mechanism can be simulated in the coarse-grained domain in CAC.

In a perfect lattice without a dislocation, as illustrated by a 2D model in Fig. 5.4(a),

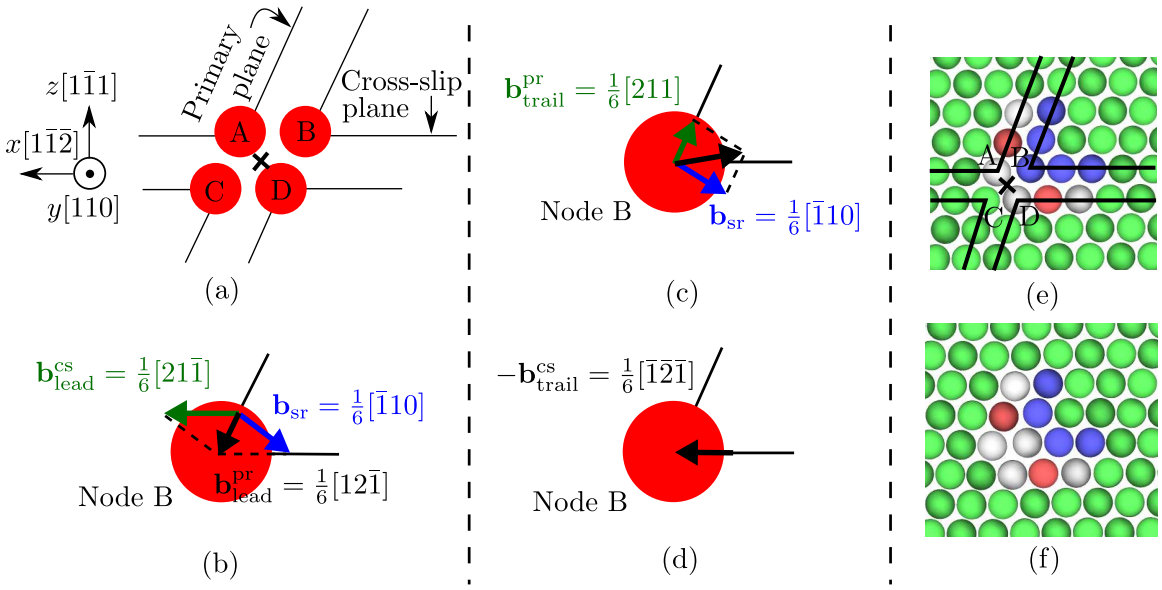

Figure 5.4: (a) A 2D illustration of four nodes (A, B, C, and D) belonging to adjacent elements in a perfect lattice without a dislocation; the black cross denotes the line of intersection between the primary and cross-slip planes. (b) According to Eq. 5.3, the leading partial dislocation on the primary slip plane $\mathbf{b}^{\rm pr}_{\rm lead}$ (black arrow) splits into the leading partial dislocation on the cross-slip plane $\mathbf{b}^{\rm cs}_{\rm lead}$ (green arrow) and a stair-rod dislocation $\mathbf{b}_{\rm sr}$ (blue arrow). (c) According to Eq. 5.4, the trailing partial dislocation on the primary plane $\mathbf{b}^{\rm pr}_{\rm trail}$ (green arrow) reacts with the stair-rod dislocation $\mathbf{b}_{\rm sr}$ (blue arrow) to form the trailing partial dislocation on the cross-slip plane $\mathbf{b}^{\rm cs}_{\rm trail}$. (d) The trailing partial dislocation $\mathbf{b}^{\rm cs}_{\rm trail}$ glides on the cross-slip plane away from the line of intersection, leaving behind the same perfect lattice as in (a). Note that only the edge components of partial dislocations are shown because their screw components are pointing outward along the positive y direction. Atomic configurations of the dislocation folding over the plane intersection via the FL mechanism in the (e) coarse-grained and (f) atomistic domains are also shown. The four nodes (A, B, C, and D) and the cross in (e) correspond to those in (a) [305].

four nodes (labeled A, B, C, and D), each of which belongs to a different element, are located adjacent to each other. Then at the plane intersection, denoted by the black cross in Fig. 5.4(a), the leading partial on the primary plane $\mathbf{b}^{\rm pr}_{\rm lead}$ splits into a stair-rod dislocation $\mathbf{b}_{\rm sr}$ and the leading partial on the cross-slip plane $\mathbf{b}^{\rm cs}_{\rm lead}$, i.e.,

$$\frac{1}{6}a_0[12\bar{1}]^{\rm pr}_{\rm lead} \rightarrow \frac{1}{6}a_0[\bar{1}10]_{\rm sr} + \frac{1}{6}a_0[21\bar{1}]^{\rm cs}_{\rm lead}, \tag{5.3}$$

which is illustrated in Fig. 5.4(b), where the overall Burgers vector $\mathbf{b}^{\rm pr}_{\rm lead}$ is exhibited by displacing the node B while fixing the other three nodes. It follows that the trailing partial on the primary plane $\mathbf{b}^{\rm pr}_{\rm trail}$ reacts with $\mathbf{b}_{\rm sr}$ to form the trailing partial on the cross-slip plane

$\mathbf{b}^{\text{cs}}_{\text{trail}}$, i.e.,

$$\frac{1}{6}a_0[\bar{1}10]_{\text{sr}} + \frac{1}{6}a_0[211]^{\text{pr}}_{\text{trail}} \rightarrow \frac{1}{6}a_0[121]^{\text{cs}}_{\text{trail}}, \tag{5.4}$$

which is illustrated in Fig. 5.4(c) and the resulting Burgers vector is $\mathbf{b}^{\text{cs}}_{\text{trail}}$. In the end, the trailing partial glides on the cross-slip plane, away from the plane intersections, leaving behind the perfect lattice in Fig. 5.4(d). In Fig. 5.4(b–d), node B is displaced by the black arrow in each subfigure while the other three nodes are fixed; after Fig. 5.4(d), node B is restored to its original position shown in Fig. 5.4(a) — in other words, the vector sum of the three black arrows in Fig. 5.4(b–d) is zero.

In the procedure described above, worth further discussion is the movement of node B along the $[\bar{1}10]$ direction on the (001) plane: the corresponding displacement is left after the leading partial dislocation on the cross-slip plane $\mathbf{b}^{\text{cs}}_{\text{lead}}$ glides away, i.e., after Eq. 5.3, but before the trailing partial dislocation on the primary plane $\mathbf{b}^{\text{pr}}_{\text{trail}}$ reacts with the stair-rod dislocation $\mathbf{b}_{\text{sr}}$, i.e., before Eq. 5.4. At first glance, node B moving on a (001) plane is contradictory to the assumption that only {111} planes exist between elements in the coarse-grained domain. Nevertheless, such a process is possible because node B (i) can move along any direction with respect to the other three nodes and (ii) only moves by a very short distance $(a_0/6)[\bar{1}10]$ such that it does not overlap with the neighboring elements; note that each element in the coarse-grained domain in CAC is a nonlocal hyperelastic body and overlap between elements is impossible [300]. In other words, the stair-rod dislocation is formed by both sliding and separation of the node B with respect to the other three nodes, as shown in Fig. 5.4(e). Although the structural reconstruction is more limited in the coarse-grained domain than in the atomistic domain, moving node B by a short distance does not require a much higher stress, as will be discussed below.

5.3.4 Applied shear stress-dependent cross-slip

The applied shear stress τ_{zy} has a small projection on the primary plane, $\tau^{\text{pr}}_{zy} = \tau_{zy}\cos\theta$, to overcome the Peierls stress σ_{P} and drive dislocation glide, where $\theta = 70.53°$ is the acute angle formed between the primary and cross-slip planes. Thus, $\tau^{\text{pr}}_{zy} = (1/3)\tau_{zy}$.

The critical shear stresses for the cross-slip via the FE and FL mechanisms are denoted

as τ_c^{FE} and τ_c^{FL}, respectively. In the case of $L_d = 77.66$ nm, the following events are observed as τ_{zy} increases:

1. $\tau_{zy}^{pr} < \sigma_P$: the dislocation on the primary plane does not move;
2. $\tau_{zy}^{pr} \geq \sigma_P$ and $\tau_{zy} < \tau_c^{FE}$: the dislocation on the primary plane moves toward the negative z direction without cross-slip;
3. $\tau_c^{FE} \leq \tau_{zy} < \tau_c^{FL}$: the dislocation on the primary plane cross-slips via the FE mechanism;
4. $\tau_{zy} \geq \tau_c^{FL}$: the dislocation on the primary plane cross-slips via the FL mechanism.

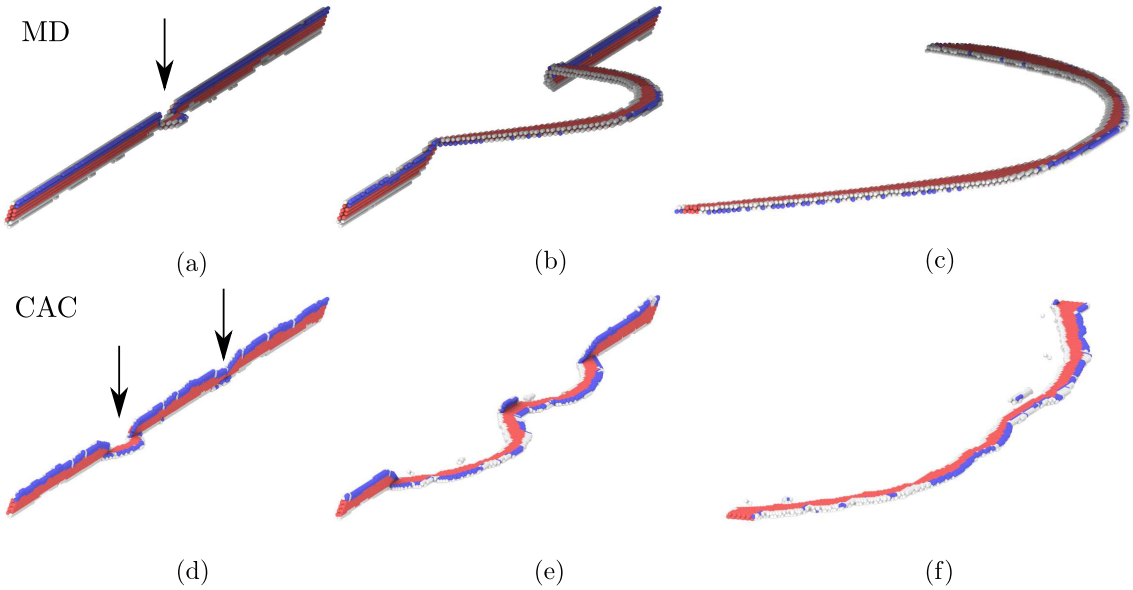

Figure 5.5: Cross-slip of a screw dislocation via the FE mechanism subject to a shear stress of (a–c) 1.36 GPa in MD and (d–f) 1.47 GPa in CAC with element size $N_{ape} = 1331$. The initial length of the dislocation line in one periodic cell $L_d = 77.66$ nm. Segments near the center of the dislocation line, indicated by arrows in (a) and (d), bow out first [305].

The snapshots of dislocation cross-slip via the FE and FL mechanisms are shown in Figs. 5.5 and 5.6, respectively, for both MD and CAC simulations with element size $N_{ape} = 1331$, in the case of $L_d = 77.66$ nm. For the FE mechanism, segments near the center of the dislocation line, indicated by arrows in Figs. 5.5(a) and 5.5(d), bow out first. As a result, curved dislocations glide on the cross-slip plane. Note that it is not the bowing

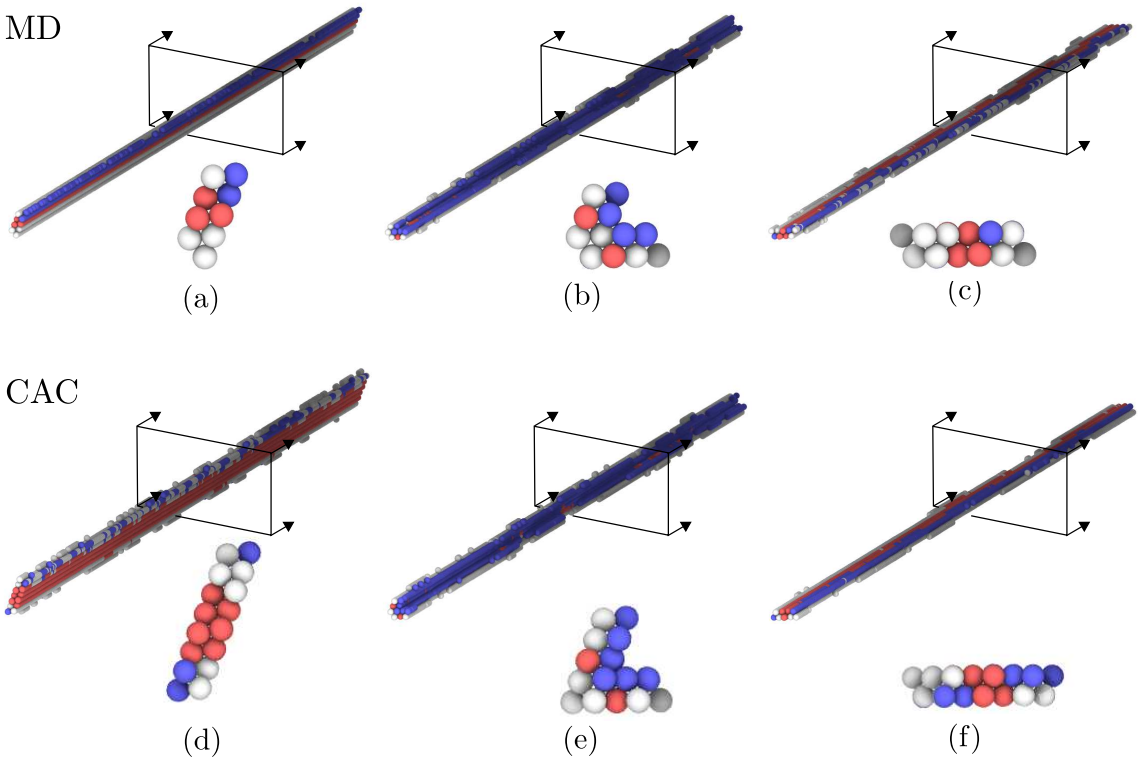

Figure 5.6: Cross-slip of a screw dislocation via the FL mechanism subject to a shear stress of (a–c) 1.4 GPa in MD and (d–f) 1.51 GPa in CAC with element size $N_{\text{ape}} = 1331$. The initial length of the dislocation line in one periodic cell $L_{\text{d}} = 77.66$ nm. Cross-sections of the dislocation line at the center are shown, where CAC gives a wider stacking fault than MD on both primary and cross-slip planes [305].

of the dislocation, but the expansion of the stacking fault ribbon on the cross-slip plane or reduction in enthalpy, that supplies the driving force [83, 221]. For the FL mechanism (Fig. 5.6), the entire dislocation line folds over the plane intersection altogether, with the help of a stair-rod dislocation. In both MD and CAC, the critical shear stress for the FE mechanism is always smaller than that for the FL mechanism, i.e., $\tau_{\text{c}}^{\text{FE}} < \tau_{\text{c}}^{\text{FL}}$, because the creation of a stair-rod dislocation in the FL process is more energetically expensive than the recombination of two partials in the FE process [90]. Moreover, the FE mechanism has a limited stress regime($\sim$ 40 MPa), above which the cross-slip follows the FL process. This suggests that (i) the interpretation of atomistic simulations of cross-slip in terms of mechanism should be made carefully and (ii) a shear stress that is close to the critical value needs to be applied to promote the FE process.

For both mechanisms, the CAC simulations accurately give the key characteristic of the

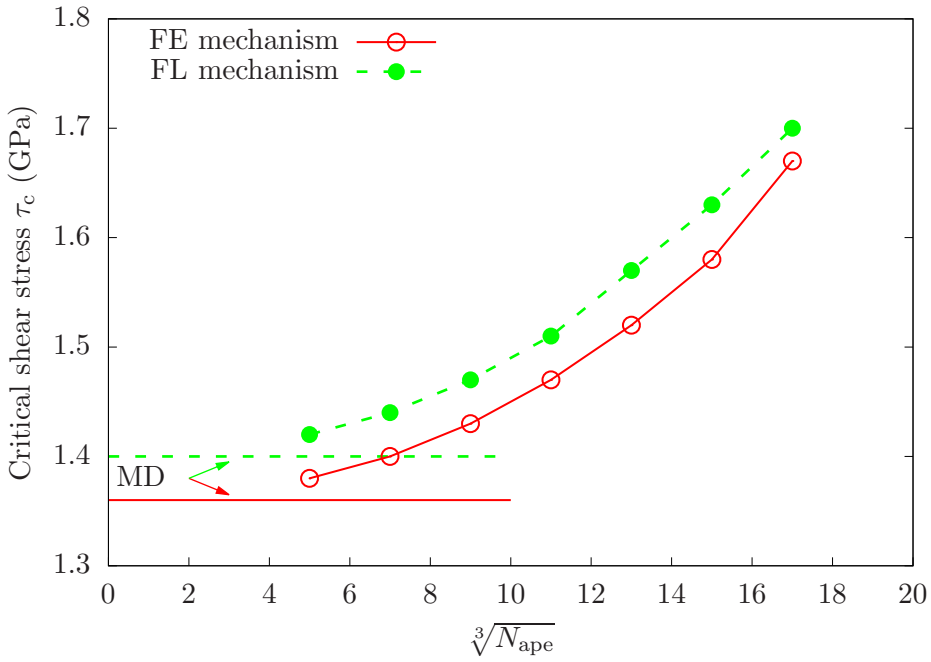

Figure 5.7: The critical shear stress τ_c for both FE and FL mechanisms as a function of the number of atoms per element N_{ape} in CAC simulations, compared with the results obtained by MD simulations which are indicated by the horizontal lines. It is shown that for both mechanisms, τ_c converges to the atomistics as the elements become smaller and contain fewer atoms. The initial length of the dislocation line in one periodic cell $L_d = 77.66$ nm [305].

cross-slip, yet the critical shear stresses are higher than MD results, as shown in Fig. 5.7. Dislocations are less relaxed in the coarse-grained domain such that (i) a higher stress is required to form the stair-rod dislocation and (ii) compressing or expanding the stacking fault requires a higher Escaig stress [300]. However, note that the trends are monotonic and convergent with regard to coarse-graining error. The finding that cross-slip is easier to operate based on MD simulations agrees with the fact that the cross-slip is favored when the applied stress increases the width of the stacking fault ribbon in the cross-slip plane while decreasing it on the primary plane [201]. Nevertheless, it should be emphasized that (i) the relative error in τ_c between MD and CAC with $\sqrt[3]{N_{ape}} = 11$, i.e., $N_{ape} = 1331$ which has the fewest DOFs according to Tab. 5.1, is about 8.09% and 7.86% for the FE and FL mechanisms, respectively, and (ii) both τ_c converge to the atomistics as the elements become smaller and contain fewer atoms, as shown in Fig. 5.7.

The level of stress predicted from current CAC and MD simulations for cross-slip is at GPa level. Although this is comparable to that from MD simulations in the literature

[124, 204], it is significantly higher than that in experiments in FCC pure metals. There are two major reasons that may contribute to the overestimation of the critical stress:

1. In this chapter, the shear strain is applied to the CAC and MD models and the process is stress-driven and largely athermal. Cross-slip typically occurs in these simulations within a few picoseconds, and is not thermally activated. The reaction pathway for the thermally activated cross-slip process is well-preserved, on the other hand. As a consequence, the critical stress predicted from CAC or MD is much higher than the measurement in traditional low-strain-rate experiments for much longer time during which thermal fluctuations have high enough probability to drive cross-slip. This does not mean that the simulations in this chapter are in any way inaccurate or aphysical — they simply reflect the limiting case of essentially athermal, stress-driven cross-slip along the same reaction pathway. In the current CAC approach, the time step size is established based on the requirements of the fully atomistic domain to ensure accuracy. To reduce the strain rate in these dynamic simulations, a multi-time-scaling algorithm is required to increase the time step in the coarse-grain domains and is the subject of ongoing work.

2. In experiments, dislocation density is relatively high and cross-slip occurs with the influence of dislocation interactions and internal stresses in contrast to the case of cross-slip of an isolated screw dislocation considered in current simulations. As such, the critical cross-slip stress predicted in this chapter is expected to provide an upper bound.

5.3.5 Dislocation line length-dependent cross-slip

The cross-slip process for different dislocation line lengths in Ni, L_{d}, is studied next, as shown in Fig. 5.8. When $L_{\mathrm{d}} > 20$ nm, dynamic CAC simulations with $N_{\mathrm{ape}} = 1331$ are carried out; otherwise MD simulations are performed. Because of the difference in τ_{zy} between MD and CAC, an analysis of the variation of τ_{zy} as a function of L_{d} is more meaningful within each type of simulation. It is found that as L_{d} increases, both $\tau_{\mathrm{c}}^{\mathrm{FE}}$ and $\tau_{\mathrm{c}}^{\mathrm{FL}}$ decrease. This suggests that, like in Al [116], the energy barrier for cross-slip in Ni is

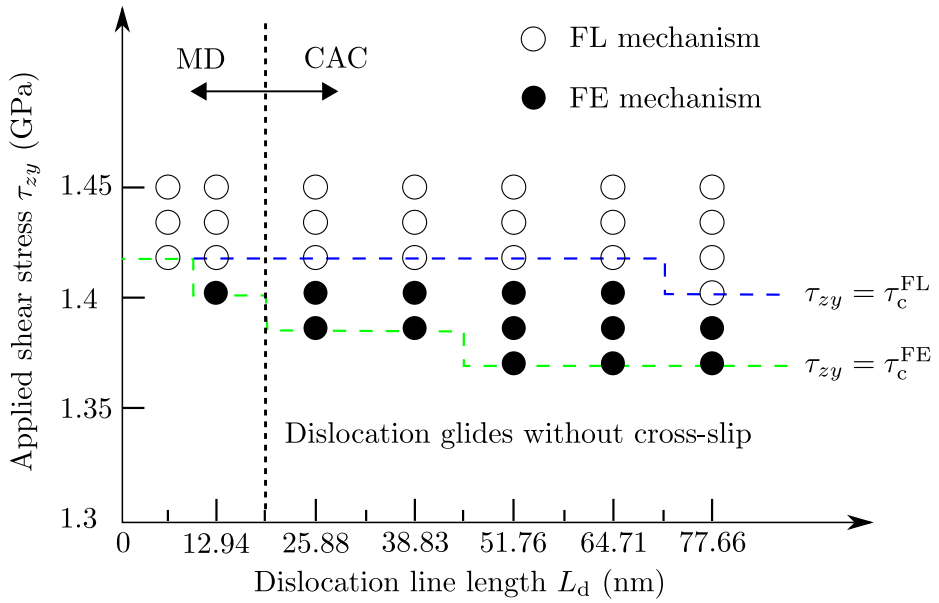

Figure 5.8: Dislocation behavior as a function of both the applied shear stress τ_{zy} and dislocation line length L_d in Ni. It is found that with an increasing τ_{zy}, dislocation begins to move but without cross-slip; at a higher τ_{zy}, it cross-slips via the FE or FL mechanisms. The critical stresses for cross-slip, τ_c^{FE} and τ_c^{FL}, are L_d-dependent. Note that when $L_d > 20$ nm, dynamic CAC simulations with element size $N_{ape} = 1331$ are carried out, otherwise MD simulations are performed instead [305].

dislocation line length-dependent. Moreover, MD simulations show that while both FE and FL types of cross-slip operate at different τ_{zy} in the case of $L_d = 12.94$ nm, the dislocation only cross-slips via the FL mechanism for $L_d = 6.47$ nm. In comparison, note that (i) Kang et al. [124] observed dislocation cross-slip via the FE mechanism for $L_d = 10.56$ nm in Ni using NEB and (ii) the critical dislocation line length between the FE and FL mechanisms is 6.3 nm in Al [116].

5.4 Summary

In this chapter, dynamic CAC and MD simulations are performed to study the shear stress- and line length-dependent screw dislocation cross-slip in FCC Ni. Results are summarized as follows:

1. At a significantly reduced computational cost, CAC simulations can accurately describe the pathway of the cross-slip process via both FE and FL mechanisms as obtained via MD, as well as predict relatively accurate critical shear stresses for cross-slip

operation, with coarse-graining errors.

2. In the case of a dislocation of length 77.66 nm subject to a constant applied shear stress of increasing values, the following events operate consecutively: (i) the dislocation begins to move once the resolved shear stress on the primary plane overcomes the Peierls stress, (ii) the dislocation cross-slips via the FE mechanism, and (iii) the dislocation cross-slips via the FL mechanism. This suggests that the cross-slip process is applied shear stress-dependent.

3. The dislocation cross-slip mechanism, manifested by the relevant critical shear stress, is also line length-dependent. In particular, the FE mechanism is not observed for a short dislocation line of 6.47 nm, but for a longer dislocation of 12.94 nm. Moreover, a longer dislocation line has a slightly lower critical shear stresses for cross-slip operation.

CHAPTER VI

EDGE DISLOCATIONS BOWING OUT FROM OBSTACLES IN AL

6.1 Introduction

Dislocation bow-out between pinning points is central to dislocation/obstacle interactions in crystalline materials [252]. Investigating the detailed process of dislocations bowing out and moving through a field of obstacles in metals aids in understanding the onset of dislocation migration through lattice, work hardening, and dislocation multiplication from FR sources [93]. Several modelling techniques, including MD [66, 148], DD [22, 104], phase field method (PFM) [24, 213], and level set method [286], have been employed to simulate dislocation bow-out. In most of these studies, only one dislocation segment bows out from an isolated pair of obstacles. In reality, obstacles are distributed randomly in pure metals and alloys, with an average spacing L of about 30 $\sim$ 300 nm and an average obstacles radius of about 10 nm [214, 224]. Therefore, it is important to account for the effects of distributed bowed-out segments in modeling a given dislocation bow-out process, in a way that considers both medium and long range elastic interactions as well as dislocation core effects.

Traditional dislocation bow-out analysis is based on dislocation line tension theory. Continuum dislocation theory predicts that the effective line tension of a curved dislocation segment is a logarithmic function of its initial distance L between two neighboring obstacles, namely, $\ln L$ [114]. In the presence of adjacent dislocation segments, however, the line tension of a given dislocation segment is altered [236]. Specifically, the negative interaction energy between a dislocation and its adjacent bowed-out segments reduces its line tension and hence lowers the critical stress required to bypass the obstacles [110]. This effect is particularly important for a dislocation line lying in a single slip plane and pinned by regularly spaced obstacles [110]. Simulations based on the dislocation self-stress show that, because of their opposite Burgers vector, the dipole-like attractive force between dislocation

branches terminating on a given obstacle results in a "pinching" effect and facilitates dislocation bow-out [11, 91]. The role of adjacent dislocation segments becomes more important with decreasing D/L, where D is the obstacle diameter [12]. In dislocation/obstacle interactions, dislocations that depin from adjacent obstacles aid in pulling the branches together and diminish the strengthening effect [220].

Continuum models for dislocation/obstacle interactions apply to the dislocation bow-out process if the dislocation bypasses the obstacles following the Orowan bypass mechanism [94]. Most of these models assume that an infinitely long dislocation bypasses an infinite array of equally spaced obstacles. For obstacles with a finite size D, the term $\ln L$ is replaced by $\ln \bar{D}$ by taking into account of the interactions between three closest dislocation branches, where $\bar{D} = (D^{-1} + L^{-1})^{-1}$ [12]. Most simulations employ PBCs along the dislocation line direction. In dislocation/precipitate interactions, Bacon et al. [12] included three precipitates in one simulation supercell with PBCs to represent an infinite row of precipitates. Crone et al. [61] found that introducing additional voids beyond three does not show a significant influence on the critical depinning stress in dislocation/void interactions. Studies of a dislocation passing a random array of obstacles have been pursued using line tension models [92, 133, 181] and DD simulations [238] . Nevertheless, the effects of bow-out of other dislocation segments on the critical shear stress of a given dislocation bow-out in an image-free model have not been explored quantitatively, to the best of the author's knowledge.

In this chapter, quasistatic CAC simulations are performed in the athermal limit to investigate edge dislocations bowing-out from a row of collinear cylindrical holes in Al, which is chosen because of its high stable SFE (≈ 146 mJ/m^2) and low elastic anisotropy index (≈ 1.21) [200], enabling the simulation results to be compared with most isotropic continuum models that do not consider dislocation dissociation [302]. Nevertheless, discrepancies between CAC simulations and continuum predictions still exist partly due to the largely ignored details of core/obstacle interactions in continuum; these details are are important because the stacking fault width is on the order of the relatively small D and L explored in this chapter, which are close to those of peak strengthening via Orowan looping.

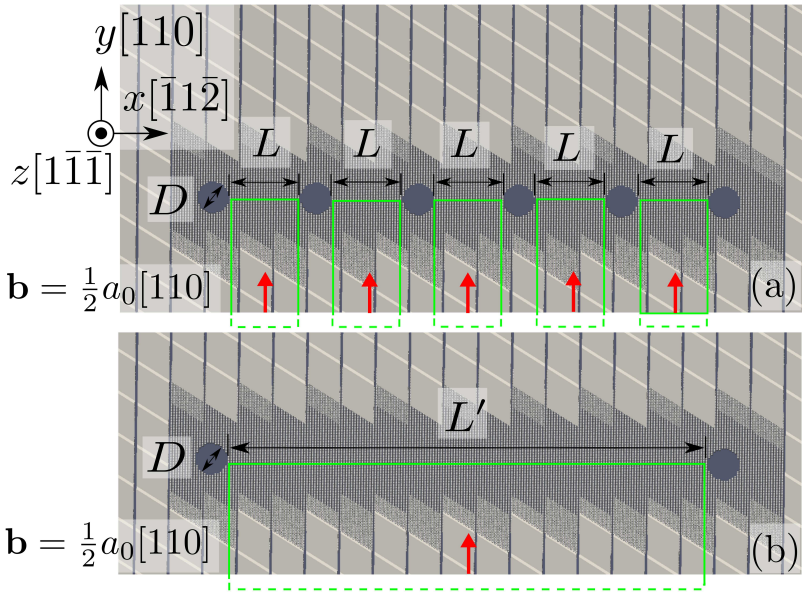

Figure 6.1: CAC simulation cell containing (a) a row of 5 collinear initial dislocation segments each of which has a length of L and (b) one initial dislocation segment with length $L' = 5L + 4D$, where $L = 5.61$ nm and $D = 2.81$ nm. Cylindrical holes are throughout the specimen along the z direction. An atomistic domain is retained in the vicinity of the holes, while the coarse-grained domain is employed elsewhere. All cell boundaries are assumed traction free to alleviate spurious periodic image forces. Edge dislocations are formed by moving atoms/nodes inside the green lines by Burgers vector $\mathbf{b} = (a_0/2)[110]$ [302].

Figure 6.1(a) presents the simulation cell containing a row of 6 collinear cylindrical holes throughout the specimen along the z direction, which would potentially accommodate 5 dislocation segments between them. Full atomistic resolution is applied in the vicinity of holes such that the hole surface is at least 2 nm from the atomistic/coarse-grained domain interface; away from the holes, 3D rhombohedral elements that have discontinuities between them, each of which contains 2197 atoms, are used. The lattice orientations are $x[\bar{1}1\bar{2}]$, $y[110]$, and $z[1\bar{1}\bar{1}]$. With the lattice parameter $a_0 = 4.05$ Å, the simulation cell has a size of 300.59 nm by 297.22 nm by 45.49 nm; in all simulations, a uniform hole cross-sectional diameter on the x-y plane $D = 2.81$ nm is used. With a constant interhole ligament distance $L = 5.61$ nm, the number of initial dislocation segments n varies from 1 to 14, corresponding to a total ligament distance $L' = nL + (n-1)D$ between the leftmost and rightmost holes of $5.61 \sim 115.07$ nm. As a result, the model with only one dislocation

segment of L has 108,163 elements and 1,200,322 atoms, with 2,065,626 DOFs in total, compared with 238,834,433 atoms in an equivalent full atomistic model, which would be highly computationally intensive. Simulations containing only two holes distanced by L' are also performed for comparative purposes, as shown in Fig. 6.1(b). All boundaries of the simulation cell as well as the hole surfaces are traction free such that spurious forces arising from periodic images are eliminated [251].

Straight edge dislocations are introduced on the mid-plane normal to the z axis by moving atoms/nodes inside the green lines in Fig. 6.1 by $\mathbf{b} = (a_0/2)[110]$, followed by energy minimization. Subsequently, a homogeneous shear stress τ_{zy} is applied, with atoms adjacent to the holes constrained within the x-y plane to exclude dislocation climb and cross-slip of screw segments which do not accompany the dislocation bow-out under consideration here. It is emphasized that in the initial configuration, no dislocation segments pre-exist beyond the leftmost and rightmost holes, unlike those for dislocation/obstacle interactions where an infinitely long dislocation and an infinite array of obstacles are introduced [176, 184]. The model employed in this chapter is specifically designed to study the effects of adjacent bowed-out segments on a given dislocation bow-out, as well as whether, in terms of such effects, an increasing, finite number of obstacles would converge to an infinite number of obstacles.

A successful modeling technique for this problem needs to reasonably accurately predict (i) stress fields of dislocations, (ii) dislocation dissociation, (iii) Peierls stress, (iv) dislocation core energy, (v) image forces on dislocations at a hole surface, (vi) stress concentration around the hole, (vii) surface energy of a hole, and (viii) elastic anisotropy of crystals. For CAC, items (i–iv) have been evaluated in Chap. 3; the values of (v) and (vii) are given error-free because the regions adjacent to holes have an atomistic resolution in the CAC model; item (viii) is naturally incorporated because the element boundaries in the coarse-grained domain are assumed to correspond to actual atomic sites; quantity (vi), which reduces the critical shear stress for dislocation bow-out [61], is captured correctly, as will be shown in Fig. 7.2, indicating that CAC not only gives an accurate description of the stresses

around the holes, but also ensures continuous stress fields across the atomistic/coarse-grained domain interface. These results suggest that (i) the CAC approach is an enabling method to simulate the process of a dislocation segment bowing-out from obstacles and (ii) CAC is useful in informing the structure of constitutive models at even higher scales, e.g., PFM and CPFEM.

6.3 Results and discussion

The image stresses acting on the bow-out from all traction free cell boundaries can be estimated by assuming that all image dislocations are straight [251]. Consequently, the image stresses arising from the surfaces normal to the x axis are zero according to Brown's formula [35]. The effective images stress $\tau_{\text{img,eff}}$ from the 2D image dislocation array along both the y and z directions are [251]:

$$\tau_{\text{img,eff}} = -\frac{4\mu b H}{45 L_y^2 L_z^2} \cdot \left[L_y^2 A(\bar{L}) + L_z^2 B(\bar{L}) \right] \tag{6.1}$$

$$A(\bar{L}) = \frac{2}{\pi(1-\nu)} \int_0^\infty \frac{n^3 \tanh^2(n) \sin\left[(2N_{\text{img}}+1)(n\bar{L})\right]}{[n - \cosh(n)\sinh(n)]\sin(n\bar{L})} \, \mathrm{d}n \tag{6.2}$$

$$B(\bar{L}) = \frac{\pi}{1-\nu} \left[\sum_{n=1}^{\infty} (-1)^n \operatorname{csch}^2\left(\frac{n\pi}{\bar{L}}\right) \left(1 - \frac{2n\pi}{\bar{L}} \coth\left(\frac{n\pi}{\bar{L}}\right)\right) - \frac{1}{6} \right] \tag{6.3}$$

where $N_{\text{img}} = 25$; L_y and L_z are the length of the simulation cell along the y and z axes, respectively; $\bar{L} = L_y/L_z = 6.5345$. Substituting the values of μ, b, ν, L_y, L_z, and H at the critical configuration for the largest L into Eqs. 6.1–6.3 yields $\tau_{\text{img,eff}}$. Note that (i) this net image shear stress promotes dislocation bow-out and (ii) the actual image stress in the CAC model is smaller than $\tau_{\text{img,eff}}$ because the three equations above assume PBCs, resulting in an infinite array of dislocations of the same Burgers vector along the y direction; on the other hand, the traction free boundaries of the CAC simulation cell lead to an infinite array of dislocations of alternating Burgers vector along the y direction, hence reducing the net image stress.

As mentioned earlier, atoms adjacent to the holes are constrained within the x-y plane in CAC simulations to exclude dislocation climb and cross-slip. To examine if the constraints influence the critical shear stress, quasistatic CAC simulations are first performed without constraining any atoms adjacent to the holes. It is found that the screw components of the

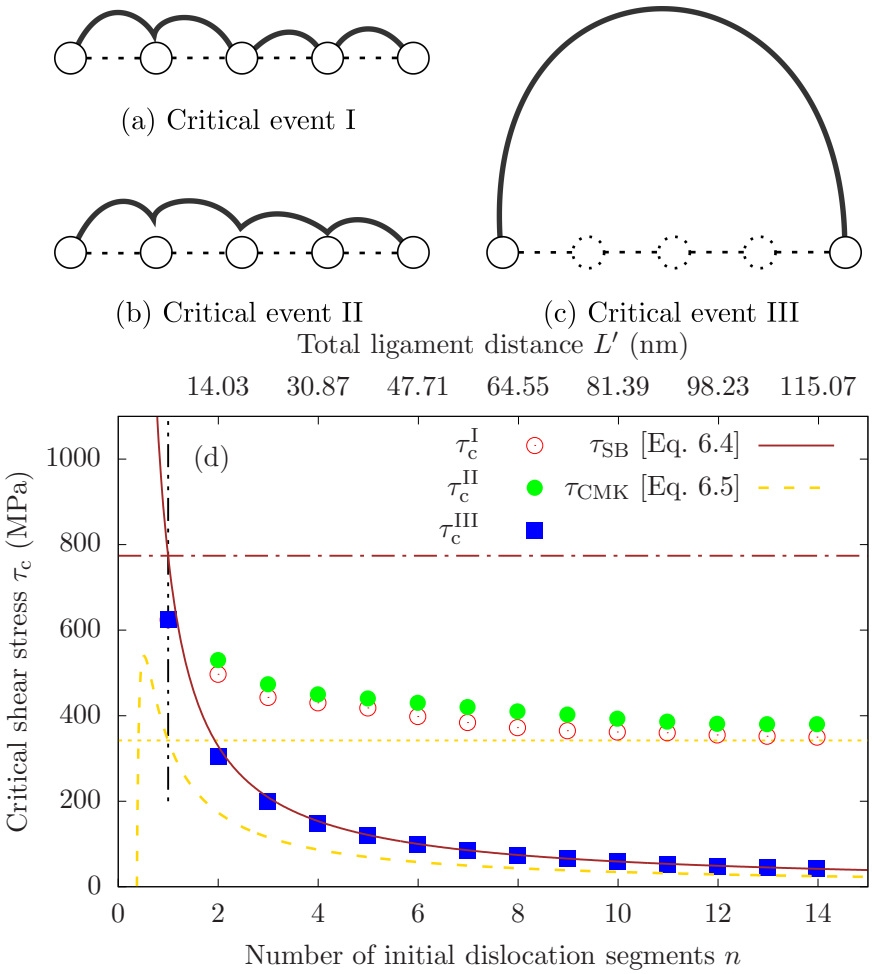

Figure 6.2: (a–c) Dislocation configurations at the three critical events studied in this chapter; (d) shear stresses τ_c calculated in CAC simulations for three critical events, with respect to the number of initial dislocation segments n. Critical shear stresses for one dislocation segment with length L' predicted by continuum models Eqs. 6.4 and 6.5 are also shown. The horizontal dash-dot and dotted lines are the critical shear stresses predicted by Eqs. 6.4 and 6.5, respectively, for $L' = 5.61$ nm [302].

bowed-out dislocation cross slip in energy minimization because the resolved shear stress is large enough for the athermal limit of cross-slip to be approached. The same phenomenon was also reported in MD simulations [108, 235]. As a result, the critical stress is increased by about 15%, compared with the case without cross-slip. Unlike in MD, dislocation climb is not observed as it usually involves atomic diffusion which cannot occur at 0 K. Thus, it is noted that while the constraints might influence the critical stress, one may not be able to obtain meaningful results without them because such simulations do not satisfy the classical assumption regarding Orowan bypass made in most continuum models. As the constraints

are only applied on atoms near the holes, they do not affect coarse-graining error in any way.

To obtain the critical shear stress and critical dislocation configuration, quasistatic CAC simulations are conducted at 0 K with a constant increment of applied shear stress $\Delta\tau_{zy} =$ 1 MPa, until the minimum stress for any of the critical events defined below is reached [182]. Two critical events are considered: (I) any dislocation is about to be detached from any hole surface (Fig. 6.2(a), at τ_{zy}^{I}) and (II) all dislocations are about to be detached from all but the leftmost and rightmost holes (Fig. 6.2(b), at τ_{zy}^{II}). Clearly, $\tau_{zy}^{\mathrm{I}} < \tau_{zy}^{\mathrm{II}}$. In simulations containing only one dislocation segment of length L', as shown in Fig. 6.1(b), a critical event III is considered for which the bowed-out dislocation segment pinned on two holes continues growing until reaching the unstable overall semi-elliptic configuration (Fig. 6.2(c), at τ_{zy}^{III}). For each critical event, similar to the Peierls stress calculation in Sec. 4.5, the stress $\tau_{\mathrm{c}}^{k} = \tau_{zy}^{k} - \Delta\tau_{zy}$ ($k = \mathrm{I}, \mathrm{II}, \mathrm{or\ III}$) is taken as the critical shear stress [243] and the segment shape at the end of an energy minimization subject to τ_{c}^{k} is recorded as the critical dislocation configuration [61]. In particular for the critical event III, in the case of $n = 1$, it is found that (i) as each element has a larger number of atoms, $\tau_{\mathrm{c}}^{\mathrm{III}}$ becomes smaller and (ii) the relative coarse-graining error of $\tau_{\mathrm{c}}^{\mathrm{III}}$ for 2197 atoms per element is approximately 9.5%, with respect to the fully resolved atomistic simulation, as will be shown in Fig. 7.6(b).

Shear stresses τ_{c} calculated in CAC simulations for critical events I and II are plotted in Fig. 6.2(d) with respect to the number of initial dislocation segments n. The calculated critical stresses $\tau_{\mathrm{c}}^{\mathrm{III}}$ for an isolated dislocation segment with length L' to reach the unstable semi-elliptic shape is also shown, where L' is determined by n which is taken as the bottom axis. Also given in Fig. 6.2(d) are the Scattergood-Bacon (SB) [220] and Crone-Munday-Knap (CMK) [61] continuum models for dislocation/obstacle interactions, i.e.,

$$\tau_{\mathrm{SB}} = \frac{A\mu b}{2\pi L'}\left[\ln\left(\frac{\bar{D}}{r_0}\right) + B\right] \tag{6.4}$$

$$\tau_{\mathrm{CMK}} = \frac{A\mu b}{2\pi(L' + D/2)}\ln\left(\frac{\bar{D}}{r_0}\right) \tag{6.5}$$

where μ is the isotropic shear modulus and the dislocation core radius $r_0 = b$. For edge dislocations, $A = 1$; let the obstacles be precipitates or voids, $B = 0.7$ and 1.52, respectively

[220]. Note that (i) Eq. 6.5 is proposed based on DD by accurately accounting for the image forces on the dislocation due to the void's free surface and (ii) both continuum models assume an infinite row of uniformly spaced obstacles with a ligament distance of L' between two neighboring obstacles; in other words, the number of initial dislocation segments $n \to \infty$.

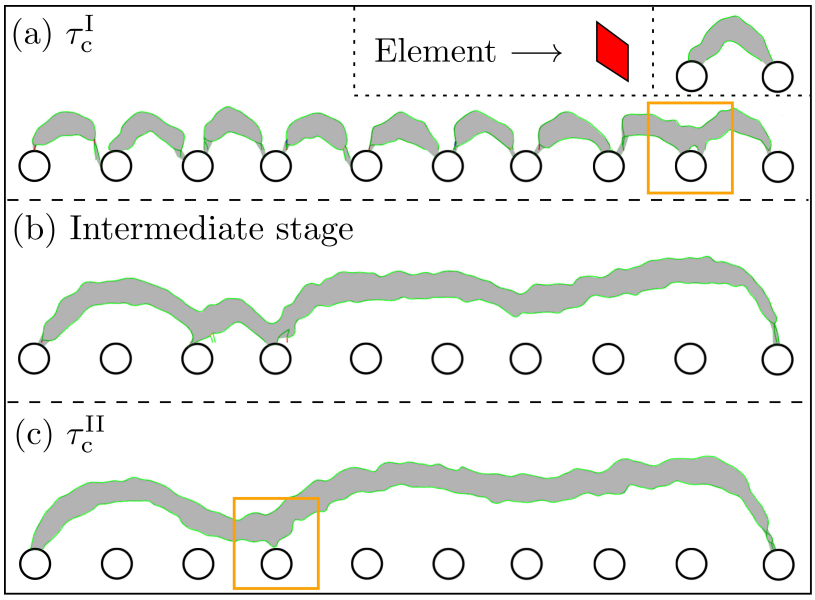

Figure 6.3: Snapshots of dislocation configurations at the critical events I and II, as well as an intermediate stage. The green curves represent Shockley partial dislocations identified by a DXA [247]; the gray ribbons are intrinsic stacking faults. In (a) and (c), dislocations are about to be detached from the holes marked by the solid brown lines. The critical dislocation configuration for an isolated pair of holes distanced by $L'(= L)$ at τ_c^{III} is given at the top right corner of (a). The kinks along dislocations have a size on the order of that of an element, which is illustrated as a red parallelogram [302].

For an isolated pair of holes distanced by $L'(= L)$, namely, $n = 1$, the critical shear stress τ_c^{III} lies between the predictions of Eqs. 6.4 and 6.5. As n increases, both τ_c^{I} and τ_c^{II} decrease; for each $n > 1$ (equivalently, $L' > 5.61$ nm), there is $\tau_c^{\mathrm{II}} > \tau_c^{\mathrm{I}} > \tau_c^{\mathrm{III}}$. This suggests that as long as dislocations are detached from all holes except the leftmost and rightmost ones (i.e., corresponding to the critical event II), they can always grow beyond the unstable semi-elliptic configuration. For the largest n of 14, τ_c^{I} and τ_c^{II} are 356 MPa and 382 MPa, respectively. Note that the relative errors arising from the image stresses are $42/356 = 11.8\%$ and $42/382 = 10.99\%$, respectively. On the other hand, for the same

interhole ligament distance $L'(=L)$, the CMK model Eq. 6.5 (which assumes $n \to \infty$) gives $\tau_{\text{CMK}} = 342$ MPa marked by the horizontal dotted line in Fig. 6.2(d). The convergence of $\tau_{\text{c}}^{\text{I}}$ and $\tau_{\text{c}}^{\text{II}}$ to τ_{CMK} for a larger n shows that an increasing number of obstacles indeed approaches an infinite array of equally spaced obstacles, as assumed in the continuum models.

Direct comparisons between simulations and continuum models should be made carefully. For example, critical shear stresses $\tau_{\text{c}}^{\text{III}}$ calculated by MD simulations [235] are found to fit Eq. 6.4. In Ref. [235], however, (i) the periodic initial dislocation segments are not immediately adjacent to each other, (ii) PBCs are adopted in all directions, and (iii) the simulations are dynamical with inertial effects. All these issues potentially result in a higher critical stress compared with the quasistatic continuum models. On the other hand, Eq. 6.4 is known to overestimate the critical stress because of a number of significant simplifications in the model [61], which is also demonstrated in CAC simulations in that the critical stresses for an isolated pair of obstacles surprisingly agree with Eq. 6.4 which assumes an infinite array of obstacles. Thus, the agreement with MD simulations does not necessarily suggest the accuracy of Eq. 6.4. In this chapter, the above-mentioned issues in MD simulations [235] are circumvented by performing quasistatic CAC simulations using sufficiently large models.

Snapshots of dislocation configurations for the critical events I and II are shown in Fig. 6.3. Subject to the critical shear stress $\tau_{\text{c}}^{\text{I}}$, a dislocation segment is about to be detached from the 2^{nd} hole from the right in Fig. 6.3(a); its configuration is similar to an isolated pair of holes at $\tau_{\text{c}}^{\text{III}}$ (for $L' = L$). As the stress increases to $\tau_{\text{c}}^{\text{II}}$, the dislocation pinned at the leftmost and rightmost holes is about to be detached from the 4^{th} hole from the left in Fig. 6.3(c). By analyzing the intermediate configurations during energy minimization subject to $\tau_{\text{c}}^{\text{II}}$, it is found that dislocations are sequentially detached from holes in a random order, as shown in Fig. 6.3(b).

It is also interesting to explore whether the presence of the intermediate holes in the middle influences the dislocation behavior following the critical event II. To calculate $\tau_{\text{c}}^{\text{III}}$ in models with collinear obstacles, the applied shear stress is first reduced to 10 MPa from

τ_c^{II} after dislocations are detached from all intermediate holes; then an increment of shear stress $\Delta\tau_{zy} = 1$ MPa is added until the critical event III is observed. It is shown that the critical stresses are close to those in the case of an isolated pair of holes distanced by L', which may reflect that the intermediate holes do not exert long range stress fields.

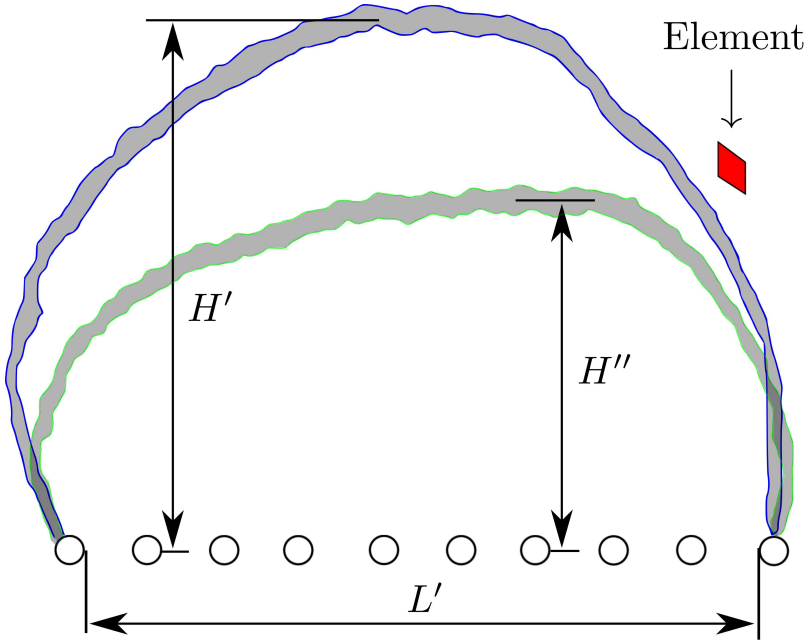

Figure 6.4: Snapshots of dislocation configurations at the critical event III in the case of 9 adjacent initial dislocation segments (leading and trailing Shockley partials are shown in green) and the case of 1 isolated initial segment with length L' (both partials are in blue). Dislocations and stacking faults are identified in the same way as in Fig. 6.3. The dislocation half-loop heights H' and H'' are about $0.75L'$ and $0.5L'$, respectively [302].

The dislocation configurations at τ_c^{III}, however, are affected by the presence of the intermediate holes, as shown in Fig. 6.4. The ratio of height (H'' or H') to length L' of the dislocation half-loop is about 0.5 and 0.75, with and without the intermediate holes, respectively. The decrease in the dislocation half-loop height is larger for a larger n. In all cases, the coarse-grained domain in CAC retains one key signature of the bowed-out dislocation that the edge components have a larger stacking fault width than the screw components. The segments are nearly semi-elliptic in shape since a screw component is formed to lower the elastic energy [91, 104]. Moreover, because of the elastic anisotropy of the Shockley partial dislocations, the dislocation half-loop is asymmetric with respect to the y axis [113]. Note that the kinks along dislocations have a size on the order of that

of an element, which is illustrated as a red parallelogram in Fig. 6.4. Clearly, element discretization is a source of coarse-graining error in the dislocation line energy.

6.4 Summary

In this chapter, quasistatic CAC simulations are performed to explore the critical shear stress and critical dislocation configuration in the process of edge dislocations bow-out from a row of collinear, uniformly spaced cylindrical holes in FCC Al. It is demonstrated that (i) CAC simulations can explore cooperative dislocations bowing-out in sufficiently large models at the submicron scale, (ii) as the number of adjacent bowed-out segments increases, the critical shear stress for dislocation depinning approaches that for an infinite array of collinear obstacles, and (iii) for the unstable semi-elliptic dislocation configuration, the presence of intermediate obstacles does not influence the critical shear stress, but reduces the dislocation half-loop height.

CHAPTER VII

DISLOCATION MULTIPLICATION FROM FRANK-READ SOURCES IN CU, NI, AND AL

7.1 Introduction

Plastic deformation typically increases the dislocation content of a crystal, a process termed dislocation multiplication [279]. Among many possible mechanisms such as Bardeen-Herring climb source and multiple cross glide mechanism, the FR source and spiral pole sources [257] are usually considered two of the most important in generating dislocations in the bulk of a crystalline material [110]. In a polycrystalline FCC metal, an FR source can produce a series of dislocations on one slip plane, which may then pile up against a GB and manifest grain size-dependent metal plasticity [200]. As more dislocations are generated from the FR sources, size-scaling hardening is exhibited due to an increasing back stress [250]. In Stage I work hardening, the scarcity of interfering dislocations allows operation of multiple FR sources, which is responsible for a majority of the rise in dislocation density, especially at low temperatures in the absence of dislocation climb [134]. Compared with other dislocation sources such as homogeneous nucleation or dislocations injected from GBs and precipitates, FR sources have a larger characteristic length and a lower critical shear stress to activate [235]. At strain rates greater than 10^8 s^{-1}, however, the strength of FR sources no longer controls the yield point of a crystalline metal because they are unable to operate before homogeneous dislocation nucleation relaxes elastic stresses [104]. FR sources are suppressed in Stage II work hardening because dislocations on multiple slip systems interact with each other, reduce the mean free path of dislocations, and shut down the sources. Also note that the dislocation pile-up do not account for size effects in body-centered cubic (BCC), hexagonal close-packed (HCP), or other crystals [1].

The operation of an FR source is a complex process. Take the case when voids are pinning obstacles as an example. Initially, a straight dislocation line is pinned between

two voids; then, subject to a shear stress, the segment begins to bow out until the critical configuration is reached, as shown in Fig. 7.1(a–c). Note that both ends of the dislocation move around the void periphery. If the applied shear stress is larger than the critical shear stress, the bowed-out dislocation will continue to grow until two parts of the "kidney shaped" segments collide to form a dislocation loop, leaving behind a new, straight dislocation line pinned between two voids, as shown in Fig. 7.1(d–e).

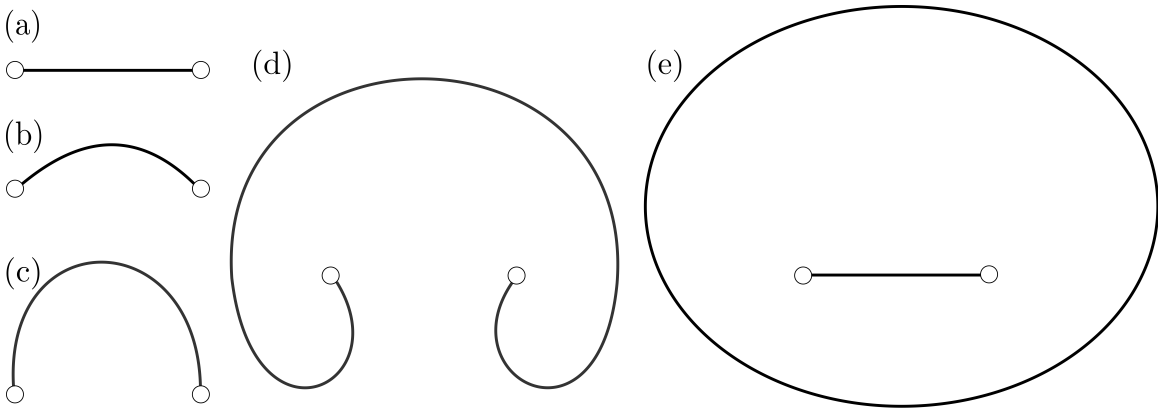

Figure 7.1: Illustrations of the FR source process. (a) A straight dislocation line is pinned between two voids. (b) The dislocation begins to bow out subject to a shear stress applied on the gliding plane. (c) The dislocation reaches its critical semi-elliptic shape. (d) If the applied stress is larger than the critical shear stress, the dislocation will pass the critical point and continue bowing-out. (e) Two parts of the "kidney shaped" bowed out segments collide to form a dislocation loop, leaving behind a new, straight dislocation line pinned between two voids. Note that both ends of the dislocation move around the void periphery [301].

Prior to the discovery of the FR source [93], the problem of a dislocation bypass of an array of obstacles was studied using line tension [178]. The line tension for paired obstacle bypass, introduced by Orowan [164] to balance the glide force on a curved dislocation, is considered a parameter of the configurational force on an entire dislocation line segment [110], and is given by

$$\tau_{\mathrm{OR}} = \frac{\mu b}{L} \tag{7.1}$$

where μ is the isotropic shear modulus, b is the Burgers vector of a full dislocation, and L is the distance between two non-shearable obstacles. Taking into account the elastic interactions between different segments [11], the bowing of a dislocation segment was studied directly using self-stress by Brown [34]. Foreman [91] discretized curved dislocations into

short straight segments and considered the self-stress at each node; the critical stress for dislocation bow-out from a pointlike FR source is expressed as

$$\tau_{\mathrm{FO}} = \frac{A\mu b}{2\pi L}\left[\ln\left(\frac{L}{r_0}\right) + B\right] \tag{7.2}$$

where A and B are parameters, r_0 is the full dislocation core radius. Elastic theory predicts that $A = 1$ and $A = 1/(1-\nu)$ for edge and screw dislocations, respectively, where ν is the isotropic Poisson's ratio; B, which is difficult to estimate using the line tension model, is associated with the dislocation core field [303]. Note that for curved or finite dislocation segments, r_0 sometimes refers to the cut-off radius for dislocation/dislocation interactions. In this chapter, this cut-off radius is assumed to equal the core radius as they both correlate positively with the dislocation core energy.

Bacon et al. [12] and Scattergood and Bacon [220] addressed another problem of a dislocation bypassing a periodic array of finite size obstacles and calculated its critical stress by Eq. 6.4. Free surfaces at voids are accounted for in this model, compared with previous models with pointlike obstacles; for precipitates, dislocations are not allowed to move around the obstacle periphery. At present, Eq. 6.4 is among the most widely used models for a dislocation bypass of periodic obstacles; it is sometimes employed to approximate the self-force on a dislocation segment exerted on itself [321].

All these models assume that dislocations move at an infinitesimal speed [96]. At strain rates beyond 10^6 s^{-1}, the static continuum theories need to be modified to include inertia effects on the motion of dislocations whose speed exceeds the domain of validity of the linear viscous drag law [27]. Another major assumption is that dislocations bypass of obstacles following the Orowan bypass mechanism [94], i.e., a dislocation bows out greatly to leave a loop on the same slip plane around the impenetrable obstacle. As a result, these models are applicable to the process of a dislocation bowing-out from an FR source. Models based on other mechanisms, e.g., Hirsch bypass mechanism [107] and shearing mechanism [114], however, do not fit the FR source process and may yield incorrect critical stresses. These two assumptions stated above are enforced in the CAC simulations in this chapter to make the results comparable to the continuum models.

The early work based on dislocation self-stress can be considered as precursors of modern superposition-based DD [268]. Comparing the Foreman model (Eq. 7.2) with DD simulations, Gómez-García et al. [97] found that $r_0 = 2b$ and $B \approx 1$ for an FR source without side arms in a model crystal; Huang et al. [113] derived $r_0 = 1.5b$ for edge FR sources in FCC Ag by introducing dislocation dissociation and a back force between two partial dislocations; Shishvan et al. [236] and Gurrutxaga-Lerma et al. [104] obtained $B = 0.5$ and -3.4 for FCC Cu and Al, respectively, for edge FR sources. In most DD simulations, the elastic fields of dislocations are time-independent, and so the results are comparable to the elastostatic continuum models. Effects of strain rates up to 10^{10} s^{-1} are explored in some DD studies [104] but will not be discussed in this dissertation.

It is emphasized that special treatments are necessary in DD to remove the singularities of stress fields and elastic energy at dislocation core center [40]. Although the DD method can be informed atomistically [142, 165], a dislocation in a crystal is intrinsically discrete and atomistic in character; its dynamics is governed by a classical physics which may not be reducible to continuum theory [58]. Szajewski et al. [252] found that even after fitting parameters to match the atomistic line tension, the standard DD technique still cannot match the atomistic configurations for the screw FR source. Thus, atomistic simulations are desirable in capturing the nonlinear dislocation core field [156], compared to continuum approaches such as DD, PFM [24], and level set method [286]. In the last decade, a number of MD simulations were performed to explore a dislocation bowing-out from an FR source [66, 148, 235]. In these calculations, periodic array of dislocations (PAD) models are usually employed to impose an infinite array of obstacles and an infinitely long dislocation, where the simulation supercell has a limited size [13]. Accompanied by non-negligible spurious image forces up to half of the true applied force, the PAD models overestimate the critical shear stress of an FR source [251]. Thus, an ideal simulation of the FR source process needs to accurately capture both the core effect at the nano-scale and the long range stress fields of the dislocation loop at the submicron-scale, using a sufficiently large model free of image forces. Recently, an attempt has been made to explore the dislocation bow-out configuration via an image-free multiscale simulation using the CADD method [252].

Nevertheless, a systematic study of multiple aspects of the FR sources in different metals is still lacking, to the best of the author's knowledge.

In this chapter, both dynamic and quasistatic CAC simulations are performed to investigate the process of an edge dislocation bowing-out from an FR source. Focus will be on the dislocation nucleation/loop formation time, critical shear stress, and critical dislocation configuration — three key characteristics of the FR source process that can be used as a set of constitutive rules in DD simulations [23]. Three FCC metals, Cu, Ni, and Al will be studied because of their different SFE and elastic anisotropy index [200]. From the methodological viewpoint, it will be shown that CAC is able to simulate 3D dislocation loop generation from an FR source, a benchmark problem for multiscale simulations and one of the building blocks for more complicated 3D dislocation substructure evolution [44]. Moreover, the fact that the FR source process involves both elastic interactions between dislocations as well as atomistic details makes it a good "test problem" to validate the CAC method by comparing the results with those predicted by continuum models.

7.2 Methodology

The simulation cell containing a pair of cylindrical holes extruding through the specimen along the z direction is shown in Fig. 7.2(a), similar to that shown in Fig. 6.1(b). Full atomistic resolution is applied in the vicinity of holes such that the hole surface is more than 2 nm from the atomistic/coarse-grained interface. Away from the holes, rhombohedral elements are employed in the coarse-grained domain. Unless indicated otherwise, a uniform element size of 2197 atoms solved by first order Gaussian quadrature is employed to achieve a balance between high accuracy and high efficiency [303], as discussed in Chap. 3; in DD simulations, elements sized on the order of b are required for the FR process to achieve converged results [61]. The lattice orientations are $x[\bar{1}1\bar{2}]$, $y[110]$, and $z[1\bar{1}\bar{1}]$. All cell boundaries are assumed traction free to alleviate spurious image stresses, which were evaluated quantitatively in Sec. 6.3. The model size for three materials differs only by their lattice parameter a_0, which is 3.615 Å for Cu, 3.52 Å for Ni, and 4.05 Å for Al. For Cu, the simulation cell has a size of 268.3 nm by 265.3 nm by 40.6 nm; in all simulations, the

hole diameter on the x-y plane $D = 2.51$ nm, while the ligament distance between holes L varies from 5.01 nm to 102.68 nm, a range comparable to precipitate spacings in many alloys [214, 224, 252]. As a result, with the smallest L, the model has 108,163 elements and 1,200,322 atoms, with 2,065,626 DOFs in total compared with otherwise 238,834,433 in an equivalent full atomistic model.

A straight edge dislocation with length L is introduced on the mid plane normal to the z axis by moving atoms/nodes inside the solid green lines by Burgers vector $\mathbf{b} = (a_0/2)[110]$, as illustrated in Fig. 7.2(a), followed by energy minimization. This is equivalent to introducing an extra plane of atoms between the two holes on the x-z plane without moving any atoms/nodes. In this way, only one dislocation segment is created and pinned between two cylindrical holes without side arms. Once the equilibrium atomic configuration of the FR source is achieved, a homogeneous shear stress τ_{zy} is applied — note that a symmetric stress favors the Orowan mechanism over the Hirsch mechanism [107]. To exclude dislocation cross-slip near the hole surface [108] which does not accompany the classical FR process, atoms adjacent to the holes are constrained within the x-y plane, the effect of which has been discussed in Sec. 6.3.

To show that this model can indeed describe the FR source process illustrated in Fig. 7.1, a dynamic CAC simulation of the FR source process is performed at 10 K with time step of 2 fs for Ni. In each run, a constant applied shear stress 1.4 GPa is maintained using a PR barostat [186], resulting in a slightly increasing shear strain due to an increasing plastic shear strain caused by dislocation multiplication. The dislocation "nucleation time" t_{nuc} is defined as the waiting time for a dislocation segment to reach its critical configuration [21]; the loop formation time t_{loop} is defined as the time for the occurrence of a collision of two parts of the "kidney shaped" bowed out dislocation segments [236]. Note that in dynamic CAC with an fs-scale time step, the values of t_{nuc} and t_{loop} are not directly comparable with those of elastostatic predictions [109], yet their ratio $t_{\text{loop}}/t_{\text{nuc}}$ should not be much different from the continuum estimation.

In the literature, there exists at least three methods to calculate the critical shear stress for dislocation bow-out, which is difficult to obtain [322, 323]. In some DD simulations

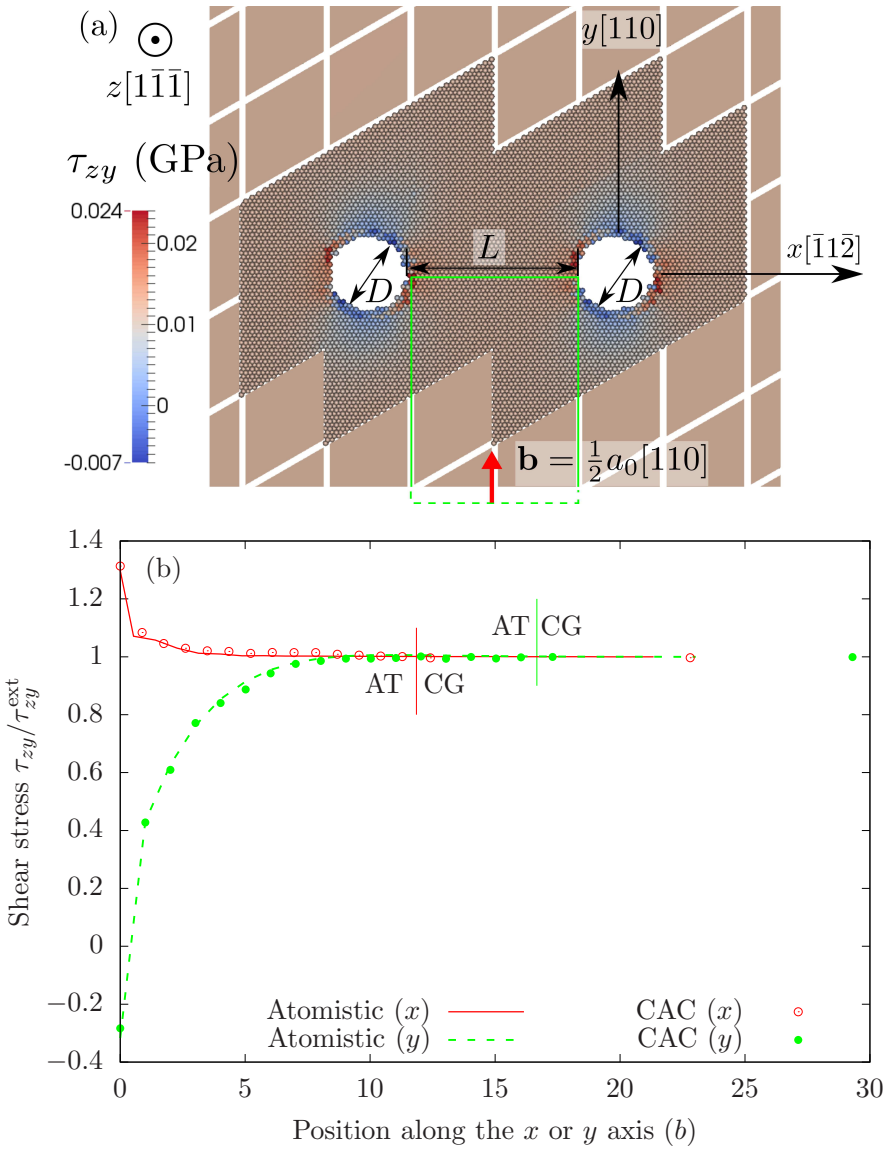

Figure 7.2: (a) CAC simulation cell of an edge dislocation bowing-out between a pair of cylindrical holes throughout the specimen along the z direction introduced as an FR source. An atomistic (AT) domain is meshed in the vicinity of the holes, while the coarse-grained (CG) domain is employed elsewhere. An external shear stress of 11.36 MPa is applied; atoms/elements are colored by shear stress τ_{zy}. All cell boundaries are assumed traction free to alleviate spurious image effects. The edge dislocation is formed by moving atoms/nodes inside the solid green lines by Burgers vector $\mathbf{b}$. (b) The ratio of τ_{zy} relative to the far field external loading $\tau_{zy}^{\text{ext}} = 11.36$ MPa as a function of the distance from the hole surface along the x and y directions labelled in (a). Stress concentrations around holes are captured correctly in CAC, compared with an equivalent full atomistic model of the same size [301].

[104, 236], different levels of shear stress are attempted and kept constant in each run; the minimum stress that bows out a dislocation is termed the critical shear stress. In some MD simulations [235], the strain is incrementally increased from zero; the critical stress is taken corresponding to the critical dislocation configuration. For dislocation/obstacle interactions, the maximum stress of the stress-strain curve is considered the depinning stress [14, 142]. In this chapter, the same method in Chap. 6 is employed, i.e., quasistatic simulations with an increment of shear stress $\Delta\tau_{zy} = 1$ MPa are conducted. Let the minimum stress to form the dislocation loop be τ''_{zy}, the critical shear stress for the FR source $\tau_{\mathrm{CAC}} = \tau''_{zy} - \Delta\tau_{zy}/2$. The dislocation bow-out segment at the end of an energy minimization subject to a stress of $(\tau''_{zy} - \Delta\tau_{zy})$ is recorded as the critical configuration, similar to the method used by Crone et al. [61]. The quasistatic simulations ensure that the results are comparable with elastostatic continuum models.

7.3 Results and discussion

The image stresses from all cell boundaries, calculated by Eqs. 6.1–6.3, are presented in Tab. 7.1. For Cu, Ni, and Al, the critical shear stresses for the largest L are 0.044 GPa, 0.09 GPa, and 0.042 GPa, respectively. Thus, the relative errors arising from the effective image stresses are 0.00865/0.044 = 19.7%, 0.01478/0.09 = 16.4%, and 0.00553/0.042 = 13.2%, respectively. The image stresses are greatly reduced for smaller L and are not element size-dependent, i.e., they are not the source of the differences between CAC and fully-resolved atomistic simulations.

Table 7.1: The length of the simulation cell along the y and z axes L_y and L_z (in nm), dislocation half-loop height for the largest FR source length H (in nm), shear modulus μ (in GPa), magnitude of the Burgers vector of the full dislocation b (in nm), Poisson's ratio ν, and effective image stress $\tau_{\mathrm{img,eff}}$ (in GPa) calculated by Eqs. 6.1–6.3 [301].

	L_y	L_z	H	μ	b	ν	$\tau_{\mathrm{img,eff}}$
Cu	265.3	40.6	72.9	41.16	0.256	0.34	0.00865
Ni	258.33	39.53	69.99	74.67	0.249	0.31	0.01478
Al	297.22	45.49	78.22	28	0.286	0.33	0.00553

7.3.1 Frank-Read source process in dynamic CAC

As shown in Fig. 7.3 for Ni, the critical dislocation configuration is reached after 4 ps while the dislocation loop is formed at about 14 ps, resulting in $t_{\text{loop}}/t_{\text{nuc}} = 3.5$. In comparison, DD simulations [236] based on an elastostatic theory predict that $t_{\text{loop}}/t_{\text{nuc}} \approx 2.89$ and 2.92 for isotropic and anisotropic drag coefficients, respectively. MD simulations [235] with an incrementally increased applied strain give the ratio of about 1.11. If the dislocation velocity is assumed proportional to the applied stress which increases linearly prior to t_{loop}, t_{nuc} would be halved should a constant critical shear stress be applied; the ratio $t_{\text{loop}}/t_{\text{nuc}}$ would become about 2.21 in Ref. [235]. In dynamic CAC simulations, both t_{nuc} and t_{loop}

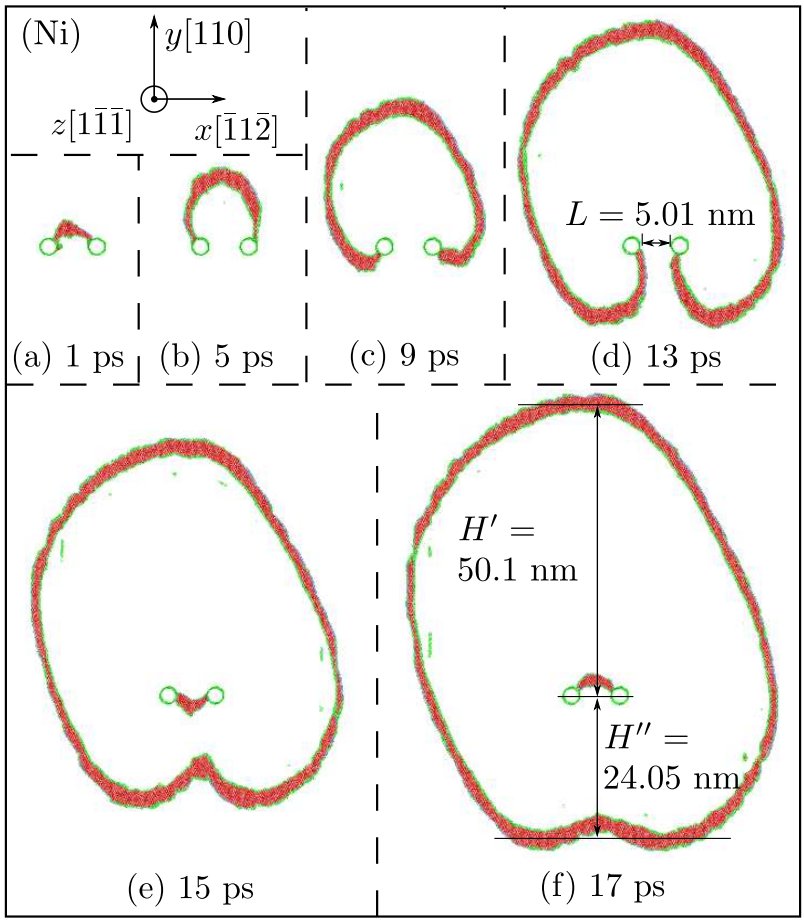

Figure 7.3: Snapshots of dislocation loop multiplication from the FR source in Ni subject to a constant applied shear stress of 1.4 GPa. Atoms are colored by a-CNA [246]: red are of HCP local structure, green are either hole surfaces or Shockley partial dislocations, and all FCC atoms are deleted. In (f), the distance between the top of the loop and holes (H') is about twice the distance between the bottom of the loop and holes (H'') [301].

display a nearly linear dependence on L for the same material, in agreement with the elastostatic Benzerga theory [21]. As a result, the ratio is almost invariant with respect to L: $t_{\text{loop}}/t_{\text{nuc}} = 3.7$, 3.5, and 3.4 for Cu, Ni, and Al, respectively. In Fig. 7.3(f), the distance between the top of the loop and the hole center (H') is about twice the distance between the bottom of the loop and the hole center (H'').

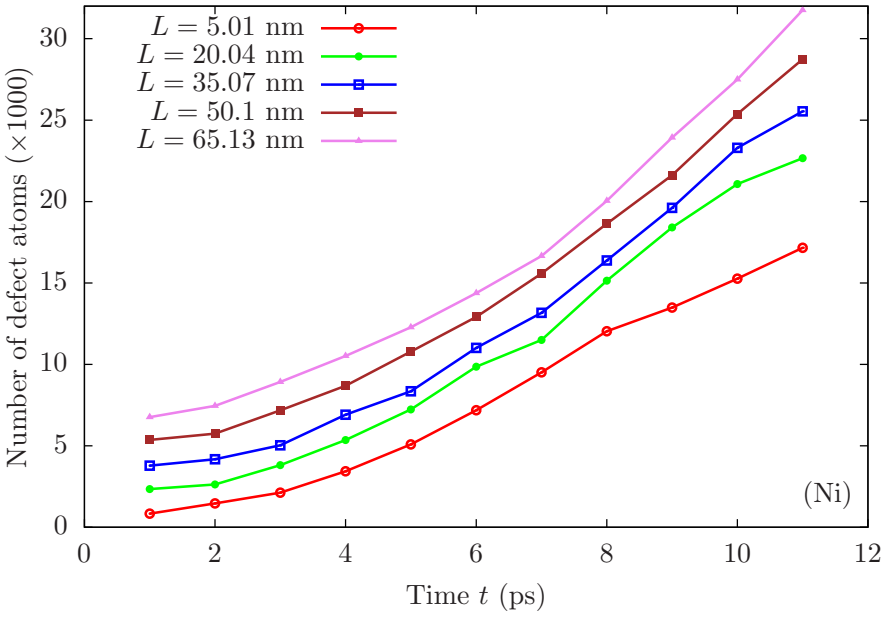

Figure 7.4: Evolution of the number of defect (i.e., non-FCC) atoms identified by a-CNA [246] with time for different FR source length L in Ni. While a larger L is accompanied by a larger number of defect atoms, the growth rate of the number of defect atoms is similar for different L. For $L = 5.01$ nm, the dislocation nucleation time $t_{\text{nuc}} = 4$ ps, while the loop formation time $t_{\text{loop}} = 14$ ps [301].

Shimokawa and Kitada [235] found that there exists a "dramatic change" of the number of defect atoms (i.e., non-FCC) atoms immediately following the critical dislocation configuration. In CAC simulations, the evolution of the number of defect atoms that are identified by a-CNA [246] is presented in Fig. 7.4. Interestingly, the "dramatic change" of the number of defect atoms is not observed, indicating that at a constant shear stress, the number of defect atoms cannot be used as an indicator of the onset of instability. More general indicators based on dislocation configuration, such as the activation volume and line tension, may be more appropriate in the present cases.

7.3.2 Critical shear stress calculated by quasistatic CAC

Equations 6.4, 6.5, and 7.2 contain only one adjustable parameter, namely, the full dislocation core radius r_0, which is introduced to avoid singularities in the stress field and elastic energy of a dislocation. The dislocation core energy E_{core} associated with r_0 is not explicitly included because it is assumed to be on the order of one-tenth of the total energy [91]. In estimating the line tension of a curved dislocation, E_{core} becomes non-negligible when $L < 120$ nm [252]. For the FR source, the neglect of E_{core} leads to an underestimation of the critical shear stress τ_{c}. A common practice is to deliberately use a small r_0 such that the total energy of a dislocation matches that in atomistic simulations [146]. However, the ambiguities caused by different choices of r_0 and E_{core} may affect the calculation of the dislocation energy [143, 156]. In some recent DD simulations, E_{core} was explicitly added to the elastic energy [165, 236], in which its estimation, beyond the scope of elasticity theory [12], is based on *ab initio* and atomistic calculations, with r_0 on the order of the Burgers vector of a full dislocation [41, 165].

Along this line of thought, Eq. 6.5 is modified by explicitly including E_{core}. First, according to the line tension model [114], i.e.,

$$\tau_{\text{c}} = \frac{T}{bR} = \frac{\alpha\mu b}{R} \tag{7.3}$$

where T is the line tension, R is the dislocation line radius, and α is a parameter. Comparing Eq. 7.3 to Eq. 6.5, one sees that

$$\alpha = \frac{A}{4\pi} \ln\left(\frac{\bar{D}}{r_0}\right) \tag{7.4}$$

$$R = \frac{L}{2} + \frac{D}{4}. \tag{7.5}$$

Then, the line tension T is augmented by the core energy E_{core}. For an edge FR source, Eq. 7.3 becomes

$$\tau_{\text{c}} = \frac{T + C_0(r_0; E_{\text{core}})}{bR} = \frac{\alpha\mu b^2 + C_0(r_0; E_{\text{core}})}{bR} \tag{7.6}$$

where, to a first order approximation [252], one assigns

$$C_0(r_0; E_{\text{core}}) = \frac{1-2\nu}{1-\nu} \cdot E_{\text{core}}(r_0). \tag{7.7}$$

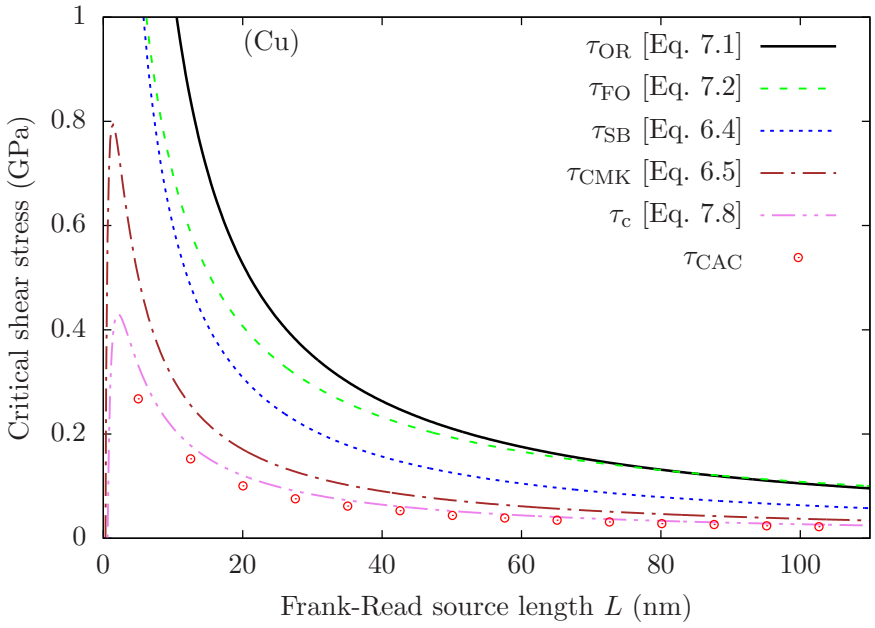

(a)

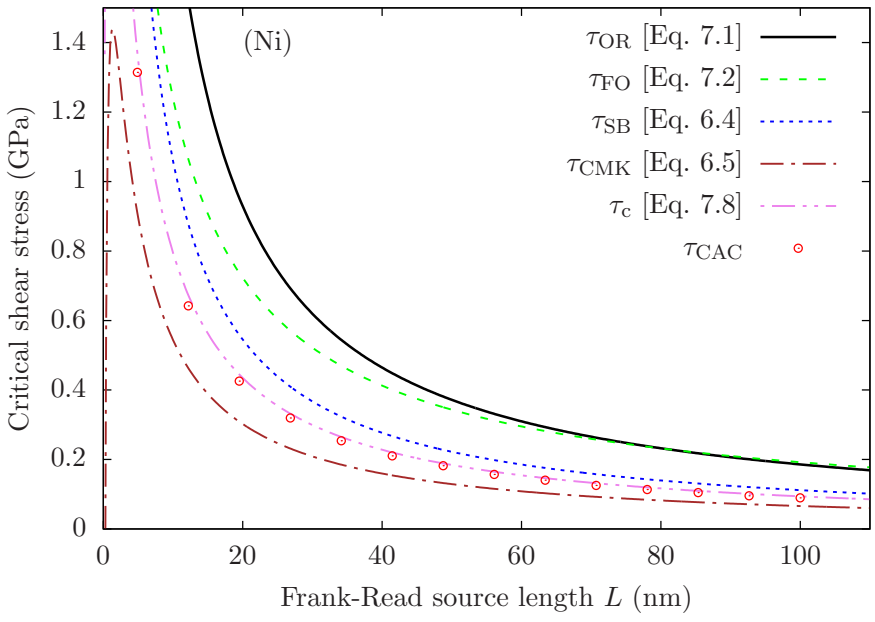

(b)

Figure 7.5: The critical shear stress predicted by continuum models and CAC simulations with respect to the FR source length in (a) Cu and (b) Ni [301].

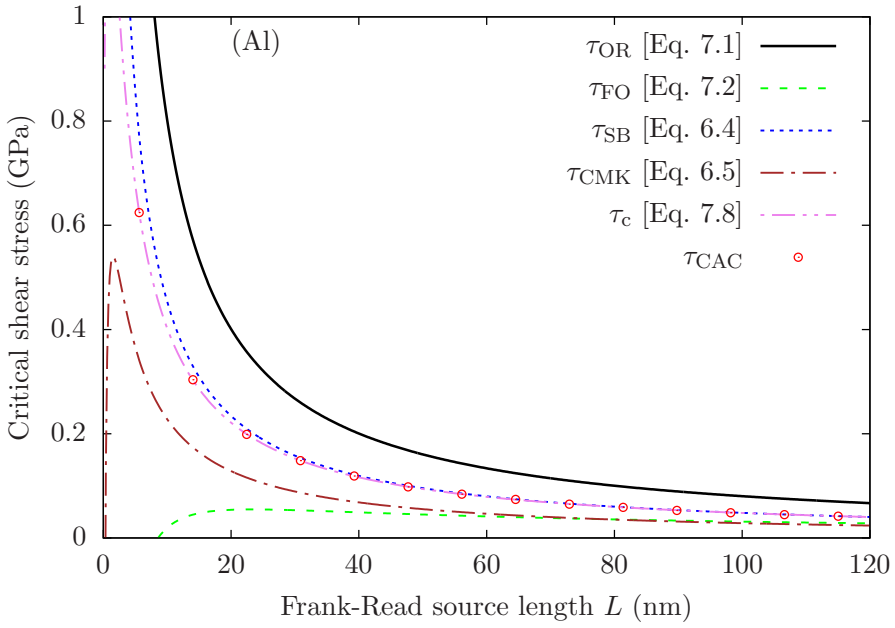

(a)

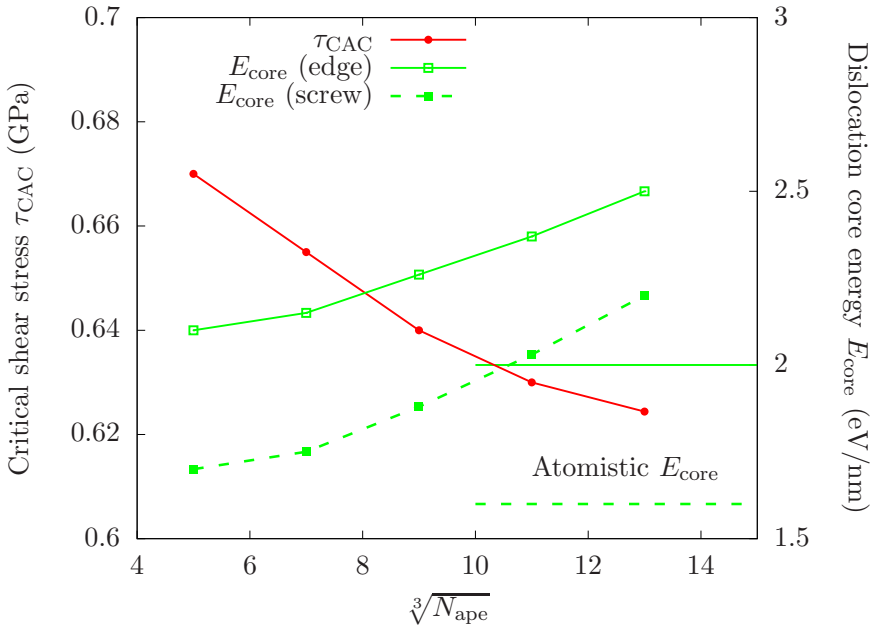

(b)

Figure 7.6: (a) The same plot as in Fig. 7.5, but for Al. (b) The critical shear stress τ_{CAC} and dislocation core energy E_{core} for both types of dislocation, as a function of the element size N_{ape} for Al in the case of $L = 5.61$ nm. Larger elements give a lower critical shear stress and higher dislocation core energy for both types of dislocation. In particular, E_{core} converges to the atomistics (horizontal lines) as each element has a smaller number of atoms N_{ape} [301].

Substituting Eqs. 7.4, 7.5, and 7.7 into Eq. 7.6 yields

$$\tau_{\mathrm{c}} = \frac{A\mu b}{2\pi(L + D/2)} \left[\ln\left(\frac{\bar{D}}{r_0}\right) + \frac{1-2\nu}{1-\nu} \cdot \frac{4\pi E_{\mathrm{core}}(r_0)}{\mu b^2} \right] \tag{7.8}$$

where the last term can be viewed as the material dependent parameter B in Eqs. 6.4 and 7.2.

Equations 6.4, 6.5, 7.1, 7.2, and 7.8 are represented in Figs. 7.5(a), 7.5(b), and 7.6(a) for Cu, Ni, and Al, respectively, as a function of the FR source length. In Eqs. 6.4, 6.5, and 7.2, the core radius $r_0 = b$, as in their original forms. In Eq. 7.8, r_0 and E_{core} are assumed invariant subject to the shear stresses applied in the present simulations. Also, because both core radius r_0 and energy E_{core} vary along the bowed-out dislocation with mixed characters [156], the line averages of their respective values for pure edge and pure screw dislocations in Tab. 4.1 are used. Similar to the drag coefficient in DD simulations [165], both r_0 and E_{core} are assumed to take a simple dislocation character-dependent form:

$$r_0(\theta) = r_0^{\mathrm{edge}} \sin^2\theta + r_0^{\mathrm{screw}} \cos^2\theta \tag{7.9}$$

$$E_{\mathrm{core}}(\theta) = E_{\mathrm{core}}^{\mathrm{edge}} \sin^2\theta + E_{\mathrm{core}}^{\mathrm{screw}} \cos^2\theta. \tag{7.10}$$

Here, θ is the dislocation character angle: $\theta = 0$ for pure screw and $\theta = \pi/2$ for pure edge. Assume a semi-circular shape of the critical configuration, which is the most relevant to the critical shear stress, the line average of r_0 is given by

$$\begin{aligned} r_0^{\mathrm{ave}} &= \frac{2}{\pi L} \int_0^{\frac{\pi L}{2}} r_0(\theta) \mathrm{d}\, l = \frac{4}{\pi L} \int_0^{\frac{\pi L}{4}} r_0(\theta) \mathrm{d}\, l = \frac{4}{\pi L} \int_0^{\frac{\pi}{2}} r_0(\theta) \cdot \frac{L}{2} \mathrm{d}\,\theta \\ &= \frac{2}{\pi} \int_0^{\frac{\pi}{2}} \left(r_0^{\mathrm{edge}} \sin^2\theta + r_0^{\mathrm{screw}} \cos^2\theta \right) \mathrm{d}\,\theta = \frac{1}{2} \left(r_0^{\mathrm{edge}} + r_0^{\mathrm{screw}} \right). \end{aligned} \tag{7.11}$$

Similarly,

$$E_{\mathrm{core}}^{\mathrm{ave}} = \frac{1}{2} \left(E_{\mathrm{core}}^{\mathrm{edge}} + E_{\mathrm{core}}^{\mathrm{screw}} \right). \tag{7.12}$$

Note that the line averages over character/orientation are approximation, which may yield less accurate results than direct DD simulations in which the dislocation core is a function of the character angle, as dictated by elasticity theory. Moreover, the values of r_0 and E_{core} are taken from the coarse-grained domain, in which the FR source mainly operates. Since both quantities vary with element size, as shown in Figs. 4.8(b) and 7.6(b),

the critical stress calculated by Eq. 7.8, τ_c, is also element size-dependent: larger elements result in a larger r_0, which decreases τ_c, and a larger E_{core}, which increases τ_c — the net effect is that a lower τ_c is yielded, in agreement with the CAC simulations for Al, as shown in Fig. 7.6(b). The combined effect of the element size-dependent r_0 and E_{core} also results in a less pronounced dependence of τ_c on the element size. It is found that the element size- and L-dependent coarse-graining error (i) is reduced for a larger L, suggesting that the precise value of E_{core} becomes less important as the FR source length increases, and (ii) increases for a smaller L, yet the majority of the dislocation half-loop would reside in the atomistic domain because the domains adjacent to the holes are modeled with full atomistic resolution. It should be emphasized that the form of Eq. 7.8, suggested by the coarse-grained simulations, is most relevant to informing higher scale continuum models such as CPFEM or certain DD models that involve constitutive equations for FR source generation [15, 69]. In such relations, *ab initio* and atomistic values of r_0 and E_{core} should be used.

For application purposes, the scaling of the critical stress with respect to the FR source length L is more important than the critical stress itself and can be used to obtain the dislocation core energy or line tension for a given material system. For all three materials, the critical stress calculated by the CAC simulations, τ_{CAC}, scales with L logarithmically, as predicted by the continuum models. In terms of the values of τ_{CAC} for a given L, however, only the critical stresses in Al agree well with Eq. 7.8. For Cu and Ni, τ_{CAC} are lower than the continuum predictions, which may be attributed to two simplifications in deriving the model. First, dislocations in Cu and Ni have pronounced dissociation due to a low SFE. As a result, the total energy of an extended dislocation, which is proportional to the total b^2, is smaller than an undissociated one [11]. It follows that the work that needs to be done by the external stress is reduced, a conclusion also reached by a recent DD simulation [113]. Second, all continuum models described above assume isotropic shear modulus and Poisson's ratio. On the other hand, the anisotropy of a crystal has been known to alter the relative energies/core radius of edge and screw dislocations [91], as well as the elastic strain around a dislocation which is important for dislocation/void interactions [109]. For a cubic system,

the elastic anisotropy index $A_{\text{cubic}} = 2c_{44}/(c_{11} - c_{12})$ [203], which gives 3.22, 2.53, and 1.21 for Cu, Ni, and Al, respectively, based on EAM potentials predicted elastic constants c. Fitzgerald [87] found that the critical shear stress for an FR source decreases with an increasing A_{cubic}. In other words, the isotropic models overestimate the bowing-out stress, especially for Cu which has the largest elastic anisotropy.

This dependence of model accuracy on materials was also reported for the SB model (Eq. 6.4). For Al, the SB model accurately predicts the critical shear stress of an FR source in comparison with MD simulations [235]. For Cu and Fe, however, Eq. 6.4 gives a higher depinning stress for dislocation/void interactions than MD [109, 142]. A common strategy in the literature is to vary the value of r_0. In Eq. 7.8, a core radius of $1.1r_0$ correctly reproduces the critical shear stress for Ni, while the value of E_{core} is taken at $1.1r_0$, as given in Sec. 4.4. For Cu, Scattergood and Bacon [220] found that when $r_0 = 3b$, τ_{SB} (Eq. 6.4) is in reasonable quantitative agreement with the experimentally measured value for a screw FR source; in Eq. 7.8, an agreement with CAC simulations is obtained when the core radius is $1.2r_0 = 4.974b$ for the edge FR source explored here.

Therefore, the significance of dislocation dissociation and elastic anisotropy suggests reconsideration of isotropic elastic models employed in continuum theory and DD simulations. Although methods have been developed to calculate the energy and force on a dislocation in an anisotropic elastic media [9], the author is not aware of any existing fully anisotropic continuum model for the FR source.

7.3.3 Critical dislocation configuration calculated by quasistatic CAC

The critical dislocation configuration corresponds to an extremum point in the dislocation total energy [236], the largest dislocation line tension [252], and the moment when the dislocation becomes tangent to the surface in the Orowan mechanism [61]. In CAC, snapshots of dislocations at the onset of instability are shown in Fig. 7.7 for Cu and Al. The segments are nearly semi-elliptic in shape with slight horizontal outward bowing near two holes, as a result of a dislocation inclining to have as large a screw component, which has a smaller

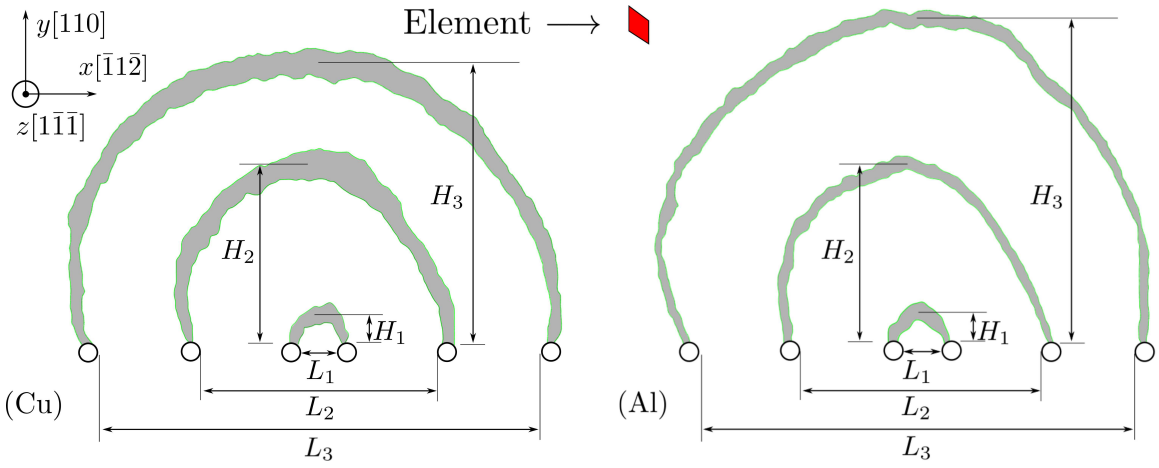

Figure 7.7: Snapshots of critical dislocation configurations for different FR source length L in Cu and Al. The green curves represent Shockley partial dislocations identified by a DXA [247]; the gray ribbons are intrinsic stacking faults. The kinks along dislocations have a size on the order of that of an element, which is illustrated as a red parallelogram. For Cu, $L_1 = 5.01$ nm with $H_1 = 0.7L_1$, $L_2 = 35.07$ nm with $H_2 = 0.77L_2$, and $L_3 = 65.13$ nm with $H_3 = 0.69L_3$. For Al, $L_1 = 5.61$ nm with $H_1 = 0.8L_1$, $L_2 = 39.29$ nm with $H_2 = 0.8L_2$, and $L_3 = 72.97$ nm with $H_3 = 0.75L_3$ [301].

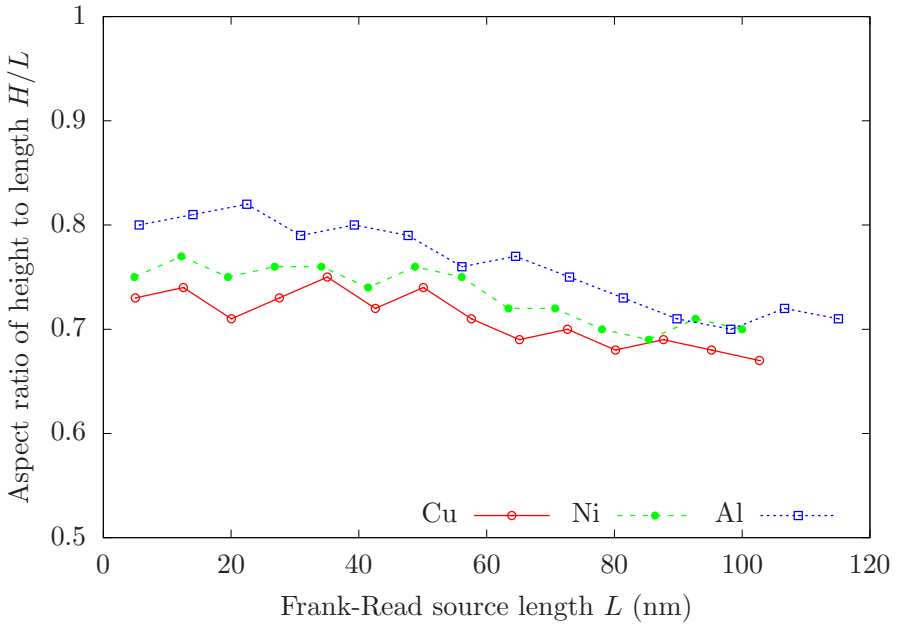

Figure 7.8: The aspect ratio of the dislocation half-loop height to the FR source length H/L, as a function of L. For the same L, the ratio for Cu is the smallest while that for Al is the largest. In general, the ratio H/L decreases with an increasing L [301].

elastic energy than the edge component, as possible [91, 104, 114]. In addition, the dislocation half-loop is asymmetric with respect to the y axis due to the anisotropic behavior of

the Shockley partial dislocations, which tend to adopt their screw orientations close to holes to reduce the total energy [73, 109, 113]. Note that an anisotropic elastic theory without dislocation dissociation still results in a symmetric shape [113]. In both materials, the edge components have a larger w_{SF} than the screw components. Compared with Al, the same dislocation component has a larger w_{SF} because of a smaller SFE in Cu. Note that the kinks along dislocations have a size on the order of that of an element, which is illustrated as a red parallelogram in Fig. 7.7.

The ratio of the dislocation half-loop height H to the FR source length L is plotted in Fig. 7.8 for three materials. Both the anisotropic elastic theory [73] and MD simulations [235] predict that $H/L = 1/(2-2\nu)$. DD simulations of a pointlike FR source using a uniform drag coefficient without dislocation dissociation give an H of $0.83L$ [11] or $0.75L$ [91], independent of L. In contrast, CAC simulations show that the aspect ratio H/L varies between 0.67 and 0.82 for different L. The general trend is that a larger L is accompanied by a smaller H/L, in agreement with a DD simulation with finite size FR sources [12] or pointlike FR sources with an anisotropic drag coefficient [11,104]. Compared with Ni and Al, the aspect ratio H/L is smaller in Cu in general, suggesting that a larger w_{SF} reduces H/L, a phenomenon also found by Huang et al. [113]. The difference of the critical dislocation configuration in different materials may also be attributed to the material anisotropy, which is found to greatly influence the equilibrium dislocation shape [86].

7.4 Summary

In this chapter, large scale dynamic and quasistatic CAC simulations are employed to calculate the dislocation nucleation/loop formation time, critical shear stress, and critical dislocation configuration, for the process of an edge dislocation segment bowing-out from a classical FR source associated with cylindrical holes as obstacles in Cu, Ni, and Al. Results are summarized as follows:

1. Dynamic CAC simulations find that both dislocation nucleation time and loop formation time grow linearly with the FR source length, in agreement with the elastostatic Benzerga theory. The ratio of the loop formation time to the dislocation nucleation

time for Cu is the largest while that for Al is the smallest. In addition, at a constant shear stress, the number of defect atoms cannot be used as an indicator of the onset of instability, in contrast to the case where the applied strain is incrementally increased.

2. It is found that the critical stresses calculated by quasistatic CAC simulations in all three metals scale with the FR source length in the same way as predicted by a continuum model that explicitly includes the dislocation core energy. The value of the critical stress for a given FR source length, however, only agrees well with the continuum model in Al, but not in Cu and Ni which have a stronger dislocation dissociation and a higher elastic anisotropy index. The element size-dependent critical stress in CAC is explored in which a larger element yields a lower FR source strength, in agreement with the continuum model. CAC simulations suggest reconsideration of isotropic elastic models without dislocation dissociation in deriving continuum theories for the FR source process.

3. Quasistatic CAC simulations show that the critical dislocation segments have an asymmetric semi-elliptic shape, as a result of both dislocation dissociation and material anisotropy. The ratio of the dislocation half-loop height to the FR source length decreases with an increasing FR source length. For the same FR source length, the largest ratio is obtained for Al while the smallest for Cu.

CHAPTER VIII

SEQUENTIAL SLIP TRANSFER OF CURVED MIXED CHARACTER DISLOCATIONS ACROSS A Σ3 COHERENT TWIN BOUNDARY IN CU AND AL

8.1 Introduction

GBs play a fundamental role in size-dependent mechanical properties of metals [110]. In polycrystalline metals subjected to an applied shear stress, a series of dislocations in a single pile-up move through a lattice in individual grains until encountering a GB [277,303]. In general, as more dislocations add to the end of the pile-up, the leading dislocation experiences a higher stress, which is eventually large enough for the tip of the pile-up to react with the GB, lowering the overall stress and allowing further deformation of the material if the dislocation is transmitted or absorbed and desorbed. As such, a larger grain accommodating a larger number of dislocations requires a lower applied stress to "yield" the GBs in a polycrystal, manifested as the Hall-Petch effect. Generally referred to as slip transfer processes, the interactions between a series of dislocations and GBs are the topic of this and the next chapter.

On the basis of experimental observations and previous work of Shen et al. [225,226], Lee et al. [140,141] formulated the Lee-Robertson-Birnbaum (LRB) slip transfer criteria which take into account geometry, resolved shear stress, and residual GB dislocations. In recent years, a series of *in situ* TEM studies have been conducted in sequential slip transfer through GBs/interphase boundaries in FCC [122], HCP [123], and BCC metals [25] containing a variety of dislocations and boundaries with the influence of impurities or irradiation at different strain rate/temperature [121]. While the local stress is considered to be the most important for slip transfer, other factors including dislocation/GB types, lattice orientation, loading direction, dislocation impingement sites, and the nature of neighboring grains can also be influential [62]. For a symmetric Σ3 CTB on a {111} plane, screw dislocation pile-ups

can either cross slip onto a plane close and parallel to the twin plane or be absorbed by the CTB before being emitted into the twinned grain [47]. This chapter focuses on a $\Sigma 3$ CTB because it is a dominant feature in twinned FCC metals and manifests excellent mechanical properties [327]; moreover, it is among the most prevalent GBs in FCC polycrystals [200].

Atomistic simulations have been performed to quantify dislocation/CTB reactions [47, 84, 117, 118, 325, 327]. These simulations have typically involved small simulation cells with PBCs. It is found that in FCC pure metals, a screw dislocation can either be directly transmitted through the CTB by the FL mechanism [325, 327], be absorbed and then desorbed into the twinned grain by the FE mechanism [118, 325, 327], or glide on the twin boundary (TB) plane [118]. The process that controls the reaction mechanism is subject to debate [47] and will be discussed in Chap. 9. Ezaz et al. [84] proposed that the energy barrier in slip/CTB interactions is proportional to the magnitude of the Burgers vector of the residual dislocation, with the screw dislocation be directly transmitted through the CTB and non-screw dislocations leaving a residual dislocation on the CTB, which then elevates the local stress and energy barrier for further dislocation transmission. Using the climbing image NEB method, Zhu et al. [327] found for Cu that at a low applied stress, the activation energy for absorption is lower than that for direct transmission, the latter of which temporarily leaves a stair-rod dislocation on the CTB; further, the desorption energy barrier is much higher because two TB Shockley partials which were widely separated during absorption need to be constricted. Chassagne et al. [47] showed that there exists a critical reaction stress below which the screw dislocation glides on the CTB and above which the dislocation is absorbed and then desorbed into the nanotwin. In their study and that of Jin et al. [118], no FL type direct transmission of screw dislocation through a CTB was observed.

However, typical atomistic simulations employ only an isolated, short, straight dislocation segment associated with a periodic image in a quasi-2D specimen [10, 47, 117, 118, 241, 265, 325, 327], or situate the source very near the interface with a very limited volume of a periodic unit cell [84, 217, 218]. In such cases of confined volumes and highly constrained

simulation cells, image forces originating from the interactions between periodic or non-periodic boundaries and dislocations are typically non-negligible [145, 251, 277]. In some atomistic simulations [65], a short crack in adjacent to GB is introduced to nucleate a 3D dislocation network which, like an indenter or a void, is not suitable for this chapter where a series of dislocations in a single pile-up is desired over extended distances. Moreover, experiments show that the slip transfer with an increasing number of incoming dislocations can activate additional slip systems or alter the dislocation emission [120]. It is therefore difficult to use results obtained for a single dislocation/GB interaction to extrapolate to the practical case of sequential slip transfer of multiple dislocations in a pile-up.

A commonly stated goal to enhance dislocation-based continuum modeling of polycrystals is to include effects of sequential slip transfer. Such models include CPFEM [161, 166], DD [197], field dislocation mechanics [193], and PFM [144]. In CPFEM, for example, a core-mantle type of approach can be employed where, compared with dislocation motion in grain interior, the slip transfer overcomes either a higher energy barrier [161], a larger slip resistance [166], a higher work hardening rate [95], or a higher dislocation density region [230]. However, details of the dislocation structure, including stacking fault and core structures that affect GB slip transfer [47, 118], are not explicitly addressed in CPFEM or other continuum approaches such as DD. While DD updates the positions and velocities of all dislocation segments at each instant and tracks the long range elastic interactions of dislocations, the short-range dislocation interaction follows prescribed rules [210]. DD largely ignores the role of GBs as dislocation sources in the absence of pile-ups, as well as GB sliding/migration and elastic anisotropy [86]. For these reasons, atomistic simulations are preferred to understand GB structure-specific slip transfer responses.

The sequential slip transfer process in a dislocation pile-up bypass of GBs is inherently multiscale; the GB structure evolution requires explicit atomistic treatment, while the dislocation pile-up itself has long range character [167]. In this spirit, multiscale modeling has been pursued using the QC method [227, 234, 255, 318] with adaptive remeshing and the CADD method [70–72, 232] to investigate sequential slip transfer. While simulations following both methods employed a sufficiently large continuum domain to incorporate long range

fields of dislocation pile-ups and an atomistic domain for representation of GBs, to the author's knowledge these work has considered either quasi-2D approximations for segments or PBCs along the dislocation line direction. In these models, (i) curved dislocations of mixed character have been excluded because of the 2D setup and (ii) both ends of the outgoing dislocation line are forced to be "reconnected" across the periodic boundary, effectively changing the length and forcing unrealistic constriction events.

In this chapter, CAC simulations are performed for Cu and Al to clarify the mechanisms of sequential interactions between a number of curved incoming dislocations in a single pile-up and a $\Sigma 3$ CTB, to the author's knowledge the first attempt to do so in the literature [303]. Dewald and Curtin [71] conducted simulations of straight pure screw dislocation segments impinging on a $\Sigma 3$ CTB for Al using the CADD method, and had elucidated several additional criteria for slip transfer beyond those of the classical LRB criteria [140]; this chapter aims to explore if the findings of that kind of quasi-2D study hold up for cases of larger scale full 3D simulations of sequential dislocation slip transfer reactions with more realistic boundary conditions, which prevail in *in situ* TEM experiments [125]. The differences between experimental and computational studies are analyzed. These two FCC systems are selected based on the work of Chassagne et al. [47] and Jin et al. [117, 118] as they have significantly different stacking/twin fault energies that affect the slip transfer reactions. Dislocation reactions upon transmission and the corresponding CTB structure evolution will be investigated for a sequence of reactions of successive dislocations in a pile-up. Three scientific questions are explored:

1. How do the interactions of curved, mixed character dislocations with the CTB in a full 3D simulation differ from those of straight dislocation/CTB interactions in a quasi-2D simulation cell?

2. How does the dislocation/CTB reaction change with different applied shear stress, dislocation line length, and dislocation line curvature?

3. How do initial slip transfer events influence subsequent interactions of pile-up dislocations with the CTB?

While large scale atomistic simulations are desirable in studying slip transfer across GBs, the purpose of this and the next chapter is to demonstrate the efficacy of coarse-graining in facilitating parametric studies of dislocation/GB reactions concerning a wide range of dislocations and GBs for the same computational resources as atomistic simulations.

8.2 Methodology

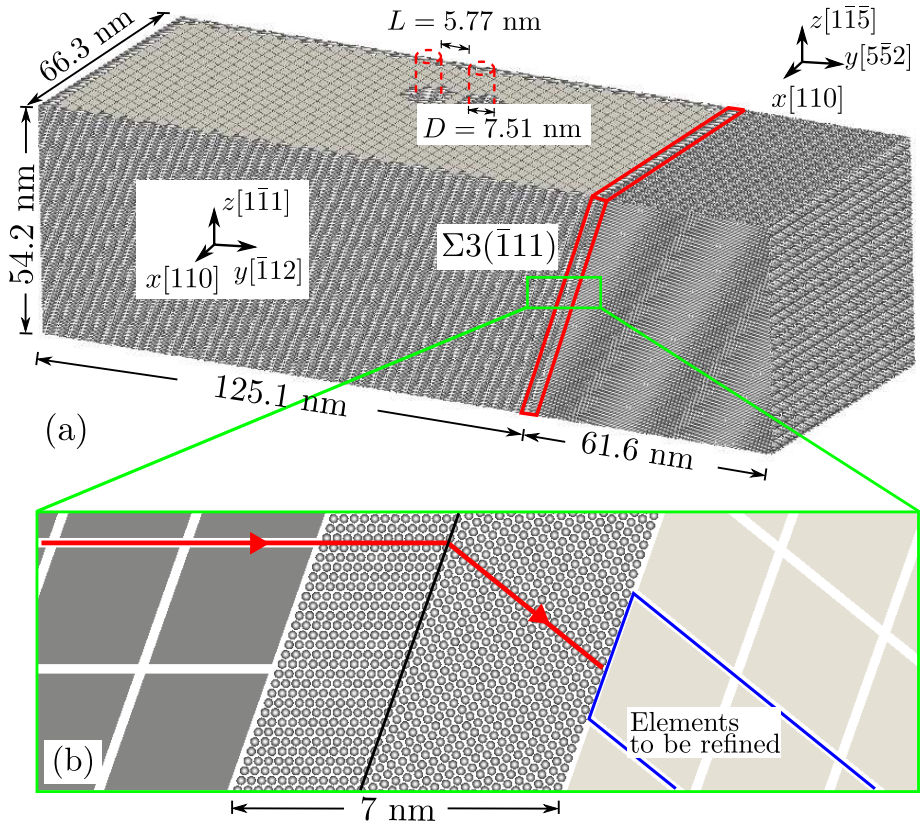

Figure 8.1: (a) Bicrystal simulation cell to study sequential slip transfer across a Σ3 CTB in FCC metals. A pair of cylindrical holes is introduced as an FR source for dislocation multiplication. An atomistic domain is meshed in the vicinity of the CTB, FR source, and at the otherwise zigzag cell boundaries; away from the CTB, holes, and cell boundaries are those of the coarse-grained finite elements, each of which contains 2,197 atoms. All cell boundaries are assumed traction free to allow a full 3D description. (b) A zoom-in of the CTB region shows that the elements marked by the blue lines need to be refined for outgoing dislocations to propagate as they exit the atomistically resolved domain of the CTB. Note that all distances labelled here are for Cu; the size of the model for Al differs by the ratio of their lattice parameters [303].

The bicrystal simulation cell containing a Σ3 CTB is shown in Fig. 8.1, with a pair of cylindrical holes introduced in the incoming grain throughout the specimen along the z

direction. Full atomistic resolution is applied within 7 nm in the vicinity of CTB, around the holes, and at the otherwise zigzag cell boundaries [300]; away from the CTB, holes, and cell boundaries are elements that have discontinuities between them in the course-grained domain. A uniform element size of 2197 atoms solved by 1^{st} order Gaussian quadrature is chosen. The lattice orientations are $x[110]$, $y[\bar{1}12]$, and $z[1\bar{1}1]$ in the incoming grain and $x[110]$, $y[5\bar{5}2]$, and $z[1\bar{1}\bar{5}]$, in the outgoing grain, respectively. The cylindrical holes effectively serve as an FR source to generate a series of curved dislocations in a single-ended pile-up as they are shown to strongly pin dislocations in FCC metals in the presence of traction free cell boundaries [281]. Such a simulation cell is introduced because this and the next chapter intend to promote a full 3D effect and modeling specimen thicknesses that are comparable to those of TEM foils to facilitate a more direct comparison with *in situ* TEM experiments. Effects of free surfaces on dislocation curvature are of interest; to the best of the author's knowledge, these effects have not been pursued in prior atomistic simulations. The domain around the FR source has full atomistic resolution because (i) the elements are of rhombohedral shape and (ii) dislocation nucleation from a free surface cannot be accurately described by the coarse-grained domain alone, as discussed in Sec. 4.6. Similar to Ref. [281], it is found that the Lomer-Cottrell type sessile lock is either unstable or does not act as dislocation source in the present model. The simulation cell size of the two materials differs only by their lattice parameter a_0, which is 3.615 Å for Cu and 4.05 Å for Al. The length along each direction in each grain is chosen by taking several factors into account: (i) curved dislocations should evolve freely in 3D — the box length along the x direction L_x for both grains needs to be large enough, e.g., $L_x = 66.3$ nm $= 260b$ for Cu is sufficient to distinguish between quasi-2D and 3D [42] and allow dislocation segments to have a non-negligible curvature between traction free surfaces, where b is the magnitude of Burgers vector of incoming dislocation $\mathbf{b} = (a_0/\sqrt{2})[110]$; (ii) the potential CTB dislocations need to migrate far from the initial site of dislocation/CTB interaction to minimize the back stress on subsequent slip transfer, so the box length along the z direction for Cu is assigned as $L_z = 54.2$ nm $= 213b$, which is larger than $196b$ used in a QC simulation [234]; (iii) the outgoing dislocations should also be allowed to travel far from the interaction

site on slip plane, so the outgoing grain length along the y direction is selected for Cu as $L_y^{\text{out}} = 61.6$ nm $= 242b$; (iv) to minimize the image forces from the leftmost boundary, the incoming grain length along the y direction L_y^{in} is chosen to be 125.1 nm for Cu. As a result, the simulation cell contains 21,812 elements and about 9 million atoms, with 9,076,792 DOFs in total compared to otherwise 56,823,260 in an equivalent full atomistic model. The dislocation density in the incoming grain containing one dislocation loop is about $2.95 \times 10^{14}/\text{m}^2$.

To account for both dislocation migration over relatively long distances and CTB structure evolution, a combined approach of quenched dynamic CAC accompanied by periodic quasistatic energy minimization is taken in the simulations, as described in Sec. 3.3.4. This approach is important to alleviate the finite temperature effect and focus on obtaining trajectories that are close to minimum energy pathways for evolution of structure during slip transfer because even MD cannot account for thermally activated processes which are important in explaining TEM results [47]. The Velocity Verlet algorithm is used to integrate the equation of motion, with a constant time step of 2 fs for both domains. Note that the time advancement in this and the next chapter is for quenched dynamics only. For all practical purposes, the simulations are regarded to pertain to 0 K (or very nearly so) conditions.

In preparation for the simulations, 0 K equilibrium structure of the CTB is first computed, which due to its simplicity can be achieved using energy minimization without trying different in-plane translations [212]. A straight edge dislocation is introduced on the mid plane normal to the z axis by moving atoms/nodes between two cylindrical holes by Burgers vector $\mathbf{b} = (a_0/2)[110]$, followed by energy minimization. Only one dislocation segment is created to avoid the interaction between a dislocation dipole on parallel slip planes [235], as dicussed in Chaps. 6–7. Once the equilibrium atomic configuration of the FR source is achieved, quenched dynamic CAC simulations are carried out with an increment of applied shear stress $\Delta\sigma_{zx} = 4$ MPa for each step until the shear stress reaches 1.2 GPa, which is then maintained using the PR method [186]. While a large shear stress is necessary to bow out dislocations from the FR source and drive the dislocation pile-up towards the CTB, the

high stress and accompanying inertia effect favor transmission over absorption [47]. Note that the quenched dynamic CAC still has some, albeit small, inertia effects because it is not strictly static energy minimization. To alleviate inertia effects and accurately reproduce the CTB structure during dislocation impingement, the quasistatic CAC simulation (0 K energy minimization) is performed every 500 steps before and every 100 steps after the first dislocation/CTB reaction.

8.3 Results and discussion

In both Cu and Al, the initially straight edge dislocation segment that was anchored at two cylindrical holes in the absence of external stress responds to application of the shear stress σ_{zx} by bowing out, as shown in Fig. 8.2. In Fig. 8.2(b), the critical configuration of a semi-ellipse is reached; then the segment continues growing until two parts contact and annihilate each other, as shown in Fig. 8.2(c). In Fig. 8.2(d), a dislocation loop is formed, leaving a straight edge dislocation segment behind as the new FR source. The segment of the dislocation loop with edge component has a wider core than that with screw component, consistent with both elasticity theory [110] and atomistic simulations [183]. As the dislocation loop continues to expand, the segment with edge component exits at the traction free surfaces, leaving a screw dislocation dipole in the incoming grain, as shown in Fig. 8.2(e). Subject to a shear stress σ_{zx}, one curved dislocation segment moves towards the CTB while the other eventually exits at the leftmost traction free cell boundary.

In both materials, the core of the dislocation splits into two Shockley partial dislocations, i.e.,

$$\frac{1}{2}a_0[110]^{\text{in}} \rightarrow \frac{1}{6}a_0[121]^{\text{in}}_{\text{lead}} + \frac{1}{6}a_0[21\bar{1}]^{\text{in}}_{\text{trail}}. \tag{8.1}$$

In this and the next chapter, the superscripts "in" and "out" are used to distinguish the two grains in which the dislocation is located, while the subscripts "lead" and "trail" refer to leading and trailing partial dislocations, respectively. The reaction is energetically favorable according to Frank's rule [110]. In the coarse-grained domain, the two partials are separated by 29 Å and 19 Å in Cu (Fig. 8.3(a)) and Al (Fig. 8.3(e)), respectively, somewhat wider than separations computed using full atomistic simulations. Once the dislocation

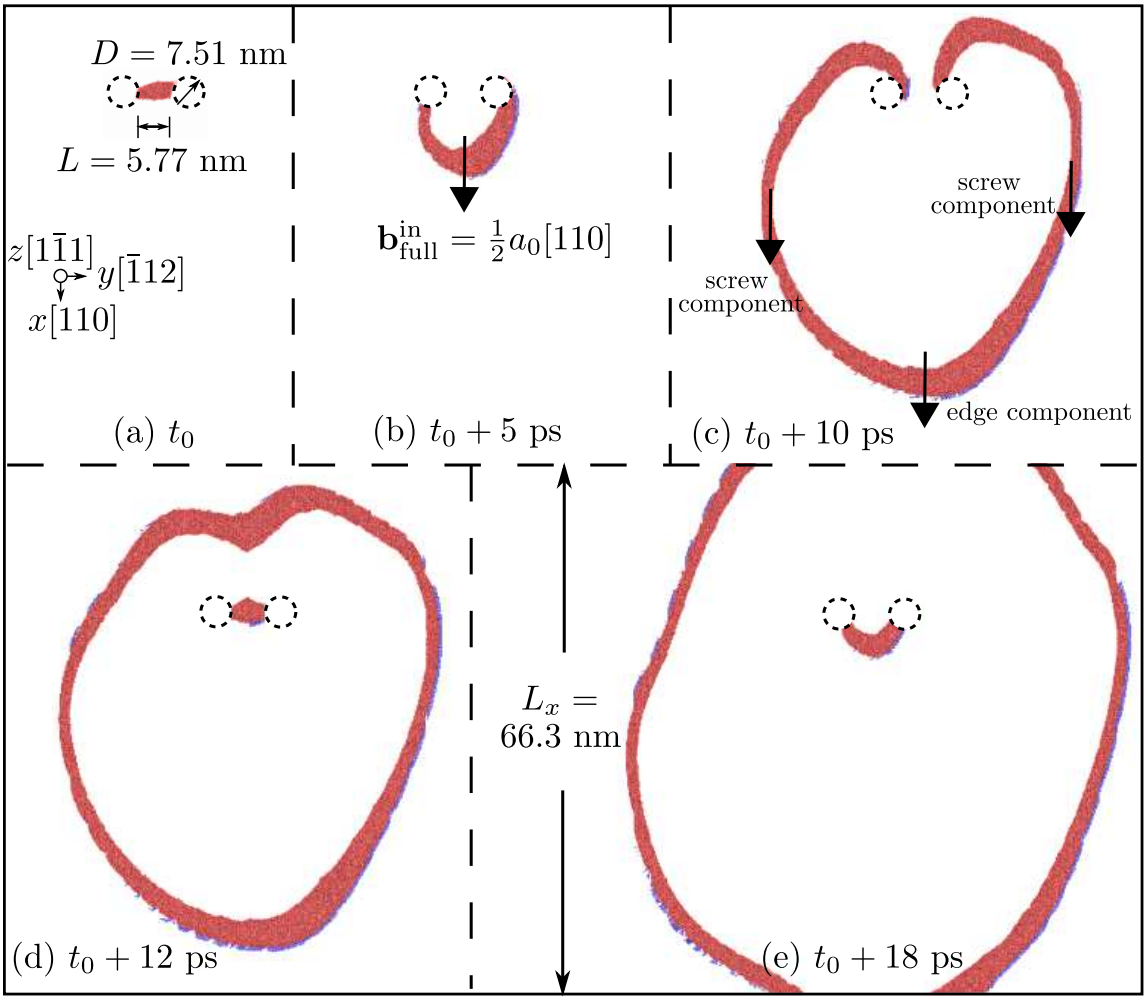

Figure 8.2: Snapshots of dislocation loop multiplication in Cu between a pair of cylindrical holes, which serve as an FR source. Atoms are colored by a-CNA [246]: red are of HCP local structure, blue are BCC atoms, and all FCC atoms are deleted. In (a), a straight edge dislocation is introduced between two cylindrical holes. In (b), the dislocation reaches the critical semi-elliptical configuration; then it continues growing in (c) until a dislocation loop is formed in (d). In (e), the segments of dislocation loop with edge component are swept out at the traction free cell boundaries, leaving a curved dislocation moving along the positive y direction towards the CTB. Similar phenomena are observed for Al [303].

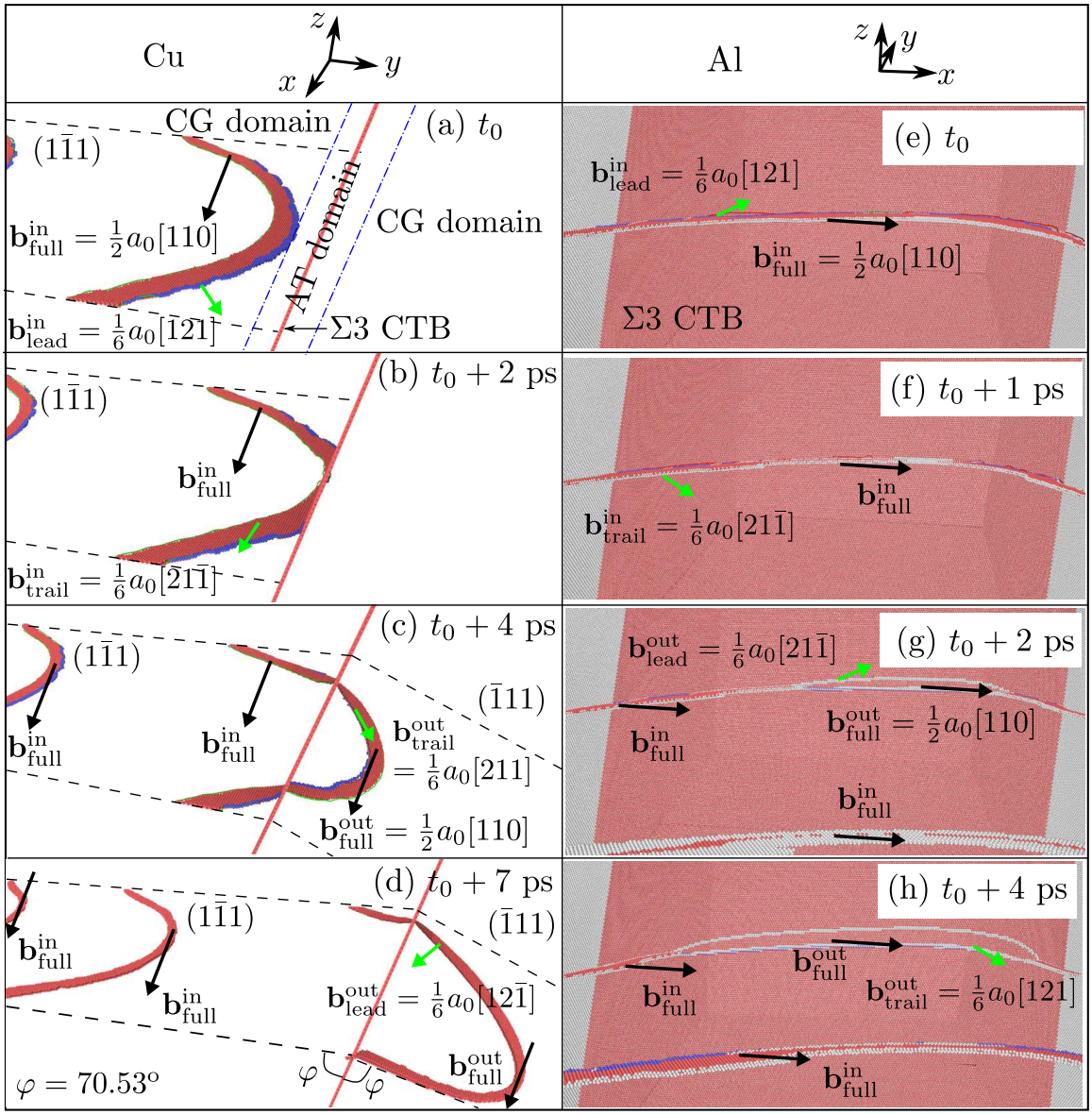

Figure 8.3: Snapshots of dislocation pile-up impingement with dominant leading screw character against $\Sigma 3$ CTB in both Cu (a–d) and Al (e–h) subject to a shear stress $\sigma_{zx} = 1.2$ GPa. Atoms are colored in the same way as in Fig. 8.2. A fully atomistic domain is meshed in the vicinity of the CTB, as shown in (a). In both materials, the incoming dislocation is constricted at the CTB, where two Shockley partial dislocations are recombined into a full dislocation. In Cu, the dislocation cuts into the outgoing twinned grain and is redissociated into two partials; in Al, the redissociated dislocation is absorbed by the CTB, with two partials gliding on the twin plane in the same direction. Different views of the CTB are taken for Cu and Al, which are illustrated in the first row of each column [303].

migrates into the atomistic domain in the vicinity of the CTB, it obtains the same stacking fault width and core structure as those from full atomistics [300] and feels a repulsive force from the CTB in Cu but an attractive force in Al because of the relatively low CTB shear strength in Al [54]. At a shear stress of 1.2 GPa, two dislocation/CTB interaction modes are found:

1. In Cu, the leading partial in the incoming grain is stopped at the CTB, with the stacking fault width constricting up to the point where the trailing partial also reaches the CTB, as shown in Fig. 8.3(b). Then the full dislocation is re-dissociated into two Shockley partials and transmitted into the outgoing grain, i.e.,

$$\mathbf{R}_{\Sigma 3} \cdot \frac{1}{2} a_0 [110]^{\text{in}} \rightarrow \frac{1}{2} a_0 [110]^{\text{out}} \rightarrow \frac{1}{6} a_0 [12\bar{1}]^{\text{out}}_{\text{lead}} + \frac{1}{6} a_0 [211]^{\text{out}}_{\text{trail}}. \tag{8.2}$$

   Here, the slip plane in the outgoing grain is $(\bar{1}11)$ and the rotation matrix between two grains is

$$\mathbf{R}_{\Sigma 3} = \frac{1}{3} \begin{pmatrix} 1 & 2 & 2 \\ 2 & 1 & -2 \\ -2 & 2 & -1 \end{pmatrix}. \tag{8.3}$$

2. In Al, the leading and trailing partial dislocations are spontaneously absorbed by and constricted at the CTB because of the attractive force [54]. However, instead of being transmitted into the outgoing grain, the full dislocation is re-dissociated to two Shockley partials in the twin plane, i.e.,

$$\mathbf{R}_{\Sigma 3} \cdot \frac{1}{2} a_0 [110]^{\text{in}} \rightarrow \frac{1}{2} a_0 [110]^{\text{out}} \rightarrow \frac{1}{6} a_0 [21\bar{1}]^{\text{out}}_{\text{lead}} + \frac{1}{6} a_0 [121]^{\text{out}}_{\text{trail}} \tag{8.4}$$

   where the slip plane (i.e., twin plane) for the second grain is $(1\bar{1}1)$.

In both materials, up to three dislocation loops are nucleated from the FR source and sequentially interact with the CTB. Each time a dislocation loop is generated, the cylindrical holes acquire steps at the free surface which potentially affects the source behavior; however, this is not of significant concern here as this chapter intends only to introduce successive dislocations on the same slip plane. Driven by the shear stress, the first dislocation migrates toward the CTB but stops at a distance when the applied shear stress, dislocation self force,

repulsive force from the CTB, and the force required to create surface steps are balanced during energy minimization. In the subsequent quenched dynamics, the second dislocation loop is formed, which drives the first dislocation towards the CTB. The defected CTB structure is found by energy minimization. The last dislocation is nucleated from the FR source after the first but before the second dislocation/CTB interaction occurs. As more dislocation loops are formed, the FR source becomes progressively exhausted for a given applied stress as dislocations interact with upstream dislocations in the pileup. To better understand the geometric conditions involved in the present simulations and compare the results with quasi-2D simulations and *in situ* TEM experiments in the literature, cases of different applied shear stresses, dislocation line length, and dislocation line curvature are also studied.

The critical stress for an edge dislocation bow-out between two cylindrical holes can be estimated by the SB equation (Eq. 6.4), in which the interhole ligament distance $L =$ 5.77 nm and the hole diameter $D = 7.51$ nm. If the dislocation core radius $r_0 = b$, the critical stress is 1.18 GPa for Cu and 803 MPa for Al. In the present simulations, after generating the first dislocation, the applied stress is ramped to and maintained at 1.2 GPa for both materials to bow out subsequent dislocations from the FR source and drive curved dislocations towards the CTB. The image forces on a dislocation with dominant screw character caused by the traction free cell boundaries, which are naturally captured in CAC via nonlocal, nonlinear interatomic force instead of by superposition via linear elastic solutions as in DD [277], are much smaller than those on edge and mixed type dislocations [183]. Particularly for the top and bottom surfaces, the image forces are negligible because the Burgers vector is parallel to these cell boundaries [183].

CAC simulations suggest that for both Cu and Al, the dissociated dislocations in the incoming grain are constricted into a full dislocation at the CTB. This is because the arrangement of the leading and trailing dislocations must be switched before either entering the outgoing grain or gliding on the twin plane. Using a DXA [247], it is found that the reaction of dislocation at the CTB in terms of the spatial Burgers vector is

$$[1.28, 0.74, 0]^{\text{in}}_{\text{lead}} + [1.28, -0.74, 0]^{\text{in}}_{\text{trail}} \rightarrow [1.28, -0.32, 0.54]^{\text{out}}_{\text{lead}} + [1.28, 0.32, -0.54]^{\text{out}}_{\text{trail}} \quad (8.5)$$

for Cu, and

$$[1.43, 0.83, 0]^{\text{in}}_{\text{lead}} + [1.43, -0.83, 0]^{\text{in}}_{\text{trail}} \rightarrow [1.43, -0.26, 0.65]^{\text{out}}_{\text{lead}} + [1.43, -0.26, -0.65]^{\text{out}}_{\text{trail}} \tag{8.6}$$

for Al. Equations 8.5–8.6 show that for at least one of the incoming partials, the y component of the spatial Burgers vector, i.e., the pure edge component, changes sign, a process not possible without re-combination and re-dissociation since no stair-rod dislocation (as in the FL mechanism) is observed at the CTB. This requirement of two partial dislocations to exchange their order at the CTB is attributed to the twin symmetry [117,118]. Particularly for a 3D curved dislocation, part of the segment with pure screw component is constricted first, leaving the dissociated segment with mixed type component behind in the incoming grain, as shown in Figs. 8.3(c) and 8.3(g). This phenomenon, similar to the twinning dislocation multiplication at a CTB [145], cannot be described using quasi-2D simulations but is reported in experiments [121].

For Cu, the leading dislocation does not penetrate into the outgoing grain when the trailing partial is still in the incoming grain; the direct transmission of dislocations by the FL mechanism is not observed. In other words, the dislocation reaction is of FE type, i.e., the dissociated dislocation is always recombined at the CTB before any further motion can proceed, a phenomenon supported by atomistic simulations [47,118]. Interestingly, results didn't show any CTB dislocations in the process of dislocation constriction, while NEB [327] predicts that the dislocations are absorbed to form CTB dislocations followed by desorption. Note that MS is used by practitioners of NEB to determine initial and final replicates and MD is sometimes employed to explore candidate transition states between these two replicates, before the 0 K energy minimized NEB method is used to identify the correct saddle point on the minimum energy pathway. In the case of extended defects with complex reactions, this can be problematic when using overdriven dynamics of MD since the reaction pathway taken in such simulations may differ substantially from the near equilibrium trajectory associated with thermally activated, low stress regime. After the first dislocation passes the CTB, the elements with edges along the blue lines in Fig. 8.1 are refined, because the outgoing dislocation path is not aligned with the interelement boundaries

and it would therefore be impeded, requiring cross-slip along the atomistic/coarse-grained interface and posing an aphysical back stress acting on subsequent dislocation reactions as shown in Sec. 4.10. The outgoing dislocation then continues migrating on the $(\bar{1}11)$ plane until it exits the rightmost traction free cell boundary.

For Al, the incoming dislocation is always spontaneously absorbed and constricted by the CTB. After re-combination, the full dislocation splits onto the CTB instead of passing it because of its relatively higher stable SFE [47, 118]. In other words, the screw dislocation cross-slips on the CTB following the FE mechanism. The CTB partials, with Burgers vectors parallel to the CTB, belong to the displacement shift complete (DSC) lattice for the CTB and therefore migrate freely in the same direction. This result differs from those obtained using quasi-2D atomistic [47, 118] and multiscale simulations via the CADD method [71], where two CTB partials move in opposite directions, adding one layer of atoms to the outgoing grain at the expense of the incoming grain, a process termed detwinning. In CAC simulation, only a local detwinning process that grows the incoming grain is temporarily observed; the CTB remains perfect after both partials glide to and are eventually swept out at the top traction free cell boundary.

The different dislocation reactions at the CTB for Cu and Al under the same applied stress may relate to the fact that the normalized Hall-Petch coefficient for Cu is about twice that for Al [200]. For both materials, since each dislocation/CTB slip transfer event does not leave residual Burgers vector in the CTB interface, the interaction mechanism for subsequent dislocations is found to be precisely the same as for the first dislocation for each same material. It is emphasized that this finding is particular to the $\Sigma 3$ CTB and to the nature of the incoming dislocations considered here.

To further explore the differences between CAC simulations and those in the literature, the applied stress is varied from 100 MPa up to 2.4 GPa for Al, with an increment of 100 MPa. Note that a shear stress lower than 803 MPa is reached using the PR approach after each dislocation loop is emitted from the source at a higher stress, past the saddle point of the transition. With a Peierls stress of about 16 MPa [183] for a screw dislocation in Al, the stress levels employed in the simulations are high enough to retain a curved

dislocation induced by the surface steps at traction free cell boundaries. To study the influence of dislocation line length which is 260b shown in Fig. 8.1, models with smaller dislocation line lengths L_x of 125b and 26b are investigated, respectively. Since 26b is too small to accommodate the FR source, three screw dislocations spaced 50 nm from each other are introduced on the mid plane normal to the z axis via a Volterra displacement followed by energy minimization. For $L_x = 125b$, the effect of dislocation line curvature is also studied, which is adjusted by varying the boundary conditions along the dislocation line direction: applying PBCs and traction free boundary conditions result in straight and curved dislocation lines, respectively.

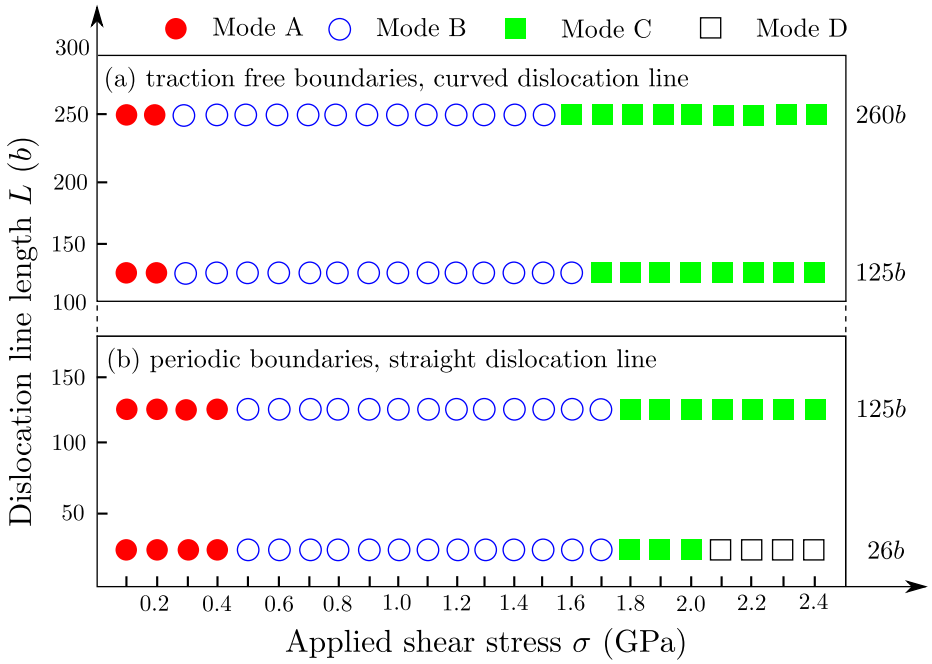

Figure 8.4: Four different dislocation/CTB reaction modes for Al, as a function of applied shear stress, dislocation line length, and dislocation line curvature. Prior atomistic simulations and multiscale methods in the literature only reported mode A reaction while other modes are observed in *in situ* TEM experiments. The surface steps at the traction free cell boundaries in (a) retain curved dislocations while the PBCs applied on the dislocation line direction in (b) result in straight dislocation segments, regardless of the dislocation line length [303].

It is found that four dislocation/CTB interaction modes exist for Al, which relate to applied shear stress, dislocation line length, and dislocation line curvature, as shown in Fig. 8.4. The detailed stress-dependent dislocation/CTB reactions in the case of $L_x = 26b$

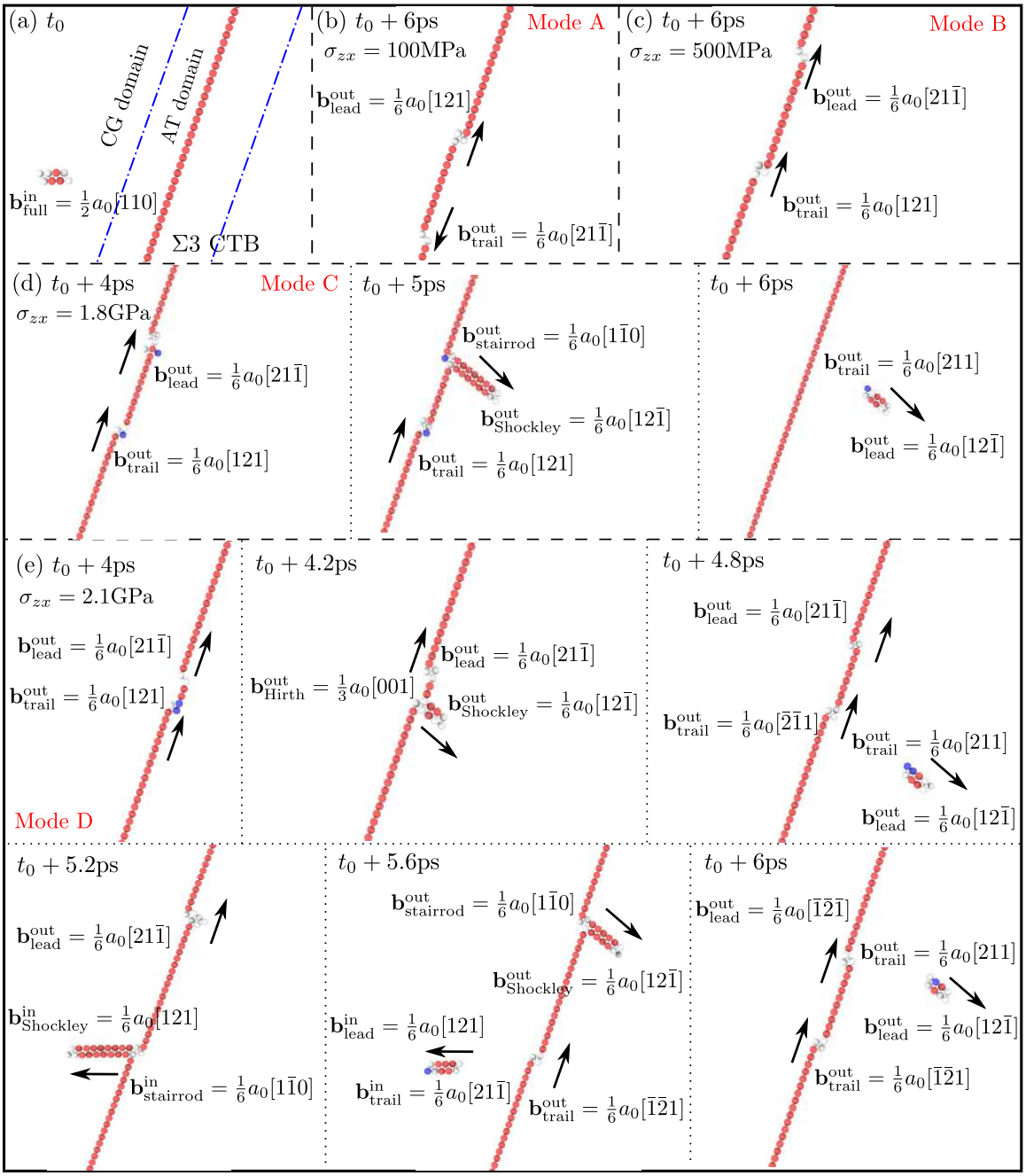

Figure 8.5: Snapshots of a straight screw dislocation interacting with a Σ3 CTB in a quasi-2D model for Al. Atoms are colored in the same manner as in Fig. 8.2. The length of the dislocation line is reduced from 260b in Fig. 8.1 to 26b. (a) Incoming screw dislocation is in the coarse-grained domain; (b) at an applied stress of 100 MPa, the incoming dislocation splits into two Shockley partials, which then move in opposite directions; (c) at a 500 MPa applied stress, the two CTB partial dislocations move in the same direction, leaving no CTB migration behind; (d) at a 1.8 GPa applied stress, the incoming dislocation is first absorbed by the CTB then desorbed into the twinned grain, leaving behind a perfect CTB, similar to the NEB prediction for Cu [327]; (e) at the largest stress of 2.1 GPa, dislocations are desorbed into both incoming and outgoing grains [303].

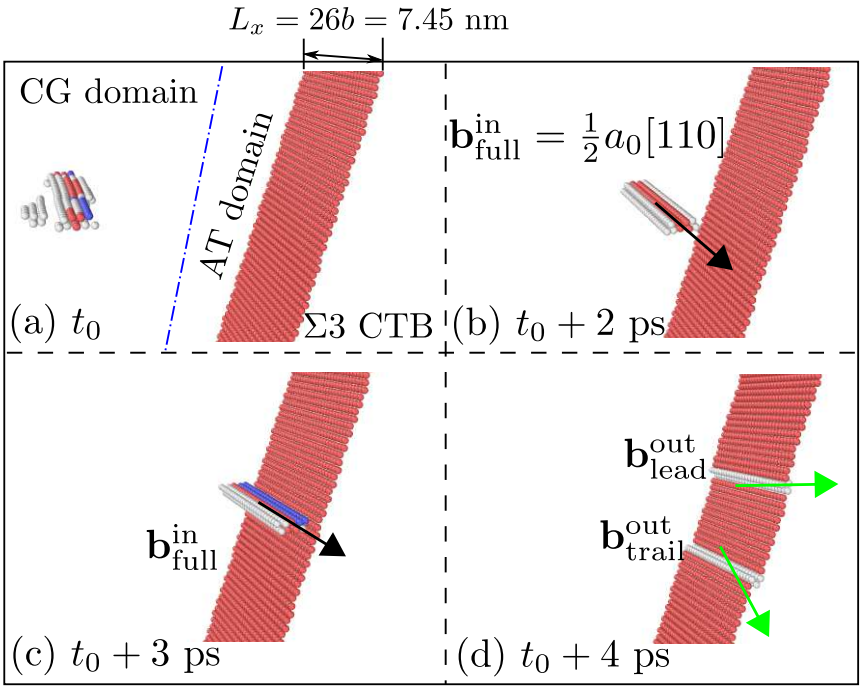

Figure 8.6: Snapshots of a straight screw dislocation interacting with a Σ3 CTB in a quasi-2D model for Al. Atoms are colored in the same manner as in Fig. 8.2. The length of the dislocation line is $26b$ and the applied stress is 500 MPa. It is found that the two CTB partial dislocations move in the same directions, leaving no CTB migration behind.

are shown in Fig. 8.5, which agree with the equivalent fully atomistic simulations with a combined quenched dynamics and quasistatic periodic energy minimization scheme. In mode A, a screw dislocation is first absorbed by the CTB subject to a 100 MPa applied stress, then the two CTB partials move in opposite directions, as shown in Fig. 8.5(b). This mode is reported in both atomistic [47,118] and CADD simulations [71], but is not observed using *in situ* TEM to the best of the author's knowledge. At a higher stress of 500 MPa, the screw dislocation cross-slips onto the CTB via the FE mechanism, forming two CTB partials that move in the same direction, as shown in Figs. 8.5(c) and 8.6. This interaction result, referred to as mode B, has been reported in a high resolution TEM experiment [316]. When the applied stress increases to 1.8 GPa and 2.1 GPa, dislocations are desorbed by the CTB into either the outgoing or both grains, referred to as modes C and D, respectively, as shown in Figs. 8.5(d–e). The penetration of a curved dislocation across a CTB in Al is observed in *in situ* TEM experiments in the presence of a large dislocation pile-up [125].

In all four modes, the incoming dislocations are re-combined before being re-dissociated

at the CTB. In Cu, atomistic [47, 85, 118] and QC simulations [234], as well as *in situ* TEM experiments [121] found that a lower applied shear stress tends to result in dislocation absorption by a CTB while a higher shear stress facilitates dislocation transmission. This applied shear stress-dependent reaction agrees with the transition from modes A/B to modes C/D found in the present CAC simulations in Al. In particular for modes C and D, dislocation nucleation from pre-existing kink ledges in a CTB subject to shearing was observed in previous MD simulations in Cu [278]. A transitional mode between mode A and mode C subject to an intermediate stress level, i.e., mode B, however, was not found in Cu [85]. In the literature, an analog of the modes A, B, C here can be found in MD simulations [280] of screw dislocation/extrinsic stacking fault interactions subject to different applied shear strain ε in Cu, where the extrinsic stacking fault, (i) is transformed into an intrinsic stacking fault when $0.7\% \leq \varepsilon \leq 1.7\%$, (ii) is transformed into a three-layer thick twin when $\varepsilon = 1.8\%$, (iii) is penetrated by the screw dislocation when $\varepsilon \geq 1.9\%$.

Two differences between mode A and mode B — (i) two CTB partial dislocations move in the same or opposite directions and (ii) different grains are grown — cannot be attributed to the energy barrier because both modes migrate the CTB by one atomic layer at the cost of the same TB migration energy. Since these two modes operate at different applied shear stress levels, the transition from mode A to mode B may be understood by analyzing the stress tensor. On the one hand, unlike in a dissociated lattice dislocation, there is no intrinsic stacking fault between the two CTB partial dislocations; as a result, without increasing any SFE, the two CTB partial dislocations move away from each other due to the repulsive force between them. On the other hand, the applied shear stress σ_{zx}, when projected on the TB plane, consists of an out-of-plane and an in-plane shear stress component. The out-of-plane shearing drives both CTB partial dislocations along the same direction while the in-plane shearing does not exert any PK force on either partial dislocation. Therefore, the first difference between modes A and B can be attributed to the competition between repulsion of the two CTB partial dislocations which drives them in opposite directions (mode A) and the influence of applied shear stress, which drives them in the same direction (mode B). An attempt is also made below to account for the second difference between these two modes.

Previous MD simulations in Cu found that an out-of-plane shearing along a ⟨110⟩ direction results in sliding of a perfect CTB without migration [112] but does not alter the position of a pre-existing kink step contained in a CTB [85]. On the other hand, the in-plane shearing moves the pre-existing kink step such that the incoming grain is grown [85], in agreement with the transition from mode A to mode B in the present CAC simulations. Also note that a kink step in a CTB can be considered as a very narrow incoherent TB on a {112} plane. Previous MD simulations [276] showed that subject to shearing, the incoherent TB migrates in Al but not in Cu because of their different SFE. This may be why mode B was not observed in Cu [85].

For the same dislocation line length of $125b$ at a shear stress of 300 MPa or 400 MPa, the reaction of a quasi-2D straight dislocation segment at the CTB follows mode A, while the 3D curved dislocation line interacts with the CTB via mode B. While CAC simulations consider all contributions to energy change, including surface steps at the traction free cell boundaries, it is not the surface steps but the dislocation line curvature that leads to different reaction modes, because the surface steps are far from the center of the dislocation line where the dislocation/CTB interaction is locally initiated. In quasi-2D, the dislocation only has pure screw component along its straight segment; in a fully 3D model, an initially curved dislocation first encounters the CTB with dominant leading screw character, while the remainder of the dislocation line is of mixed type. This dislocation line curvature dependence of the dislocation/CTB reaction has not been previously reported in the literature to the best of the author's knowledge.

With the same boundary conditions, dislocations with different line lengths interact with the CTB differently. In quasi-2D, the mode D reaction is only observed for $L_x = 26b$ but not for $L_x = 125b$. In a 3D model at a shear stress of 1.6 GPa, dislocations with a line length of $125b$ and $260b$ lead to mode B and C reactions with the CTB, respectively. The dislocation line length dependence of the dislocation/CTB reaction can be attributed to the energetics of dislocation constriction and dissociation, which are length-dependent. Similarly, constraints on the TB length also affect the type of dissociation/absorption events that are possible. This is an important result, as it indicates limitations on veracity of computed results for

slip transfer using quasi-2D atomistic simulations in which the incoming straight dislocation line is of pure screw character in confined volumes [47, 84, 117, 118, 218, 327]. Note that in reality the probability of such an encounter is exceedingly low.

There are four possible reasons why atomistic [47, 118] and multiscale simulations based on CADD [71], either involving a single dislocation or dislocation pile-up, predict only mode A interaction, but not other modes that are observed in *in situ* TEM experiments. The first reason is the accuracy of the interatomic potential, which will be explored in Chap. 9. Refs. [71, 118] use Mishin's EAM potential [173] and Ercolessi-Adams EAM potential [81], respectively, while Ref. [47] shows that both EAM potentials predict the same interaction mode. The second reason is the stress level; in Ref. [118], a 100 MPa shear stress is applied, while in Refs. [47, 71], no external shear stress is applied, and the screw dislocation moves towards the CTB because the attractive stress between them overcomes the Peierls stress. In TEM experiments [121], although it is difficult to measure local stress, it is expected that the stress level at the tip of the pile-up is much higher than 100 MPa because a large number of dislocations exist in a pile-up. The third reason is the atomic scale CTB structure: both TEM experiments [47] and MD simulations [278] show that a defected CTB responds differently from a perfect one. The last possible reason is the boundary condition. In most atomistic and multiscale simulations, PBCs are imposed along the dislocation line direction to enforce a short, straight dislocation segment, while dislocations in experiments are usually much longer and curved.

8.4 Summary

In this chapter, 0 K quenched dynamic CAC simulations with periodic energy minimization are employed to study 3D sequential slip transfer across a $\Sigma 3$ CTB in Cu and Al to render interface reactions that may be considered close to minimum energy pathways for thermally activated processes. A series of curved dislocations are nucleated from an FR source, which then move towards the CTB subject to a constant applied shear stress. While the leading screw segment cuts into the twinned grain in Cu, it is absorbed and glides on the CTB in Al. In particular for Al, four dislocation/CTB interaction modes are identified, which are

affected by (i) applied shear stress, (ii) dislocation line length, and (iii) dislocation line curvature. Although the effect of the number of incoming dislocations is not explicitly studied, the effect of a dislocation pile-up can be manifested by varying the applied stress according to recent MD simulations [277]. In all cases studied in this chapter, the dislocation/CTB reactions always follow the recombination-redissociation process, without forming any CTB dislocations in the process of recombination. It is emphasized that the results obtained for a single dislocation/CTB interaction cannot be directly extrapolated to understand the practical case of slip transfer of dislocations in a pile-up in which the leading dislocation experiences a higher stress. The discrepancies between prior computational studies and experiments highlight the significance of this chapter: it is important to directly model dislocation pile-ups, to let dislocations evolve freely in 3D, and to probe the mechanisms of slip transfer in polycrystalline and twinned metals using sufficiently large models.

Note that these quasi-2D limitations are not confined to slip transfer processes. For example, there exists a characteristic length of a screw dislocation segment in BCC Fe above which more than one kink-pair can form which then strongly influences the dislocation mobility [42]. Chapter 5 has confirmed that the screw dislocation cross-slip is line length-dependent. These observations suggest that 3D modeling using faithful interatomic potentials, though much less prevalent in the literature than quasi-2D simulations, is potentially of high utility in exploring more realistic dislocation behavior. In this regard, the fully 3D CAC method opens a promising avenue to explore sequential slip transfer reactions, allowing the possibility for direct comparison of numerical simulations with quasi-four-dimensional (spatial correlation with time) characterization of dislocations reconstructed from *in situ* TEM experiments [121].

CHAPTER IX

SEQUENTIAL SLIP TRANSFER OF CURVED MIXED CHARACTER DISLOCATIONS ACROSS A Σ3 COHERENT TWIN BOUNDARY AND A Σ11 SYMMETRIC TILT GRAIN BOUNDARY IN NI

9.1 Introduction

As discussed in Chap. 8, direct studies of sequential incoming lattice dislocations interacting with GBs at the sub-micron scale are important. While atomistic simulations are desirable, a multiscale approach is more practical in facilitating parametric studies of dislocation/GB reactions concerning a wide range of dislocations and GBs with the same computational resources [304]. Based on a series of CADD simulations, Dewald and Curtin [72] proposed a set of modified LRB criteria, taking into account both Schmid and non-Schmid stresses, as well as GB dislocation nucleation. They also found for Al that the precise location of the dislocation/GB interaction affects the reaction of a screw dislocation with a $\Sigma9\langle110\rangle\{114\}$ GB, but not a $\Sigma11\langle110\rangle\{113\}$ GB [71]. Multiscale modeling has also been pursued using the QC method, revealing that reversing the Burgers vector of an edge dislocation on a given slip plane significantly changes its interactions with a $\Sigma11\langle112\rangle\{113\}$ GB in Cu [320]. These concurrent multiscale methods, however, are limited by the need to pass defects from a DD region to the atomistic region near the interface (CADD) or by the need for significant computational effort devoted to adaptive mesh refinement in the continuum region to accommodate dislocations (QC) [304].

In this chapter, large scale CAC simulations are performed to study the sequential slip transfer of mixed character dislocations across two symmetric GBs in FCC Ni: a $\Sigma3\langle110\rangle\{111\}$ CTB and a $\Sigma11\langle110\rangle\{113\}$ STGB. These two GBs are chosen because they have the simplest GB structure and lowest GB energy among all STGBs with a common $\langle110\rangle$ misorientation axis [218]. CADD simulations for pure Al showed that while a series of straight pure screw dislocations are absorbed by both $\Sigma3\{111\}$ CTB and $\Sigma11\{113\}$

STGB [72], a mixed character dislocation pile-up is transmitted across both boundaries [71]. In Ni, QC and atomistic simulations revealed that (i) a single pure screw dislocation may be transmitted across or absorbed by a $\Sigma3$ CTB, depending on the interatomic potential adopted [47,118], (ii) a single mixed type dislocation is transmitted across a $\Sigma3$ CTB [117], and (iii) a single pure edge dislocation is transmitted across a $\Sigma11\{113\}$ STGB [319]. Nevertheless, the dependence of a mixed character dislocation pile-up impingement against these two boundaries on the interatomic potential for Ni remains to be addressed. This chapter also attempts to shed light on slip transfer criteria in the literature. For example, Sangid et al. [218] proposed that the energy barrier to direct transmission of a dislocation across a GB is inversely related to the static energy of each GB; in particular for the $\Sigma3$ CTB, based on certain material properties such as the stacking and twinning fault energies, Jin et al. [118] and Chassagne et al. [47] proposed different criteria (discussed in detail later in Sec. 9.3) in discriminating between dislocation transmission and absorption in screw dislocation/CTB interactions. In this chapter, the applicability of these criteria will be studied across multiple interatomic potentials for Ni.

9.2 Methodology

Two bicrystal simulation cells containing a $\Sigma3$ CTB and a $\Sigma11$ STGB, respectively, are shown in Fig. 9.1. An atomistic domain is meshed in the vicinity of both GBs to naturally accommodate GB structure evolution at the atomic scale. In the coarse-grained domain, 3D rhombohedral 2NN elements are employed with surfaces corresponding to $\{111\}$ slip planes; each element, containing 2,197 atoms and solved by 1^{st} order Gaussian quadrature, employs a piecewise continuous first order interpolation scheme [300]. For both GBs, the lattice orientations are $x[110]$, $y[\bar{1}12]$, and $z[1\bar{1}1]$ in the incoming grain. In the outgoing grain, the lattice orientations are $x[110]$, $y[5\bar{5}2]$, and $z[1\bar{1}\bar{5}]$ in the case of the $\Sigma3$ CTB, and $x[110]$, $y[\bar{1}\bar{9}, 19, 2]$, and $z[1, \bar{1}, \bar{1}\bar{9}]$ in the case of the $\Sigma11$ STGB. All boundaries of the simulation cell are traction free to allow a 3D evolution of dislocations, as in Chap. 8. The cell length along each direction in each grain follows Chap. 8, with a lattice parameter $a_0 = 3.52$ Å. As a result, each simulation cell roughly contains 15,703 elements and 7

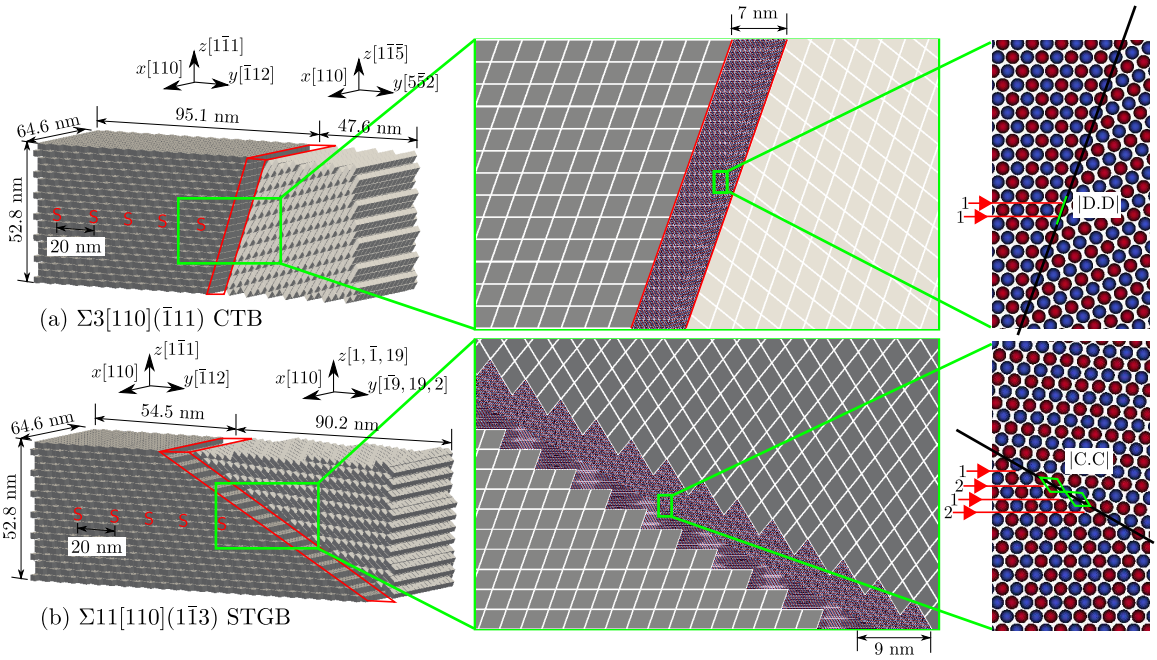

Figure 9.1: Bicrystal simulation cells used to study sequential slip transfer of five $(a_0/2)[110](1\bar{1}1)$ dislocations across (a) a $\Sigma3$ CTB and (b) a $\Sigma11$ STGB in Ni. An atomistic domain is meshed in the vicinity of both GBs; the jagged interstices at the cell boundaries are also filled in with atoms, which are not shown here. Away from the GBs and cell boundaries are coarse-grained finite elements, each containing 2,197 atoms. All cell boundaries are assumed traction free to allow a full 3D description. Zoom-ins of the GB region are given in the rightmost column, where atoms in different (110) atomic layers have different colors. The top right zoom-in shows that the $\Sigma3$ CTB is composed of all D SUs, and all sites along the CTB are equivalent; the bottom right zoom-in suggests the $\Sigma11$ STGB is composed of all C SUs, indicating that two distinct dislocation/STGB interaction sites (1 and 2) should be considered in terms of slip planes of incoming dislocations [304].

million discrete atoms, with 7.1 million DOFs in CAC compared to otherwise 43 million in an equivalent fully resolved atomistic model.

The macroscopic GB geometry is defined using five DOFs that fully describe the crystallographic orientation of the two crystals (three DOFs) and the GB plane (two DOFs) [249]. On a microscopic level, the translation between the two crystal lattices requires three additional DOFs. In preparation for the simulations, the global 0 K equilibrium structure of GBs is first computed by sampling a number of different configurations which are constructed following a series of rigid body translation and atom deletion [303]. For each initial configuration, the nonlinear conjugate gradient algorithm is employed to render the final configuration, as described in Sec. 3.3.6. For a certain set of five macroscopic DOFs, the

GB with the lowest energy in final configuration is considered the energy minimized GB and is used in subsequent simulations. This globally energy minimized GB structure finding procedure was first proposed by Wolf [283] and then improved and employed in previous atomistic simulation studies in McDowell group [239, 259, 264, 267].

Table 9.1: For five EAM potentials, certain quantities of interest are calculated in comparison with the experimental (EXP) [173] or *ab initio* (AI) [128] simulations results in the literature, including magnitude of the Burgers vector of a Shockley partial dislocation b_p (nm), shear modulus for the $\langle 110\rangle\{111\}$ system μ (GPa), stable SFE e_SF (mJ/m^2), unstable SFE e_USF (mJ/m^2), stable twinning energy (also the static $\Sigma3\{111\}$ CTB energy) e_T (mJ/m^2), unstable twinning energy e_UT (mJ/m^2), static energy of the $\Sigma11\{113\}$ STGB e_STGB (mJ/m^2), as well as three screw dislocation/CTB interaction criteria proposed by Jin et al. [118] and Chassagne et al. [47] as a function of these energies. Following Ref. [118], $R = (e_\mathrm{USF} - e_\mathrm{SF})/(\mu b_\mathrm{p})$ and $R' = (e_\mathrm{UT} - e_\mathrm{SF})/(\mu b_\mathrm{p})$. Mechanisms of dislocation interacting with a $\Sigma3$ CTB and a $\Sigma11$ STGB in CAC simulations are also shown, either transmission (T) or absorption (A) [304].

	Mishin [173]	Angelo [7]	Foiles [89]	Voter [274]	Zhou [326]	EXP or AI
b_p	0.144	0.144	0.144	0.144	0.144	0.144 [173]
μ	75	75	70	73.67	76.33	75 [173]
e_SF	125.86	89.2	127.11	58.22	99.31	125 [173]
e_USF	366.12	214.51	255.12	226.34	251.81	273 [128]
e_T	63.25	49.7	63.05	29.42	49.45	43 [173]
e_UT	362.36	204.92	250.35	224.84	248.7	281 [128]
e_STGB	526.28	369.63	417.36	398.03	422.17	
R	0.0223	0.0116	0.0127	0.0159	0.0139	0.0137
R/R'	1.02	1.08	1.04	1.01	1.02	0.95
$e_\mathrm{SF}/(\mu b_\mathrm{p})$	0.0117	0.0083	0.0126	0.0055	0.009	0.0116
$\Sigma3$ CTB	T	A	A	T	A	
$\Sigma11$ STGB	A	A	A	A	A	

It follows that five straight, equidistant, pure screw dislocations in a single pile-up, each of which has a Burgers vector $\mathbf{b} = (a_0/2)[110]$, are introduced on the mid plane normal to the z axis [118]. The $\Sigma3$ CTB is composed of all D structural units (SUs), while the $\Sigma11$ STGB is composed of all C SUs, as shown in the rightmost column of Fig. 9.1. As such, only one dislocation impingement site is considered for the $\Sigma3$ CTB while two distinct sites are for the $\Sigma11$ STGB. Once the equilibrium configuration is achieved, a uniform shear stress is applied on the simulation cell to drive the dislocation pile-up toward the GBs. For each dislocation, part of the line with pure screw component encounters the GBs first, leaving behind the dissociated segment with mixed type component in the incoming grain, a process

reported in experiments [121] yet cannot be described using quasi-2D simulations [303]. After the first transmission event, certain elements ahead of the leading dislocations in the outgoing grain are refined to the atomic scale, following Sec. 4.10, to allow dislocations to continue migrating. A combined approach of quenched dynamic CAC accompanied by periodic quasistatic energy minimization is taken in simulations, to account for both long-distance dislocation migration and GBs structure evolution, as employed in Chap. 8. In particular, at increments of applied loading, the energy minimization is performed every 500 steps before and every 100 steps after the first dislocation/GB reaction. The Velocity Verlet algorithm is used to integrate the equations of motion in quenched dynamic CAC, with a constant time step of 2 fs for both domains.

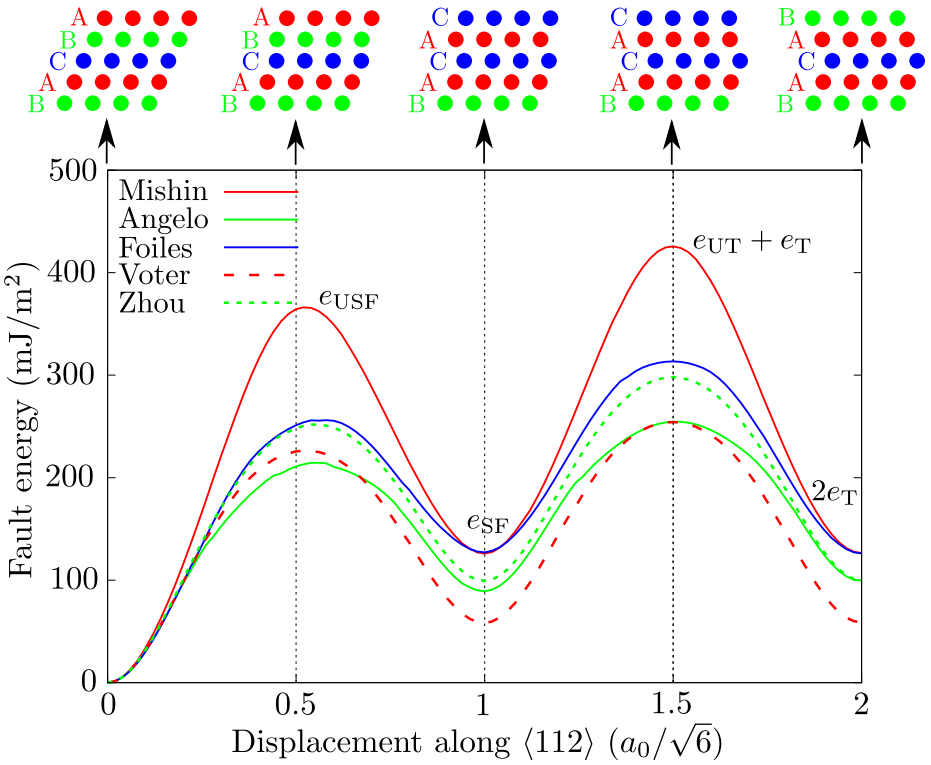

Figure 9.2: Generalized fault energy curves along a $\langle 112 \rangle$ direction on a $\{111\}$ plane in Ni, calculated using five EAM potentials [7, 89, 173, 274, 326]. Certain quantities of interest, including the unstable SFE e_{USF}, stable SFE e_{SF}, unstable twinning energy e_{UT}, and stable twinning energy e_{T}, are labelled. Five atomic configurations are given in the top row, corresponding to a displacement of 0, 0.5, 1, 1.5, and 2, respectively, in unit of $a_0/\sqrt{6}$, along the $\langle 112 \rangle$ direction [304].

Five EAM potentials, by Mishin et al. [173], Angelo et al. [7], Foiles and Hoyt [89], Voter

and Chen [274], and Zhou et al. [326], respectively, are employed. In this chapter, these potentials are referred to by the last name of the first author; for example, Mishin-EAM. For all these interatomic potentials, certain material parameters of interest are calculated and listed in Tab. 9.1 in comparison with experimental [173] or *ab initio* simulation [128] results, including magnitude of the Burgers vector of the Shockley partial dislocation b_{p}, shear modulus for the $\langle 110 \rangle \{111\}$ system μ, stable SFE e_{SF}, unstable SFE e_{USF}, stable twinning energy (also the static $\Sigma 3$ CTB energy) e_{T}, unstable twinning energy e_{UT}, and static energy of the $\Sigma 11$ STGB e_{STGB}. Generalized fault energy curves along the $\langle 112 \rangle$ direction on a $\{111\}$ plane for all five potentials are given in Fig. 9.2. Note that for prior studies of dislocation/GB interactions in Ni, Mishin-EAM was used in Ref. [47, 117, 118], Angelo-EAM was used in Ref. [47], Foiles-EAM was used in Ref. [218], Voter-EAM was used in Ref. [319], while the last potential, Zhou-EAM, has not been employed for this purpose, to the best of the author's knowledge. By employing the same potentials adopted in previous quasi-2D QC and MD simulations, this chapter will shed light on the sensitivity of the simulated slip transfer mechanism to the interatomic potentials and the significance of large scale full 3D simulations.

9.3 Results and discussion

The initially straight pure screw dislocation lines bow out subject to the applied stress in the presence of traction free boundaries, obtaining mixed character. In the incoming grain, each curved dislocation splits into two Shockley partial dislocations, following Eq. 8.1. In the coarse-grained domain, the two partial dislocations are separated by a stable width of 22 Å using the Mishin-EAM potential (Fig. 9.3(a)), somewhat wider than the separation for a screw dislocation computed using full atomistic simulations [301].

9.3.1 $\Sigma 3\{111\}$ coherent twin boundary

At a shear stress of about 206 MPa, the leading partial in the incoming grain is stopped at the $\Sigma 3\{111\}$ CTB, with the stacking fault width constricting up to the point where the trailing partial also reaches the CTB, as shown in Fig. 9.3(b). Subsequently, two dislocation/CTB interaction modes are found:

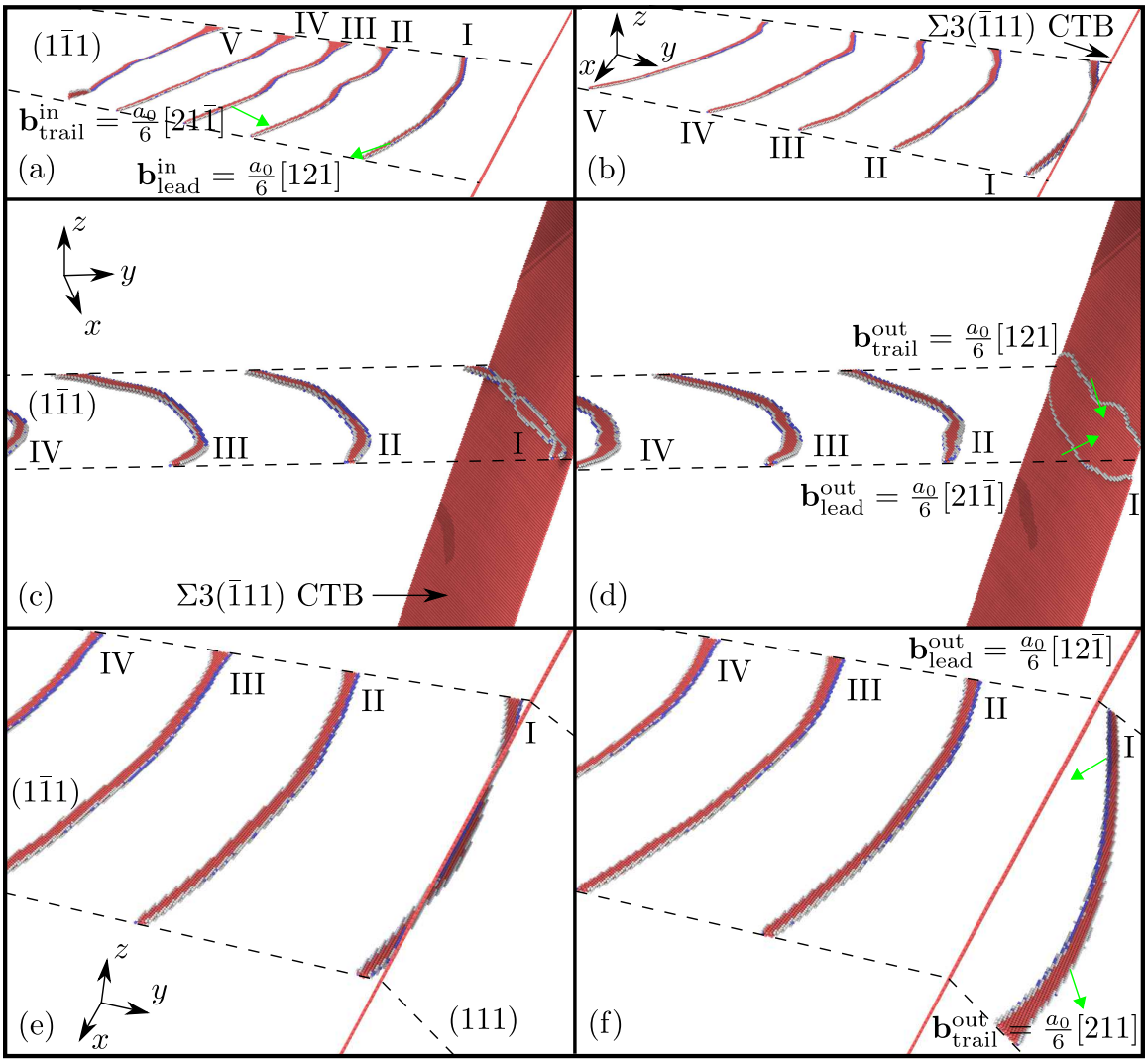

Figure 9.3: Snapshots of dislocation pile-up with dominant leading screw character impinging against a $\Sigma3\{111\}$ CTB. Each of the five incoming dislocations has Burgers vector $(a_0/2)[110]$. Atoms are colored by a-CNA [246]: red are of HCP local structure, blue are BCC atoms, and all FCC atoms are deleted. In (a), five incoming dislocations approach the CTB subject to an applied shear stress. In (b), the leading dislocation is constricted at the CTB, where two Shockley partial dislocations are recombined into a full dislocation. In (c–d), with Angelo-EAM, Foiles-EAM, and Zhou-EAM potentials, the redissociated dislocation is absorbed by the CTB, with two partials gliding on the twin plane in opposite directions, according to Eq. 8.4. In (e–f), with Mishin-EAM and Voter-EAM potentials, the dislocation effectively cross-slips into the outgoing twinned grain via redissociation into two partials, according to Eq. 8.2. Views of (a–b), (c–d), and (e–f) are illustrated in (b), (c), and (e), respectively [304].

1. For Angelo-EAM, Foiles-EAM, and Zhou-EAM potentials, the full dislocation is redissociated to two Shockley partials in the twin plane, following Eq. 8.4. The two CTB partial dislocations then move in opposite directions, migrating the CTB, growing the

outgoing grain by one atomic layer, and eventually exiting the top/bottom traction free cell boundaries, as shown in Figs. 9.3(c–d).

2. For Mishin-EAM and Voter-EAM potentials, however, instead of being absorbed by the CTB, the full dislocation is constricted and then re-dissociated into two Shockley partial dislocations which are transmitted into the outgoing grain, following Eq. 8.2; the outgoing dislocation continues migrating until exiting the rightmost traction free cell boundary, as shown in Figs. 9.3(e–f).

Reactions predicted by employing Mishin-EAM and Angelo-EAM potentials in CAC agree with previous MD simulations of a screw dislocation interacting with a $\Sigma 3$ CTB in Ni using the same potentials [47, 118]. In both modes of the dislocation/CTB interactions, the two partial dislocations exchange their order after encountering the CTB due to the twin symmetry, as in Chap. 8. Since each dislocation/CTB reaction does not leave residual Burgers vector in the CTB interface, the interaction mechanism for subsequent dislocations is found to be precisely the same as for the first dislocation. The minimum stress for each dislocation transmission/absorption, however, increases as there are fewer dislocations residing in the incoming pile-up. By comparison, a minimum applied shear stress of 480 MPa is needed for a single pure screw dislocation to be transmitted across the CTB with the Mishin-EAM potential [47].

Based on MD simulations of screw dislocation/CTB interactions, Jin et al. [118] employed two dimensionless parameters, i.e., (i) the resistance encountered by a screw dislocation to be transmitted through the CTB, $R = (e_{\mathrm{USF}} - e_{\mathrm{SF}})/\mu b_{\mathrm{p}}$, and (ii) the resistance to cross-slip on the CTB plane, $R' = (e_{\mathrm{UT}} - e_{\mathrm{SF}})/\mu b_{\mathrm{p}}$. In Jin et al.'s criterion [118], dislocation absorption by a $\Sigma 3$ CTB is predicted to occur if $R/R' = (e_{\mathrm{USF}} - e_{\mathrm{SF}})/(e_{\mathrm{UT}} - e_{\mathrm{SF}})$ is negative; otherwise, a dislocation would be transmitted through the CTB. For all five EAM potentials employed in this chapter, R/R' is between 1.01 and 1.08, whereas dislocation absorption is observed with three potentials. Thus, this criterion is not adequate to discriminate between screw dislocation absorption and transmission upon encountering a CTB [47]. Based on MD simulations, Chassagne et al. [47] proposed a new slip transfer criterion that materials

with a low $e_{\mathrm{SF}}/\mu b_{\mathrm{p}}$ have widely dissociated dislocations with a high constriction stress that favors transmission over absorption. In CAC simulations, the Voter-EAM potential has the smallest $e_{\mathrm{SF}}/\mu b_{\mathrm{p}}$ and gives dislocation transmission, while the Foiles-EAM potential, which has the largest $e_{\mathrm{SF}}/\mu b_{\mathrm{p}}$, results in dislocation absorption. The criterion of Chassagne et al. [47], however, does not sufficiently discriminate between dislocation transmission and absorption at a CTB either: although the Mishin-EAM potential has a higher $e_{\mathrm{SF}}/\mu b_{\mathrm{p}}$ than the Zhou-EAM potential, the incoming dislocation is transmitted across the CTB using the former while is absorbed by the CTB using the latter, at the same applied stress level. Inspection of Tab. 9.1 shows that the value of R itself, which is related to the nucleation of the trailing partial dislocation according to Rice's theory [211], can be used to predict dislocation/CTB reactions: Mishin-EAM and Voter-EAM potentials, which have the largest R, yield dislocation transmission, while the other EAM potentials with smaller R predict dislocation absorption. It is, however, difficult to predict what the dislocation/CTB reaction would be in a full *ab initio* simulation, because the *ab initio* value of R is smaller than that of Mishin-EAM potential, which yields dislocation transmission, but larger than that of Zhou-EAM potential, which results in dislocation absorption.

9.3.2 Σ11{113} symmetric tilt grain boundary

At a shear stress of 257 MPa, unlike the case of the Σ3 CTB, the full dislocation is not necessarily recombined at the Σ11{113} STGB. The leading partial in the incoming grain first splits into a leading partial dislocation belonging to the DSC lattice of the STGB and a stair-rod type of dislocation (Fig. 9.4(a–c)), i.e.,

$$\frac{1}{6}a_0[121]^{\mathrm{in}}_{\mathrm{lead}} \rightarrow \frac{1}{22}a_0[471]^{\mathrm{in}}_{\mathrm{lead}} + \frac{1}{66}a_0[\bar{1}18]^{\mathrm{in}}_{\mathrm{sr}} \tag{9.1}$$

where the subscript "sr" refers to the stair-rod type of dislocation, which then reacts with the trailing partial in the incoming grain (Fig. 9.4(d)), i.e.,

$$\frac{1}{66}a_0[\bar{1}18]^{\mathrm{in}}_{\mathrm{sr}} + \frac{1}{6}a_0[21\bar{1}]^{\mathrm{in}}_{\mathrm{lead}} \rightarrow \frac{1}{22}a_0[74\bar{1}]^{\mathrm{in}}_{\mathrm{trail}}. \tag{9.2}$$

The overall reaction in Eqs. 9.1 and 9.2 is

$$\frac{1}{6}a_0[121]^{\mathrm{in}}_{\mathrm{lead}} + \frac{1}{6}a_0[21\bar{1}]^{\mathrm{in}}_{\mathrm{trail}} \rightarrow \frac{1}{22}a_0[471]^{\mathrm{in}}_{\mathrm{lead}} + \frac{1}{22}a_0[74\bar{1}]^{\mathrm{in}}_{\mathrm{trail}}, \tag{9.3}$$

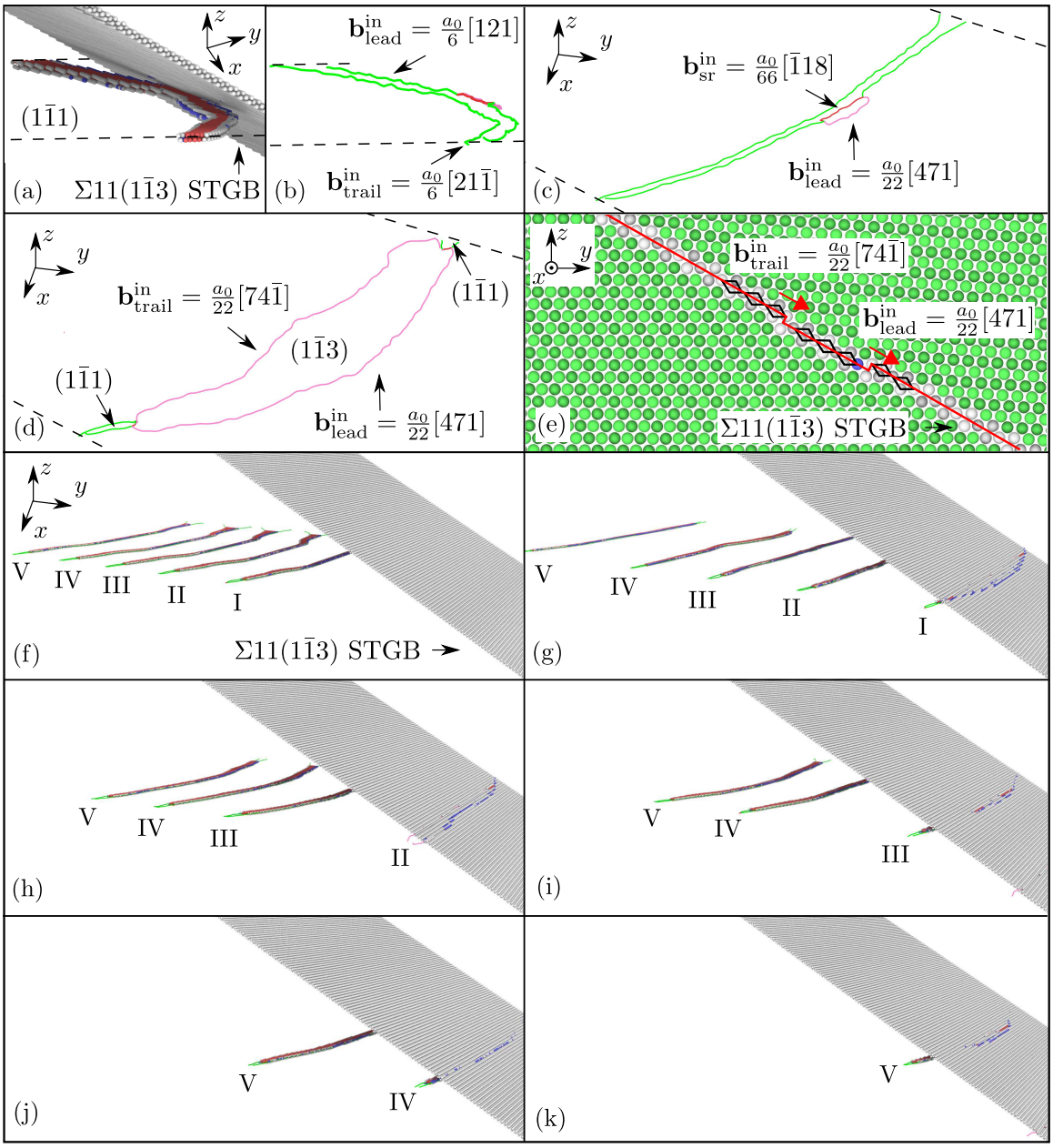

Figure 9.4: Snapshots of a series of $(a_0/2)[110]$ dislocations impinging on a $\Sigma 11\{113\}$ STGB. In (a) and (e–k), atoms are colored in the same matter as in Fig. 9.3, except that the FCC atoms (green) are not deleted in (e). In (b–d) and (f–k), a DXA is employed to illustrate dislocations as curved lines. (a–c) are taken at the same time but with different views and/or visualization methods, where the leading partial in the incoming grain splits into a partial dislocation on the STGB and a stair-rod type of dislocation, according to Eq. 9.1. (d–e) are taken at the same time but with different views and visualization methods, where the trailing partial in the incoming grain reacts with the stair-rod dislocation to form another partial dislocation on the STGB, according to Eq. 9.2. In (g–k), the interaction mechanism for subsequent dislocations is found to be precisely the same as for the first dislocation, because each dislocation/STGB reaction does not leave residual Burgers vector in the STGB interface. Views of (a–b), (c–d), (e), and (f–k) are illustrated in (a), (c), (e), and (f), respectively [304].

which is energetically favorable according to Frank's rule [110], since the original $b^2_{\text{lead}} + b^2_{\text{trail}} = (1/3)a_0^2$ while the resultant $b^2_{\text{lead}} + b^2_{\text{trail}} = (3/11)a_0^2$. The two STGB partials, with Burgers vectors parallel to the GB plane, locally grow the outgoing grain by one atomic layer. The PK forces drive the two STGB partials, separated by 101 Å, to migrate in the same positive y direction, before they eventually exit the bottom traction free surface. Note that a different applied stress tensor may alter the STGB partial dislocation migration, as suggested by Dewald and Curtin [72]. For the same $\Sigma 11\{113\}$ STGB, the two-step dislocation absorption in Eqs. 9.1 and 9.2 was observed for edge dislocations in a QC simulation in Ni [319], as well as edge and 60° mixed type dislocations in CADD simulations in Al [70, 72], but not for screw dislocations in a CADD simulation in Al [71], an MD simulation in Cu [189], or a high resolution TEM experiment in Ni [191], in which only reactions according to Eq. 9.3 were reported. This is probably due to an insufficient fidelity in monitoring the computational/experimental output. Similar to the $\Sigma 3$ CTB, the interaction mechanism for subsequent dislocations is found to be precisely the same as for the first dislocation, because each dislocation/STGB reaction does not leave residual Burgers vector in the STGB interface, as shown in Figs. 9.4(f–k). All five EAM potentials in the case of two interaction sites predict similar results.

9.3.3 A comparison between the two grain boundaries

In both $\Sigma 3\{111\}$ CTB and $\Sigma 11\{113\}$ STGB, dislocation absorption is manifested by a step height of one interplanar spacing in the GB, which grows the outgoing grain at the expense of the incoming grain. With certain interatomic potentials, both GBs act as sinks for lattice dislocations, absorbing dislocations from one grain and transferring to GB-mediated structural evolution. For Mishin-EAM and Voter-EAM potentials, however, the $\Sigma 3$ CTB acts as a barrier to dislocation motion, followed by transmission of full dislocations across the CTB under an applied stress; in this case, plastic behavior is apparently governed by lattice dislocation processes rather than CTB processes.

Based on MD simulations in Ni involving an isolated dislocation in a confined volume using the Foiles-EAM potential, Sangid et al. [218] proposed that GBs with lower static

interfacial energy offer a stronger barrier against slip transmission. In their work, dislocations of either pure edge or mixed type with dominant leading edge characters were employed, which are known to be transmitted through most GBs [150]. However, it raises a question whether the same model holds for incoming mixed dislocations with dominant leading screw character, which may be absorbed by GBs [304]. In CAC simulations, all five EAM potentials yield a much higher energy for the Σ11 STGB (e_{STGB}) than the Σ3 CTB (e_{T}). Angelo-EAM, Foiles-EAM, and Mishin-EAM potentials predict absorption of mixed type dislocations by both Σ3 CTB and Σ11 STGB, and thus it is difficult to determine which GB acts as a stronger barrier to slip transmission in these cases. On the other hand, Mishin-EAM and Voter-EAM potentials predict transmission of dislocations across a Σ3 CTB (with a low static energy) but absorption of the same dislocations by a Σ11 STGB (with a high static energy), in violation of Sangid et al.'s model [218]. This suggests that the static GB energy may serve as a slip transmission indicator under certain conditions, e.g., with particular dislocation types and interatomic potentials. In other words, the extraction of general dislocation/GB interaction criteria from limited studies is too simplistic and potentially misleading.

9.4 Summary

In this chapter, 0 K quenched dynamic CAC simulations with periodic energy minimization are employed to study 3D sequential slip transfer across a Σ3{111} CTB and a Σ11{113} STGB using five different interatomic potentials in Ni. A series of curved dislocations are driven toward both GBs subject to an applied shear stress. For the Σ3 CTB, the leading screw segment is transmitted into the twinned grain using two interatomic potentials, while it is absorbed and glides on the CTB when the other three potentials are employed. In both reactions, each dislocation always follows the recombination-redissociation process, without forming any CTB dislocations in the process of recombination. For the Σ11 STGB, however, all five interatomic potentials predict dislocation absorption, during which the leading partial dislocation in the incoming grain splits into an STGB partial dislocation and a stair-rod type dislocation, which subsequently reacts with the trailing partial dislocation in

the incoming grain to form another STGB partial dislocation. It is also found that certain slip transmission criteria in the literature, which are proposed based on limited studies, do not adequately predict the dislocation/GB reaction for different GBs and interatomic potentials. This chapter highlights the significance of 3D modeling of slip transfer across GBs and lays the foundation for multiscale computer models involving a large number of dislocations in pile-ups and a variety of GB types.

CHAPTER X

CONTRIBUTIONS AND RECOMMENDATIONS

10.1 Contributions

This dissertation has mainly contributed towards advancing multiple aspects of the CAC approach and exploring a series of dislocation plasticity phenomena in FCC metals. Key contributions are as follows:

1. In Chap. 2, the theoretical foundation, mathematical formulation, and numerical implementation of the CAC method are described in detail. In particular, the choice of integration points, Gaussian quadrature, and the coarse-graining efficiency are discussed. The computational mechanics of materials community can benefit from this chapter, in which the method is described in a detailed, mathematically rigorous manner sufficient for CAC simulation results to be reproducible.

2. In Chap. 3, four main advancements of the CAC method are made. First, new types of finite elements are proposed, giving an accurate GSFE without mesh refinement to atomistic scale which, to the author's knowledge, is beyond the capability of existing coarse-grained methods in the literature. Second, zero temperature CAC approaches are developed to avoid common overdriven conditions associated with very high strain rates in MD and/or thermal fluctuation. The combined quenched dynamic and quasistatic CAC method minimizes the energy of dislocated ensemble that evolves with a sequence of constrained nonequilibrium configurations. Third, two mesh refinement schemes are introduced that expand the CAC method's capability to handle the evolution of more complex extended defect structures. Last, the CAC code is re-written using the object-oriented FORTRAN 2003. Although the algorithm has similarities with full atomistics, some distinctions are addressed, including the integration points, the force/energy/stress calculation, periodic boundaries, and parallel computing implementation.

3. In Chap. 4, the advanced CAC approach is employed to study certain benchmark problems including GSFE, stress fields and core structure/radius/energy of a single dislocation, Peierls stress, indentation at a surface, dislocations migration through the interface between atomistic and coarse-grained domains, overall Burgers vector of dislocations, BTD transition in dynamic fracture, and curved dislocation migration. In this chapter, dislocations in the coarse-grained domain are systematically studied for the first time; direct evidence is provided to show that the overall Burgers vector and long range stress field of dislocations are preserved. The success of these calculations suggests the viability of using CAC simulations in the context of more complicated processes of plastic deformation of FCC metals.

4. In Chap. 5, dynamic CAC and MD simulations are conducted to study the shear stress- and line length-dependent screw dislocation cross-slip in Ni. In the case of a dislocation of length 77.66 nm, the following events operate at increasing applied shear stress levels: (i) the dislocation begins to move once the resolved shear stress on the primary plane overcomes the Peierls stress, (ii) the dislocation cross-slips via the FE mechanism, and (iii) the dislocation cross-slips via the FL mechanism. This suggests that the cross-slip process depends on the applied shear stress. The dislocation cross-slip mechanism is also line length-dependent. In particular, the FE mechanism at low applied shear stresses is not observed for a short dislocation line of 6.47 nm, but for a longer dislocation of 12.94 nm. Moreover, a longer dislocation line has a slightly lower critical shear stress for cross-slip operation.

5. In Chap. 6, quasistatic CAC simulations are conducted to study the bowing of edge dislocations from a row of collinear obstacles in Al. By calculating the critical shear stresses and critical dislocation bow-out configurations, it is found that as the number of adjacent bowed-out dislocation segments increases, the critical dislocation depinning stress approaches that for an infinite array of collinear obstacles. In addition, for the unstable critical semi-elliptic dislocation configuration, the presence of intermediate bowed-out segments does not influence the critical shear stress, but reduces

the dislocation half-loop height.

6. In Chap. 7, dislocation multiplication from FR sources is systematically explored in Cu, Ni, and Al via dynamic and quasistatic CAC simulations. Three key characteristics of the FR source process, namely dislocation nucleation/loop formation time, critical shear stress, and critical dislocation configuration, are studied. In all these materials, the critical stresses and the aspect ratio of the dislocation half-loop height to the FR source length scale well with respect to the FR source length. In Al, the critical stress calculated by CAC simulations for a given FR source length agrees reasonably well with an isotropic continuum model that explicitly includes the dislocation core energy. Nevertheless, the predictions of the isotropic elastic theory do not accurately capture the FR source responses in Cu and Ni, which have a relatively large stacking fault width and stronger elastic anisotropy.

7. In Chap. 8, CAC simulations are performed to study sequential slip transfer of a series of curved dislocations from a given pile-up on $\Sigma 3$ CTB in fully 3D models for Cu and Al, the first attempt to do so in the literature, to the author's knowledge. It is found that incoming dislocations transfer into the twinned grain in Cu via a cross-slip mechanism but glide on the twin plane in Al. In particular for Al, four dislocation/CTB interaction modes are identified. The effect of a dislocation pile-up is manifested by varying the applied stress. It is emphasized that the results obtained for a single dislocation/CTB interaction cannot be directly extrapolated to understand the practical case of slip transfer of dislocations in a pile-up.

8. In Chap. 9, large scale CAC simulations are performed to address the slip transfer of mixed character dislocations across GBs in Ni. Two symmetric GBs, a $\Sigma 3\{111\}$ CTB and a $\Sigma 11\{113\}$ STGB, are investigated using five different interatomic potentials. It is shown that for the $\Sigma 3$ CTB, two of these potentials predict dislocation transmission while the other three predict dislocation absorption. In contrast, all five potentials predict that dislocations are absorbed by the $\Sigma 11$ STGB. Simulation results are examined in terms of several slip transfer criteria in the literature, highlighting the

complexity of dislocation/GB interactions and the significance of directly modeling the slip transfer process involving a large number of dislocations and a wide variety of GBs.

10.2 Recommendations for future work

The work in this dissertation establishes that the CAC approach is useful at intermediate length scales between fully-resolved atomistics and DD/PFM/CPFEM. In this regard, CAC can serve as a complement to methods at the lower and higher length scales. Compared with MD/MS, the advantage of CAC is that with greatly reduced DOFs, the key characteristics of complex dislocation behavior can be reasonably well described, despite coarse-graining errors of a wider stacking fault width, a lower SFE, a flatter dislocation core, a larger core radius, a higher core energy, and a lower Peierls stress. Hence, even with systematic coarse-graining error, as quantified in Chap. 4, CAC can provide useful guidance regarding the form of higher scale constitutive models. As the element size is reduced, the CAC predictions properly converge to the fully atomistic results. Compared to DD, in which only the dislocation lines are resolved, CAC simulations contain more DOFs and are less computationally efficient; however, CAC resolves dislocation core effects explicitly, in addition to long range elastic interactions. Note that the CAC method is especially useful to explore problems in which full atomistic resolution is required in some regions (e.g., complex atomistic phenomena involving dislocations reactions with other defects), with coarse-graining employed elsewhere to support representation of dislocation interactions and transport. In such cases, dislocation lines span between fully resolved atomistic and coarse-grained domains with the same constitutive equation used everywhere. Examples include, but are not limited to, dislocation/GB interactions, dislocation/obstacle interactions, and dislocation substructure evolution.

Some possible extensions of the work conducted in this dissertation and future directions are as follows.

10.2.1 Finite temperature dynamic CAC

Section 3.3 extends the CAC method to the regime of zero temperature modeling, i.e., zero temperature dynamics and quasistatics, which are formulated in most other concurrent multiscale methods as well [254]. For most multiscale methods, one of the biggest challenges is to enable finite temperature dynamics in both atomistic and continuum domains in a consistent manner [162, 260, 288, 289, 315]. As discussed in Sec. 3.3.1, the equilibrium dynamic CAC, which involves only two of the three governing equations, Eqs. 2.2 and 2.3, suffer from the ill-defined temperature (Eq. 3.4) and kinetic energy (Eq. 3.5). Thus, the next step to further advance CAC is to develop a novel description of the temperature in the coarse-grained domain such that it is consistent with that in the atomistic domain. Another future work, which is more challenging, is to advance non-equilibrium finite temperature dynamic CAC, requiring implementing the balance equation of energy (Eq. 2.4).

It is advisable to learn from the way other concurrent simulations handle finite temperature dynamics. Consider the QC method as an example. It took about two decades to develop both equilibrium and non-equilibrium finite temperature QC methods. The first finite temperature QC approach was proposed in 1998, where the atomic velocity is replaced by the nodal velocity in the kinetic energy formulation for equilibrium finite temperature [228], according to Eqs. 3.4 and 3.5. In 2002, Miller and Tadmor [171] discussed the preliminary idea of implementing local harmonic approximation into QC for non-equilibrium finite temperature dynamics — this method is called QC Monte Carlo or QC free energy minimization. Later in 2005, Dupuy et al. [75] employed a potential of mean force method. Then in 2008, Kulkarni et al. [135] combined the variational mean-field theory and the maximum-entropy (max-ent) formalism to extend quasistatic QC to both equilibrium and non-equilibrium finite temperature dynamics. Marian et al. [163] gave a finite temperature extension of the QC method using Langevin dynamics. In 2013, Tadmor et al. [253] presented a generalization of the QC method to finite temperature dynamics termed "hot-QC". More recently in 2014, Venturini et al. [272] formulated a theory of non-equilibrium statistical thermodynamics for ensembles of atoms to reproduce equilibrium properties and long-term behavior of complex systems in QC.

10.2.2 Adaptive mesh refinement schemes for CAC

For dislocation migration, mesh refinement schemes are developed in CAC in Sec. 3.4.5. However, this work by no means completely addresses the issues of consistency of thermodynamics between atomistic and continuum domains during adaptive mesh refinement. In the future, a fully adaptive mesh refinement scheme for dislocation migration in 3D models will be developed. In particular, instead of refining an element into atomic scale, an element will split into two smaller ones, as has been manually done by Xiong et al. [291]. The key to such an approach is to identify the dislocations concurrent with the simulations: in the atomistic domain, a dislocation can be detected using a DXA [247]; in the coarse-grained domain, a nodal-based dislocation detection method can be employed to track dislocations. This coarse-grained dislocation detection method would render a much faster post-processing than the full atomistic approach. Developing such a method is not only important for CAC simulations, but also may aid in analyzing results from more general discontinuous field simulations.

Other types of adaptive mesh refinement under consideration include, but are not limited to, p-refinement, h-refinement in which a collection of atoms are coarsened into elements, as well as an adaptive conversion between a 1NN element, which is faster but less accurate and used away from defects, and a 2NN element, which is slower but more accurate and used in the vicinity of defects [300]. Attention will also be paid in constructing an *a posteriori* error estimator as well as dealing with multiple time scale issues which are potentially relevant to mesh refinement.

10.2.3 Screw dislocation cross-slip

In Chap. 5, both the low temperature dynamic and quasistatic simulations can only calculate the critical stress for an event, e.g., dislocation gliding, cross-slip, but not its energy barrier [100]. The NEB method [101], which has been employed to quantify the activation energy of cross-slip [116, 124, 205, 207, 271], can be applied with CAC to explore the energy barrier and more detailed minimum energy pathway for much more extended dislocations at the submicron and micron scales. Also, only the bulk dislocation cross-slip via an acute

angle is investigated in Chap. 5. Other types of cross-slip, such as surface and dislocation intersection cross-slip [115], via an obtuse angle, which has a higher activation energy and, for the FL mechanism, a stair-rod dislocation of (1/6)[200] type [88], will receive future attention. The issue of screw dislocation cross-slip in a single pile-up, which involves a length scale inaccessible to classical atomistic simulations, will be explored using CAC as well — such simulations are expected to provide important input to higher scale theory or simulation tool.

10.2.4 Dislocation bowing-out and Frank-Read source process

Chapter 6 studies the process of edge dislocations bowing-out from a collinear row of equidistant obstacles. Future work will include applying CAC to more realistic models with obstacles that are nonuniformly spaced, of varying size, randomly distributed, and/or with long range stress fields, e.g., forest dislocations. Note that if the dislocation continues to grow, beyond the critical configuration shown in Fig. 6.4, it will wrap around and interact with the holes. Such interactions, i.e., void hardening [127], will be addressed in a future study that is focused on work hardening behavior that results from dislocation/void interactions.

In Chap. 7, three key characteristics of the FR source process are analyzed. Results obtained can be used to assist in formulating constitutive laws and rules that may be useful upstream in PFM, certain DD codes [15, 69], and CPFEM for obstacle-induced work hardening. For example, in some CPFEM work [105], the critical shear stress is incorporated into the isotropic hardening term and the yield surface. FR sources with other initial dislocation character such as pure screw and mixed type, different line orientations and shearing directions, as well as the influence of FR source exhaustion will be assessed in future work.

Under dynamic loading, the work dissipated by the bow-out may not be balanced by the dislocation line tension, suggesting reformulation of the continuum models for critical stress discussed in Chaps. 6 and 7. Moreover, dislocation segments have the lowest mean glide velocity at the critical shape [21], and a high strain rate and/or applied shear stress will reduce the aspect ratio H/L [104]; the dislocation configuration is further complicated by

that the mobility of an edge component is higher than that of a screw component [42] such that the critical configuration at different stress levels will be significantly different [236], a phenomenon that merits further investigation. Following earlier CAC simulations [298] which found that a high strain rate reduces the void strengthening effect, it will also be interesting to explore the FR source behavior dependence on the strain rate.

10.2.5 Slip transfer of dislocations across general grain boundaries

Slip transfer of curved dislocations with dominant leading screw character across a $\Sigma 3$ CTB and a $\Sigma 11$ GB are studied in Chaps. 8 and 9. The slip transfer of more general dislocation types with different curvatures interacting with more general GBs will be addressed in future work.

For example, the $\Sigma 3 \langle 110 \rangle \{111\}$ CTB has a misorientation angle θ of 109.5° around the $\langle 110 \rangle$ axis and the highest maximum tensile stress among all GBs. $\langle 110 \rangle$ STGBs with $\theta > 109.5^\circ$, however, require only extremely low stresses to emit dislocations, which does not fit the model for dislocation nucleation from $\langle 110 \rangle$ STGBs with $\theta < 109.5^\circ$ [242]. Tschopp et al. [263] attribute this phenomenon to the E structural unit (SU) contained in the GB, which has a unique free volume spatial distribution and connectivity. Atomistic simulations also indicate that the natural conformation of the interface porosity with respect to the primary dislocation slip systems is responsible for the easy emission of Shockley partial dislocations from GBs containing the E SU during a tensile deformation [240]. Using QC simulations, Sansoz and Molinari [219] found that the E SU in the period of Σ tilt GBs is responsible for the onset of sliding by atomic shuffling. Among all $\langle 110 \rangle$ STGBs with $\theta > 109.5$, $\Sigma 9 \langle 110 \rangle \{221\}$ and $\Sigma 11 \langle 110 \rangle \{332\}$ have the smallest Σ number and the simplest structures. Despite the significance of the E SU, most simulations (either full atomistic or multiscale) of slip transfer through $\Sigma 9$ and $\Sigma 11$ GBs study either $\Sigma 9 \langle 112 \rangle \{114\}$ GBs [70], $\Sigma 11 \langle 112 \rangle \{113\}$ GBs [70, 71, 318–320], $\Sigma 9 \langle 110 \rangle \{114\}$ GBs [72], $\Sigma 11 \langle 110 \rangle \{113\}$ GBs [72], or $\Sigma 11 \langle 110 \rangle$ asymmetric tilt GBs [277]; none of these GBs contains the E SU.

Therefore, it will be interesting to perform CAC simulations to investigate sequential slip transfer across $\Sigma 11 \langle 110 \rangle \{332\}$ GB ($\theta = 129.5^\circ$), as well as its vicinal boundaries

$\Sigma 123\,\langle 110\rangle\,\{775\}$ GB with $\theta = 126.4^\circ$ and $\Sigma 291\,\langle 110\rangle\,\{11, 11, 7\}$ GB with $\theta = 131.5^\circ$, all of which contain the E SU. Atomistic simulations show that only relatively slight change of the misorientation angle can completely modify the GB structure and dislocation-mediated behavior [261, 262]. The role of the E SU in dislocation/GB interactions, including dislocation glide in the outgoing grain and GB structure evolution, will be explored using CAC simulations. The same study is difficult for full atomistics because the high Σ number GBs (i.e., $\Sigma 123$ and $\Sigma 291$) have a large lattice periodic length. In DD, while low angle GBs are described by arrays of dislocations, high angle GBs are typically avoided, considered as impenetrable walls, or the stress field at the leading dislocation in the pile-up activates dislocation sources that are embedded either at GBs or in the neighboring grain [154]. For these reasons, the CAC method is well-suited for the proposed work.

Besides the tilt GBs, another important type of GBs in polycrystalline materials is that with twist characters [249]. The $\Sigma 3$ CTB can be viewed as a twist GB with the twist angle $\theta = 60^\circ$ on a $\{111\}$ plane. Most studies in the literature, however, involve only tilt GBs. Atomistic simulations found that compared with tilt GBs, both energy and maximum tensile stress of twist GBs are much less sensitive to the misorientation angle [239]. MD simulations in Cu reveal that subject to a shear deformation, while dislocation nucleation controls the yield stress of low angle twist GBs, GB sliding dominates the yielding for high angle twist GBs [324]. Liu et al. [155] found that a low angle twist GB consists of a network of screw dislocations while the tilt GB can be represented by a network of edge dislocations. Although a few efforts have been put in investigating twist GB energy/structure and dislocation-mediated behavior, no simulation, to the author's best knowledge, has been employed to explore dislocation/twist GB interactions.

Therefore, CAC simulations will be performed in the future to investigate sequential slip transfer across three $\{111\}$ twist low angle GBs in FCC metals, with the twist angles θ of 1.2°, 4°, and 8°, respectively. Dai et al. [63] showed that the energy and structures of these three twist GBs can be derived by a generalized PN model of a hexagonal dislocation network. High angle twist GBs with $\theta > 12.5^\circ$ may not be considered because their structures will change under an applied shear stress, even in the absence of incoming dislocations [324];

in studying the slip transfer process, one may prefer that the GB evolution subject to the applied stress and that due to the dislocation impingement are decoupled.

10.2.6 Miscellaneous recommendations

Some other recommendations for future work in the context of methodological advancements and applications of CAC that were not discussed in the foregoing include:

1. Providing a comprehensive convergence and error analysis involving different integration schemes in the coarse-grained domain, in the spirit of Ref. [309];

2. Implementing higher order shape/interpolation functions and/or enrichment functions within elements to admit dislocations in element interior regions [19]; also, general parallelogrammic elements, in which all edges are not necessarily the same length, will be developed to accommodate more general simulation cell geometry and dislocation structure;

3. Employing new types of finite elements to replace the filled-in atoms at the otherwise zigzag simulation cell boundaries to reduce the computational cost, particularly in the case of PBCs;

4. Developing new types of finite elements in the coarse-grained domain in CAC for BCC and HCP systems. For example, possible slip systems in BCC lattice include 12 sets of $\{110\}\langle 111\rangle$-type, 12 sets of $\{112\}\langle 111\rangle$-type, and 24 sets of $\{123\}\langle 111\rangle$-type; care will be taken in that screw dislocations in a BCC lattice may not have a planar core [42]. Slip in HCP is even more complicated, describing which may require each node of an element to contain two atoms [285];

5. Employing transition state theory with activation energy barriers assessed using NEB or autonomous basin climbing methods [136] in CAC to extend the time scale and to obtain coarse-grained energy barrier, e.g., Peierls barrier, to complement the Peierls stress that was calculated in Sec. 4.5, and to provide such information to coarse-grained continuum models. Accelerated MD approaches such as hyperdynamics [45] can also be adopted to increase the time step in dynamic CAC;

6. Investigating the "valve effect" in fracture [153] using models with graded element size to account for the effects of strain gradient at a crack tip. Dynamic fracture will also be explored: on other one hand, a high strain rate favors brittle fracture [55]; on the other hand, a high strain rate is accompanied by a high overall stress which favors ductile fracture. The combined effects of strain rate and applied stress in ductile versus brittle fracture will be quantified;

7. Applying CAC to dislocation substructure evolution problems. Dislocation/dislocation interactions will be quantified. At large plastic strains, significant dislocation network density dominates the work hardening; dislocation multiplication is restricted, pile-up is relaxed, and the dependence of strength on grain size then diminishes relative to the dependence on the dislocation substructure scale(s) [80]. The scaling law between dislocation density and flow stress [79] will be investigated.

REFERENCES

[1] Abad, O. T., Wheeler, J. M., Michler, J., Schneider, A. S., and Arzt, E., "Temperature-dependent size effects on the strength of Ta and W micropillars," *Acta Mater.*, vol. 103, pp. 483–494, Jan. 2016.

[2] Abraham, F. F., "On the transition from brittle to plastic failure in breaking a nanocrystal under tension (NUT)," *Europhys. Lett.*, vol. 38, pp. 103–106, Apr. 1997.

[3] Abraham, F. F., Broughton, J. Q., Bernstein, N., and Kaxiras, E., "Spanning the continuum to quantum length scales in a dynamic simulation of brittle fracture," *Europhys. Lett.*, vol. 44, pp. 783–787, Dec. 1998.

[4] Abraham, F. F., Schneider, D., Land, B., Lifka, D., Skovira, J., Gerner, J., and Rosenkrantz, M., "Instability dynamics in three-dimensional fracture: An atomistic simulation," *J. Mech. Phys. Solids*, vol. 45, pp. 1461–1471, Sept. 1997.

[5] Alankar, A., Field, D. P., and Zbib, H. M., "Explicit incorporation of cross-slip in a dislocation density-based crystal plasticity model," *Philos. Mag.*, vol. 92, pp. 3084–3100, Aug. 2012.

[6] Allen, M. P. and Tildesley, D. J., *Computer simulation of liquids*. Oxford University Press, USA, June 1989.

[7] Angelo, J. E., Moody, N. R., and Baskes, M. I., "Trapping of hydrogen to lattice defects in nickel," *Modelling Simul. Mater. Sci. Eng.*, vol. 3, no. 3, p. 289, 1995.

[8] Arndt, M. and Luskin, M., "Goal-oriented adaptive mesh refinement for the quasi-continuum approximation of a Frenkel-Kontorova model," *Comput. Meth. Appl. Mech. Eng.*, vol. 197, pp. 4298–4306, Sept. 2008.

[9] Aubry, S., Fitzgerald, S. P., and Arsenlis, A., "Methods to compute dislocation line tension energy and force in anisotropic elasticity," *Modelling Simul. Mater. Sci. Eng.*, vol. 22, no. 1, p. 015001, 2014.

[10] Bachurin, D. V., Weygand, D., and Gumbsch, P., "Dislocation-grain boundary interaction in ⟨111⟩ textured thin metal films," *Acta Mater.*, vol. 58, pp. 5232–5241, Sept. 2010.

[11] Bacon, D. J., "A method for describing a flexible dislocation," *Phys. Stat. Sol. (b)*, vol. 23, pp. 527–538, Jan. 1967.

[12] Bacon, D. J., Kocks, U. F., and Scattergood, R. O., "The effect of dislocation self-interaction on the Orowan stress," *Philos. Mag.*, vol. 28, pp. 1241–1263, Dec. 1973.

[13] Bacon, D. J., Osetsky, Y. N., and Rodney, D., "Dislocation-obstacle interactions at the atomic level," in *Dislocations in Solids* (Kubin, L. and Hirth, J. P., eds.), vol. 15, pp. 1–90, Elsevier, 2009.

[14] Bacon, D. J. and Osetsky, Y. N., "The atomic-scale modeling of dislocation-obstacle interactions in irradiated metals," *JOM*, vol. 59, pp. 40–45, June 2007.

[15] Balint, D. S., Deshpande, V. S., Needleman, A., and Van der Giessen, E., "Discrete dislocation plasticity analysis of the grain size dependence of the flow strength of polycrystals," *Int. J. Plast.*, vol. 24, pp. 2149–2172, Dec. 2008.

[16] Beissel, S. and Belytschko, T., "Nodal integration of the element-free Galerkin method," *Comput. Meth. Appl. Mech. Eng.*, vol. 139, pp. 49–74, Dec. 1996.

[17] Belytschko, T. and Black, T., "Elastic crack growth in finite elements with minimal remeshing," *Int. J. Numer. Meth. Eng.*, vol. 45, pp. 601–620, June 1999.

[18] Belytschko, T., Moës, N., Usui, S., and Parimi, C., "Arbitrary discontinuities in finite elements," *Int. J. Numer. Meth. Eng.*, vol. 50, pp. 993–1013, Feb. 2001.

[19] Belytschko, T., Gracie, R., and Ventura, G., "A review of extended/generalized finite element methods for material modeling," *Modelling Simul. Mater. Sci. Eng.*, vol. 17, p. 043001, June 2009.

[20] Belytschko, T., Liu, W. K., Moran, B., and Elkhodary, K., *Nonlinear finite elements for continua and structures*. Chichester, West Sussex, United Kingdon: Wiley, 2nd ed., Jan. 2014.

[21] Benzerga, A. A., "An analysis of exhaustion hardening in micron-scale plasticity," *Int. J. Plast.*, vol. 24, pp. 1128–1157, July 2008.

[22] Benzerga, A. A., Bréchet, Y., Needleman, A., and Van der Giessen, E., "Incorporating three-dimensional mechanisms into two-dimensional dislocation dynamics," *Modelling Simul. Mater. Sci. Eng.*, vol. 12, no. 1, p. 159, 2004.

[23] Benzerga, A. A., "Micro-pillar plasticity: 2.5D mesoscopic simulations," *J. Mech. Phys. Solids*, vol. 57, pp. 1459–1469, Sept. 2009.

[24] Berry, J., Provatas, N., Rottler, J., and Sinclair, C. W., "Phase field crystal modeling as a unified atomistic approach to defect dynamics," *Phys. Rev. B*, vol. 89, p. 214117, June 2014.

[25] Bieler, T. R., Eisenlohr, P., Zhang, C., Phukan, H. J., and Crimp, M. A., "Grain boundaries and interfaces in slip transfer," *Curr. Opin. Solid State Mater. Sci.*, vol. 18, pp. 212–226, Aug. 2014.

[26] Bitzek, E., Brandl, C., Derlet, P. M., and Van Swygenhoven, H., "Dislocation cross-slip in nanocrystalline fcc metals," *Phys. Rev. Lett.*, vol. 100, p. 235501, June 2008.

[27] Bitzek, E. and Gumbsch, P., "Atomistic study of drag, surface and inertial effects on edge dislocations in face-centered cubic metals," *Mater. Sci. Eng.: A*, vol. 387–389, pp. 11–15, Dec. 2004.

[28] Bitzek, E., Kermode, J. R., and Gumbsch, P., "Atomistic aspects of fracture," *Int. J. Fract.*, vol. 191, pp. 13–30, Feb. 2015.

[29] Bitzek, E., Koskinen, P., Ghler, F., Moseler, M., and Gumbsch, P., "Structural relaxation made simple," *Phys. Rev. Lett.*, vol. 97, p. 170201, Oct. 2006.

[30] Biyikli, E. and To, A. C., "Multiresolution molecular mechanics: Adaptive analysis," *Comput. Meth. Appl. Mech. Eng.*, vol. 305, pp. 682–702, June 2016.

[31] Biyikli, E. and To, A. C., "Multiresolution molecular mechanics: Implementation and efficiency," *J. Comput. Phys.*, vol. 328, pp. 27–45, Jan. 2017.

[32] Biyikli, E., Yang, Q., and To, A. C., "Multiresolution molecular mechanics: dynamics," *Comput. Meth. Appl. Mech. Eng.*, vol. 274, pp. 42–55, June 2014.

[33] Brommer, D. B. and Buehler, M. J., "Failure of graphdiyne: structurally directed delocalized crack propagation," *J. Appl. Mech.*, vol. 80, p. 040908, May 2013.

[34] Brown, L. M., "The self-stress of dislocations and the shape of extended nodes," *Philos. Mag.*, vol. 10, pp. 441–466, Sept. 1964.

[35] Brown, L. M., "A proof of Lothe's theorem," *Philos. Mag.*, vol. 15, pp. 363–370, Feb. 1967.

[36] Brünger, A., Brooks III, C. L., and Karplus, M., "Stochastic boundary conditions for molecular dynamics simulations of ST2 water," *Chem. Phys. Lett.*, vol. 105, pp. 495–500, Mar. 1984.

[37] Buehler, M. J., Hartmaier, A., Gao, H., Duchaineau, M. A., and Abraham, F. F., "The dynamical complexity of work-hardening: a large-scale molecular dynamics simulation," *Acta Mech. Sinica*, vol. 21, pp. 103–111, Apr. 2005.

[38] Bulatov, V. and Cai, W., *Computer simulations of dislocations*. Oxford ; New York: Oxford University Press, Dec. 2006.

[39] Bulatov, V., Cai, W., Fier, J., Hiratani, M., Hommes, G., Pierce, T., Tang, M., Rhee, M., Yates, K., and Arsenlis, T., "Scalable line dynamics in ParaDiS," in *Proceedings of the 2004 ACM/IEEE Conference on Supercomputing*, SC '04, (Washington, DC, USA), p. 19, IEEE Computer Society, 2004.

[40] Cai, W., Arsenlis, A., Weinberger, C. R., and Bulatov, V. V., "A non-singular continuum theory of dislocations," *J. Mech. Phys. Solids*, vol. 54, pp. 561–587, Mar. 2006.

[41] Cai, W., Bulatov, V. V., Chang, J., Li, J., and Yip, S., "Anisotropic elastic interactions of a periodic dislocation array," *Phys. Rev. Lett.*, vol. 86, pp. 5727–5730, June 2001.

[42] Cai, W., Bulatov, V. V., Chang, J., Li, J., and Yip, S., "Dislocation core effects on mobility," in *Dislocations in Solids* (Hirth, J. and Nabarro, F., eds.), vol. 12, pp. 1–80, Elsevier, 2005.

[43] Cai, W., de Koning, M., Bulatov, V. V., and Yip, S., "Minimizing boundary reflections in coupled-domain simulations," *Phys. Rev. Lett.*, vol. 85, pp. 3213–3216, Oct. 2000.

[44] Cantrell, J. H., "Substructural organization, dislocation plasticity and harmonic generation in cyclically stressed wavy slip metals," *Proc. R. Soc. Lond. A*, vol. 460, pp. 757–780, Mar. 2004.

[45] Chakraborty, S., Zhang, J., and Ghosh, S., "Accelerated molecular dynamics simulations for characterizing plastic deformation in crystalline materials with cracks," *Comput. Mater. Sci.*, vol. 121, pp. 23–34, Aug. 2016.

[46] Chapra, S. and Canale, R., *Numerical methods for engineers*. Boston: McGraw-Hill Science/Engineering/Math, 6th ed., Apr. 2009.

[47] Chassagne, M., Legros, M., and Rodney, D., "Atomic-scale simulation of screw dislocation/coherent twin boundary interaction in Al, Au, Cu and Ni," *Acta Mater.*, vol. 59, pp. 1456–1463, Feb. 2011.

[48] Chen, Y. and Lee, J., "Atomistic formulation of a multiscale field theory for nano/micro solids," *Philos. Mag.*, vol. 85, no. 33-35, pp. 4095–4126, 2005.

[49] Chen, Y., Lee, J., and Xiong, L., "A generalized continuum theory and its relation to micromorphic theory," *J. Eng. Mech.*, vol. 135, no. 3, pp. 149–155, 2009.

[50] Chen, Y., "Reformulation of microscopic balance equations for multiscale materials modeling," *J. Chem. Phys.*, vol. 130, p. 134706, Apr. 2009.

[51] Chen, Y. and Lee, J. D., "Connecting molecular dynamics to micromorphic theory. (I). Instantaneous and averaged mechanical variables," *Phys. A: Statis. Mech. Appl.*, vol. 322, pp. 359–376, May 2003.

[52] Chen, Y. and Lee, J. D., "Connecting molecular dynamics to micromorphic theory. (II). Balance laws," *Phys. A: Statis. Mech. Appl.*, vol. 322, pp. 377–392, May 2003.

[53] Chen, Y., Zimmerman, J., Krivtsov, A., and McDowell, D. L., "Assessment of atomistic coarse-graining methods," *Int. J. Eng. Sci.*, vol. 49, pp. 1337–1349, Dec. 2011.

[54] Chen, Z., Jin, Z., and Gao, H., "Repulsive force between screw dislocation and coherent twin boundary in aluminum and copper," *Phys. Rev. B*, vol. 75, p. 212104, June 2007.

[55] Cheung, K. S. and Yip, S., "A molecular-dynamics simulation of crack-tip extension: The brittle-to-ductile transition," *Modelling Simul. Mater. Sci. Eng.*, vol. 2, pp. 865–892, July 1994.

[56] Cho, J., Junge, T., Molinari, J.-F., and Anciaux, G., "Toward a 3D coupled atomistic and discrete dislocation dynamics simulation: dislocation core structures and Peierls stresses with several character angles in FCC aluminum," *Adv. Model. Simul. Eng. Sci.*, vol. 2, p. 12, June 2015.

[57] Cockburn, B., Karniadakis, G. E., and Shu, C.-W., *Discontinuous galerkin methods: Theory, computation and applications*. Springer, softcover reprint of the original 1st ed. 2000 ed., Sept. 2011.

[58] Cottrell, A. H., "Commentary. A brief view of work hardening," in *Dislocations in Solids* (Duesbery, M. S. and Nabarro, F. R. N., eds.), vol. 11, pp. vii–xvii, Elsevier, 2002.

[59] Counts, W. A., Braginsky, M. V., Battaile, C. C., and Holm, E. A., "Predicting the Hall-Petch effect in fcc metals using non-local crystal plasticity," *Inter. J. Plast.*, vol. 24, pp. 1243–1263, July 2008.

[60] Courtney, T. H., *Mechanical behavior of materials*. Waveland Pr Inc, 2 ed., Dec. 2005.

[61] Crone, J. C., Munday, L. B., and Knap, J., "Capturing the effects of free surfaces on void strengthening with dislocation dynamics," *Acta Mater.*, vol. 101, pp. 40–47, Dec. 2015.

[62] Cui, B., Kacher, J., McMurtrey, M., Was, G., and Robertson, I. M., "Influence of irradiation damage on slip transfer across grain boundaries," *Acta Mater.*, vol. 65, pp. 150–160, Feb. 2014.

[63] Dai, S., Xiang, Y., and Srolovitz, D. J., "Structure and energy of (111) low-angle twist boundaries in Al, Cu and Ni," *Acta Mater.*, vol. 61, pp. 1327–1337, Feb. 2013.

[64] Daw, M. S. and Baskes, M. I., "Embedded-atom method: Derivation and application to impurities, surfaces, and other defects in metals," *Phys. Rev. B*, vol. 29, pp. 6443–6453, June 1984.

[65] de Koning, M., Kurtz, R. J., Bulatov, V. V., Henager, C. H., Hoagland, R. G., Cai, W., and Nomura, M., "Modeling of dislocation-grain boundary interactions in FCC metals," *J. Nucl. Mater.*, vol. 323, pp. 281–289, Dec. 2003.

[66] de Koning, M., Cai, W., and Bulatov, V. V., "Anomalous dislocation multiplication in FCC metals," *Phys. Rev. Lett.*, vol. 91, p. 025503, July 2003.

[67] Deng, Q. and Chen, Y., "A coarse-grained atomistic method for 3D dynamic fracture simulation," *Int. J. Multiscale Comput. Eng.*, vol. 11, no. 3, pp. 227–237, 2013.

[68] Deng, Q., Xiong, L., and Chen, Y., "Coarse-graining atomistic dynamics of brittle fracture by finite element method," *Int. J. Plast.*, vol. 26, pp. 1402–1414, Sept. 2010.

[69] Deshpande, V. S., Needleman, A., and Van der Giessen, E., "Plasticity size effects in tension and compression of single crystals," *J. Mech. Phys. Solids*, vol. 53, pp. 2661–2691, Dec. 2005.

[70] Dewald, M. P. and Curtin, W. A., "Multiscale modelling of dislocation/grain-boundary interactions: I. Edge dislocations impinging on Σ11(113) tilt boundary in Al," *Modelling Simul. Mater. Sci. Eng.*, vol. 15, p. S193, Jan. 2007.

[71] Dewald, M. P. and Curtin, W. A., "Multiscale modelling of dislocation/grain boundary interactions. II. Screw dislocations impinging on tilt boundaries in Al," *Philos. Mag.*, vol. 87, no. 30, pp. 4615–4641, 2007.

[72] Dewald, M. P. and Curtin, W. A., "Multiscale modeling of dislocation/grain-boundary interactions: III. 60° dislocations impinging on Σ3, Σ9 and Σ11 tilt boundaries in Al," *Modelling Simul. Mater. Sci. Eng.*, vol. 19, p. 055002, July 2011.

[73] deWit, G. and Koehler, J. S., "Interaction of dislocations with an applied stress in anisotropic crystals," *Phys. Rev.*, vol. 116, pp. 1113–1120, Dec. 1959.

[74] Duesbery, M. S., "Dislocation motion, constriction and cross-slip in fcc metals," *Modelling Simul. Mater. Sci. Eng.*, vol. 6, no. 1, p. 35, 1998.

[75] Dupuy, L. M., Tadmor, E. B., Miller, R. E., and Phillips, R., "Finite-temperature quasicontinuum: molecular dynamics without all the atoms," *Phys. Rev. Lett.*, vol. 95, p. 060202, Aug. 2005.

[76] Dyka, C. T., Randles, P. W., and Ingel, R. P., "Stress points for tension instability in SPH," *Inter. J. Numer. Meth. Eng.*, vol. 40, no. 13, pp. 2325–2341, 1997.

[77] E, W. and Huang, Z., "Matching conditions in atomistic-continuum modeling of materials," *Phys. Rev. Lett.*, vol. 87, p. 135501, Sept. 2001.

[78] E, W. and Ming, P., "Analysis of multiscale methods," *J. Comput. Math.*, vol. 22, no. 2, pp. 210–219, 2004.

[79] Edington, J. W. and Smallman, R. E., "The relationship between flow stress and dislocation density in deformed vanadium," *Acta Metall.*, vol. 12, pp. 1313–1328, Dec. 1964.

[80] El-Awady, J. A., "Unravelling the physics of size-dependent dislocation-mediated plasticity," *Nature Comm.*, vol. 6, p. 5926, Jan. 2015.

[81] Ercolessi, F. and Adams, J. B., "Interatomic potentials from first-principles calculations: The force-matching method," *Europhys. Lett.*, vol. 26, no. 8, p. 583, 1994.

[82] Eringen, A. C., ed., *Nonlocal Continuum Field Theories*. New York, NY: Springer New York, 2004.

[83] Escaig, B., "Sur le glissement dvi des dislocations dans la structure cubique faces centres," *J. Phys.*, vol. 29, no. 2-3, pp. 225–239, 1968.

[84] Ezaz, T., Sangid, M. D., and Sehitoglu, H., "Energy barriers associated with slip-twin interactions," *Philos. Mag.*, vol. 91, no. 10, pp. 1464–1488, 2011.

[85] Fang, Q. and Sansoz, F., "Influence of intrinsic kink-like defects on screw dislocation-coherent twin boundary interactions in copper," *Acta Mater.*, vol. 123, pp. 383–393, Jan. 2017.

[86] Fitzgerald, S. P., Aubry, S., Dudarev, S. L., and Cai, W., "Dislocation dynamics simulation of Frank-Read sources in anisotropic α-Fe," *Modelling Simul. Mater. Sci. Eng.*, vol. 20, p. 045022, June 2012.

[87] Fitzgerald, S. P., "Frank-Read sources and the yield of anisotropic cubic crystals," *Philos. Mag. Lett.*, vol. 90, pp. 209–218, Mar. 2010.

[88] Fleischer, R. L., "Cross slip of extended dislocations," *Acta Metall.*, vol. 7, pp. 134–135, Feb. 1959.

[89] Foiles, S. M. and Hoyt, J., "Computation of grain boundary stiffness and mobility from boundary fluctuations," *Acta Mater.*, vol. 54, pp. 3351–3357, July 2006.

[90] Foreman, A. J. E., "Dislocation energies in anisotropic crystals," *Acta Metall.*, vol. 3, pp. 322–330, July 1955.

[91] Foreman, A. J. E., "The bowing of a dislocation segment," *Philos. Mag.*, vol. 15, pp. 1011–1021, May 1967.

[92] Foreman, A. J. E. and Makin, M. J., "Dislocation movement through random arrays of obstacles," *Philos. Mag.*, vol. 14, pp. 911–924, Oct. 1966.

[93] Frank, F. C. and Read, W. T., "Multiplication processes for slow moving dislocations," *Phys. Rev.*, vol. 79, pp. 722–723, Aug. 1950.

[94] Friedel, J., *Dislocations*. Pergamon Press, 1964.

[95] Fu, H.-H., Benson, D. J., and Andr Meyers, M., "Computational description of nanocrystalline deformation based on crystal plasticity," *Acta Mater.*, vol. 52, pp. 4413–4425, Sept. 2004.

[96] Ghoniem, N. M., Tong, S.-H., and Sun, L. Z., "Parametric dislocation dynamics: A thermodynamics-based approach to investigations of mesoscopic plastic deformation," *Phys. Rev. B*, vol. 61, pp. 913–927, Jan. 2000.

[97] Gómez-García, D., Devincre, B., and Kubin, L., "Dislocation dynamics in confined geometry," *J. Comput.-Aided Mater. Design*, vol. 6, pp. 157–164, May 1999.

[98] Gracie, R. and Belytschko, T., "Concurrently coupled atomistic and XFEM models for dislocations and cracks," *Int. J. Numer. Meth. Eng.*, vol. 78, pp. 354–378, Apr. 2009.

[99] Gracie, R. and Belytschko, T., "An adaptive concurrent multiscale method for the dynamic simulation of dislocations," *Int. J. Numer. Meth. Eng.*, vol. 86, pp. 575–597, Apr. 2011.

[100] Gröger, R., Racherla, V., Bassani, J. L., and Vitek, V., "Multiscale modeling of plastic deformation of molybdenum and tungsten: II. Yield criterion for single crystals based on atomistic studies of glide of screw dislocations," *Acta Mater.*, vol. 56, pp. 5412–5425, Nov. 2008.

[101] Gröger, R. and Vitek, V., "Constrained nudged elastic band calculation of the Peierls barrier with atomic relaxations," *Modelling Simul. Mater. Sci. Eng.*, vol. 20, no. 3, p. 035019, 2012.

[102] Gropp, W., Hoefler, T., Thakur, R., and Lusk, E., *Using Advanced MPI: Modern Features of the Message-Passing Interface*. Cambridge, Massachusetts: The MIT Press, 1st ed., Nov. 2014.

[103] Gumbsch, P., Riedle, J., Hartmaier, A., and Fischmeister, H. F., "Controlling factors for the brittle-to-ductile transition in tungsten single crystals," *Science*, vol. 282, pp. 1293–1295, Nov. 1998.

[104] Gurrutxaga-Lerma, B., Balint, D. S., Dini, D., and Sutton, A. P., "The mechanisms governing the activation of dislocation sources in aluminum at different strain rates," *J. Mech. Phys. Solids*, vol. 84, pp. 273–292, Nov. 2015.

[105] Han, C.-S., Wagoner, R. H., and Barlat, F., "On precipitate induced hardening in crystal plasticity: theory," *Int. J. Plast.*, vol. 20, pp. 477–494, Mar. 2004.

[106] Hartley, C. S. and Mishin, Y., "Characterization and visualization of the lattice misfit associated with dislocation cores," *Acta Mater.*, vol. 53, pp. 1313–1321, Mar. 2005.

[107] Hatano, T., "Dynamics of a dislocation bypassing an impenetrable precipitate: The Hirsch mechanism revisited," *Phys. Rev. B*, vol. 74, p. 020102, July 2006.

[108] Hatano, T., Kaneko, T., Abe, Y., and Matsui, H., "Void-induced cross slip of screw dislocations in fcc copper," *Phys. Rev. B*, vol. 77, p. 064108, Feb. 2008.

[109] Hatano, T. and Matsui, H., "Molecular dynamics investigation of dislocation pinning by a nanovoid in copper," *Phys. Rev. B*, vol. 72, p. 094105, Sept. 2005.

[110] Hirth, J. P. and Lothe, J., *Theory of Dislocations*. Krieger Pub Co, May 1992.

[111] Hoover, W. G., "Canonical dynamics: Equilibrium phase-space distributions," *Phys. Rev. A*, vol. 31, pp. 1695–1697, Mar. 1985.

[112] Hu, Q., Li, L., and Ghoniem, N., "Stick-slip dynamics of coherent twin boundaries in copper," *Acta Mater.*, vol. 57, pp. 4866–4873, Sept. 2009.

[113] Huang, M.-S., Zhu, Y.-X., and Li, Z.-H., "Dislocation dissociation strongly influences on Frank-Read source nucleation and microplasticy of materials with low stacking fault energy," *Chin. Phys. Lett.*, vol. 31, p. 046102, Apr. 2014.

[114] Hull, D. and Bacon, D. J., *Introduction to Dislocations*. Butterworth-Heinemann, 5th ed., Apr. 2011.

[115] Hussein, A. M., Rao, S. I., Uchic, M. D., Dimiduk, D. M., and El-Awady, J. A., "Microstructurally based cross-slip mechanisms and their effects on dislocation microstructure evolution in fcc crystals," *Acta Mater.*, vol. 85, pp. 180–190, Feb. 2015.

[116] Jin, C., Xiang, Y., and Lu, G., "Dislocation cross-slip mechanisms in aluminum," *Philos. Mag.*, vol. 91, pp. 4109–4125, Nov. 2011.

[117] Jin, Z.-H., Gumbsch, P., Albe, K., Ma, E., Lu, K., Gleiter, H., and Hahn, H., "Interactions between non-screw lattice dislocations and coherent twin boundaries in face-centered cubic metals," *Acta Mater.*, vol. 56, pp. 1126–1135, Mar. 2008.

[118] Jin, Z.-H., Gumbsch, P., Ma, E., Albe, K., Lu, K., Hahn, H., and Gleiter, H., "The interaction mechanism of screw dislocations with coherent twin boundaries in different face-centred cubic metals," *Scripta Mater.*, vol. 54, pp. 1163–1168, Mar. 2006.

[119] Junge, T., Anciaux, G., and Molinari, J.-F., "Dynamic stability of displacement-based atomistic/continuum coupling methods," *J. Mech. Phys. Solids*, vol. 80, pp. 103–120, July 2015.

[120] Kacher, J. P., Liu, G. S., and Robertson, I. M., "Visualization of grain boundary/dislocation interactions using tomographic reconstructions," *Scripta Mater.*, vol. 64, pp. 677–680, Apr. 2011.

[121] Kacher, J., Eftink, B. P., Cui, B., and Robertson, I. M., "Dislocation interactions with grain boundaries," *Curr. Opin. Solid State Mater. Sci.*, vol. 18, pp. 227–243, Aug. 2014.

[122] Kacher, J. and Robertson, I. M., "Quasi-four-dimensional analysis of dislocation interactions with grain boundaries in 304 stainless steel," *Acta Mater.*, vol. 60, pp. 6657–6672, Nov. 2012.

[123] Kacher, J. and Robertson, I. M., "*In situ* and tomographic analysis of dislocation/grain boundary interactions in α-titanium," *Philos. Mag.*, vol. 94, pp. 814–829, Mar. 2014.

[124] Kang, K., Yin, J., and Cai, W., "Stress dependence of cross slip energy barrier for face-centered cubic nickel," *J. Mech. Phys. Solids*, vol. 62, pp. 181–193, Jan. 2014.

[125] Kashihara, K. and Inoko, F., "Effect of piled-up dislocations on strain induced boundary migration (SIBM) in deformed aluminum bicrystals with originally $\Sigma 3$ twin boundary," *Acta Mater.*, vol. 49, pp. 3051–3061, Sept. 2001.

[126] Kelchner, C. L., Plimpton, S. J., and Hamilton, J. C., "Dislocation nucleation and defect structure during surface indentation," *Phys. Rev. B*, vol. 58, pp. 11085–11088, Nov. 1998.

[127] Khraishi, T. A., Zbib, H. M., Rubia, T. D. d. l., and Victoria, M., "Localized deformation and hardening in irradiated metals: Three-dimensional discrete dislocation dynamics simulations," *Metall. Mater. Trans. B*, vol. 33, pp. 285–296, Apr. 2002.

[128] Kibey, S., Liu, J., Johnson, D., and Sehitoglu, H., "Predicting twinning stress in fcc metals: Linking twin-energy pathways to twin nucleation," *Acta Mater.*, vol. 55, pp. 6843–6851, Dec. 2007.

[129] Kikuchi, H., Kalia, R. K., Nakano, A., Vashishta, P., Branicio, P. S., and Shimojo, F., "Brittle dynamic fracture of crystalline cubic silicon carbide (3C-SiC) via molecular dynamics simulation," *J. Appl. Phys.*, vol. 98, p. 103524, Nov. 2005.

[130] Kim, J. H., Lim, J. H., Lee, J. H., and Im, S., "A new computational approach to contact mechanics using variable-node finite elements," *Int. J. Numer. Meth. Eng.*, vol. 73, pp. 1966–1988, Mar. 2008.

[131] Kluge, M. D., Wolf, D., Lutsko, J. F., and Phillpot, S. R., "Formalism for the calculation of local elastic constants at grain boundaries by means of atomistic simulation," *J. Appl. Phys.*, vol. 67, pp. 2370–2379, Mar. 1990.

[132] Knap, J. and Ortiz, M., "An analysis of the quasicontinuum method," *J. Mech. Phys. Solids*, vol. 49, pp. 1899–1923, Sept. 2001.

[133] Kocks, U. F., "Statistical treatment of penetrable obstacles," *Can. J. Phys.*, vol. 45, pp. 737–755, Feb. 1967.

[134] Kuhlmann-Wilsdorf, D., "The LES theory of solid plasticity," in *Dislocations in Solids* (Nabarro, F. R. N. and Duesbery, M., eds.), vol. 11, pp. 211–342, Elsevier, 2002.

[135] Kulkarni, Y., Knap, J., and Ortiz, M., "A variational approach to coarse graining of equilibrium and non-equilibrium atomistic description at finite temperature," *J. Mech. Phys. Solids*, vol. 56, pp. 1417–1449, Apr. 2008.

[136] Kushima, A., Eapen, J., Li, J., Yip, S., and Zhu, T., "Time scale bridging in atomistic simulation of slow dynamics: viscous relaxation and defect activation," *Euro. Phys. J. B*, vol. 82, no. 3, pp. 271–293, 2011.

[137] Kwon, S., Lee, Y., Park, J. Y., Sohn, D., Lim, J. H., and Im, S., "An efficient three-dimensional adaptive quasicontinuum method using variable-node elements," *J. Comput. Phys.*, vol. 228, pp. 4789–4810, July 2009.

[138] Lee, D. T. and Schachter, B. J., "Two algorithms for constructing a Delaunay triangulation," *Int. J. Comput. Info. Sci.*, vol. 9, pp. 219–242, June 1980.

[139] Lee, D. W., Kim, H., Strachan, A., and Koslowski, M., "Effect of core energy on mobility in a continuum dislocation model," *Phys. Rev. B*, vol. 83, p. 104101, Mar. 2011.

[140] Lee, T. C., Robertson, I. M., and Birnbaum, H. K., "TEM *in situ* deformation study of the interaction of lattice dislocations with grain boundaries in metals," *Philos. Mag. A*, vol. 62, pp. 131–153, July 1990.

[141] Lee, T. C., Robertson, I. M., and Birnbaum, H. K., "Interaction of dislocations with grain boundaries in Ni_3Al," *Acta Metall. Mater.*, vol. 40, pp. 2569–2579, Oct. 1992.

[142] Lehtinen, A., Granberg, F., Laurson, L., Nordlund, K., and Alava, M. J., "Multiscale modeling of dislocation-precipitate interactions in Fe: From molecular dynamics to discrete dislocations," *Phys. Rev. E*, vol. 93, p. 013309, Jan. 2016.

[143] LeSar, R., "Ambiguities in the calculation of dislocation self energies," *Phys. Stat. Sol. (b)*, vol. 241, pp. 2875–2880, Nov. 2004.

[144] Levitas, V. I. and Javanbakht, M., "Phase transformations in nanograin materials under high pressure and plastic shear: nanoscale mechanisms," *Nanoscale*, vol. 6, no. 1, pp. 162–166, 2014.

[145] Li, B., Li, B., Wang, Y., Sui, M., and Ma, E., "Twinning mechanism via synchronized activation of partial dislocations in face-centered-cubic materials," *Scripta Mater.*, vol. 64, pp. 852–855, May 2011.

[146] Li, J., Wang, C.-Z., Chang, J.-P., Cai, W., Bulatov, V. V., Ho, K.-M., and Yip, S., "Core energy and Peierls stress of a screw dislocation in bcc molybdenum: A periodic-cell tight-binding study," *Phys. Rev. B*, vol. 70, p. 104113, Sept. 2004.

[147] Li, M., Chu, W. Y., Gao, K. W., and Qiao, L. J., "Molecular dynamics simulation of cross-slip and the intersection of dislocations in copper," *J. Phys.: Condens. Matter*, vol. 15, p. 3391, May 2003.

[148] Li, X. Y. and Yang, W., "Atomistic simulations for the evolution of a U-shaped dislocation in fcc Al," *Phys. Rev. B*, vol. 74, p. 144108, Oct. 2006.

[149] Lim, J. H., Im, S., and Cho, Y.-S., "Variable-node elements for non-matching meshes by means of MLS (moving least-square) scheme," *Int. J. Numer. Meth. Eng.*, vol. 72, pp. 835–857, Nov. 2007.

[150] Lim, L. C. and Raj, R., "Continuity of slip screw and mixed crystal dislocations across bicrystals of nickel at 573 K," *Acta Metall.*, vol. 33, pp. 1577–1583, Aug. 1985.

[151] Lin, P., "Convergence analysis of a quasi-continuum approximation for a two dimensional material without defects," *SIAM J. Numer. Anal.*, vol. 45, pp. 313–332, Jan. 2007.

[152] Lin, P., "Theoretical and numerical analysis for the quasi-continuum approximation of a material particle model," *Math. Comp.*, vol. 72, no. 242, pp. 657–675, 2003.

[153] Lipkin, D. M., Clarke, D. R., and Beltz, G. E., "A strain-gradient model of cleavage fracture in plastically deforming materials," *Acta Mater.*, vol. 44, pp. 4051–4058, Oct. 1996.

[154] Liu, B., Raabe, D., Eisenlohr, P., Roters, F., Arsenlis, A., and Hommes, G., "Dislocation interactions and low-angle grain boundary strengthening," *Acta Mater.*, vol. 59, pp. 7125–7134, Nov. 2011.

[155] Liu, X. M., You, X. C., Liu, Z. L., Nie, J. F., and Zhuang, Z., "Atomistic simulations of tension properties for bi-crystal copper with twist grain boundary," *J. Phys. D: Appl. Phys.*, vol. 42, p. 035404, Feb. 2009.

[156] Lothe, J. and Hirth, J. P., "Dislocation core parameters," *Phys. Stat. Sol. (b)*, vol. 242, pp. 836–841, Mar. 2005.

[157] Lu, G., Bulatov, V. V., and Kioussis, N., "Dislocation constriction and cross-slip: An *ab initio* study," *Phys. Rev. B*, vol. 66, p. 144103, Oct. 2002.

[158] Lubarda, V. A. and Markenscoff, X., "Configurational force on a lattice dislocation and the Peierls stress," *Arch. Appl. Mech.*, vol. 77, no. 2-3, pp. 147–154, 2007.

[159] Luskin, M. and Ortner, C., "An analysis of node-based cluster summation rules in the quasicontinuum method," *SIAM J. Numer. Anal.*, vol. 47, pp. 3070–3086, Jan. 2009.

[160] Luskin, M. and Ortner, C., "Atomistic-to-continuum coupling," *Acta Numer.*, vol. 22, pp. 397–508, 2013.

[161] Ma, A., Roters, F., and Raabe, D., "On the consideration of interactions between dislocations and grain boundaries in crystal plasticity finite element modeling — Theory, experiments, and simulations," *Acta Mater.*, vol. 54, pp. 2181–2194, May 2006.

[162] Makridakis, C. and Süli, E., "Finite element analysis of Cauchy-Born approximations to atomistic models," *Arch. Rational. Mech. Anal.*, vol. 207, no. 3, pp. 813–843, 2013.

[163] Marian, J., Venturini, G., Hansen, B. L., Knap, J., Ortiz, M., and Campbell, G. H., "Finite-temperature extension of the quasicontinuum method using Langevin dynamics: entropy losses and analysis of errors," *Modelling Simul. Mater. Sci. Eng.*, vol. 18, p. 015003, Jan. 2010.

[164] Martin, J. W., *Precipitation Hardening*. Butterworth-Heinemann, 2nd ed., Oct. 1998.

[165] Martínez, E., Marian, J., Arsenlis, A., Victoria, M., and Perlado, J. M., "Atomistically informed dislocation dynamics in fcc crystals," *J. Mech. Phys. Solids*, vol. 56, pp. 869–895, Mar. 2008.

[166] Mayeur, J. R., Beyerlein, I. J., Bronkhorst, C. A., and Mourad, H. M., "Incorporating interface affected zones into crystal plasticity," *Int. J. Plast.*, vol. 65, pp. 206–225, Feb. 2015.

[167] McDowell, D. L., "Viscoplasticity of heterogeneous metallic materials," *Mater. Sci. Eng. R: Rep.*, vol. 62, pp. 67–123, Aug. 2008.

[168] McDowell, D. L., "A perspective on trends in multiscale plasticity," *Int. J. Plast.*, vol. 26, pp. 1280–1309, Sept. 2010.

[169] Mercier, D., Zambaldi, C., and Bieler, T. R., "A Matlab toolbox to analyze slip transfer through grain boundaries," *IOP Conf. Ser.: Mater. Sci. Eng.*, vol. 82, p. 012090, Apr. 2015.

[170] Meyers, M., Mishra, A., and Benson, D., "Mechanical properties of nanocrystalline materials," *Prog. Mater. Sci.*, vol. 51, pp. 427–556, May 2006.

[171] Miller, R. E. and Tadmor, E. B., "The quasicontinuum method: Overview, applications and current directions," *J. Comput.-Aided Mater. Design*, vol. 9, pp. 203–239, Oct. 2002.

[172] Miller, R. E. and Tadmor, E. B., "A unified framework and performance benchmark of fourteen multiscale atomistic/continuum coupling methods," *Modelling Simul. Mater. Sci. Eng.*, vol. 17, p. 053001, July 2009.

[173] Mishin, Y., Farkas, D., Mehl, M. J., and Papaconstantopoulos, D. A., "Interatomic potentials for monoatomic metals from experimental data and *ab initio* calculations," *Phys. Rev. B*, vol. 59, pp. 3393–3407, Feb. 1999.

[174] Mishin, Y., Mehl, M. J., Papaconstantopoulos, D. A., Voter, A. F., and Kress, J. D., "Structural stability and lattice defects in copper: *Ab initio*, tight-binding, and embedded-atom calculations," *Phys. Rev. B*, vol. 63, p. 224106, May 2001.

[175] Moës, N., Dolbow, J., and Belytschko, T., "A finite element method for crack growth without remeshing," *Int. J. Numer. Meth. Eng.*, vol. 46, pp. 131–150, Sept. 1999.

[176] Monnet, G., "Mechanical and energetical analysis of molecular dynamics simulations of dislocation-defect interactions," *Acta Mater.*, vol. 55, pp. 5081–5088, Sept. 2007.

[177] Moseley, P., Oswald, J., and Belytschko, T., "Adaptive atomistic-to-continuum modeling of propagating defects," *Int. J. Numer. Meth. Eng.*, vol. 92, pp. 835–856, Dec. 2012.

[178] Mott, N. and Nabarro, F., *Report of a Conference on Strength of Solids*, vol. 1. Physical Society, 1948.

[179] Mott, P. H., Argon, A. S., and Suter, U. W., "The atomic strain tensor," *J. Comput. Phys.*, vol. 101, pp. 140–150, July 1992.

[180] Ngan, A. H. W., "On generalizing the Peierls-Nabarro model for screw dislocations with non-planar cores," *Philos. Mag. Lett.*, vol. 72, pp. 207–213, Oct. 1995.

[181] Nogaret, T. and Rodney, D., "Finite-size effects in dislocation glide through random arrays of obstacles: Line tension simulations," *Phys. Rev. B*, vol. 74, p. 134110, Oct. 2006.

[182] Ohashi, T., Kawamukai, M., and Zbib, H., "A multiscale approach for modeling scale-dependent yield stress in polycrystalline metals," *Int. J. Plast.*, vol. 23, pp. 897–914, May 2007.

[183] Olmsted, D. L., Hardikar, K. Y., and Phillips, R., "Lattice resistance and Peierls stress in finite size atomistic dislocation simulations," *Modelling Simul. Mater. Sci. Eng.*, vol. 9, p. 215, May 2001.

[184] Osetsky, Y. N. and Bacon, D. J., "An atomic-level model for studying the dynamics of edge dislocations in metals," *Modelling Simul. Mater. Sci. Eng.*, vol. 11, no. 4, pp. 427–446, 2003.

[185] Park, J. Y. and Im, S., "Adaptive nonlocal quasicontinuum for deformations of curved crystalline structures," *Phys. Rev. B*, vol. 77, p. 184109, May 2008.

[186] Parrinello, M. and Rahman, A., "Polymorphic transitions in single crystals: A new molecular dynamics method," *J. Appl. Phys.*, vol. 52, pp. 7182–7190, Dec. 1981.

[187] Pavia, F. and Curtin, W. A., "Parallel algorithm for multiscale atomistic/continuum simulations using LAMMPS," *Modelling Simul. Mater. Sci. Eng.*, vol. 23, p. 055002, July 2015.

[188] Pearce, O., Gamblin, T., de Supinski, B. R., Arsenlis, T., and Amato, N. M., "Load balancing N-body simulations with highly non-uniform density," in *Proceedings of the 28th ACM International Conference on Supercomputing*, ICS '14, (New York, NY, USA), pp. 113–122, ACM, 2014.

[189] Pestman, B. J., de Hosson, J. T. M., Vitek, V., and Schapink, F. W., "Interaction between lattice dislocations and grain boundaries in F.C.C. materials," *Scripta Metall.*, vol. 23, pp. 1431–1435, Aug. 1989.

[190] Plimpton, S., "Fast parallel algorithms for short-range molecular dynamics," *J. Comput. Phys.*, vol. 117, pp. 1–19, Mar. 1995.

[191] Priester, L., Poulat, S., Décamps, B., and Thibault, J., "Dislocation-grain boundary interaction in nickel bicrystals evolution of the resulting defects under thermal treatment," *MRS Proc.*, vol. 652, Jan. 2000.

[192] Proville, L. and Patinet, S., "Atomic-scale models for hardening in fcc solid solutions," *Phys. Rev. B*, vol. 82, p. 054115, Aug. 2010.

[193] Puri, S., Acharya, A., and Rollett, A. D., "Controlling plastic flow across grain boundaries in a continuum model," *Metall. Mater. Trans. A*, vol. 42, no. 3, pp. 669–675, 2011.

[194] Püschl, W., "Models for dislocation cross-slip in close-packed crystal structures: a critical review," *Prog. Mater. Sci.*, vol. 47, no. 4, pp. 415–461, 2002.

[195] Qian, D. and Gondhalekar, R. H., "A virtual atom cluster approach to the mechanics of nanostructures," *Int. J. Multiscale Comput. Eng.*, vol. 2, no. 2, pp. 277–290, 2004.

[196] Qu, S., Shastry, V., Curtin, W. A., and Miller, R. E., "A finite-temperature dynamic coupled atomistic/discrete dislocation method," *Modelling Simul. Mater. Sci. Eng.*, vol. 13, p. 1101, Oct. 2005.

[197] Quek, S. S., Wu, Z., Zhang, Y. W., and Srolovitz, D. J., "Polycrystal deformation in a discrete dislocation dynamics framework," *Acta Mater.*, vol. 75, pp. 92–105, Aug. 2014.

[198] Rabczuk, T., Belytschko, T., and Xiao, S., "Stable particle methods based on Lagrangian kernels," *Comput. Meth. Appl. Mech. Eng.*, vol. 193, pp. 1035–1063, Mar. 2004.

[199] Rafii-Tabar, H., Shodja, H. M., Darabi, M., and Dahi, A., "Molecular dynamics simulation of crack propagation in fcc materials containing clusters of impurities," *Mech. Mater.*, vol. 38, pp. 243–252, Mar. 2006.

[200] Ramesh, K., *Nanomaterials: Mechanics and Mechanisms*. New York: Springer, June 2009.

[201] Ramírez, B. R., Ghoniem, N., and Po, G., "*Ab initio* continuum model for the influence of local stress on cross-slip of screw dislocations in fcc metals," *Phys. Rev. B*, vol. 86, p. 094115, Sept. 2012.

[202] Ramos, A. and Simões, J. A., "Tetrahedral versus hexahedral finite elements in numerical modelling of the proximal femur," *Med. Eng. Phys.*, vol. 28, pp. 916–924, Nov. 2006.

[203] Ranganathan, S. I. and Ostoja-Starzewski, M., "Universal elastic anisotropy index," *Phys. Rev. Lett.*, vol. 101, p. 055504, Aug. 2008.

[204] Rao, S. I., Dimiduk, D. M., El-Awady, J. A., Parthasarathy, T. A., Uchic, M. D., and Woodward, C., "Activated states for cross-slip at screw dislocation intersections in face-centered cubic nickel and copper via atomistic simulation," *Acta Mater.*, vol. 58, pp. 5547–5557, Oct. 2010.

[205] Rao, S. I., Dimiduk, D. M., El-Awady, J. A., Parthasarathy, T. A., Uchic, M. D., and Woodward, C., "Screw dislocation cross slip at cross-slip plane jogs and screw dipole annihilation in FCC Cu and Ni investigated via atomistic simulations," *Acta Mater.*, vol. 101, pp. 10–15, Dec. 2015.

[206] Rasmussen, T., Jacobsen, K. W., Leffers, T., and Pedersen, O. B., "Simulations of the atomic structure, energetics, and cross slip of screw dislocations in copper," *Phys. Rev. B*, vol. 56, pp. 2977–2990, Aug. 1997.

[207] Rasmussen, T., Jacobsen, K. W., Leffers, T., Pedersen, O. B., Srinivasan, S. G., and Jónsson, H., "Atomistic determination of cross-slip pathway and energetics," *Phys. Rev. Lett.*, vol. 79, pp. 3676–3679, Nov. 1997.

[208] Rasmussen, T., "Cross slip in the face centred cubic structure: An atomistic approach," in *Multiscale Phenomena in Plasticity: From Experiments to Phenomenology, Modelling and Materials Engineering* (Lépinoux, J., Mazière, D., Pontikis, V., and Saada, G., eds.), no. 367 in NATO Science Series, pp. 281–292, Springer Netherlands, 2000.

[209] Ratanaphan, S., Olmsted, D. L., Bulatov, V. V., Holm, E. A., Rollett, A. D., and Rohrer, G. S., "Grain boundary energies in body-centered cubic metals," *Acta Mater.*, vol. 88, pp. 346–354, Apr. 2015.

[210] Rhee, M., Zbib, H. M., Hirth, J. P., Huang, H., and Rubia, T. d. l., "Models for long-/short-range interactions and cross slip in 3D dislocation simulation of BCC single crystals," *Modelling Simul. Mater. Sci. Eng.*, vol. 6, p. 467, July 1998.

[211] Rice, J. R., "Dislocation nucleation from a crack tip: An analysis based on the Peierls concept," *J. Mech. Phys. Solids*, vol. 40, pp. 239–271, Jan. 1992.

[212] Rittner, J. D. and Seidman, D. N., "$\langle 110 \rangle$ symmetric tilt grain-boundary structures in fcc metals with low stacking-fault energies," *Phys. Rev. B*, vol. 54, pp. 6999–7015, Sept. 1996.

[213] Rodney, D., Le Bouar, Y., and Finel, A., "Phase field methods and dislocations," *Acta Mater.*, vol. 51, pp. 17–30, Jan. 2003.

[214] Rosalie, J. M., Somekawa, H., Singh, A., and Mukai, T., "Effect of precipitation on strength and ductility in a MgZnY alloy," *J. Alloys Compd.*, vol. 550, pp. 114–123, Feb. 2013.

[215] Rountree, C. L., Kalia, R. K., Lidorikis, E., Nakano, A., Van Brutzel, L., and Vashishta, P., "Atomistic aspects of crack propagation in brittle materials: Multimillion atom molecular dynamics simulations," *Annu. Rev. Mater. Res.*, vol. 32, no. 1, pp. 377–400, 2002.

[216] Rudd, R. and Broughton, J., "Concurrent coupling of length scales in solid state systems," *Phys. Status Solidi (b)*, vol. 217, no. 1, pp. 251–291, 2000.

[217] Sangid, M. D., Ezaz, T., and Sehitoglu, H., "Energetics of residual dislocations associated with slip-twin and slip-GBs interactions," *Mater. Sci. Eng.: A*, vol. 542, pp. 21–30, Apr. 2012.

[218] Sangid, M. D., Ezaz, T., Sehitoglu, H., and Robertson, I. M., "Energy of slip transmission and nucleation at grain boundaries," *Acta Mater.*, vol. 59, pp. 283–296, Jan. 2011.

[219] Sansoz, F. and Molinari, J. F., "Mechanical behavior of tilt grain boundaries in nanoscale Cu and Al: A quasicontinuum study," *Acta Mater.*, vol. 53, pp. 1931–1944, Apr. 2005.

[220] Scattergood, R. O. and Bacon, D. J., "The strengthening effect of voids," *Acta Metall.*, vol. 30, pp. 1665–1677, Aug. 1982.

[221] Schoeck, G., "The cross-slip energy unresolved," *Philos. Mag. Lett.*, vol. 89, pp. 505–515, Aug. 2009.

[222] Schroeder, W., Martin, K., and Lorensen, B., *Visualization Toolkit: An Object-Oriented Approach to 3D Graphics*. Kitware, 4th ed., Dec. 2006.

[223] Schulson, E. M. and Barker, D. R., "A brittle to ductile transition in NiAl of a critical grain size," *Scripta Metall.*, vol. 17, pp. 519–522, Apr. 1983.

[224] Seidman, D. N., Marquis, E. A., and Dunand, D. C., "Precipitation strengthening at ambient and elevated temperatures of heat-treatable Al(Sc) alloys," *Acta Mater.*, vol. 50, pp. 4021–4035, Sept. 2002.

[225] Shen, Z., Wagoner, R. H., and Clark, W. A. T., "Dislocation pile-up and grain boundary interactions in 304 stainless steel," *Scripta Metall.*, vol. 20, pp. 921–926, June 1986.

[226] Shen, Z., Wagoner, R. H., and Clark, W. A. T., "Dislocation and grain boundary interactions in metals," *Acta Metall.*, vol. 36, pp. 3231–3242, Dec. 1988.

[227] Shenoy, V. B., Miller, R., Tadmor, E. B., Phillips, R., and Ortiz, M., "Quasicontinuum models of interfacial structure and deformation," *Phys. Rev. Lett.*, vol. 80, pp. 742–745, Jan. 1998.

[228] Shenoy, V., Shenoy, V., and Phillips, R., "Finite temperature quasicontinuum methods," in *Symposium J Multiscale Modelling Mater.*, vol. 538 of *MRS Online Proceedings Library*, pp. 465–471, 1998.

[229] Sheppard, D., Terrell, R., and Henkelman, G., "Optimization methods for finding minimum energy paths," *J. Chem. Phys.*, vol. 128, p. 134106, Apr. 2008.

[230] Shi, J. and Zikry, M. A., "Modeling of grain boundary transmission, emission, absorption and overall crystalline behavior in Σ1, Σ3, and Σ17b bicrystals," *J. Mater. Res.*, vol. 26, no. 14, pp. 1676–1687, 2011.

[231] Shiari, B., Miller, R. E., and Curtin, W. A., "Coupled atomistic/discrete dislocation simulations of nanoindentation at finite temperature," *J. Eng. Mater. Technol*, vol. 127, pp. 358–368, Jan. 2005.

[232] Shilkrot, L., Miller, R. E., and Curtin, W. A., "Multiscale plasticity modeling: coupled atomistics and discrete dislocation mechanics," *J. Mech. Phys. Solids*, vol. 52, pp. 755–787, Apr. 2004.

[233] Shimizu, F., Ogata, S., and Li, J., "Theory of shear banding in metallic glasses and molecular dynamics calculations," *Mater. Trans.*, vol. 48, no. 11, pp. 2923–2927, 2007.

[234] Shimokawa, T., Kinari, T., and Shintaku, S., "Interaction mechanism between edge dislocations and asymmetrical tilt grain boundaries investigated via quasicontinuum simulations," *Phys. Rev. B*, vol. 75, p. 144108, Apr. 2007.

[235] Shimokawa, T. and Kitada, S., "Dislocation multiplication from the Frank-Read source in atomic models," *Mater. Trans.*, vol. 55, no. 1, pp. 58–63, 2014.

[236] Shishvan, S. S., Mohammadi, S., and Rahimian, M., "A dislocation-dynamics-based derivation of the Frank-Read source characteristics for discrete dislocation plasticity," *Modelling Simul. Mater. Sci. Eng.*, vol. 16, p. 075002, Oct. 2008.

[237] Singh, C. V., Mateos, A. J., and Warner, D. H., "Atomistic simulations of dislocationprecipitate interactions emphasize importance of cross-slip," *Scripta Mater.*, vol. 64, pp. 398–401, Mar. 2011.

[238] Sobie, C., Bertin, N., and Capolungo, L., "Analysis of obstacle hardening models using dislocation dynamics: Application to irradiation-induced defects," *Metall. Mater. Trans. A*, vol. 46, pp. 3761–3772, May 2015.

[239] Spearot, D., *Atomistic calculations of nanoscale interface behavior in FCC metals.* PhD thesis, Georgia Institute of Technology, 2005.

[240] Spearot, D. E., "Evolution of the E structural unit during uniaxial and constrained tensile deformation," *Mech. Res. Comm.*, vol. 35, pp. 81–88, Jan. 2008.

[241] Spearot, D. E. and Sangid, M. D., "Insights on slip transmission at grain boundaries from atomistic simulations," *Curr. Opin. Solid State Mater. Sci.*, vol. 18, pp. 188–195, Aug. 2014.

[242] Spearot, D. E., Tschopp, M. A., Jacob, K. I., and McDowell, D. L., "Tensile strength of $\langle 100 \rangle$ and $\langle 110 \rangle$ tilt bicrystal copper interfaces," *Acta Mater.*, vol. 55, pp. 705–714, Jan. 2007.

[243] Srinivasan, S. G., Liao, X. Z., Baskes, M. I., McCabe, R. J., Zhao, Y. H., and Zhu, Y. T., "Compact and dissociated dislocations in aluminum: Implications for deformation," *Phys. Rev. Lett.*, vol. 94, p. 125502, Mar. 2005.

[244] Stukowski, A. and Arsenlis, A., "On the elastic-plastic decomposition of crystal deformation at the atomic scale," *Modelling Simul. Mater. Sci. Eng.*, vol. 20, p. 035012, Apr. 2012.

[245] Stukowski, A., "Visualization and analysis of atomistic simulation data with OVITO—the Open Visualization Tool," *Modelling Simul. Mater. Sci. Eng.*, vol. 18, no. 1, p. 015012, 2010.

[246] Stukowski, A., "Structure identification methods for atomistic simulations of crystalline materials," *Modelling Simul. Mater. Sci. Eng.*, vol. 20, no. 4, p. 045021, 2012.

[247] Stukowski, A., Bulatov, V. V., and Arsenlis, A., "Automated identification and indexing of dislocations in crystal interfaces," *Modelling Simul. Mater. Sci. Eng.*, vol. 20, no. 8, p. 085007, 2012.

[248] Sun, Y. Q., "Line tension of screw dislocations on cross-slip planes," *Philos. Mag. Lett.*, vol. 74, pp. 175–188, Sept. 1996.

[249] Sutton, A. and Balluffi, R., *Interfaces in Crystalline Materials*. Oxford University Press, reprint ed., Mar. 2007.

[250] Szajewski, B. A., Chakravarthy, S. S., and Curtin, W. A., "Operation of a 3D Frank-Read source in a stress gradient and implications for size-dependent plasticity," *Acta Mater.*, vol. 61, pp. 1469–1477, Mar. 2013.

[251] Szajewski, B. A. and Curtin, W. A., "Analysis of spurious image forces in atomistic simulations of dislocations," *Modelling Simul. Mater. Sci. Eng.*, vol. 23, p. 025008, Mar. 2015.

[252] Szajewski, B. A., Pavia, F., and Curtin, W. A., "Robust atomistic calculation of dislocation line tension," *Modelling Simul. Mater. Sci. Eng.*, vol. 23, no. 8, p. 085008, 2015.

[253] Tadmor, E. B., Legoll, F., Kim, W. K., Dupuy, L. M., and Miller, R. E., "Finite-temperature quasi-continuum," *Appl. Mech. Rev.*, vol. 65, p. 010803, Mar. 2013.

[254] Tadmor, E. B. and Miller, R., *Modeling Materials: Continuum, Atomistic and Multiscale Techniques*. Cambridge University Press, Jan. 2012.

[255] Tadmor, E. B., Ortiz, M., and Phillips, R., "Quasicontinuum analysis of defects in solids," *Philos. Mag. A*, vol. 73, no. 6, pp. 1529–1563, 1996.

[256] Tadmor, E. and Miller, R., *Modeling materials: Continuum, atomistic and multiscale techniques*. Cambridge ; New York: Cambridge University Press, 1 ed., Jan. 2012.

[257] Tang, H., Schwarz, K. W., and Espinosa, H. D., "Dislocation-source shutdown and the plastic behavior of single-crystal micropillars," *Phys. Rev. Lett.*, vol. 100, p. 185503, May 2008.

[258] Tang, S., Hou, T. Y., and Liu, W. K., "A mathematical framework of the bridging scale method," *Int. J. Numer. Meth. Eng.*, vol. 65, pp. 1688–1713, Mar. 2006.

[259] Tiwari, S., *Methods for atomistic input into the initial yield and plastic flow criteria for nanocrystalline materials*. PhD thesis, Georgia Institute of Technology, Nov. 2014.

[260] To, A. C., Liu, W. K., and Kopacz, A., "A finite temperature continuum theory based on interatomic potential in crystalline solids," *Comput. Mech.*, vol. 42, pp. 531–541, Jan. 2008.

[261] Tschopp, M. A. and McDowell, D. L., "Structures and energies of $\Sigma 3$ asymmetric tilt grain boundaries in copper and aluminium," *Philos. Mag.*, vol. 87, pp. 3147–3173, Aug. 2007.

[262] Tschopp, M. A. and McDowell, D. L., "Dislocation nucleation in $\Sigma 3$ asymmetric tilt grain boundaries," *Int. J. Plast.*, vol. 24, pp. 191–217, Feb. 2008.

[263] Tschopp, M. A., Tucker, G. J., and McDowell, D. L., "Structure and free volume of ⟨110⟩ symmetric tilt grain boundaries with the E structural unit," *Acta Mater.*, vol. 55, pp. 3959–3969, June 2007.

[264] Tschopp, M. A., *Atomistic simulations of dislocation nucleation in single crystals and grain boundaries*. PhD thesis, Georgia Institute of Technology, 2007.

[265] Tsuru, T., Shibutani, Y., and Kaji, Y., "Fundamental interaction process between pure edge dislocation and energetically stable grain boundary," *Phys. Rev. B*, vol. 79, p. 012104, Jan. 2009.

[266] Tsuru, T. and Shibutani, Y., "Atomistic simulations of elastic deformation and dislocation nucleation in Al under indentation-induced stress distribution," *Modelling Simul. Mater. Sci. Eng.*, vol. 14, p. S55, July 2006.

[267] Tucker, G. J., *Atomistic simulations of defect nucleation and free volume in nanocrystalline materials*. PhD thesis, Georgia Institute of Technology, May 2011.

[268] van der Giessen, E. and Needleman, A., "Discrete dislocation plasticity: a simple planar model," *Modelling Simul. Mater. Sci. Eng.*, vol. 3, no. 5, p. 689, 1995.

[269] Van Koten, B. and Luskin, M., "Analysis of energy-based blended quasi-continuum approximations," *SIAM J. Numer. Anal.*, vol. 49, pp. 2182–2209, Jan. 2011.

[270] Van Swygenhoven, H., Derlet, P. M., and Frøseth, A. G., "Stacking fault energies and slip in nanocrystalline metals," *Nature Mater.*, vol. 3, pp. 399–403, May 2004.

[271] Vegge, T., "Atomistic simulations of screw dislocation cross slip in copper and nickel," *Mater. Sci. Eng. A*, vol. 309310, pp. 113–116, July 2001.

[272] Venturini, G., Wang, K., Romero, I., Ariza, M. P., and Ortiz, M., "Atomistic long-term simulation of heat and mass transport," *J. Mech. Phys. Solids*, vol. 73, pp. 242–268, Dec. 2014.

[273] Verlet, L., "Computer "experiments" on classical fluids. I. Thermodynamical properties of Lennard-Jones molecules," *Phys. Rev.*, vol. 159, pp. 98–103, July 1967.

[274] Voter, A. F. and Chen, S. P., "Accurate interatomic potentials for Ni, Al and Ni_3Al," *MRS Proc.*, vol. 82, pp. 175–180, Jan. 1986.

[275] Voter, A. F., Montalenti, F., and Germann, T. C., "Extending the time scale in atomistic simulation of materials," *Annu. Rev. Mater. Res.*, vol. 32, no. 1, pp. 321–346, 2002.

[276] Wang, J., Misra, A., and Hirth, J. P., "Shear response of $\Sigma3\{112\}$ twin boundaries in face-centered-cubic metals," *Phys. Rev. B*, vol. 83, p. 064106, Feb. 2011.

[277] Wang, J., "Atomistic simulations of dislocation pileup: grain boundaries interaction," *JOM*, vol. 67, pp. 1515–1525, May 2015.

[278] Wang, Y. M., Sansoz, F., LaGrange, T., Ott, R. T., Marian, J., Barbee Jr, T. W., and Hamza, A. V., "Defective twin boundaries in nanotwinned metals," *Nature Mater.*, vol. 12, pp. 697–702, Aug. 2013.

[279] Weertman, J. and Weertman, J., *Elementary Dislocation Theory*. New York: Oxford University Press, June 1992.

[280] Wei, H. and Wei, Y., "Interaction between a screw dislocation and stacking faults in FCC metals," *Mater. Sci. Eng.: A*, vol. 541, pp. 38–44, Apr. 2012.

[281] Weinberger, C. R. and Tucker, G. J., "Atomistic simulations of dislocation pinning points in pure face-centered-cubic nanopillars," *Modelling Simul. Mater. Sci. Eng.*, vol. 20, p. 075001, Oct. 2012.

[282] Wetherhold, R. C. and Forand, J. A., "Improving stability in the double-cantilever-beam fracture test," *Mater. Sci. Eng.: A*, vol. 147, pp. L17–L20, Oct. 1991.

[283] Wolf, D., "Energy and structure of (001) coincident-site twist boundaries and the free (001) surface in MgO: A theoretical study," *J. Am. Ceram. Soc.*, vol. 67, pp. 1–13, Jan. 1984.

[284] Woodward, C. and Rao, S. I., "*Ab-initio* simulation of isolated screw dislocations in bcc Mo and Ta," *Philos. Mag. A*, vol. 81, pp. 1305–1316, May 2001.

[285] Wu, Z. and Curtin, W. A., "The origins of high hardening and low ductility in magnesium," *Nature*, vol. 526, pp. 62–67, Oct. 2015.

[286] Xiang, Y., Cheng, L.-T., Srolovitz, D. J., and E, W., "A level set method for dislocation dynamics," *Acta Mater.*, vol. 51, pp. 5499–5518, Oct. 2003.

[287] Xiao, S. P. and Belytschko, T., "Material stability analysis of particle methods," *Adv. Comput. Math.*, vol. 23, pp. 171–190, July 2005.

[288] Xiao, S. and Yang, W., "Temperature-related Cauchy-Born rule for multiscale modeling of crystalline solids," *Comput. Mater. Sci.*, vol. 37, pp. 374–379, Sept. 2006.

[289] Xiao, S. and Yang, W., "A temperature-related homogenization technique and its implementation in the meshfree particle method for nanoscale simulations," *Int. J. Numer. Meth. Eng.*, vol. 69, pp. 2099–2125, Mar. 2007.

[290] Xiong, L., Chen, X., Zhang, N., McDowell, D. L., and Chen, Y., "Prediction of phonon properties of 1D polyatomic systems using concurrent atomistic-continuum simulation," *Arch. Appl. Mech.*, vol. 84, pp. 1665–1675, July 2014.

[291] Xiong, L. and Chen, Y., "Coarse-grained atomistic modeling and simulation of inelastic material behavior," *Acta Mech. Solida Sinica*, vol. 25, pp. 244–261, June 2012.

[292] Xiong, L., Deng, Q., Tucker, G., McDowell, D. L., and Chen, Y., "A concurrent scheme for passing dislocations from atomistic to continuum domains," *Acta Mater.*, vol. 60, pp. 899–913, Feb. 2012.

[293] Xiong, L., Deng, Q., Tucker, G. J., McDowell, D. L., and Chen, Y., "Coarse-grained atomistic simulations of dislocations in Al, Ni and Cu crystals," *Int. J. Plast.*, vol. 38, pp. 86–101, Nov. 2012.

[294] Xiong, L., McDowell, D. L., and Chen, Y., "Nucleation and growth of dislocation loops in Cu, Al and Si by a concurrent atomistic-continuum method," *Scripta Mater.*, vol. 67, pp. 633–636, Oct. 2012.

[295] Xiong, L., McDowell, D. L., and Chen, Y., "Sub-THz Phonon drag on dislocations by coarse-grained atomistic simulations," *Int. J. Plast.*, vol. 55, pp. 268–278, Apr. 2014.

[296] Xiong, L., Rigelesaiyin, J., Chen, X., Xu, S., McDowell, D. L., and Chen, Y., "Coarse-grained elastodynamics of fast moving dislocations," *Acta Mater.*, vol. 104, pp. 143–155, Feb. 2016.

[297] Xiong, L., Tucker, G., McDowell, D. L., and Chen, Y., "Coarse-grained atomistic simulation of dislocations," *J. Mech. Phys. Solids*, vol. 59, pp. 160–177, Feb. 2011.

[298] Xiong, L., Xu, S., McDowell, D. L., and Chen, Y., "Concurrent atomistic-continuum simulations of dislocation-void interactions in fcc crystals," *Int. J. Plast.*, vol. 65, pp. 33–42, Feb. 2015.

[299] Xu, G., "Dislocation nucleation from crack tips and brittle to ductile transitions in cleavage fracture," in *Dislocations in Solids* (Hirth, J. and Nabarro, F., eds.), vol. 12, pp. 81–145, Elsevier, 2005.

[300] Xu, S., Che, R., Xiong, L., Chen, Y., and McDowell, D. L., "A quasistatic implementation of the concurrent atomistic-continuum method for FCC crystals," *Int. J. Plast.*, vol. 72, pp. 91–126, Sept. 2015.

[301] Xu, S., Xiong, L., Chen, Y., and McDowell, D. L., "An analysis of key characteristics of the Frank-Read source process in FCC metals," *J. Mech. Phys. Solids*, vol. 96, pp. 460–476, Nov. 2016.

[302] Xu, S., Xiong, L., Chen, Y., and McDowell, D. L., "Edge dislocations bowing out from a row of collinear obstacles in Al," *Scripta Mater.*, vol. 123, pp. 135–139, Oct. 2016.

[303] Xu, S., Xiong, L., Chen, Y., and McDowell, D. L., "Sequential slip transfer of mixed-character dislocations across $\Sigma 3$ coherent twin boundary in FCC metals: a concurrent atomistic-continuum study," *npj Comput. Mater.*, vol. 2, p. 15016, Jan. 2016.

[304] Xu, S., Xiong, L., Chen, Y., and McDowell, D. L., "A concurrent atomistic-continuum study of slip transfer of sequential mixed character dislocations across symmetric tilt grain boundaries in Ni," *JOM*, 2017.

[305] Xu, S., Xiong, L., Chen, Y., and McDowell, D. L., "Shear stress- and line length-dependent screw dislocation cross-slip in FCC Ni," *Acta Mater.*, vol. 122, pp. 412–419, Jan. 2017.

[306] Xu, S., Xiong, L., Deng, Q., and McDowell, D. L., "Mesh refinement schemes for the concurrent atomistic-continuum method," *Int. J. Solids Struct.*, vol. 90, pp. 144–152, July 2016.

[307] Yamakov, V., Wolf, D., Phillpot, S. R., Mukherjee, A. K., and Gleiter, H., "Deformation-mechanism map for nanocrystalline metals by molecular-dynamics simulation," *Nature Mater.*, vol. 3, no. 1, pp. 43–47, 2004.

[308] Yang, Q., Biyikli, E., and To, A. C., "Multiresolution molecular mechanics: Statics," *Comput. Meth. Appl. Mech. Eng.*, vol. 258, pp. 26–38, May 2013.

[309] Yang, Q., Biyikli, E., and To, A. C., "Multiresolution molecular mechanics: Convergence and error structure analysis," *Comput. Meth. Appl. Mech. Eng.*, vol. 269, pp. 20–45, Feb. 2014.

[310] Yang, Q., Biyikli, E., Zhang, P., Tian, R., and To, A. C., "Atom collocation method," *Comput. Meth. Appl. Mech. Eng.*, vol. 237–240, pp. 67–77, Sept. 2012.

[311] Yang, Q. and To, A. C., "Multiresolution molecular mechanics: A unified and consistent framework for general finite element shape functions," *Comput. Meth. Appl. Mech. Eng.*, vol. 283, pp. 384–418, Jan. 2015.

[312] Yang, S. and Chen, Y., "Concurrent atomistic and continuum simulation of bicrystal strontium titanate with tilt grain boundary," *Proc. Roy. Soc. London A: Math. Phys. Eng. Sci.*, vol. 471, p. 20140758, Mar. 2015.

[313] Yang, S., Xiong, L., Deng, Q., and Chen, Y., "Concurrent atomistic and continuum simulation of strontium titanate," *Acta Mater.*, vol. 61, pp. 89–102, Jan. 2013.

[314] Yang, S., Zhang, N., and Chen, Y., "Concurrent atomistic-continuum simulation of polycrystalline strontium titanate," *Philos. Mag.*, vol. 95, pp. 2697–2716, Aug. 2015.

[315] Yang, W. and Xiao, S., "Extension of the temperature-related Cauchy-Born rule: Material stability analysis and thermo-mechanical coupling," *Comput. Mater. Sci.*, vol. 41, pp. 431–439, Feb. 2008.

[316] Yang, Z. Q., Chisholm, M. F., He, L. L., Pennycook, S. J., and Ye, H. Q., "Atomic-scale processes revealing dynamic twin boundary strengthening mechanisms in face-centered cubic materials," *Scripta Mater.*, vol. 67, pp. 911–914, Dec. 2012.

[317] Yu, J., Zhang, Q., Liu, R., Yue, Z., Tang, M., and Li, X., "Molecular dynamics simulation of crack propagation behaviors at the Ni/Ni_3Al grain boundary," *RSC Adv.*, vol. 4, pp. 32749–32754, July 2014.

[318] Yu, W. and Wang, Z., "Interactions between edge lattice dislocations and $\Sigma 11$ symmetrical tilt grain boundaries in copper: A quasi-continuum method study," *Acta Mater.*, vol. 60, pp. 5010–5021, Aug. 2012.

[319] Yu, W. and Wang, Z., "Interactions between edge lattice dislocations and $\Sigma 11$ symmetrical tilt grain boundary: comparisons among several FCC metals and interatomic potentials," *Philos. Mag.*, vol. 94, pp. 2224–2246, July 2014.

[320] Yu, W. and Wang, Z., ""Positive" and "negative" edge dislocations simultaneously interacting with $\Sigma 11$ GB during nanoindentation," *Comput. Mater. Sci.*, vol. 87, pp. 150–159, May 2014.

[321] Zbib, H. M., Hiratani, M., and Shehadeh, M., "Multiscale Discrete Dislocation Dynamics Plasticity," in *Continuum Scale Simulation of Engineering Materials* (Raabe, D., Roters, F., Barlat, F., and Chen, L.-Q., eds.), pp. 201–229, Wiley-VCH Verlag GmbH & Co. KGaA, 2005.

[322] Zhang, R. F., Wang, J., Beyerlein, I. J., and Germann, T. C., "Dislocation nucleation mechanisms from fcc/bcc incoherent interfaces," *Scripta Mater.*, vol. 65, pp. 1022–1025, Dec. 2011.

[323] Zhang, R. F., Wang, J., Beyerlein, I. J., Misra, A., and Germann, T. C., "Atomic-scale study of nucleation of dislocations from fcc–bcc interfaces," *Acta Mater.*, vol. 60, pp. 2855–2865, Apr. 2012.

[324] Zhao, X.-C., Liu, X.-M., Gao, Y., and Zhuang, Z., "Molecular dynamical investigation on plastic behavior of Cu(100) twist-grain boundary under shear load," *Acta Phys. Sinica*, vol. 59, no. 9, pp. 6362–6368, 2010.

[325] Zheng, Y. G., Lu, J., Zhang, H. W., and Chen, Z., "Strengthening and toughening by interface-mediated slip transfer reaction in nanotwinned copper," *Scripta Mater.*, vol. 60, pp. 508–511, Apr. 2009.

[326] Zhou, X. W., Johnson, R. A., and Wadley, H. N. G., "Misfit-energy-increasing dislocations in vapor-deposited CoFe/NiFe multilayers," *Phys. Rev. B*, vol. 69, p. 144113, Apr. 2004.

[327] Zhu, T., Li, J., Samanta, A., Kim, H. G., and Suresh, S., "Interfacial plasticity governs strain rate sensitivity and ductility in nanostructured metals," *Proc. Natl. Acad. Sci.*, vol. 104, pp. 3031–3036, Feb. 2007.

[328] Zhu, T., Li, J., Samanta, A., Leach, A., and Gall, K., "Temperature and strain-rate dependence of surface dislocation nucleation," *Phys. Rev. Lett.*, vol. 100, p. 025502, Jan. 2008.

[329] Zienkiewicz, O. C., Taylor, R. L., and Zhu, J. Z., *The finite element method: Its basis and fundamentals*. Amsterdam: Butterworth-Heinemann, 7th ed., Sept. 2013.

[330] Zimmerman, J. A., Bammann, D. J., and Gao, H., "Deformation gradients for continuum mechanical analysis of atomistic simulations," *Int. J. Solids Struc.*, vol. 46, pp. 238–253, Jan. 2009.

[331] Zimmerman, J. A., Gao, H., and Abraham, F. F., "Generalized stacking fault energies for embedded atom FCC metals," *Modelling Simul. Mater. Sci. Eng.*, vol. 8, no. 2, p. 103, 2000.